The Microwave Radiometer Spacecraft

A Design Study

Robert L. Wright, *Editor*

NASA

The Microwave Radiometer Spacecraft

A Design Study

Robert L. Wright, *Editor*
Langley Research Center
Hampton, Virginia

PREFACE

Late in 1977, a multidisciplinary team was assembled at NASA Langley Research Center to select a potential future space mission requiring large space structures technology and to design a spacecraft to accomplish that mission. The study was sponsored by the NASA Office of Aeronautics and Space Technology (OAST) through the Large Space Systems Technology (LSST) Program Office. The overall objective of the study was to characterize the mission hardware in sufficient detail to identify enabling and pacing technologies, to establish development priorities, and to provide a focus for research and development activities. The mission was to be futuristic enough to require significant advances in technology, yet credible enough to allow an assessment of feasibility.

A previous LSST contractual effort[1] had provided a comprehensive review of future NASA missions. The study condensed approximately 200 potential missions into 10 candidate missions requiring technology advancement and large structures, of which three were judged to be representative and identified as focus missions for detailed study. These three missions, communications (electronic mail), global crop forecasting (soil moisture), and atmospheric research (radio telescope), were considered comprehensive enough to identify technology requirements applicable to many future missions. The previously mentioned design study team was selected to study the microwave radiometer spacecraft for global crop forecasting in the late 1990's.

The design study concentrated on research areas requiring the most intense attention; they are

1. Mission and spacecraft requirements

2. Design and structural concepts

3. Electromagnetic concepts

4. Control concepts

This publication presents papers describing the results of the study in these research areas. Other areas normally analyzed in a complete system study, such as data management, operations, environmental effects, and costs, have not been assessed. It is felt that no significant advances in current state of the art in these areas are necessary for the microwave radiometer spacecraft system. The spacecraft design concept underwent several iterations (e.g., changes in antenna diameter and boom length) as a result of trade analyses conducted during the study. There are discrepancies among the papers in some of the mission and spacecraft physical parameters. Many of the analyses were initiated before

---

[1]Dienemann, M. A.; and Butterfield, A. J.: A Review of Large Area Space Systems Toward Identification of Critical or Limiting Technology. NASA CR-145339, 1978.

optimization studies were complete. It is believed that the differences are not significant for this study, in that a complete final system design has not been attempted. The trade studies included in the volume vary in level of detail; a chronological presentation of all the design iteration details would be too voluminous for inclusion herein.

The use of trade names in this publication does not constitute endorsement, either expressed or implied, by the National Aeronautics and Space Administration.

Uriel M. Lovelace
Design Study Team Leader

CONTENTS

PART IV - CONTROL CONCEPTS

APPENDIXES

MICROWAVE RADIOMETER SPACECRAFT
DESIGN STUDY TEAM

Team Leader

Uriel M. Lovelace
NASA Langley Research Center

Members:

Pradeep K. Agrawal	RCA
Hans-Juergen C. Blume	NASA Langley Research Center
G. F. Brooks	Kentron International
Harold G. Bush	NASA Langley Research Center
Michael F. Card	NASA Langley Research Center
C. R. Cockrell	NASA Langley Research Center
L. Bernard Garrett	NASA Langley Research Center
J. W. Goslee	NASA Langley Research Center
William F. Hinson	NASA Langley Research Center
W. Ray Hook	NASA Langley Research Center
J. Kermit Jensen	Kentron International
Lloyd S. Keafer, Jr.	NASA Langley Research Center
John R. McIlhaney	Kentron International
Raymond C. Montgomery	NASA Langley Research Center
Larry D. Pinson	NASA Langley Research Center
James H. Ramsey	Kentron International
Leo Staton	NASA Langley Research Center
Calvin T. Swift	NASA Langley Research Center
Robert L. Wright	NASA Langley Research Center

EXECUTIVE SUMMARY

Uriel M. Lovelace
NASA Langley Research Center
Hampton, Virginia

SUMMARY

Soil moisture sensing, essential to crop forecasting, can be conducted remotely from space by using passive microwave radiometry for all-weather, day-night operations and a large antenna system (large space structure) for high spatial resolution. Studies conducted by the National Academy of Science (ref. 1) and the NASA Office of Space and Terrestrial Applications (ref. 2) have established the need and feasibility of soil moisture mapping from microwave sensing for global crop forecasting.

A conceptual design has been developed for a microwave radiometer spacecraft (MRS) using a large passive reflector, microwave radiometers, and advanced control concepts. Mission requirements and trade-offs have been defined, and major subsystems (structural, electromagnetic, surface, and attitude control) have been conceptually designed. This paper presents an overview of the mission and a summary of the study results.

INTRODUCTION

Soil moisture mapping for global crop forecasting can be conducted from space by using passive microwave radiometry. The concept of passive microwave sensing is depicted schematically in figure 1. Shown is a swath, or continuous footprint, composed of many resolution elements, along an orbital ground track. Each resolution element radiates energy at various microwave frequencies. This microwave radiation is reflected via an electromagnetic reflector to a receiving horn located at the focus of the reflector. The receiving sensor, a radiometer in this case, records the radiated energy from the surface as brightness temperature. The brightness temperature is a product of the soil ambient temperature and emissivity. The emissivity is strongly dependent on soil dielectric properties which change significantly with water content.

A large space structure for passive microwave sensing, the microwave radiometer spacecraft (MRS), has been conceptually designed. This design study assumes the MRS to be erected, aligned, and checked after delivery to an intermediate orbit by the Space Transportation System (STS). No analysis of this assembly operation has been conducted nor has the transfer from this interior orbit to the operational orbit been assessed. The MRS is also assumed to continually point to nadir. It will be in a data-gathering mode for approximately 90 percent of each orbit. Data will be coded and transmitted to Earth for analysis. The power and data handling requirements have not been analyzed in detail; however, it appears that neither will require state-of-the-art advances.

MISSION DEFINITION

In defining a remote sensing mission centered around soil moisture measurements, it is appropriate to assess the possibility for measuring other surface parameters which may be of interest in crop, weather, or other environmental forecasting. In addition to soil moisture, some needed information concerning water surface temperature, salinity, water pollutants, water roughness, and ice may be obtained via passive microwave radiometry at frequencies and resolutions similar to those required for soil moisture measurements. The mission design requirements and associated spacecraft design parameters are listed in table I. The requirement for all-weather, day-night observation results from a need to monitor all surface areas as frequently as possible at a low (<5 GHz) microwave frequency in order to penetrate clouds, haze, and ground covers. The requirement for high resolution (<1 km and 1 K) results from the need to map soil moisture, pollutants, and ice boundaries accurately enough to discern rain showers and irrigation irregularities and to closely monitor pollutant and ice boundary changes. Contiguous mapping (200-km swath width) and frequent revisits (one per week) permit complete global coverage frequently enough to sample short-term variations in the measurement parameters.

These specific mission requirements can be summarized in two broad mission objectives:

1. To collect microwave data useful in solving national problems related to food production, coastal zone safety, health and productivity, environmental quality, and climate and oceanology

2. To demonstrate the operational potential of a complete microwave space observatory with multiwavelength, multipurpose sensing for all Earth observation disciplines.

A more comprehensive description of the mission definition from which this study progressed is contained in reference 3.

SYSTEM DESIGN

Utilizing these mission requirements, along with several ground rules, the study proceeded into a conceptual system synthesis. The ground rules and study assumptions were as follows:

1. Passive rather than active microwave sensing would be used. The passive approach permits a simpler radiometric design and eliminates the environmental question of the effect of radiating microwave energy over populated regions.

2. Spacecraft design would be compatible with transport to orbit by the current STS. No definitive post-Shuttle launch system exists currently, and the NASA LSST Program is constrained by the STS.

3. Design lifetime would be at least 15 years. Resupply of expendables or repair of damaged or failed components was assumed to be available at 3-year intervals.

The previously defined measurement requirements, along with these ground rules, result in the list of system requirements in table II. Three frequencies have been selected: the lowest, 1.08 GHz, permits sensing through cloud cover and vegetation to a soil depth of about 25 cm for measuring soil moisture; the second, 2.03 GHz, has been used extensively in water surface-temperature and salinity mapping experimentation; and the third, 4.95 GHz, was selected to separate parameters with overlapping spectral signatures. The radiometers will permit controlled frequency changes of approximately 1/4 octave on either side of these center frequencies to avoid noise sources.

To meet the 1-km resolution requirement at the lowest frequency, an antenna beam aperture of 300 m is required at an altitude of 1000 km. The 1000-km altitude has been selected to provide adequate orbit lifetime. To meet the 200-km swath requirement, 200 radiometric receivers must be arrayed at the focal arc. With a simple feed horn design, this results in an overall antenna diameter of 725 m. A focal-length-to-diameter ratio of approximately 2 provides an efficient beam pattern and results in a focal length of 575 m. The antenna is being designed to a 90-percent efficiency and a 70-dB gain. At the lowest frequency, surface smoothness of 1/50 of a wavelength is required to reduce losses from rms surface errors to below 10 percent.

Two orbital inclinations have been evaluated: 60° and Sun synchronous (about 98°). Most of the measurements of interest are between latitudes of 60°; however, the Sun-synchronous orbit may offer some design relief in the thermal control area. If the thermal cycling and associated structural distortions at 60° inclination become too severe, the Sun-synchronous orbit may allow an easier thermal design with an acceptable coverage or mapping penalty.

Pointing and slew rate requirements by themselves are not particularly stringent; however, when related to a spacecraft approaching 1 km in diameter, they represent a sizable challenge. Pointing is most critical in the roll and yaw planes to provide accurate contiguous mapping. The slew rate is necessary to maintain the reflector orientation to the nadir.

Throughout this study, the Design Study Team has adhered rigidly to the mission performance requirements of reference 3 (and summarized in table I). Relaxation or modification of these requirements opens many additional possibilities for the antenna design. The effects of four design parameters on antenna overall diameter are summarized in the following table:

Electromagnetic frequency, GHz	1.0	1.4	1.4	1.4	1.4
Spatial resolution, km	1.0	1.0	2.0	2.0	2.0
Phase correction of feed horns	No	No	No	Yes	Yes
Orbit altitude, km	750	750	750	750	400
Antenna diameter, m	725	575	290	85	45

As can be seen, the single most significant factor is the inclusion of some means, such as a dielectric lens, to phase correct those feed horns not located at the reflector focus. The angular limits of such corrections have not been established; therefore, if the dielectric lens approach is pursued, other mission requirements, such as swath width and revisit frequency, may have to be modified. Diameter reduction options such as increased frequency, decreased resolution, and decreased orbital altitude would allow reduction from the 725-m baseline diameter to approximately 150 m.

Several structural approaches have been evaluated at the conceptual design level for support of the electromagnetic mesh surface. The geodesic structural concept represents the baseline configuration and is shown in figure 2. The antenna is formed from a tetrahedral truss to which a radio-frequency (RF) mesh is attached. A stiffening ring provides a structural mount for booms, feeds, tension cables, subsystem modules, and attitude control subsystem. The tetrahedral structure is attached to the stiffening ring at several locations by control actuators and is capable of three-axis articulation with respect to the structural ring and remainder of the vehicle. The spacecraft is just over 800 m in diameter, with 600 radiometers (200 at each of 3 frequencies) suspended on a 200-m-long beam at the focal arc of the reflector. These radiometers are positioned by two, 575-m-long booms with four tension cables providing stability. Attached to the structural ring are solar panels and subsystem support modules. The reflector mesh is attached to the inside of the geodesic structure after the shell is constructed. The basic structural member for all considered concepts is the graphite composite nestable tube. Cursory analysis of alternate beam concepts was made, but no attempt was made to quantify relative advantages. One concept being analyzed for pointing and slewing control is a dual rotating momentum wheel. These rings or flexible cables would be mounted on the structural rim at the edge of the reflector.

Brief consideration was given to a single-layered geodesic structure to replace the tetrahedral truss. This single-layered configuration would look much the same as that of figure 2, except the structural ring would be located somewhat inboard of the perimeter. Control required to maintain spherical shape of the RF mesh would be greatly complicated.

Another structural approach, using deployable modules, was evaluated briefly. Utilization of deployable modules significantly simplifies the erection and assembly process in orbit; however, packaging inefficiencies quickly expand transportation costs to exorbitant levels.

An alternate structural concept, radically different from others considered, is shown in figure 3. The dimensions for this concept are essentially the same as those for the geodesic approach. The rim is composed of 126-m-square sections again constructed in space from graphite composite nestable tubes. The spokes of the wheel are alternately tension cables for rim stiffness and stringer cables for reflective mesh attachment. As with the other concepts, momentum wheels are proposed as control devices and could be mounted to the upper edge of the rim. Photovoltaic power sources are shown attached to the rim.

Table III provides a summary comparison of weight, Space Shuttle flights, and structural member lengths for the three concepts. Also included in this figure is a comparison of a deployable module concept for the geodesic structure. Although not very promising from a packaging efficiency viewpoint, the approach of constructing the reflector from foldable modules was investigated. As indicated, the packing volume and associated Shuttle flights required would eliminate this approach. If sized to provide the necessary surface smoothness, the structural elements must be about 6.4 m long; if sized to the Shuttle cargo bay, they could be 18 m long. For the geodesic structure, both element lengths are compared in this table. The 18-m element would require more complex reflector attachment joints in order to provide the required surface accuracy. Listed are weights of the reflector backup structure alone as well as of the total spacecraft for the various configuration options. As indicated earlier, the tension rim approach appears promising in that the entire

system could be delivered in two Shuttle flights. The deployable double-layered geodesic dome requires 27 modules, weighing over 3200 kg each, just to build the antenna structure. Only one module will fit in the Shuttle cargo area; therefore, 29 flights are required to deliver the complete structure. The remaining components are arranged around the modules so that actually about 6400 kg is carried in each flight, still below the 29 500-kg capability.

In reviewing the requirements for and approaches to pointing and slewing control, an interesting concept has been advanced. Figure 4 depicts schematically the dual momentum vector control concept. This concept provides three-axis pointing and slewing capabilities while consuming minimal expendables. The approach utilizes two large-diameter counterrotating rings or wheels suspended magnetically in many race supports distributed around the antenna structure. When the magnets are energized, attracting the two wheels, the resulting gyroscopic torque produces a rate along the appropriate axis. Roll control is provided by altering the relative rotational velocity of the two wheels. The design of such a system presents some interesting engineering challenges. Wheels with diameters of 500 to 800 m, and with sufficient momentum storage capability, require rims only a few millimeters in diameter and, therefore, are extremely flexible. The structural dynamics and stabilization of such devices are evaluated in reference 4.

The area of surface control is extremely important in the design of large space structures. Thermal gradients, control forces, and construction tolerances can result in significant shape distortions and seriously degrade the structure performance. It is generally agreed that active surface control will be required for these large antennas. The use of electrostatics is being analyzed for mounting the reflector membrane on antennas with a structural framework, or strongback. Figure 5 is a sketch of an approach for controlling surface smoothness with electrostatic and mechanical forces. Three levels of control are depicted in this approach: first, the overall alignment is provided through position acutators at the four corners of the panel; second, boundary shape and contour are provided through tension cables along the edges of the panel; and finally, smoothness across the panel surface is maintained by electrostatically charging pads and stretching the membrane to the appropriate contour. As expected, numerous technology problems surface with this approach. Analysis and experimentation are required to establish electromagnetic effects of structural joints, control effects of the membrane boundary, electrostatic pressure requirements and distribution over the panel, surface shape-sensing approaches, and hierarchial control theory. Little effort was exerted to analyze this concept during the study. It is currently felt that this approach is much too complex and heavy for application to such a large structure. Current thinking is that the membrane would not be modular but would be a continuous surface requiring fewer electrodes and simplifying the boundary control problems. Research to understand electrostatics and membrane performance is currently underway with a test reflector depicted in figure 6. Results to date of this research are reported in reference 5.

Figure 7 shows an approach for controlling the shape of meshes attached to a flexible structure (the tension rim concept of fig. 3). A cross section of the reflective mesh is shown suspended from a catenary via a "bootlace" pulley arrangement. Drive motors at the outer edge vary the tension in the bootlace causing the mesh contour to change. Additional control is obtained by moving the mesh outer edge in a vertical direction. This approach is at the preliminary concept level, and additional analysis and testing is necessary before a detailed design can be initiated.

TECHNOLOGY IMPROVEMENT GOALS

Some technology improvements goals derived in this study are summarized in table IV. If materials with a coefficient of thermal expansion of 5×10^{-8} K^{-1} were available, thermal distortion could be significantly reduced and the shape control problem could be simplified. Current economically produced graphite composites have thermal expansion coefficients of 10^{-6} K^{-1}. Not quantified in the table but representing a significant design challenge is the material for the reflective mesh or membrane and the cables and catenaries used to varying degrees in the various concepts. Many of the candidate materials suffer severe degradations when exposed to ultraviolet radiation. New materials or protections will have to be developed. Packaging density is included as a goal simply to ensure that the limiting criterion for Shuttle flights is mass rather than volume. In order to design a 90-percent efficient, 70-dB antenna, the ratio of surface accuracy to diameter must be on the order of 10^{-7}. This is a significant advance when one considers that the best current Earth-manufactured antenna with a solid reflector has an equivalent surface accuracy. Pointing and slew control of this large reflector will require a device with momentum storage of 10^8 newton-meter-second (N-m-sec). Current laboratory test momentum wheels provide 10^5 N-m-sec. Although the pointing control and slew rate in themselves do not represent a significant state-of-the-art advance, when applied to a structure of the size and flexibility of the MRS, they do represent a significant challenge. Attitude control system optimization can result in considerable savings in the expendables required. Some surface control concepts necessitate an extremely complex control algorithm with thousands of actuators. Today's technology permits the solution of control equations with a few hundred nodes; therefore, particular attention must be paid to the design of hardware and software for the surface control system and the associated analysis and simulation algorithms.

CONCLUDING REMARKS

The concepts discussed in this paper represent a few of the novel approaches developed during this study. All these concepts must be evaluated and compared with more conventional approaches before definitive preliminary designs and the relative advantages can be established. For example, the dual momentum vector control concept must be compared with gravity gradient or mass expulsion; the electrostatic membrane, with a rigid nonflexing structure; and the graphite nestable column member, with the "beam builder." Detailed structural, dynamic, electromagnetic, and orbit design analyses must be completed before more comprehensive system design can progress; however, the study has identified system level design and technology requirements and provided a basis for ordering research and development to expand state-of-the-art capability. The study team has concluded that it is feasible to design a spacecraft to meet the mission requirements. Several of the innovative concepts advanced during this study could significantly enhance the performance of such a spacecraft as well as many other large antennas or other structures.

REFERENCES

1. Committee on Remote Sensing Programs for Earth Resource Surveys: Microwave Remote Sensing From Space for Earth Resource Surveys. Contract NASW-3043, Natl. Acad. Sci.-Natl. Res. Counc., 1977. (Available as NASA CR-157891.)

2. Proposed NASA Contribution to the Climate Program. NASA TM-80497, 1977.

3. Keafer, Lloyd S., Jr.: Mission Definition for a Large-Aperture Microwave Radiometer Spacecraft. The Microwave Radiometer Spacecraft - A Design Study, Robert L. Wright, ed., NASA RP-1079, 1981, pp. 17-32. (Paper in this compilation.)

4. Montgomery, Raymond C.; and Johnson, C. Richard, Jr.: Adaptive Control System for Large Annular Momentum Control Device. The Microwave Radiometer Spacecraft - A Design Study, Robert L. Wright, ed., NASA RP-1079, 1981, pp. 169-187. (Paper in this compilation.)

5. Goslee, J. W.; and Mihora, D. J.: Test Progress on the Electrostatic Membrane Reflector. The Year of the Shuttle, Proceedings of Eighteenth Space Congress Canaveral Council Tech. Soc., c.1979, pp. 4-13 - 4-39.

TABLE I.- MISSION REQUIREMENTS AND PARAMETERS

Requirement	Parameter
All-weather, day-night operation	Microwave frequency .... <5 GHz
High resolution	Spatial resolution .... <1 km Temperature resolution .... <1 K
Contiguous mapping	Swath width .... 200 km
Frequent revisits	Number of revisits per week .... 1 to 2

TABLE II.- SYSTEM DESIGN REQUIREMENTS

Frequency .... 1.08, 2.03, and 4.95 GHz
Antenna aperture .... 300 m/beam, 725 m total
Focal length .... 575 m
Gain .... 70 dB
Surface accuracy .... $\approx^a\lambda/50$
Orbit altitude .... 650 to 1000 km
Orbit inclination .... 60° and Sun synchronous
Lifetime .... 15 years, 3-year resupply
Pointing .... 0.01°
Slew rate .... 0.06 deg/sec
Data rate .... $\approx$30 megabits/sec
Power .... 10 kW
Launch system .... STS

[a]λ denotes wavelength.

TABLE III.- WEIGHT AND PACKAGING COMPARISONS

[Total area of spacecraft is 412 825 m^2]

Parameter	Double-layer tetrahedral truss				Single-layer geodesic truss	Tension rim
	Deployable		Erectable			
Element length, m	6.43	8.75	6.43	18.0	18.0	
Element diameter, m	0.058	0.058	[a]0.058	[a]0.1016	[a]0.1016	
Quantity of elements	104 004	57 780	106 497	13 590	[b]5424	
Module area, m^2	15 470	28 610				
Module weight, kg	3190	4153				
Total weight, kg	86 130	62 295	79 991	45 813	18 351	[c]8381
Area density, kg/m^2	0.2033	0.1470	0.1888	0.1081	0.0433	0.0198
Shuttle flights	27	15	2.7	1.6	0.6	0.3
Limiting criteria	Volume	Volume	Weight	Weight	Weight	Weight

[a]Mean diameter of tapered column.
[b]Includes stiffener ring.
[c]Includes cable weight.

TABLE IV.- STUDY-DERIVED TECHNOLOGY IMPROVEMENT GOALS

	State of the art	Goal
Material coefficient of thermal expansion, K^{-1}	10^{-6}	5×10^{-8}
Packaging density, kg/m^3		115
Ratio of reflector accuracy to diameter	10^{-6} ([a]10^{-7})	10^{-7}
Momentum storage, N-m-sec	10^5	10^8
Pointing, deg	10^{-1}	10^{-2}
Number of control actuators	10^2	10^3

[a]Solid reflector technology.
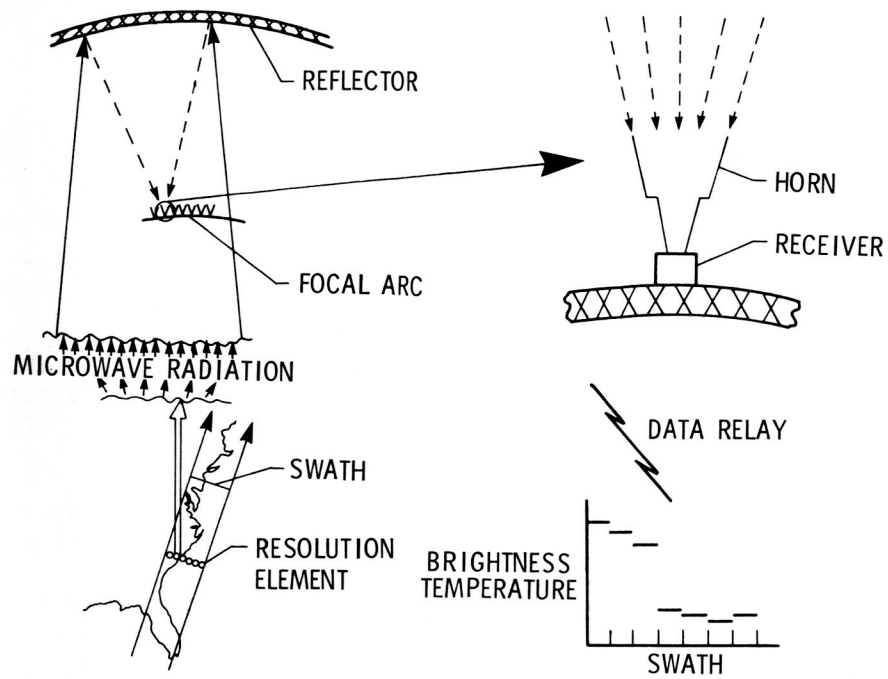
Figure 1.- Passive microwave sensing concept.
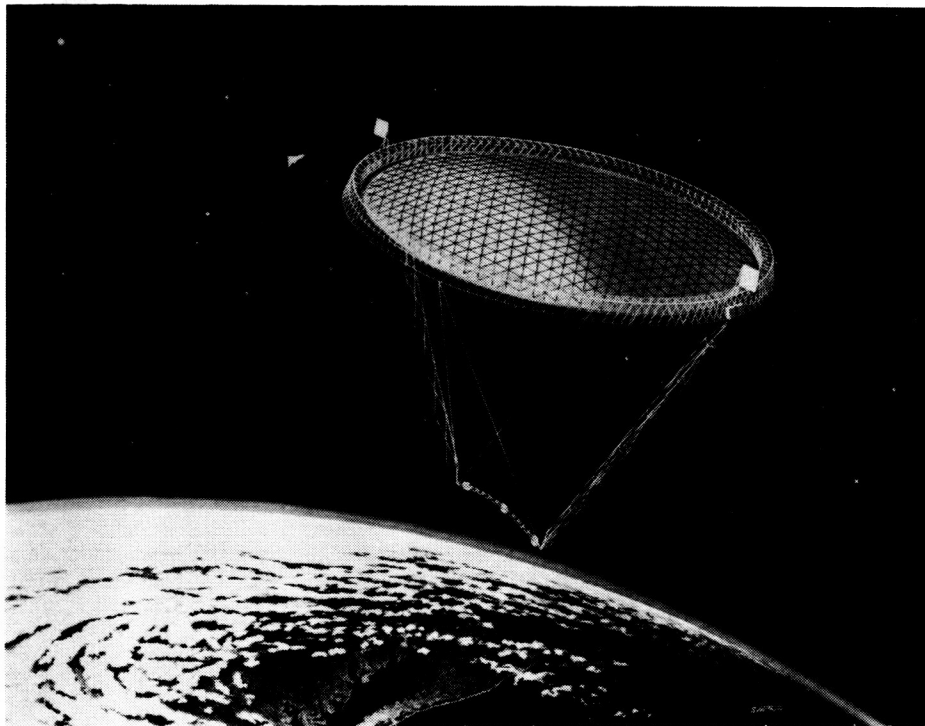
LCh-78-176

Figure 2.- Double-layered geodesic structural concept for microwave radiometer spacecraft (tetrahedral truss).

10
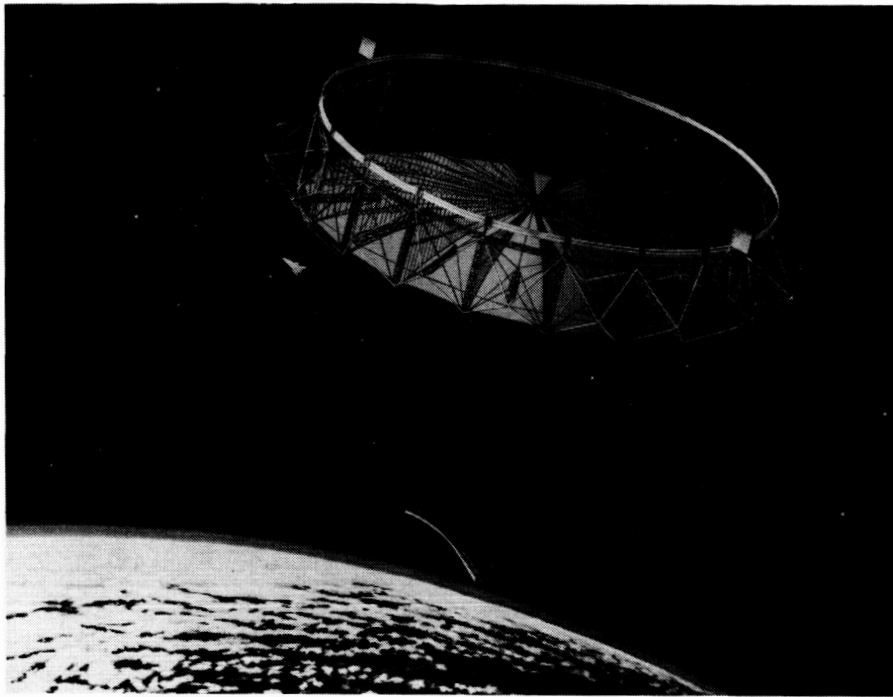
Figure 3.- Tension rim concept for microwave
radiometer spacecraft.
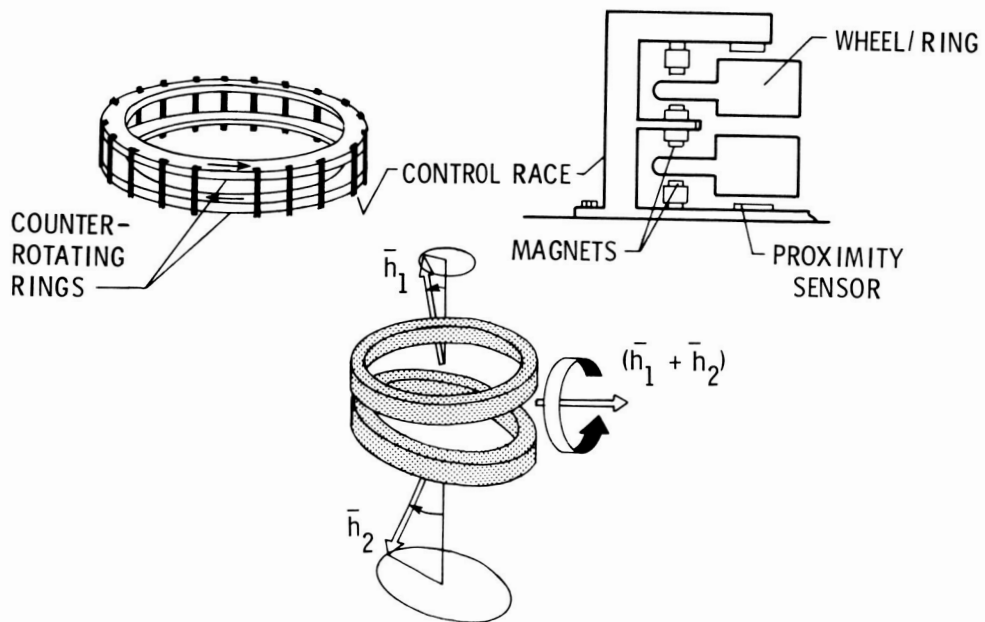
Figure 4.- Dual momentum vector control concept.
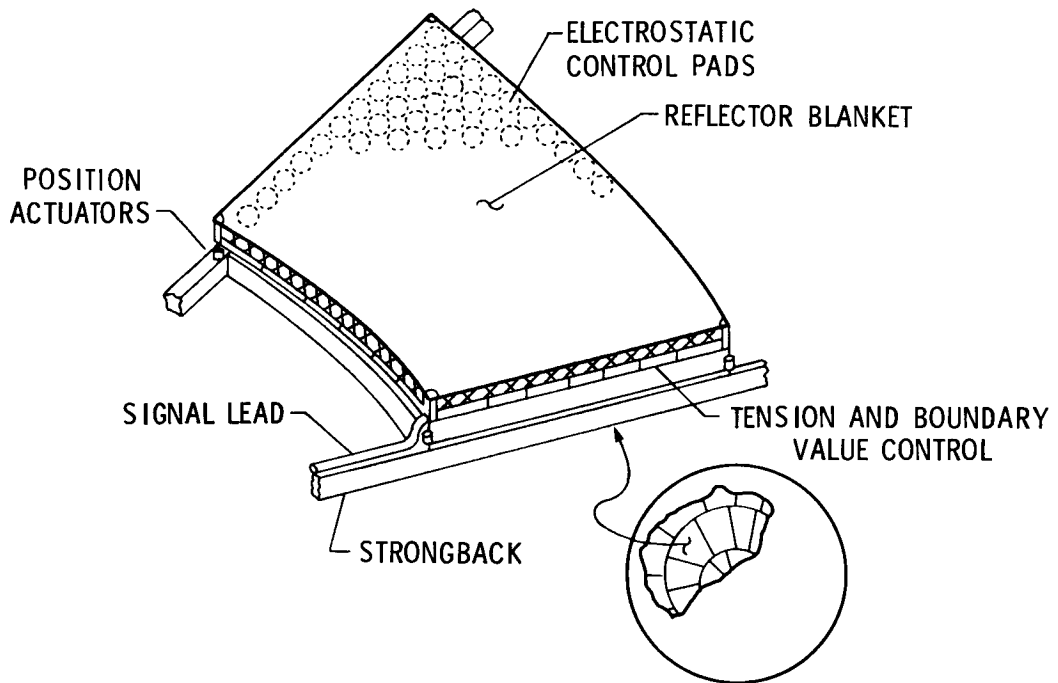
Figure 5.- Electrostatically controlled panel concept.
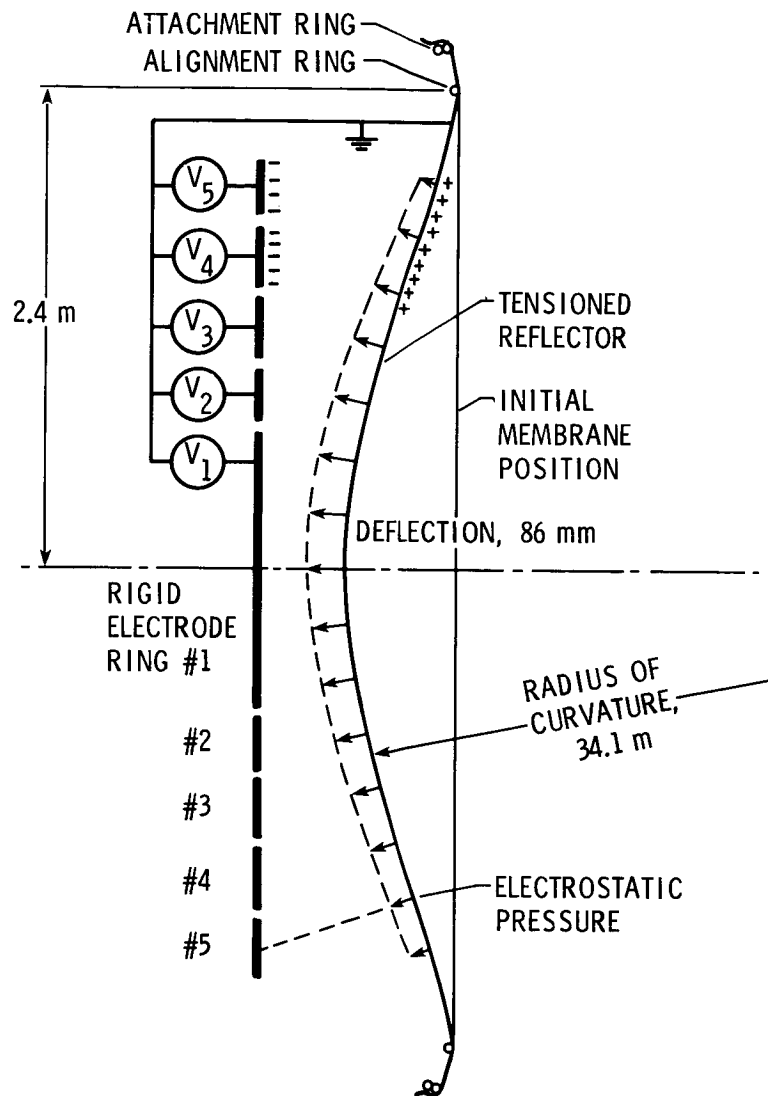
Figure 6.- Schematic of 4.8-m-diameter electrostatic
membrane reflector.
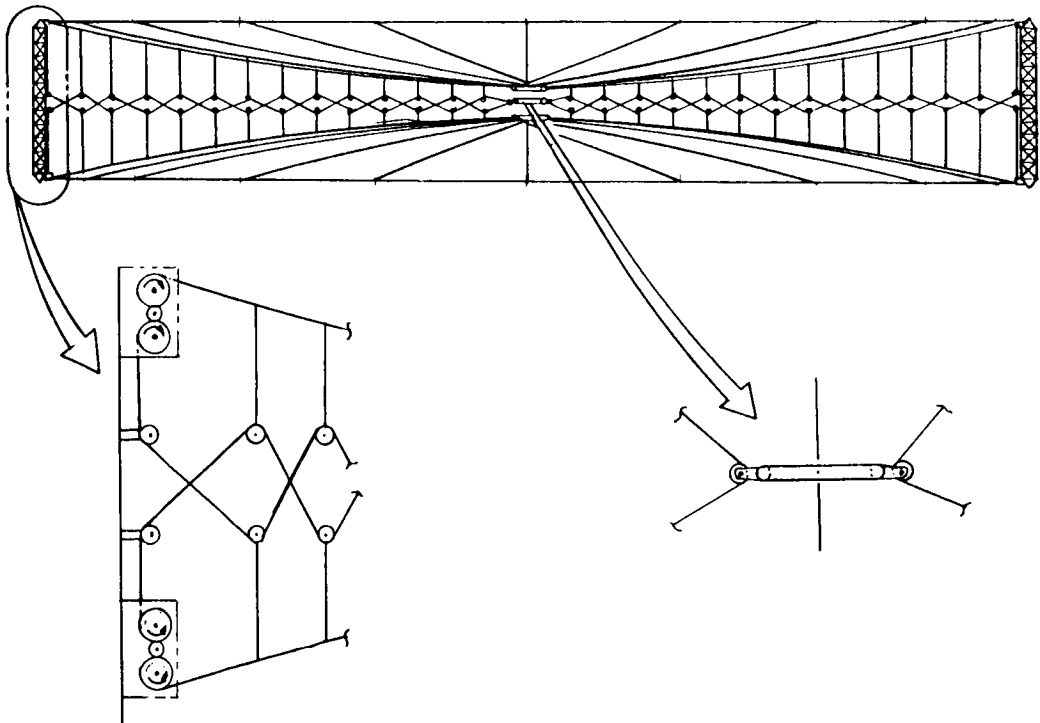
Figure 7.- Surface control concept for flexible structure.

PART I

MISSION AND SPACECRAFT REQUIREMENTS
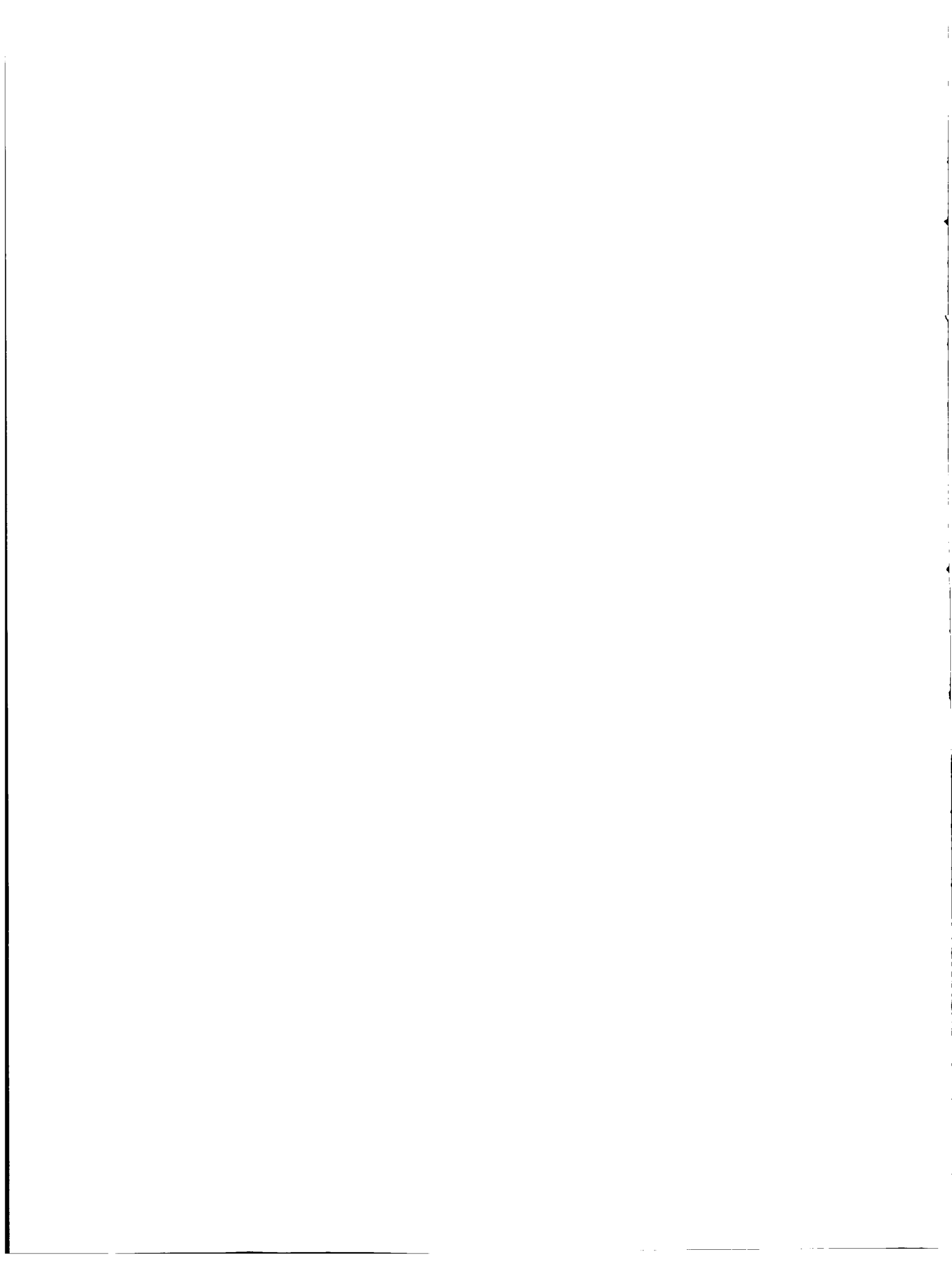
MISSION DEFINITION FOR A LARGE-APERTURE MICROWAVE RADIOMETER SPACECRAFT

Lloyd S. Keafer, Jr.
NASA Langley Research Center
Hampton, Virginia

SUMMARY

An Earth-observation measurements mission is defined for a large-aperture micro-wave radiometer spacecraft. This mission is defined without regard to any particular spacecraft design concept. Space data application needs, the measurement selection rationale, and broad spacecraft design requirements and constraints are described. The effects of orbital parameters and image quality requirements on the spacecraft and mission performance are discussed. Over the land the primary measurand is soil moisture; over the coastal zones and the oceans important measurands are salinity, surface temperature, surface winds, oil spill dimensions, and ice boundaries; and specific measurement requirements have been selected for each. Near-all-weather operation and good spatial resolution are assured by operating at low microwave frequencies using an extremely large aperture antenna in a low-Earth-orbit contiguous-mapping mode.

INTRODUCTION

During the last decade, remote sensing has become an integral part of weather forecasting and Earth resources management, and some of today's satellites, such as Improved Tiros Operational Satellite (ITOS) and Landsat, provide remotely sensed information to forecasters and resource managers on an operational basis. Much of the weather monitoring with ITOS is done with optical sensing of the clouds and atmosphere at or above cloud level, because optical sensors cannot penetrate the clouds to the lower atmosphere and to the Earth's surface. Thus, data from these regions are scarce, particularly from the ocean expanses and for the conditions of adverse weather. Likewise, Earth resources monitoring with Landsat cannot obtain surface data with its optical sensors on a full-time basis because of cloud cover. Therefore, timely monitoring of dynamic conditions cannot be guaranteed and the full applications potential of the observations may be lost. For example, failing to monitor crops at crucial growing periods makes yield forecasting less reliable.

Microwave sensors can complement the optical[1] sensors by being able to see through clouds and by sensing parameters that cannot be obtained with optical sensors. The Seasat (launched June 1978) and Nimbus-G (launched Oct. 1978) satellites have such microwave capability, but because of their small antennas, the microwave

---

[1]Optical refers to the wavelength region of approximately 0.25 μm to 250 μm while microwave refers to the adjacent region extending to approximately 1 m.

systems are limited in their spatial resolution. Consequently, they can monitor only those surface phenomena whose variations occur over large spatial scales, e.g., ocean conditions.

The need for complementing optical remote sensing of Earth phenomena with full-time, high-spatial-resolution microwave sensing and the challenge of defining and developing the enabling technology provide the impetus for this mission definition and related design study efforts. Mission definition serves as the initial step in the design process.

MISSION DEFINITION

Mission Outline

A mission envelope is defined with the aid of table I. Listed opposite the broad, long-term sensing goals or objectives are some of the major constraints they impose on the mission.

Day and night operation is possible with all microwave frequencies but the near-all-weather part of the full-time-monitoring goal imposes the constraint of operating at low frequencies.

Although relatively transparent to microwave frequencies, the atmosphere causes appreciable attenuation as illustrated by figure 1. Under clear and dry conditions this attenuation is usually less than 10 dB for frequencies up to 200 GHz. For conditions of heavy clouds and rain, however, the attenuation is much greater and, in addition, it is extremely variable both spatially and temporally. Therefore, it is difficult to make precise measurements of surface phenomena under such atmospheric conditions. Using the criterion of 10 dB as a practical maximum atmospheric attenuation (which assumes that some knowledge of cloud cover is obtained independently, e.g., visible imagery), the operating frequencies for a microwave radiometric mission are constrained to be approximately 10 GHz or less. (This is the operating frequency range called "near-all-weather" in this paper.)

Global coverage implies permission to collect information over areas where other microwave systems are operating and over foreign countries. This problem is simplified by using a passive system so no areas are irradiated by microwaves. The resolution element size at the Earth's surface of a passive microwave system is proportional to the wavelength and altitude and inversely proportional to the collecting aperture size (ref. 1). Since long wavelengths were chosen for their near-all-weather capability, high spatial resolution can be obtained only by using a large-aperture system in low Earth orbit.

Multiparameter sensing and operational monitoring reflect a view of the future for Earth monitoring satellites. The goal of collecting as broad a range of useful resources and environmental information as possible implies the use of multiple frequencies to better sense and separate data from parameters with different microwave signatures. Multiparameter sensing also dictates numerous sets of geographic and temporal coverage requirements. A mission based on contiguous mapping and frequent revisits is desired. The final comment on the mission outline deals with the microwave radiometer's role in a global services system dedicated to operational monitor-

ing of Earth resources and the environment. Simply because of its size, the micro wave radiometer is the dominant part of the multipurpose data acquisition satellite, and attention must be given to its compatibility with other remote sensing systems in order to operate all the sensors efficiently and to enhance cross-spectral synergism.

Measurement Requirements

Earth resource and environmental parameters that can be measured with a micro-wave radiometer in an orbital mission as outlined are listed in table II. Potential applications of such measurements were derived primarily from references 2 to 5. Potential domestic users of the derived information, e.g., crop yield forecasts and climate predictions, are the Federal Agencies and their constituents and clients in government, commerce, and industry. (Similar foreign users are envisioned, but no effort has been made to define them.) Thus, having established a general need for the measurements, a matrix similar to that at the top of table III summarizes the measurement requirements. In the completed matrix (not shown), measurement require-ments such as range, accuracy, spatial resolution, geographic coverage, and temporal repeat are entered in each applicable box of the matrix. Then high-priority require-ments are tagged, and the most stringent (yet reasonable) requirements for each mea-surand are labelled as pacing requirements. This technique provides a means for syn-thesizing overall requirements and making specific selections for the microwave radiometer spacecraft mission.

The selected measurement requirements are listed at the bottom of table III. The measurement range varies with each measurand. Note that the range requirements for water pollutants are paced by the sensing of oil spill thickness and the require-ments for ice are paced by determining ice boundaries. An extremely wide range of measurement needs has been expressed by data users, especially with regard to spatial resolution and temporal repeat. The selection of requirements in this table is based on an initial assessment of the mission feasibility and the benefit-to-cost ratio of the measurements. Consequently, these requirements should be viewed as being mildly flexible and subject to change based on further analysis. For example, it is known that much useful information can be obtained with relaxed requirements (e.g., micro-wave data taken with resolution elements larger than 1 km and with repeat intervals greater than 2 weeks will still complement the optical data from Landsat-type missions), but at this stage in the analysis the corresponding sacrifices in benefits do not appear necessary to assure mission feasibility or affordability. Besides, it is desirable to push the technology in design studies. In the case of the microwave radiometer spacecraft, the most stringent measurement requirements consistent with recognized physical limitations are imposed.

Radiometer Performance Requirements

The mission is defined without regard to the concept selected for the design study, i.e., the mission definition should be reasonably applicable for a beam switching, phased-array, direct reflector, or any other type of near-all-weather, high-resolution radiometer designed to meet the selected measurement requirements. Nevertheless, it is assumed that the observations are made near nadir without polari-zation preference, and the data are collected in a manner appropriate for display as images.

Performance requirements for the radiometer are detailed in table IV. The soil moisture requirement for seeing through the vegetative canopy and for penetrating the soil to a depth of 25 cm determines the lowest frequency band. Water surface temperature and salinity mapping have been done successfully using L-band and S-band, the second frequency band. A third frequency band, approximately one octave higher, provides additional measurements to separate parameters with overlapping (but different) spectral signatures. Final frequency selections within these bands are based on avoiding radar interferences.

A microwave radiometer measures the radiation in a narrow band at its operating frequency. The complete set of received radiations which can be represented by equivalent radiometric temperatures must be corrected for extraterrestrial noise and for atmospheric radiation and attenuation in order to determine the true surface-brightness temperatures. Thus, the range and accuracy requirements for the six measurands determine the requirement for the range and precision of the brightness-temperature measurements. In the brightness-temperature range from 200 to 330 K, the precision requirements expressed in terms of detectable change in brightness temperature ΔT_B is 1 K when the corresponding spatial resolution is 1 km.

Even in the lowest orbits, the $<$1 km resolution means narrow ($<$0.1°) collecting antenna beams, and 200 or more beams are required to produce the wide swath necessary for contiguous coverage.

Orbital Parameters

Altitude.- The experiment lifetime is set by those applications such as climate prediction which require measurements over a long period of time (5 to 30 years). A minimum 5-year experiment lifetime was chosen, although design lifetimes for the sensor components may be 2 to 3 times this number. The drag-to-mass ratio of the spacecraft affects the orbital lifetime (assuming no orbit boost adjustments) and thus establishes a practical lower limit on orbital altitudes, as illustrated in figure 2 (from ref. 6). The C_DA/m value for a large-aperture microwave spacecraft continually viewing in the nadir direction will probably be in the range from 0.2 to 20 and thus may allow acceptable long-life orbits as low as 500 to 900 km, respectively. The spacecraft used to calculate orbital decay had a C_DA/m of approximately 7 which requires an orbital altitude greater than 750 km. The spacecraft analyzed in reference 7, in which spacecraft weight and volume were optimized to efficiently use the space transportation system (STS), had a C_DA/m of approximately 3.5 with a resultant orbital altitude of 650 km or greater. Above this lower limit range, the final selection of orbital altitude depends primarily on the temporal repeat or revisit time. Figure 3 (adapted from ref. 8) gives the orbital altitude h necessary to achieve the specified repetition factor Q expressed in number of orbits per day. For 1-, 3-, 7-, and 14-day repeat cycles three altitude regions are possible: (1) 450 to 650 km for Q's of 15 (1-day repeat), 14 2/3 (3-day repeat), 14 6/7 (7-day repeat), and 14 13/14 (14-day repeat); (2) 800 to 1000 km for Q's of 13 2/3 to 14; and (3) 1200 to 1400 km for Q's of 12 2/3 to 13. There appears to be no advantage to orbits higher than approximately 1400 km in light of the corresponding spatial resolution sacrifice. For the two spacecraft examples cited previously, the obvious choice is the 800- to 1000-km range.

Inclination.- Orbit inclination i has a small effect on altitude; its greatest effect is on geographic coverage. Two candidate inclinations have been chosen: (1) i = 60°, to give good coverage of temperate zones and major farm belts and (2) i = 98°, to give polar coverage and the constant-time-of-day sampling associated

with Sun-synchronous orbits. For 60° inclinations, portions of two coverage plots of the United States are shown in figure 4. With a repeat interval of 1 day, only approximately 25 percent of full coverage is obtained using a 300-km swath. It is not possible to meet the requirement for contiguous coverage with this repeat interval. However, with a 1-day repeat, 100 percent or full contiguous coverage can be obtained using the selected minimum swath of 200 km. The feasibility of meeting the minimum requirement of contiguous coverage of major farm belts and coastal zones with a 1-week-repeat interval is impossible to assess at this point, for it will depend on the particular radiometer spacecraft design and the corresponding orbit parameters.

Orbit maintenance.- Orbital inclination variations are small and Earth measurements are relatively insensitive to such variations, so orbit maintenance is primarily concerned with altitude maintenance. Orbital altitude changes affect the spatial resolution, swath width, geographic coverage, and sampling repetition. Orbital altitude decreases due to atmospheric drag of the spacecraft. For example, at 900 km, using conservative estimates of antenna size, mass, cross-sectional area, and atmospheric density (solar cycle maximum), the atmospheric drag of an example spacecraft is estimated and orbital decay (semimajor axis) is calculated (fig. 5). This decay is relatively smooth as compared to the cyclic fluctuations in the perigee and apogee altitudes, also shown in figure 5, which are due to solar radiation pressure effects on the spacecraft. Performance specifications for altitude adjustments to compensate for orbital decay can be derived from the image quality requirements and from the sampling requirement. In addition to the overall sampling requirements stated previously, data users must be guaranteed that a particular orbit pass occurs with some degree of precision over the programmed area and during the programmed time. For this mission these specifications are expressed as follows:

Lateral drift of orbit   <±0.1 swath width

Sampling time drift   <±15 min for Sun-synchronous orbit
                                           <±1 hr for 60° orbit

For a particular spacecraft design, these specifications can be translated into propulsion system performance requirements and onboard propellant needs.

IMAGE QUALITY REQUIREMENTS

The need for contiguous mapping related to the goal of multiparameter sensing is listed in table II, the spatial resolution requirements for mapping are listed in table III, and the associated beam width and swath width requirements are summarized in table IV. These measurement requirements imply that "imaging" is the primary method of collecting and displaying the data for analysis and application. The quality of the images strongly affects the usefulness of the data and influences the selection of practical radiometric techniques. Consequently, it is necessary to define image quality requirements to complete the statement of performance requirements. (Surface feature mapping using data reduction algorithms is considered to be a form of imaging whose requirements are subsumed by the set derived for traditional imaging.)

In remote sensing of Earth parameters, a number of terms have been used to describe the resolution element; e.g., pixel, field of view (FOV), instantaneous field of view (IFOV), beam width, spot size, and tessera. As used herein, the resolution element is defined as the assigned field of view at the Earth's surface during a single measurement sequence.

Shape

Any shaped beam or group of beams can be stretched, compressed, or mapped by various algorithms into a continuous set of resolution elements to form a map or image. The ideal shape for the resolution element is a square but a very practical shape is a rectangle with the long dimension no greater than twice the short dimension. Actual instantaneous fields of view or beams may be elliptical and move in the line of scan to approximate a rectangle, as shown in figure 6.

Size and Size Uniformity

Traditionally in Earth observations, the size of the resolution element is determined by the half-power or 3-dB boundaries. Since the 3-dB boundaries usually are associated with the IFOV rather than the FOV during a measurement sequence, a better choice is to define the size ϵ by the largest dimension of the smallest rectangle containing 50 percent of the total power collected that is assigned to a resolution element.

The variations in resolution element sizes for a multiple beam system shall not exceed ±10 percent of the average for all beams.

Beam Efficiency

In addition to the specification of the power in the resolution element (50 percent), the beam efficiency is further defined by the specification that 90 percent of the total power collected, that is assigned to a resolution element, must emanate from an area whose dimensions are equal to or less than 2.5 times the dimensions of the resolution element (assuming the source is uniform over the whole area). This corresponds approximately to the Rayleigh, first null, or first minimum definitions of remote sensing beams.

Image Tolerances

The image consists of lines of contiguous cross-scan resolution elements. Allowable deviations from perfect contiguity and cross-scan alignment are defined in figure 7. These deviations include

(1) Static cross-scan contiguity - Gaps between individual resolution elements and overlaps of resolution elements shall not exceed ϵ.

(2) Static along scan displacement - Shall not exceed 2ϵ.

22

(3) Static image distortion of a group resolution element - Although contiguity may be maintained with some types of image distortion, the cross-scan or along-scan displacement of any single resolution element from its ideal position shall not exceed 2ε.

(4) Dynamic deviations - Jitter or oscillatory deviations of any kind with equivalent spatial wavlengths of less than 500ε shall not exceed a peak amplitude of 0.5ε.

Allowable deviations from perfect registration of resolution elements are defined as follows:

	Global	Over control points
Temporal registration offsets between two images over same area	<5ε	<0.5ε
Geodesic accuracy of an image	<5ε	<.5ε
Uncertainty between two adjacent images from different passes	<5ε	<.5ε
Rotation between adjacent images from different passes	<3°	<1.0°

These image tolerances are a type of performance specification which, for particular microwave radiometer spacecraft designs, must be translated into spacecraft performance specifications such as attitude control, pointing, and multibeam alignment.

CONCLUDING REMARKS

An Earth-observation measurements mission is defined for a large-aperture microwave radiometer spacecraft. Space data application needs, the measurement selection rationale, and broad spacecraft design requirements and constraints are described. Over the land the primary measurand is soil moisture; over the coastal zones and the oceans important measurands are salinity, surface temperature, surface winds, oil spill dimensions, and ice boundaries. Spacecraft measurement requirements have been selected for each of these measurands. Near-all-weather operation and good spatial resolution (<1 km) are assured by operating at low microwave frequencies using an extremely large antenna aperture in low Earth orbit.

The parametric study showed that an altitude range of 800 to 1000 km would meet the 5-year experiment lifetime requirement, provide satisfactory measurement repeat time, and at the same time, be weight and volume efficient for the space transportation system. A 60° inclination and a 14-day repeat cycle will provide full contiguous coverage of the United States using the minimum swath of 200 km.

To satisfy the image quality requirement, resolution elements (assigned field of view at the Earth's surface during a single measurement sequence) are sized such that at least 50 percent of the total power received emanates from the resolution element. In addition, beam efficiency specifications require that 90 percent of the total power collected must emanate from an area whose dimensions are equal to or less than 2.5 times the resolution element dimensions.

REFERENCES

1. Swift, Calvin T.: High-Resolution Passive Microwave Imaging of the Surface of the Earth. The Microwave Radiometer Spacecraft - A Design Study, Robert L. Wright, ed., NASA RP-1079, 1981, pp. 33-41.

2. Comm. on Remote Sensing Programs for Earth Resource Surveys: Microwave Remote Sensing From Space for Earth Resource Surveys. Contract NASW-3043, Natl. Acad. Sci.-Natl. Res. Counc., 1977. (Available as NASA CR-157891.)

3. Proposed NASA Contributions to the Climate Program. NASA TM-80497, 1977.

4. Staelin, David H.; and Rosenkranz, Philip W., eds.: High Resolution Passive Microwave Satellites. Contract NAS5-23677, Massachusetts Inst. Technol., Apr. 14, 1978. (Available as NASA CR-160041.)

5. Post Landsat D Advanced Concept Evaluation - Final Report. GE Doc. No. 78SDS4238 (Contract NAS2-9580), General Electric Co., Aug. 18, 1976. (Available as NASA CR-156818.)

6. Brooks, D. R.; Bess, T. D.; and Gibson, G. G.: Predicting the Probability That Earth-Orbiting Spacecraft Will Collide With Man-Made Objects in Space. IAF Paper A74-34, Sept. 1974.

7. Garrett, L. Bemard: Systems Design and Analysis of the Microwave Radiometer Spacecraft. The Microwave Radiometer Spacecraft - A Desigh Study, Robet L. Wright, ed., NASA RP-1079, 1981, pp. 69-94.

8. Brooks, David R.: An Introduction to Orbit Dynamics and Its Application to Satellite-Based Earth Monitoring Missions. NASA RP-1009, 1977.

A   area, cm^2

$C_D A/m$ drag-to-mass ratio, cm^2/g

C_D drag coefficient

h   orbit altitude, km

i   orbit inclination, deg

m   mass, g

Q repetition factor

ΔT_B change in brightness temperature, K

ε dimension of resolution element

TABLE I.- MISSION OUTLINE

Sensing goals	Imposed mission constraints

Full-time monitoring:
  All weather
  Day and night
	<10 GHz

Global coverage	Legal agreements Passive - no microwave illumination
High-resolution sensing	Large-aperture microwave systems Low altitude

Multiparameter sensing:
  Earth resources
  Environmental
	Multifrequency operation
	Contiguous mapping
	Frequent revisits

Operational monitoring:
  Coverage of electromagnetic spectrum
  Synergistic data use
	Part of an overall global services
	  space system

TABLE II.- MULTIPARAMETER SENSING

Potential applications	Parameters	Potential users
Crop yield forecasting (refs. 2, 4, and 5)	Soil moisture	Dept. of Agriculture
Climate prediction (ref. 3)	Soil moisture, ice, snow cover, salinity, sea surface temp., and sea surface wind speed	NOAA
Coastal zone productivity (ref. 4)	Salinity and water surface temperature	Coast Guard (200-mi. limit) Bureau of Fisheries
Hydrology (refs. 2 and 5)	Soil moisture	USDA, DOI, DOC
Water quality (ref. 4)	Oil slicks and other pollutants	EPA, NOAA
Coastal zone dynamics (refs. 3 and 4)	Water surface temp., water surface roughness, and wind speed	NOAA Corps of Eng. (use permits)

TABLE III.- REMOTE SENSING REQUIREMENTS

Applications	Measurand
	Soil moisture	Water surface temperatures	Salinity	Water pollutants	Water roughness (winds)	Ice
Crop yield forecasting	Ⓧ			*NA*	*NA*	*NA*
Climate prediction	X	X		*NA*	X	Ⓧ
Coastal productivity	X	Ⓧ	Ⓧ	X	*NA*	*NA*
Hydrology	X	*NA*				
Water quality		*NA*		Ⓧ		
Coastal dynamics	*NA*	X		X	Ⓧ	

Legend: ⊠ Pacing ☒ Priority ☐ Requirement ▨ NA

Selected measurement requirements

	Soil moisture	Water surface temperatures	Salinity	Water pollutants	Water roughness (winds)	Ice
Range	5 to 40% 10 to 25 cm depth	270 to 310 K	0 to 40 ppt	0 to 1 cm oil thickness	0 to 60 m/s	Boundaries
Accuracy	20% wet, 50% dry	1 K	1 ppt	1 mm thickness	3 m/s	0.5 km linear
Resolution	0.1 to 1 km	≤1 km	≤1 km	≤1 km	≤1 km	≤1 km
Coverage	Farm belts	Coastal zones	Coastal zones	Coastal zones	Coastal zones	Coastal zones, inland waters
Repeat	1/day to 1/wk	1 to 2/wk	1 to 2/wk	1/day	1 to 2/wk	1/day to 2/wk

TABLE IV.- PERFORMANCE REQUIREMENTS

Measurement requirement	Performance requirement
Radiometer	
6 measurands	3 freq. bands, approx. 1, 2, and 4 GHz
Land, water, ice radiations	Brightness temp. T_B, 200 to 350 K
6 measurand accuracies	Precision, $\Delta T_B < 1$ K
Resolution, $\leqslant 1$ km	Beam width, $\leqslant 0.1°$ (Altitude dependent)
Coverage, contiguous	Wide swath, >200 beams
Orbital parameters	
Experiment lifetime, >5 years	Altitude min., 600 km
Repeat, 1/day to 1/week	Altitude max., 1400 km
Coverage - over farm belts and coastal zones	Inclination, 60° and $\approx 98°$
Repeat precision	Alt. decay, $\leqslant 0.1$ swath/repeat equiv.
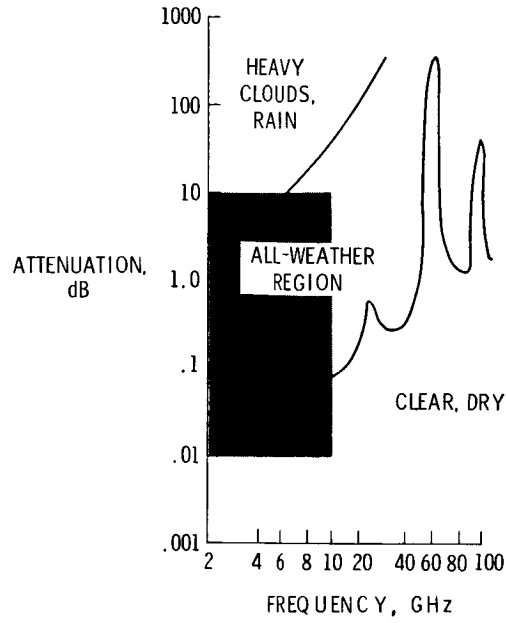
Figure 1.- Atmospheric attenuation of microwave frequencies.
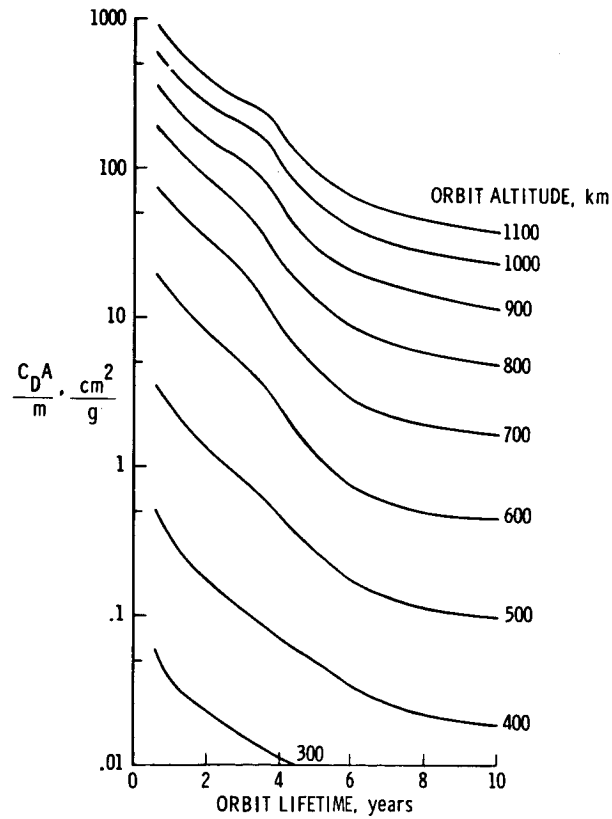
Figure 2.- Lifetimes in low Earth orbit (from ref. 6).
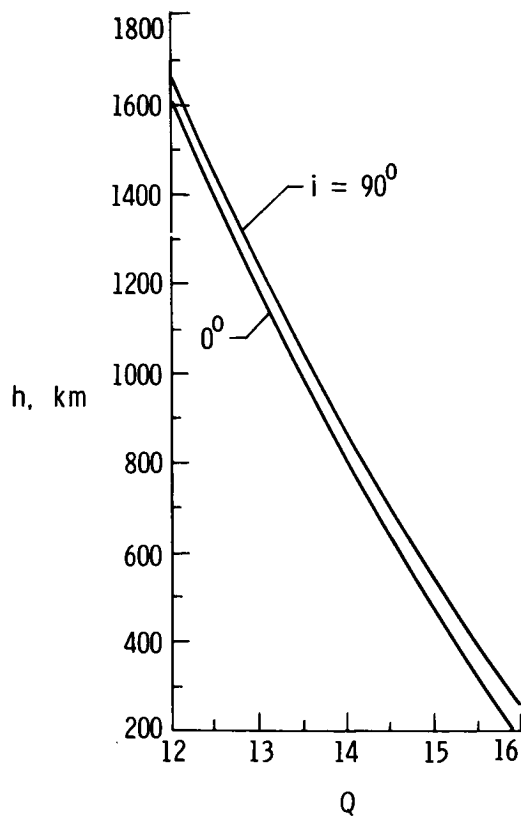
Figure 3.- Circular orbit altitudes h to
achieve specified repetition factors
(adapted from ref. 8).
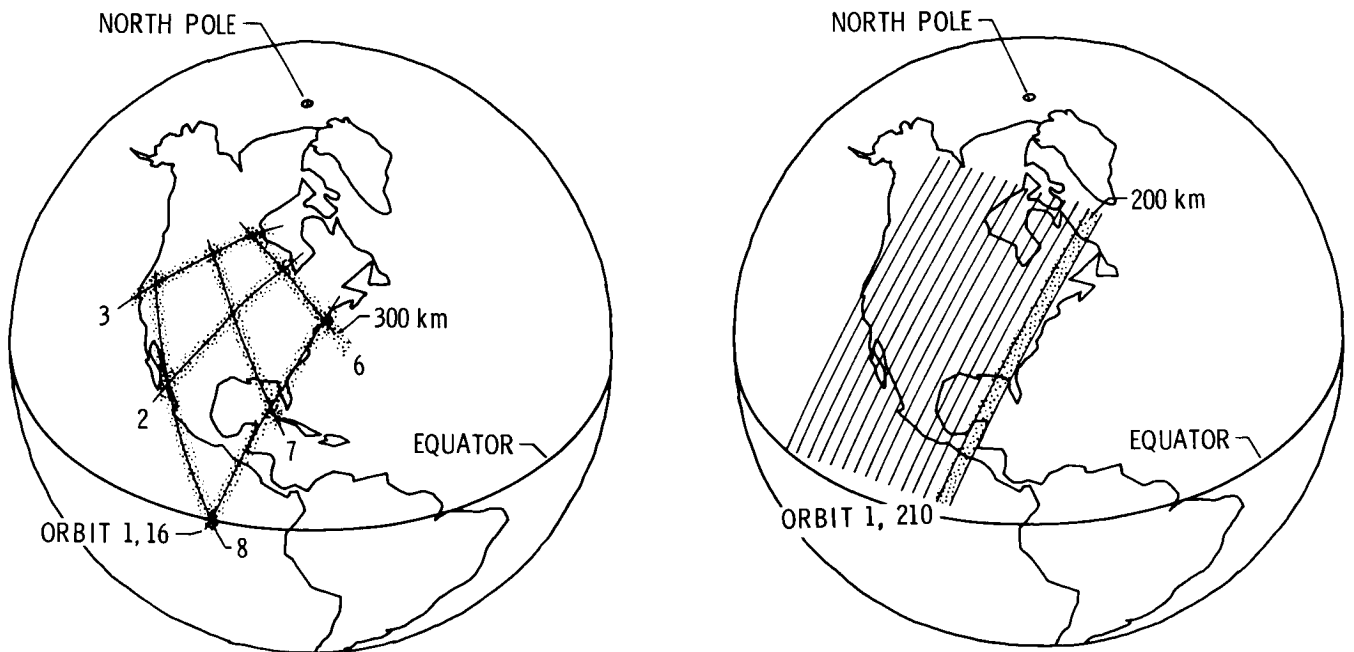
(a) 1-day revisit, 300-km swath width.

(b) 14-day revisit, 200-km swath width.

Figure 4.- Coverage examples, i = 60°.
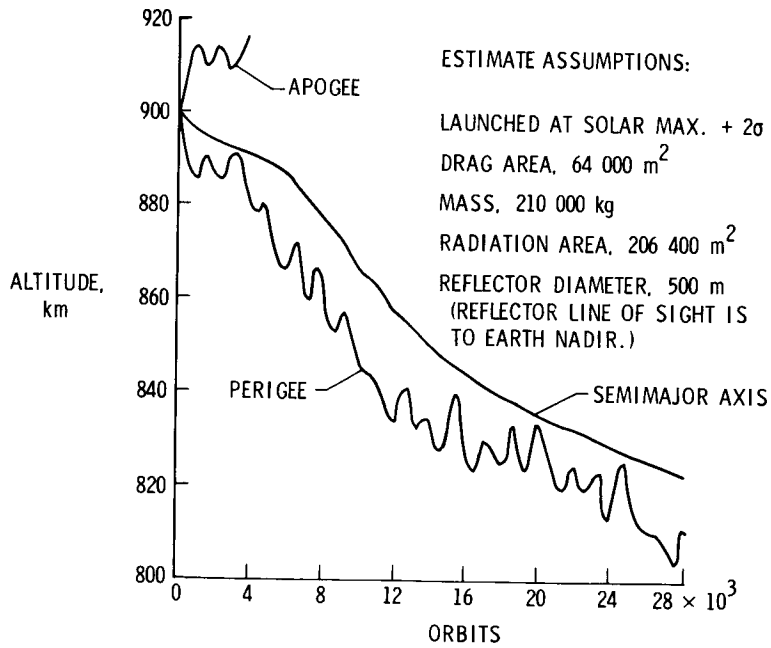
Figure 5.- Calculated estimate of orbital decay.
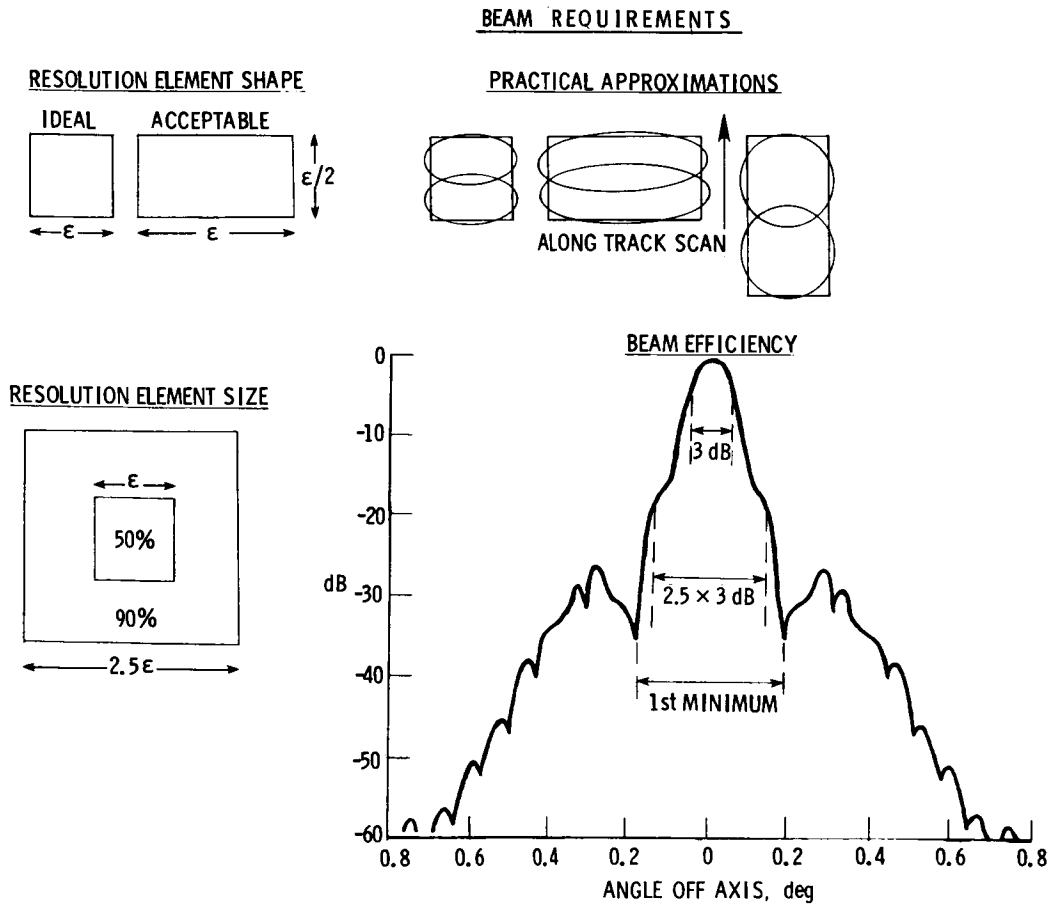
Figure 6.- Image quality requirements.

EXAMPLE: IDEAL IMAGE LINE (PUSH-BROOM SCAN) OF RESOLUTION ELEMENTS

SATELLITE TRACK

TOLERANCES FOR (1) CONTIGUITY, (2) DISPLACEMENT, (3) RESOLUTION ELEMENT GROUP DISTORTION

TEMPORAL RES.

GEODETIC REF.

ELEMENT ELEMENT
#1 #2
ELEMENT OBSERVED ELEMENT

IMAGE FRAMES AND/OR SCENES
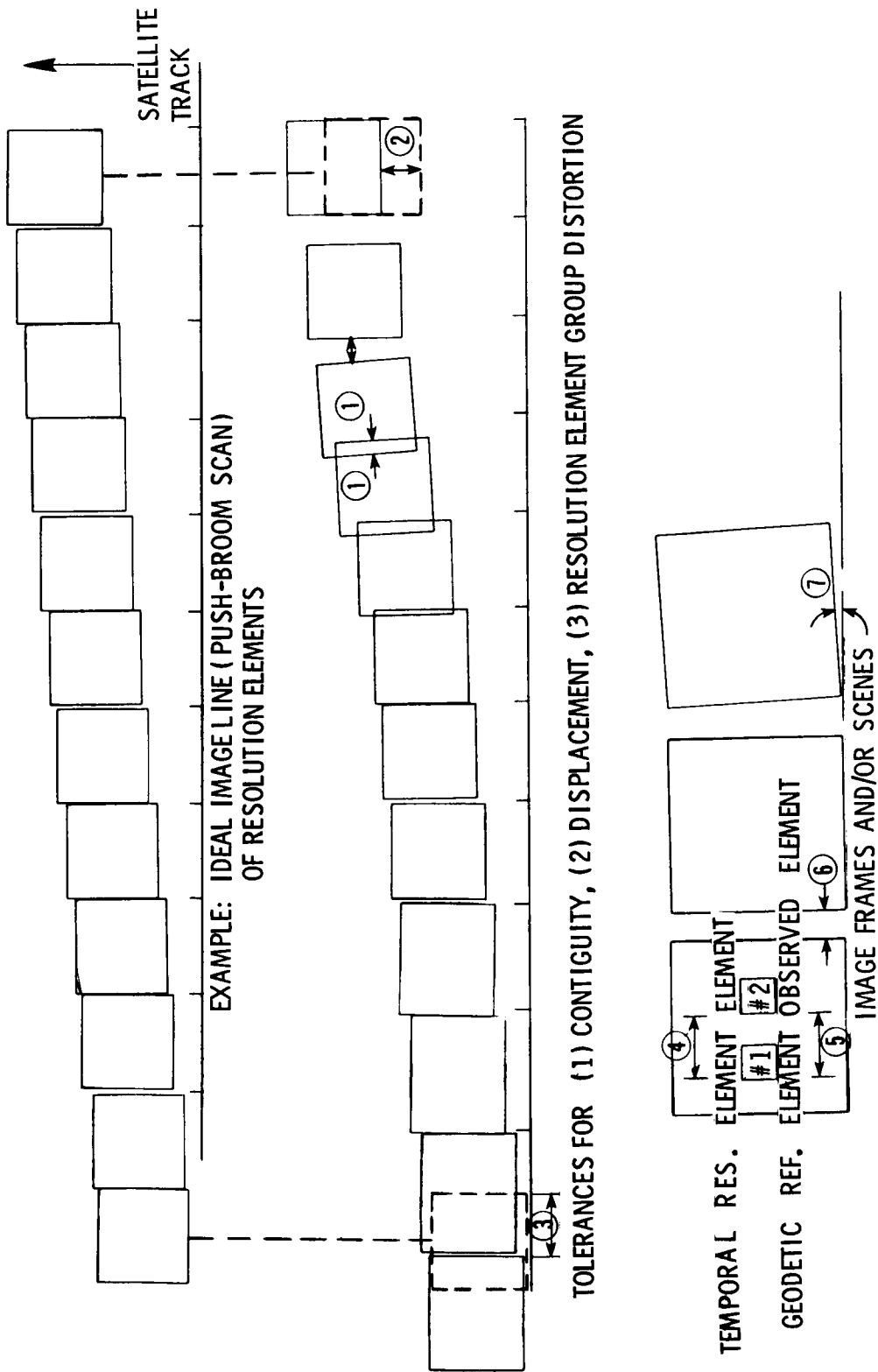
TOLERANCES FOR (4) TEMPORAL REGISTRATION, (5) GEODETIC ACCURACY, (6) ADJACENT IMAGES FROM DIFFERENT PASSES, (7) ROTATION

Figure 7.- Image tolerances.

HIGH-RESOLUTION PASSIVE MICROWAVE IMAGING

OF THE SURFACE OF THE EARTH

Calvin T. Swift*
University of Massachusetts
Amherst, Massachusetts

SUMMARY

The physics of passive microwave observations of the Earth and the system requirements for high-resolution imaging within this spectral band are summarized. High resolution is achieved in a straightforward manner by increasing the size of the primary antenna. However, with a single receiver, it is shown that the combination of high resolution and crosstrack scanning cannot produce images which have valuable geophysical content. The concept of a multiple receiver array located in the focal plane is presented as the only practical solution to the dilemma. Exploring this concept, system requirements are generated which, for the first order, appear to offer solutions to the problem.

PHYSICS OF PASSIVE MICROWAVE SENSING

When a microwave radiometer views the surface of the Earth, it receives thermal power P in accordance with the following relationship:

$$P = kT_A B \tag{1}$$

where k is the Boltzmann constant (1.38×10^{-23} J/K) and B is the predetection bandwidth of the receiver in Hz. The quantity T_A is the antenna temperature in K. The antenna temperature has absolutely nothing to do with the actual thermodynamic temperature, but is merely a convenient definition of the following integral relationship:

$$T_A = \frac{1}{4\pi} \int_\Omega T_B(\Omega)G(\Omega) \, d\Omega \tag{2}$$

where $d\Omega$ is the incremental solid angle of an antenna of gain $G(\Omega)$ viewing a surface that emits power proportional to $T_B(\Omega)$. This integral results because the microwave system operates under diffraction-limited optics. The quantity $T_B(\Omega)$ is the brightness temperature, and is explicitly given by the following relationship:

$$T_B(\Omega) = e(\Omega)T \tag{3}$$

---

*Formerly with NASA Langley Research Center, Hampton, Virginia.

where $e(\Omega)$ is the emissivity of the surface and T is its true temperature in K. If the surface under observation were perfectly smooth, the emissivity would be simply derived as follows:

$$e(\Omega) = 1 - r(\Omega) \tag{4}$$

where $r(\Omega)$ is the Fresnel reflection coefficient, which can be derived through standard electromagnetic boundary-value procedures. This coefficient is a known function of the viewing angle, polarization of the antenna, the dielectric constant of the surface under observation (which depends upon the observational wavelength), and certain physical properties of the medium itself. If the radiometer is viewing the ocean, the dielectric constant depends only upon two parameters, the salinity and temperature of the water. Prior work (ref. 1) has shown that salinity and temperature can be independently derived if two radiometers of differing wavelengths, say 10 and 20 cm, simultaneously view the same sector of the ocean.

The radiation that is collected by the antenna can be considered as uncorrelated white noise. However, because of the finite predetection bandwidth of the receiver and postdetection integration time, this noisy signal is smoothed as a result of filtering to achieve a measurement resolution ΔT in accordance with the following expression:

$$\Delta T = \frac{2(T_A + T_{RN})}{\sqrt{B\tau}} \tag{5}$$

where τ is the postdetection integration time in seconds. Therefore, the accuracy requirements for the retrieval of geophysical parameters imposes two impacts on the receiving system. First, the system must exhibit stability to produce an accurate mean value of T_A. Second, the instrument must provide a certain minimum resolution which, for the first order, is achieved by providing a sufficient amount of integration time. It is shown that integration time is the limiting factor in the design of high-spatial-resolution passive microwave sensors. Before proceeding, it should be noted that reference 2 contains a more in-depth review of the material presented thus far.

If the antenna exhibits a very narrow beam, with low side lobes, then the antenna temperature is approximately equal to the brightness temperature,

$$T_A \approx T_B \tag{6}$$

and the angular sector of observation is approximately determined by the 3-dB beam-width as given by

$$\theta_B \approx 1.22\lambda/D \tag{7}$$

34

where λ is the electromagnetic wavelength and D is the characteristic dimension of the antenna (in this case, the diameter of the circular aperture). If the circular symmetric antenna is at altitude H above the surface of the Earth, the spot size, or resolution cell ϵ, is given by

$$\epsilon = H\theta_B = 1.22\lambda H/D \tag{8}$$

The microwave radiometer is now considered as an imaging system. The radiometer is mounted on a platform at altitude H, and moves with velocity v. It is further supposed that the antenna is scanning crosstrack to the velocity vector in order to develop a given swath width S to the image. In order to develop a filled image utilizing the forward motion of the spacecraft, the following constraint must be imposed:

$$\epsilon = vt \tag{9}$$

where t is the time required to scan the antenna back and forth across the swath. Assuming that $S = N\epsilon$, where N is the number of receivers, the dwell time that is available during each crosstrack resolution cell is given by

$$\tau = \frac{t}{2N - 1} = \frac{\epsilon/v}{2N - 1} \tag{10}$$

Using equation (5), it therefore follows that

$$\Delta T = \frac{2(T_A + T_{RN})}{\sqrt{B}} \sqrt{\frac{(2N - 1)v}{\epsilon}} \tag{11}$$

which clearly illustrates the dilemma imposed upon high-resolution scanning imaging systems that only utilize one detector. That is, the measurement resolution ΔT is degraded by the desire to maximize swath width $N\epsilon$ and minimize the size of the resolution element, or pixel. Indeed, it is clear that the limiting values of N and ϵ will occur such that the value of ΔT is driven too high to be of any ultimate geophysical value. When $N = 1$, the system is not scanned, and the minimum value of ΔT is obtained for a given pixel size.

MULTIPLE RECEIVER CONCEPT

The observations discussed in the preceding section led to the concept of employing multiple receivers, each sharing the same primary reflector, but each viewing adjacent pixels crosstrack to the motion of the platform. Thus, if N receivers are employed, the desired swath width is achieved with a single nonscanning system. An additional advantage is acquired by utilizing a concept with no mechanical scanning. High resolution requires very large antennas, which impose difficulties in the dynamics of mechanical scanning.

One possible concept of utilizing multiple receivers is illustrated in figure 1. In this figure, upwelling thermal radiation from the Earth reflects from a dish antenna of radius a into a secondary antenna that delivers the radiation to a radiometer. This secondary antenna is located in the focal plane at distance f from the primary reflector, and is displaced at distance x from the focal line. This problem was initially investigated several years ago by Ruse (ref. 3). Utilizing his results for r >> f, the normalized radiation pattern p(θ), or gain distribution, in the scan plane can be expressed as

$$p(\theta) = \frac{1}{a^2} \left| \int_0^{2\pi} \int_0^a f(r,\phi') \exp\left(-j\frac{2\pi r}{\lambda}\left\{ u\cos\phi' \right.\right.\right.$$

$$\left.\left.\left. - u_s\left[1 - \left(\frac{r}{2f}\right)^2 + \left(\frac{r}{2f}\right)^4 - \cdots\right]\cos\phi'\right)\right\} r\,dr\,d\phi' \right| \tag{12}$$

where $u = \sin\theta$ and $u_s = \varepsilon x/f = \tan\theta_s$. The function $f(r,\phi')$ is the field distribution across the reflector, as specified by the radiation pattern of the secondary antenna located in the focal plane. Assuming $f(r,\phi')$ contains both amplitude and phase information which can be selected by proper design of each of the radiometer feed antennas, we investigate the consequences of choosing

$$f(r,\phi') = \exp\left\{\frac{j2\pi}{\lambda}\left[\left(\frac{r}{2f}\right)^2 - \left(\frac{r}{2f}\right)^4 + \cdots\right]\cos\phi'\right\} \tag{13}$$

If this is done, phase cancellation occurs such that

$$p(\theta) = \frac{1}{a^2} \left| \int_0^{2\pi} \int_0^a \exp\left[-\frac{j2\pi r}{\lambda}(u - u_s)\cos\phi'\right] r\,dr\,d\phi' \right| \tag{14}$$

Performing the ϕ' integration gives

$$p(\theta) = \frac{1}{a^2} \left| \int_0^a J_0\left[\frac{2\pi r}{\lambda}(u - u_s)\right] r\,dr \right| \tag{15}$$

and equation (15) readily integrates to give

$$p(\theta) = \left| \frac{J_1\left[\frac{2\pi a}{\lambda}(u - u_s)\right]}{\frac{2\pi a}{\lambda}(u - u_s)} \right| \tag{16}$$

If the squint angle of an individual beam θ_s and the main sector of an individual beam θ are substantially smaller than a radian, small angle approximations can be made so that equation (16) becomes

$$p(\theta) \approx \left| \frac{J_1\left[\frac{2\pi a}{\lambda}(\theta - \theta_s)\right]}{\frac{2\pi a}{\lambda}(\theta - \theta_s)} \right| \tag{17}$$

The first zero root of $J_1(x)$ occurs when

$$\frac{2\pi a}{\lambda}(\theta - \theta_s) = 3.832 \tag{18}$$

or when

$$(\theta - \theta_s) = 1.22\lambda/D \tag{19}$$

where $D = 2a$, the diameter of the large reflector antenna. Note that equation (19) represents a rigorous development of equation (7), which expresses the beamwidth of the antenna. The angular extent from the boresight line ($\theta = \theta_s$) to the first null (i.e., the first zero root of $J_1(x)$) is also approximately equal to the 3-dB beamwidth, which is the sector subtended by $\theta = \theta_s \pm 0.61\lambda/D$. A rough sketch of the antenna pattern for the offset feed is shown in figure 2. An image is then developed by arraying a large number of adjacent feed horns in the focal plane. The feed horns are displaced so that each squint angle θ_s is shifted by one beamwidth. In other words, the squint angle associated with the jth feed is given by

$$\theta_{sj} = 1.22j\lambda/D \tag{20}$$

where $j = 0, \pm 1, \pm 2, \ldots, \pm M$. The feed horn with $j = 0$ is located on the focal axis, and those located at θ_s define the field of view of the image. The total number of receivers is $N = 2M + 1$, and the field of view is $(N - 1)\theta_s$. The length of the array L, which is located a distance f from the reflector is given by

$$L = (N - 1)(1.22)\lambda f/D \tag{21}$$

and the spacing between feeds ΔL is given by

$$\Delta L = 1.22\lambda f/D \tag{22}$$

The spatial resolution at altitude H above the surface of the Earth is given by equation (8), and the total swath width S is given by

$$S = (N - 1)(1.22)\lambda H/D \tag{23}$$

The last pertinent parameter of interest, the required integration time, is given by

$$\tau = 1.22(\lambda/D)(H/v) \tag{24}$$

SAMPLE CALCULATION

As a sample representation of the requirements imposed upon the system, a target spatial resolution of $\varepsilon = 1$ km and a minimum swath width of $S = 200$ km are assumed. The electromagnetic wavelength is fixed at $\lambda = 0.21$ m, which represents the longest practical wavelength currently being utilized for remote sensing applications. The choice of this long wavelength will specify the maximum required size of the primary reflector antenna. The approximations used to develop the antenna pattern expression of equation (17) assume a large value of the f number. An f/D value of 2.5 is arbitrarily chosen and a maximum reflector diameter of $D = 100$ m is assumed. Utilizing these parameters, equation (8) gives an altitude of $H = 390$ km required to achieve a 1-km resolution. The swath-width requirement of equation (23) determines that the number of receivers is $N = 201$, the length of the array as derived from equation (21) is $L = 128$ m, and the spacing between the feed antennas is 0.64 m, as specified from equation (22). The field of view of the system is 0.51 radian.

The overall performance of this system tacitly assumes that an appropriate phase adjustment can be accommodated in order to prevent off-axis beam distortion due to coma (ref. 3). Assuming a satellite velocity of approximately 7 km/sec, the maximum available integration time, as given by equation (24), is $\tau = 143$ ms. Assuming a receiver bandwidth of 100 MHz and a total system noise temperature of 600 K, the measurement resolution as given by equation (5) is $\Delta T = 0.3$ K. This value of ΔT is of adequate precision for all present surface remote sensing measurements of interest (ref. 1). These sample calculations have been presented without considering other constraints such as optimum orbital altitudes, or whether phase corrections to the individual feed antennas can indeed be accomplished. Generally, it can only be said that an increase in orbital altitude, or the utilization of the primary reflector system to correct phase errors, will require a larger antenna system.

CONCLUDING REMARKS

Experimental results utilizing instrumented aircraft have confirmed the feasibility of remotely sensing surface parameters and characteristics via passive radiometry. Several approaches are possible to obtain resolution and measurement fidelity. One approach minimizes the structural and control problem by reducing the aperture required through dielectric lens correction for beam distortion; the other approach minimizes the RF design through significant increases in physical antenna size and associated control problems. The latter approach was selected for this study.

REFERENCES

1. Blume, Hans-Juergen C.; Kendall, Bruce M.; and Fedors, John C.: Measurement of Ocean Temperature and Salinity via Microwave Radiometer. Boundary-Layer Meteorology, vol. 13, Jan. 1978, pp. 295-308.

2. Swift, C. T.: Passive Microwave Remote Sensing of the Ocean - A Review. Boundary-Layer Meteorology, vol. 18, no. 1, Feb. 1980, pp. 25-54.

3. Ruse, John: Lateral-Feed Displacement in a Paraboloid. IEEE Trans. Antennas & Propag., vol. AP-13, no. 5, Sept. 1965, pp. 660-665.

SYMBOLS

a	antenna radius
D	diameter of the circular aperture
f	focal-plane distance from primary reflector
$p(\theta)$	normalized radiation patterns
r	radius
x	distance from focal line
ε	resolution cell
θ	main sector of an individual beam
θ_s	squint angle of an individual beam
λ	electromagnetic wavelength
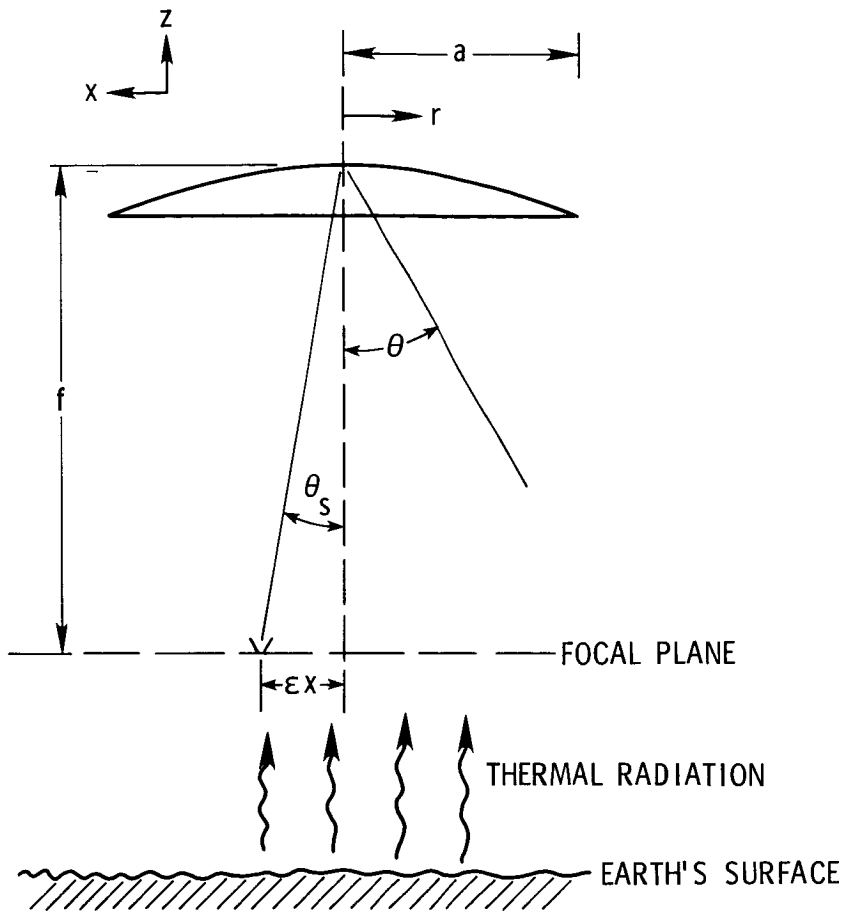
Figure 1.- Multiple receiver concept.
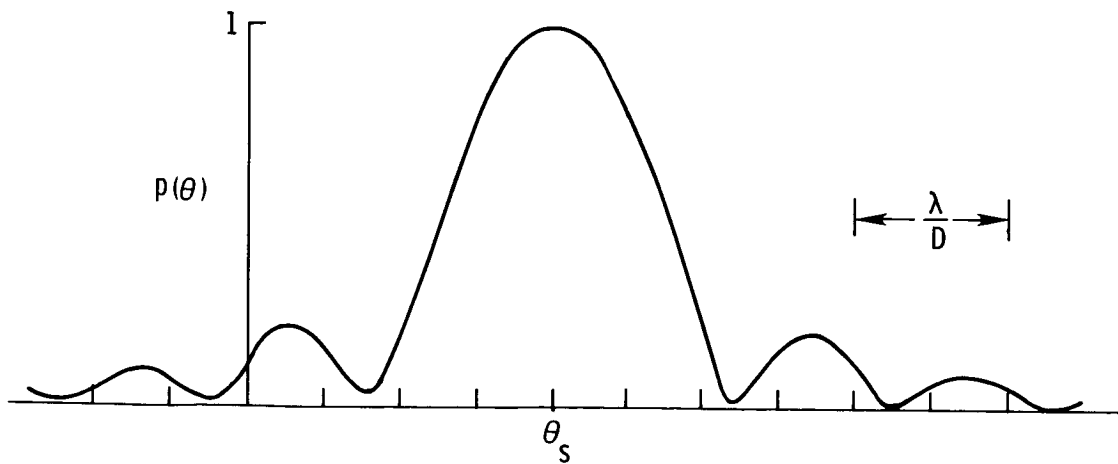
Figure 2.- Antenna pattern for off-set feed.

RADIOMETER DESIGN CONCEPTS

FOR A LARGE APERTURE MICROWAVE RADIOMETER SPACECRAFT

Lloyd S. Keafer, Jr.
NASA Langley Research Center
Hampton, Virginia

SUMMARY

Concepts involving active and passive microwave systems for soil-moisture monitoring are discussed. It appears that the first major developmental efforts should be directed toward the simpler passive design concepts. Subsequently, five passive design concepts for a microwave radiometer spacecraft are outlined and compared. Some common technology needs, such as large space structures and controls, are shown to exist. Also, some peculiar technology needs are identified, such as complicated phasing networks, dielectric lenses, tapered illumination, and reflector-surface irregularity and distortion control techniques. More detailed studies should address these design concepts and assess the associated technology needs.

INTRODUCTION

Microwave sensing systems in space possess near all-weather capability. Measurements at microwave frequencies, both active and passive, can be made under conditions of haze, fog, and clouds better than measurements at infrared and visible frequencies. In addition, microwave systems are uniquely sensitive to a variety of Earth characteristics, and thus in any particular space mission the systems can serve as prime sensors or as complements to optical sensors. As an example of how the two systems may complement each other, both microwave and optical systems are known to respond to target size features comparable to the wavelength of the sensor. Thus, microwave systems respond to features on the order of centimeters and optical systems respond to features on the order of micrometers. Consequently, optical systems sense clouds whereas microwave systems see through them to the Earth's surface; and at the surface optical systems are responsive to surface-layer phenomena whereas microwave systems can respond to target characteristics below the surface. Thus, color identification of food and fiber crops with optical sensors (on a clear day in the growing season) can be complemented with soil-moisture information from microwave sensors (regularly available regardless of meteorological conditions) to provide better crop-yield forecasts.

ACTIVE VERSUS PASSIVE MICROWAVE SYSTEMS

Active microwave systems irradiate the area of interest and measure the return (reflected, scattered, reradiated, etc.) energy. With the microwave scatterometer the backscatter coefficient of the target area is measured as a function of aspect angle. One of the primary capabilities of an active system is measuring distance by timing the reflected signal. With the radar altimeter the distance measured is used

to determine the average elevation of the surface over its footprint or resolution element. With synthetic-aperture techniques, the distance-measuring capability is extended to produce a type of imagery that shows, perhaps better than any other technique, the spatial distribution of the features within a scene. With the proper viewing angle and spatial resolution, this capability can produce data on surface features useful to geologists, land-use planners, oceanologists, and numerous other Earth scientists.

Similarly, passive microwave systems will produce useful data on different Earth characteristics. These data are derived from the radiative rather than the reflective characteristics of Earth's surface or the atmospheric media. At microwave frequencies the actual temperature differences encountered are small, but the differences in emissivities cause large observed differences in brightness temperature. Some factors affecting the emissivity are surface roughness, angle of incidence, and dielectric properties of the surface material. The dielectric properties of soil, for example, change drastically with water content, and therefore passive radiometry can be used for soil-moisture monitoring from space.

Although the mission definition of reference 1 is for a passive-microwave-radiometer spacecraft, some of the requirements may be met with active systems such as a synthetic-aperture radar or a radar scatterometer. With similar antenna sizes the resolution of the synthetic-aperture radar is 2 to 3 orders of magnitude better than a radiometer. However, being passive, the microwave radiometer does not radiate active signals that interfere with other users of the electromagnetic spectrum. For some measurements, such as soil moisture, reference 2 states: "... it appears that the accuracy of the measurements made by passive microwave is more impressive than those obtained with active microwave." In addition, passive systems require very little spacecraft electrical power.

In moving toward the objective of complementing optical sensing of Earth phenomena with all-weather, high-resolution microwave sensing, design studies of both passive and active space systems should be pursued. With the inevitable advent of large space systems technology, it appears, however, that the first major developmental efforts should be directed toward the simpler passive techniques.

PASSIVE DESIGN CONCEPTS

Of all the mission requirements for a microwave radiometer spacecraft (MRS), the one having the greatest impact on all designs is the spatial-resolution requirement of 1 km or better. The impact is similar for all design concepts since $\varepsilon \approx \lambda h/D$, where ε is the spatial resolution, λ is wavelength, h is orbital altitude, and D is the aperture size of the radiometer. The smallest aperture capable of obtaining a 1-km resolution from an altitude of 650 km at 1.4 GHz (assuming diffraction-limited operation) is approximately 140 m. This is the starting point for all designs; other considerations prevent attaining this limit with the result that the aperture size increases.

Five passive design concepts whose maximum apertures range from approximately 200 to 1300 m are introduced in table I. They are listed in approximate chronological order of their conception and the sponsoring organization of each are listed. The concepts are: (1) Single-feed, scanning radiometer, (2) phased array, (3) multiple-feed, parabolic reflector, (4) multiple-feed, parabolic torus reflector, and (5) multiple-feed, spherical reflector. Some of the older concepts ((1) and (2)) are related to space sensors with histories of flight experience (refs. 2 to 4) as

44

noted in the table. Concepts (3), (4), and (5) are new.[1] These concepts, as well as the large Parasol version of concept (2) (ref. 4) are at the design level and have no flight experience. The five concepts are compared in table II, which shows configuration features, including aperture sizes, as they relate to four major mission requirements of a soil-moisture monitoring system.

Contiguous Mapping

The major configuration differences in the various design concepts result from different approaches to meeting the mission requirement for contiguous mapping (i.e., in order to obtain the desired geographic coverage with minimum repeat intervals and minimum number of satellites). Generally the approaches either scan the beam across the suborbital track (concepts (1) and (2)) or use multiple fixed beams with up to one beam per resolution element (concepts (3), (4), and (5)). The forward motion of the satellites provides the other dimension of the scanning necessary to synthesize Earth surface imagery. Design implications of the five concepts are given in the following sections.

Concept (1).- In addition to the mechanical scanning geometry and mechanical scanning-system reliability problems, the scanning-radiometer design concept must solve the problem of limited measurement (integration) time, since the cross-track scanning of a swath 200 km wide or wider with resolution less than or equal to 1 km allows less than a 1-ms period for each resolution element. It should be noted that the design concept of a single beam pointed at selected targets of interest is not included in the table, since it is considered to be unresponsive to the general-purpose mission requirements because of its limited applicability.

Concept (2).- The phased-array design concept solves the cross-track-scanning problem electronically. Its array of feeds intercepts the wave front impinging on it, and networks adjacent to the feeds (horns) adjust the received signals to effect the equivalent of scanning without the limitation on integration time suffered by mechanical scanners. Furthermore, the phasing network can potentially compensate for some structural distortions. Compared with reflector concepts the phased array requires more receiving elements on a complicated phasing network. In addition, it has the unique problem of "frequency spreading" of the resolution element.

Concepts (3), (4), and (5).- These multiple-feed, fixed-beam designs have to solve the problem of distortion of the extreme off-nadir beams. The simple parabolic reflector concept (3) proposes to solve the problem by using a large focal length and by providing fixed phase corrections for each feed through the use of dielectric-lens elements. Unfortunately, this means that the 200 or so feeds cannot be identical. Concepts (4) and (5) propose to solve the problem by using parabolic torus and spherical reflector shapes. The resulting beams associated with each resolution element are not full overlapping and consequently the total aperture size increases by a factor equal to or greater than 1.5.

---

[1]If the resolution requirement of 1 km were relaxed, other design concepts such as the GSFC multiple-feed, scanning radiometer ("whisk broom") would be promising.

Measurands

All of the design concepts are relatively new, at least for applications requiring large apertures. Their performance with regard to various measurands varies. Comparisons of the concepts should be made on the same basis or the differences should be noted as in table II. In this example only concept (5) uses the lower (1.0 GHz) frequency to meet the depth requirement for the soil-moisture measurand. A penalty in aperture size results. Alternately, if the aperture comparisons were made at 1.0 GHz, concepts (1) to (4) would show an increase in diameter by a factor of 1.4. In addition to the low frequency for soil-moisture measurements, concepts (3) and (5) have two additional frequencies which require two additional linear feed arrays (no change in reflector aperture).

Image Quality

At the diffraction limit, microwave beams defined by the 3-dB points are not efficient with regard to energy; that is, much of the energy is contained in the side lobes. To obtain the better beam efficiency required for remote sensing, the various design concepts must use something other than uniform illumination, again with an accompanying size penalty. Concept (5) prescribes tapered illumination with the size-penalty factor ranging from 1.5 to 2.0. Beam-efficiency requirements also impose reflector-surface-irregularity and structural-distortion limits which are related to size. Reflector tolerances fall somewhere within the following ranges depending on the inherent beam efficiency of the chosen feed-design or tapered-illumination concepts:

Random roughness .... $\lambda/16$ to $\lambda/100$
Large-scale shape (deterministic) .... $\lambda/8$ to $\lambda/32$
Medium-scale shape (deterministic)
   and roughness (random) .... $\lambda/10$ to $\lambda/50$

Spatial Resolution

As stated earlier, spatial resolution has the greatest design impact, with required theoretical aperture sizes starting at approximately 140 m. Practical design concepts start with 200-m apertures and vary upward to over 1 km. Obviously development of these concepts depends strongly on the development of large space structures technology. With the structures technology also must come new surface-control technology needed to guarantee that spatial-resolution and interrelated beam-efficiency requirements are met throughout the operating lifetime of the microwave radiometer spacecraft.

CONCLUSIONS

The near all-weather capability of microwave systems makes them attractive prime sensors or complements to optical systems for sensing Earth phenomena from space. Active and passive microwaves respond to different features, so the development of both should be pursued. Based on the facts that passive systems do not require emmission from the spacecraft, that they are fundamentally simpler in concept, and that they show promise of making useful measurements, it appears that their development priority should be high.

Five passive design concepts have been outlined and compared. Some common technology needs exist, such as large space structures and controls. Also, some peculiar technology needs, such as complicated phasing networks, dielectric lenses, tapered illumination, and reflector-surface irregularity and distortion control techniques, are identified. More detailed design studies should address these design concepts and assess the associated technology needs. Concept (5) (spherical reflector with multiple fixed beams) was selected for this study, primarily to emphasize the large structures technology disciplines. The structural, controls, and electromagnetic analyses allowed the application of simple yet comprehensive tools for the concept definition and performance assessment.

REFERENCES

1. Keafer, Lloyd S.: Mission Definition for a Large-Aperture Microwave Radiometer Spacecraft. The Microwave Radiometer Spacecraft - A Design Study, Robert L. Wright, ed., NASA RP-1079, 1981, pp. 17-32. (Paper in this compilation.)

2. Comm. on Remote Sensing Programs for Earth Resource Surveys: Microwave Remote Sensing From Space for Earth Resource Surveys. Contract NASW-3043, Natl. Acad. Sci.-Natl. Res. Counc., 1977. (Available as NASA CR-157891.)

3. Staelin, D. H.; and Rosenkranz, P. W., eds.: High Resolution Passive Microwave Satellites. Contract NAS5-23677, Massachusetts Inst. Technol., Apr. 14, 1978. (Available as NASA CR-160041.)

4. Post Landsat-D Advanced Concept Evaluation - Final Report. G. E. Doc. No. 78SDS4238 (Contract NAS2-9580), General Electric Co., Aug. 18, 1976. (Available as NASA CR-156818.)

TABLE I.- PASSIVE DESIGN CONCEPTS FOR MRS

Passive design concept	Related instruments	Sponsoring organizations
Scanning radiometer[a]	SMMR (ref. 3) SIMS (ref. 2) SMMRE/ASMR (ref. 2)	GSFC, JPL
Phased array	ESMR (ref. 3) SMMRE/LESMR Parasol forerunner (ref. 4)	GSFC
Parabolic reflector[b]		LaRC
Parabolic torus reflector[b]	Microsat (ref. 4)	GSFC, G.E.
Spherical reflector[b]		LaRC

[a]Single feed.
[b]Multiple feed.

48

TABLE II.- FEATURES OF DESIGN CONCEPTS

Mission requirement and configuration feature(s)	Passive design concept				
	Single-feed, scanning radiometer	Phased array	Multiple-feed, parabolic reflector	Multiple-feed, parabolic torus reflector	Multiple-feed, spherical reflector
Contiguous mapping (greater than 200-km swath width):					
Aperture configuration	Parabolic reflector	Plane collector	Parabolic reflector	Parabolic torus reflector	Spherical reflector
Beam scanning configuration	Mechanical	Electronic	Pushbroom (fully overlapping)	Pushbroom (partially overlapping)	Pushbroom (partially overlapping)
Feed location	Focal point, offset rotating feeds	Collector plane feed array	Focal plane feed array	Focal arc feed array	Focal arc feed array
Focal-distance-to-diameter ratio	≤2	Not applicable	>2	Overall, <1 One beam, >1.5	Overall, ~1 One beam, ~2
Feed array	Not applicable	2-D pattern, phasing networks adjacent to feeds; may include feed-cluster switching	Linear pattern, phase correction with dielectric-lens feeds, all feeds different	2-D pattern, switched feed clusters; 60 beams; 81 cross-track positions	Linear pattern, identical geometry for all beams (≤200)
Measurands:					
Frequency, GHz	1.4	1.4	1.4, 2.0, 4.0	1.4	1.0, 2.0, 4.0
Image quality (90 percent beam efficiency):					
Feed illumination	Unknown	Unknown	Unknown, but likely to be tapered	Unknown	Tapered
Spatial resolution (<1 km):					
Aperture size (1.4 GHz at 650 km alt), m	200	200	200	600 by 1300	500 (675 at 1.0 GHz)

EVOLUTION AND DESIGN CHARACTERISTICS

OF THE MICROWAVE RADIOMETER SPACECRAFT

Robert L. Wright
NASA Langley Research Center
Hampton, Virginia

SUMMARY

The evolution of the design of the microwave radiometer spacecraft from conception to preliminary design is described. Alternatives and trade-off rationale are described, and the configuration and structural design features that were developed and refined during the design process are presented for the three structural configurations studied (two geodesic trusses and a flexible catenary).

INTRODUCTION

Spacecraft design is an evolutionary or iterative process. Conceptual design begins after mission objectives have been established and the system and subsystem (particularly the measurements subsystem) requirements have been defined. A conceptual or first-cut configuration design is made to develop scale, system and subsystem locations, and gross weight estimates. Alternate concepts for specific systems, or the entire spacecraft, are introduced at this point. Computer-aided design techniques and trade-off studies are used to provide proof of concept, refine the basic concept, and generate a preliminary design. Further iterations or refinements would be employed if advanced design stages become necessary.

The evolution of the microwave radiometer spacecraft (MRS) design through several iterations is described. Configuration and structural design characteristics that were developed and refined during the design process are presented for the three structural configurations studied.

EVOLUTION OF THE MRS DESIGN

The MRS mission, as conceived in references 1 and 2, was designed to provide passive monitoring of microwave radiation from the Earth to determine the amount of moisture present in the soil as an indicator for forecasting crop yield.

The initial design concept assumed an orbiting reflector with a diameter of approximately 100 m and a focal-length-to-diameter (f/d) ratio of 2.5 located at an altitude of 390 km to achieve a ground resolution of 1 km. Another reason for this selection was to minimize reflector aberration and still keep the spacecraft size compatible with projected space construction capability. Several radiometer design concepts were studied with the conclusion that a focal-arc feed array and a spherical reflector satisfy image quality and spatial resolution requirements (ref. 3). Support beams, attached at the rim of the reflector to suspend the radiometer

receiver array along a focal arc beneath the reflector, minimize the radio frequency (RF) blockage of the antenna and increase the efficiency of the system. An artist concept of the initial design concept is presented in figure 1.

The RF design approach (ref. 4) indicated that a larger reflector at a higher altitude would be required to produce the desired 3-dB circular footprint with a beam efficiency of better than 90 percent within 2.5 times the 3-dB beam width. For an operating frequency of 1 GHz, an aperture diameter of about 300 m, and subsequent reflector diameter of 660 m, would be required at an altitude of 650 km. Also, spherical aberration of the 100-m reflector complicated the electronic design, which required the inclusion of a dielectric lens in the system to correct for aberrations.

Weight becomes a dominant factor in the development of space structures of this size. Innovative uses of geodesic truss configurations have been explored as a means of providing minimal weight structures without a loss of structural strength. A structural characterization and packaging study of five truss configurations (tetrahedral, curved tetrahedral, pentahedral, hexahedral, and radial rib) is presented in reference 5. The study showed the tetrahedral truss to be the most efficient (provides maximum surface area and shortest package length).

The tetrahedral truss (identified as the double-layered geodesic dome in this paper) is formed by assembling repeating tetrahedrons, as described in reference 6 and shown in figure 2. The free apex of each tetrahedron is subsequently connected to each of the surrounding apexes with columns of the same length as shown by the dashed lines.

A single-layered geodesic concept was also studied as an option for the reflector strongback structure. The single-layer concept uses a planar triangular geodesic surface as the framework for the dome-shaped antenna and requires a stronger and heavier support ring to provide structural rigidity to the geodesic skeletal structure. A sketch of the larger reflector which uses the geodesic dome concept is presented in figure 3.

Assembly of a reflector structure using either geodesic concept can be performed in space with deployable or erectable assembly methods. Deployment of a 725-m (2380-ft) diameter reflector as a single integral unit is not feasible at this time. Instead, the complete reflector would be assembled from deployable hexagon modules as shown in figure 4. The modules collapse for packaging in the orbiter bay as shown in figure 5. For the erectable concept, tapered columns are stacked one into the other in the shuttle bay as shown in figure 6. Packaging of both the deployable and erectable concepts is described in reference 7. Erection of the truss structure can be performed by the astronauts during extravehicular activity (EVA) or with the remote manipulator system, as shown in figure 7. The results of a test program to assess the potential of manned EVA assembly of erectable space trusses are presented in reference 8. A high-speed assembler (fig. 8) is estimated to reduce the assembly time of a 1-km-square span from 140 days to 25 days.

A drastic departure from the rigid geodesic design was investigated as an alternate concept for reducing the total spacecraft weight. The tension rim concept, shown in figure 9, resembles a bicycle wheel and uses the bootlace catenary antenna shaping concept of reference 9 to maintain the shape of the flexible antenna membrane, thus eliminating the need for a reflector strongback structure. This results

in a weight saving of approximately 10 000 kg (23 000 lb) over the single-layer geo-desic dome concept and enables the entire reflector structure to be packaged and transported to orbit in one shuttle flight (ref. 7).

SPACECRAFT DESIGN CHARACTERISTICS

Conceptual designs were made for the three structural approaches (two geodesic trusses and the flexible catenary or tension rim) to the microwave radiometer space-craft. The structures for the support columns and radiometer beam are common to all of the reflector structural concepts. Configuration and structural design charac-teristics developed and refined during the design process are presented for the three structural concepts.

Material Selections

The spacecraft structure is basically a skeletal framework built from long slender columns. The structural behavior of these columns is determined by overall column (Euler) buckling. Low-mass Euler columns require materials with a high ratio of Young's modules to density (E/ρ). The structure must also undergo relatively small deflections due to thermal loading. Although thermal distortions may be con-trolled by thermal coatings or insulation, a structural material with a very low thermal expansion coefficient would greatly ease the thermal problem.

A list of physical properties for several candidate materials (metals and com-posites) is given in table I. Because of its low density and thermal stability, a composite of graphite fibers and epoxy (G/E) was selected as the primary material for basic structural elements (low-mass columns). Aluminum was chosen as the material for joints and fittings.

Structural Elements

Two types of structural elements were considered for column members of the skeletal framework of the spacecraft. Thin-walled cylindrical elements are inher-ently strong in compression, but the packing efficiency (mass to displaced volume ratio) is very low. These elements would be used for the deployable structure and the boom. Tapered tubular elements or "nestable cones" which can be stacked one into the other are more efficient from a packaging viewpoint (ref. 10). These elements are used for the erectable structures. In orbit, two half-column tubes are joined together at the large end. The resultant element will carry approximately 30 percent more load before buckling than an equal-mass constant-diameter cylinder. A tapered element with 10 percent less mass will carry the same load as a cylinder element.

Structural element lengths of 18 m (59 ft), 8.75 m (28.7 ft), and 6.43 m (21.1 ft) were considered in the weight analysis (ref. 7). The 8.75-m (28.7-ft) element would be used for deployable structures only and its length is established by the length of the cargo bay. The 6.43-m (21.1-ft) element could be used for either deployable or erectable structures and is sized from the geometry for a maximum-surface-area facet that could meet the surface accuracy requirements of the reflector without any mechanical adjustment or controls. The 18-m (59-ft) element is composed of two 9-m (29.5-ft) tapered tubes and was selected to provide maximum utilization of

the cargo bay. The tube tapers from 0.15 m to 0.05 m in diameter along its length with a wall thickness of 0.381 mm.

It should be noted that all element lengths are mean lengths only. To achieve a curved surface, a variation of element lengths is required. The variation and quantity of different length elements can be minimized by refinement of the mathematical model of the domed truss.

Buckling load data for graphite epoxy elements of the three lengths are given in table II. Tube diameters for the tapered tubes are the mean diameters of the tubes.

Fittings and Joints

Assembly of the skeletal truss structure is performed in space by the remote manipulator system, an automated assembly machine, or the astronauts during EVA. Therefore, one major requirement of fittings and joints is ease of attachment of the structural elements at their intersection. Several attachment methods (welding, explosive, mechanical) have been studied. Prototype hardware has been built and is being tested for a side-latching mechanical joint (fig. 10), and it will be used as a representative fitting capable of uniting nine structural elements at a "node." These fittings are for the erectable structure. The deployable structure would require similar fittings, without the disconnect capability, as well as a knee-joint fitting, as shown in figure 11. Weight data for the fittings are presented in table III. These are actual weight values taken from prototype parts constructed of aluminum. The target values shown are conservative predictions of weights that could be achieved with further refinement and study. Although aluminum was considered in the study, the development of graphite epoxy should improve so that graphite epoxy fittings will be available by 1985, with additional weight savings.

Spacecraft Design

The basic configuration of the microwave radiometer spacecraft is shown in figure 12. The reflector is a spherical segment, 725 m (2380 ft) in diameter, with a spherical radius of 1150 m (3770 ft). The reflector has severe requirements on maintaining this shape. Deviation from the theoretical spherical radius is limited to 6 mm (1/2 in.) or less. A reflective mesh material is the prime candidate for the reflector surface due to its low mass and efficient packaging potential (a dish constructed of 0.254-mm (0.010-in.) thick aluminum weighs about 23 times the weight of a mesh reflector). An active control system (such as the electrostatic concept of ref. 11) is required for fine shape control because of the flexibility of the mesh and the surface accuracy requirements.

A rigid structure is essential for maintaining the nominal spherical curvature of the dish reflector for all concepts except the tension rim concept. A tetrahedral planar structure, formed of 18-m tapered columns, is modified to achieve a concave spherical surface using geodesic design procedures. The outer and diagonal elements are sized according to the geometry of the inner surface members.

An 800-m (2620-ft) diameter toroidal ring provides structural support to the reflector strongback and continuity between the strongback structure and the support columns. The ring also provides mounting support at nodal attachment points for the momentum-wheel attitude control system (ref. 12), solar panels, and other subsystem (power conversion, telemetry, and data processing) modules. The support ring is of

truss-type construction, utilizing the 18-m tapered column as the structural element. The ring is connected to the reflector platform by actuators which provide a coarse antenna positioning function.

An array consisting of 600 radiometers and feed horns (200 at each microwave frequency - 1, 2, and 4 GHz) is mounted along a 200-m (656-ft) long curved beam at a focal arc of the reflector. The beam curvature is a spherical radius of 575 m (1890 ft) (one-half the spherical radius of the reflector), such that each horn is pointed at a prescribed target on the reflector. The feed beam is a truss-work construction, using the 18-m tapered columns as structural members. A conservative approach was taken in designing the feed horns (currently in the developmental stage). Although the length and the flare angle will vary with frequency, an aperture diameter of 2 m and a length of approximately 10 m were established for conceptual design. The horns are designed to be split along the longitudinal centerline for more efficient packaging, with assembly accomplished on orbit. The assembled horn snaps into a channel beam that is preformed to give proper aiming. The channel beam, in turn, snaps into fittings at the nodes of the feed beam structure. The horn design is described in more detail in reference 13.

The radiometer array is suspended beneath the reflector by two 575-m (1890-ft) long support columns. The columns are mounted at the edge of the disk for minimum aperture blockage and maximum RF efficiency. Although several concepts for column design were investigated, the tension stabilized method is a lightweight concept that minimizes buckling (the primary failure mode). Tension members (cables) are placed at an effective radius of gyration by outriggers supported by a center column. The center column effectively becomes a series of short columns. The basic column can be solid (0.305-m (12-in.) diam graphite epoxy) or a fabricated geodesic beam (a mesh of short elements). The fabricated column would be a mesh of short elements, and, therefore, lighter, but a fabrication machine would be required and would have to be budgeted in the weight of the launch package. However, it could be utilized for other structures and its weight penalty spread over several missions.

Four Kevlar tension cables attached to the end of the radiometer beam and the reflector support ring provide stability to the suspended structure and orientation between the reflector and the feed horns. Coarse alignment corrections are anticipated over the life of the spacecraft, so provisions are made to control the relative location between the feed horns and the reflector. The columns have ball sockets at each end to allow relative motion between the major components, and a powered reel mechanism mounted on the support ring controls the tension in the cables. Provisions are made for rapid deployment of the cable during assembly as well as low-speed, high-torque control while operating.

Since only one design would be carried to the preliminary design stage, trade-off studies and computer-aided design studies indicated that the double-layer tetrahedral truss configuration was more feasible in light of current and projected technology and is, therefore, used as the primary structural concept in this design study. Detailed drawings of the double-layer tetrahedral truss configuration are presented in appendix B to this design study (ref. 13).

CONCLUSIONS

The evolution of the design of the microwave radiometer spacecraft (MRS) from conception to preliminary design is described. Three structural configurations are presented for the antenna, and configuration and structural design characteristics are described.

The antenna design has evolved to a preferred concept - the double-layered geodesic structure. Although the tension rim concept offers some distinct advantages, the ability to assemble and control the surface may create significant design problems. The geodesic structure offers the advantage of relatively simple analysis, maximum strength-to-weight ratio, potentially simplified assembly (via an automated assembler), and adequate radio frequency (RF) performance.

REFERENCES

1. Keafer, Lloyd S., Jr.: Mission Definition for a Large-Aperture Microwave Radiometer Spacecraft. The Microwave Radiometer Spacecraft - A Design Study, Robert L. Wright, ed., NASA RP-1079, 1981, pp. 17-32. (Paper in this compilation.)

2. Swift, Calvin T.: High-Resolution Passive Microwave Imaging of the Surface of the Earth. The Microwave Radiometer Spacecraft - A Design Study, Robert L. Wright, ed., NASA RP-1079, 1981, pp. 33-41. (Paper in this compilation.)

3. Keafer, Lloyd S., Jr.: Radiometer Design Concepts for a Large Aperture Microwave Radiometer Spacecraft. The Microwave Radiometer Spacecraft - A Design Study, Robert L. Wright, ed., NASA RP-1079, 1981, pp. 43-49. (Paper in this compilation.)

4. Agrawal, P. K.; and Cockrell, C. R.: Electromagnetic Design of a Microwave Radiometer Antenna System. The Microwave Radiometer Spacecraft - A Design Study, Robert L. Wright, ed., NASA RP-1079, 1981, pp. 129-136. (Paper in this compilation.)

5. Barclay, D. L.; Brogren, E. W.; Fosth, D. C.; Gates, R. M.; and Straayer, J. W.: Large Space Structures - Configuration, Packaging, and Response Studies. NASA CR-158928, 1978.

6. Bush, Harold G.; Mikulas, Martin M., Jr.; and Heard, Walter L., Jr.: Some Design Considerations for Large Space Structures. AIAA/ASME 18th Structures, Structural Dynamics, and Materials Conference, Mar. 1977, pp. 186-196. (Available as AIAA Paper No. 77-395.)

7. Jensen, J. Kermit; and Wright, Robert L.: Weight Estimates and Packaging Techniques for the Microwave Radiometer Spacecraft. The Microwave Radiometer Spacecraft - A Design Study, Robert L. Wright, ed., NASA RP-1079, 1981, pp. 109-125. (Paper in this compilation.)

8. Bement, Laurence J.; Bush, Harold A.; Heard, Walter L., Jr.; and Stokes, Jack, W., Jr.: EVA Assembly of a Large Space Structure Element. NASA TP-1872, 1981.

9. Ramsey, James W.; and Wright, Robert L.: Bootlace Catenary Concept for Antenna Shape Control. The Microwave Radiometer Spacecraft - A Design Study, Robert L. Wright, ed., NASA RP-1079, 1981, pp. 205-213. (Paper in this compilation.)

10. Bush, Harold G.; and Mikulas, Martin M., Jr.: A Nestable Tapered Column Concept for Large Space Structures. NASA TM X-73927, 1976.

11. Hinson, William F.; Goslee, J. W.; McIlhaney, John R.; and Ramsey, James H.: Biaxial and Electrostatic Tensioning Effects on Thin Membrane Materials. The Microwave Radiometer Spacecraft - A Design Study, Robert L. Wright, ed., NASA RP-1079, 1981, pp. 189-204. (Paper in this compilation.)

12. Montgomery, Raymond C.; and Johnson, C. Richard, Jr.: Adaptive Control System
    for Large Annular Momentum Control Device. The Microwave Radiometer Space-
    craft - A Design Study, Robert L. Wright, ed., NASA RP-1079, 1981,
    pp. 169-187. (Paper in this compilation.)

13. Jensen, J. Kermit: Appendix B - Spacecraft Drawings. The Microwave Radiometer
    Spacecraft - A Design Study, Robert L. Wright, ed., NASA RP-1079, 1981,
    pp. 221-243. (Paper in this compilation.)

TABLE I.- PHYSICAL PROPERTIES OF CANDIDATE MATERIALS

Physical property	Material			
	Aluminum 2014/2019	Stainless steel	G/E T300/5208 (unidirectional)	Kevlar 49 (unidirectional)
Ultimate tensile strength – GPa – (lb/in^2)	0.4481 (65 000)	1.241 (180 000)	1.72 (250 000)	1.65 (240 000)
Tensile yield strength – GPa – (lb/in^2)	.3792 (55 000)	1.034 (150 000)		
Young's modulus – GPa – (lb/in^2 × 10^6)	68.95 (10)	206.84 (30)	131.00 (19)	75.84 (11)
Density – kg/m^3 – (lb/in^3)	2768 (.10)	7833 (.283)	1522 (.055)	1383 (.050)
E/ρ	100	106	345	220
Coefficient of thermal expansion – 10^{-6}/K – (× 10^{-6}/°F)	24.7 (13.7)	14.4 (8)	.54 (.3)	-3.6 (-2)
Coefficient of thermal expansion – W/m-K – (Btu-in/hr-ft^2-°F)	173 (1200)	15.6 (108)	8.7 (60)	1.44 (10)

59

TABLE II.- BUCKLING LOAD CAPACITIES OF

GRAPHITE EPOXY ELEMENTS

Element length - m	6.43	8.75	18.00
- (ft)	(21.1)	(28.7)	(59.0)
Tube diameter - m	.058	.058	[a].100
- (in.)	(2.28)	(2.28)	(4.00)
Wall thickness - mm	.38	.38	.38
- (in.)	(.015)	(.015)	(.015)
Buckling load - kg	190	102	132
- (lb)	(419)	(225)	(293)
Buckling stress - GPa	27.25	14.64	10.76
- (lb/in^2)	(3954)	(2125)	(1561)

[a]Mean diameter of tapered tube.

TABLE III.- WEIGHTS OF ELEMENTS AND FITTINGS

Item	Actual weight, kg (lb)		MRS study target weight, kg (lb)	
Elements:				
6.43 m (21.1 ft)			0.680	(1.50)
8.75 m (28.7 ft)			.923	(2.04)
18.0 m (59 ft)			3.00	(6.62)
Center joints:				
0.100 m (4.0 in.)	0.166	(0.365)	.160	(.35)
0.150 m (6.0 in.)			.228	(.50)
End fittings:				
Element terminal	.0068	(.015)	.006	(.013)
Element half	.0435	(.096)	.040	(.088)
Node half	.0567	(.125)	.027	(.060)
Node fitting	.0603	(.133)	.042	(.093)
Total weight of 18-m (59-ft) element			3.32	(7.32)
Total weight of node			.284	(.626)
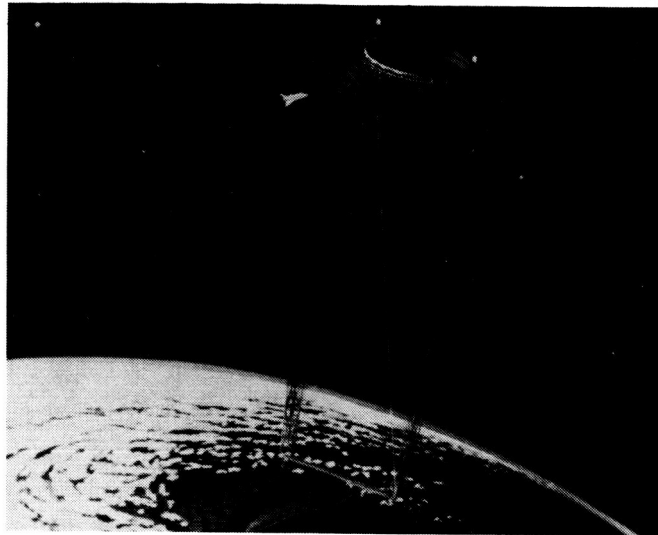
LCh-79-77

Figure 1.- Initial design concept.

BASIC REPEATING TETRAHEDRON
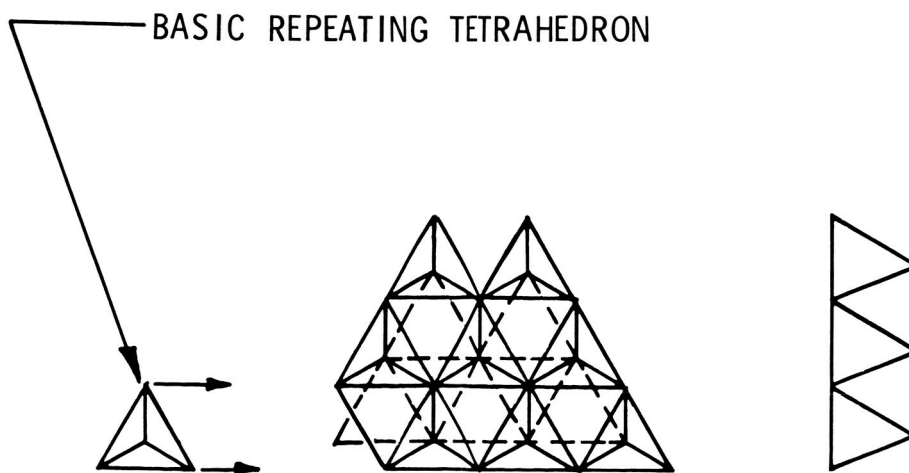
Figure 2.- Tetrahedral truss structure (from ref. 6).
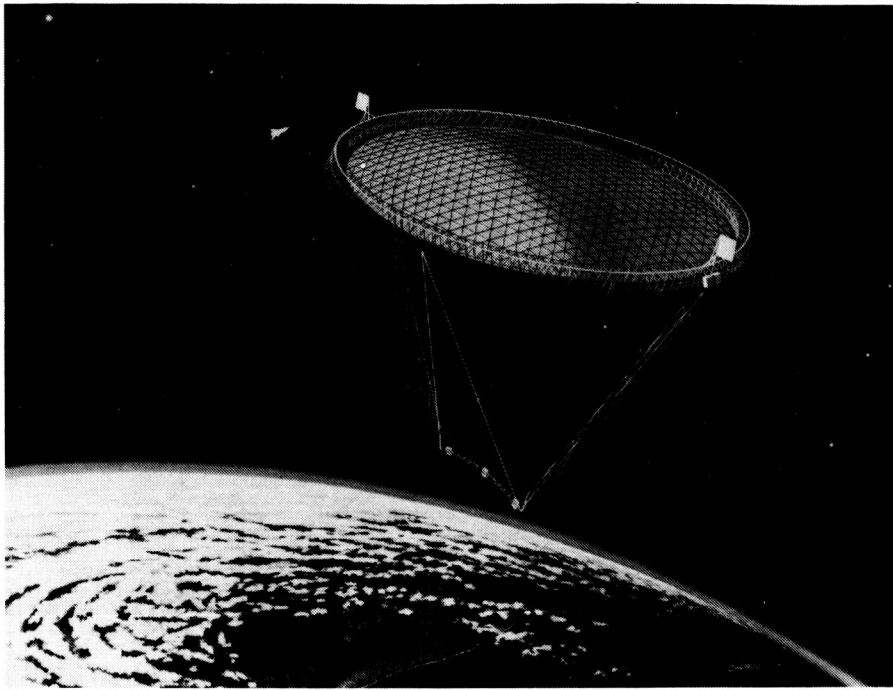
L-81-231

Figure 3.- Geodesic dome concept.

725m (2380 ft)
DIA

1150m
(3770 ft) R
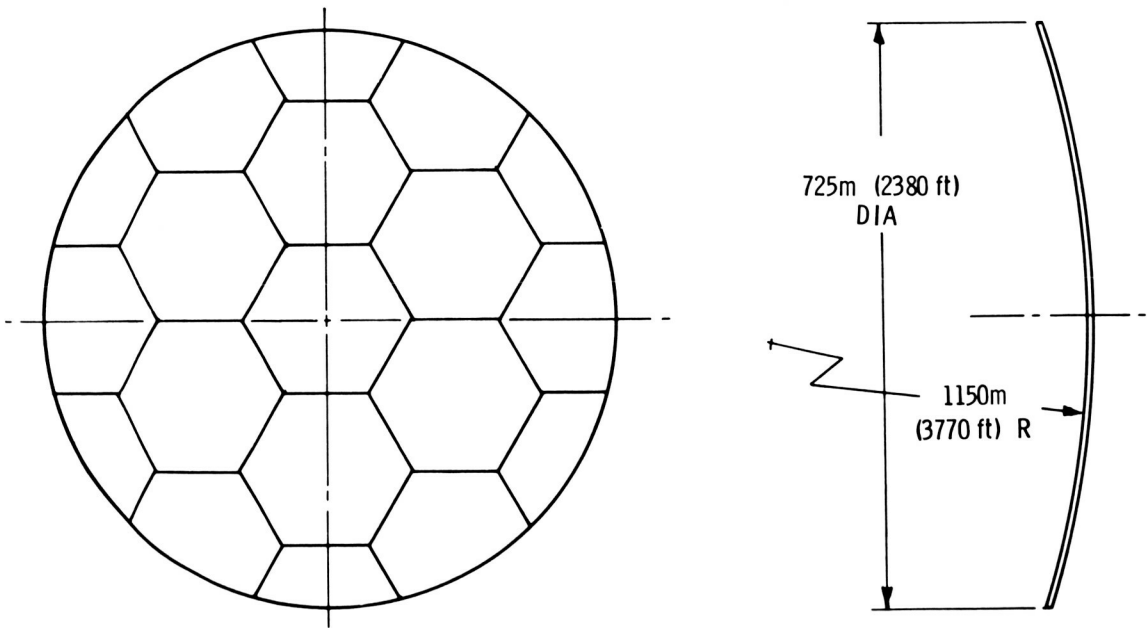
Figure 4.- Deployable concept.
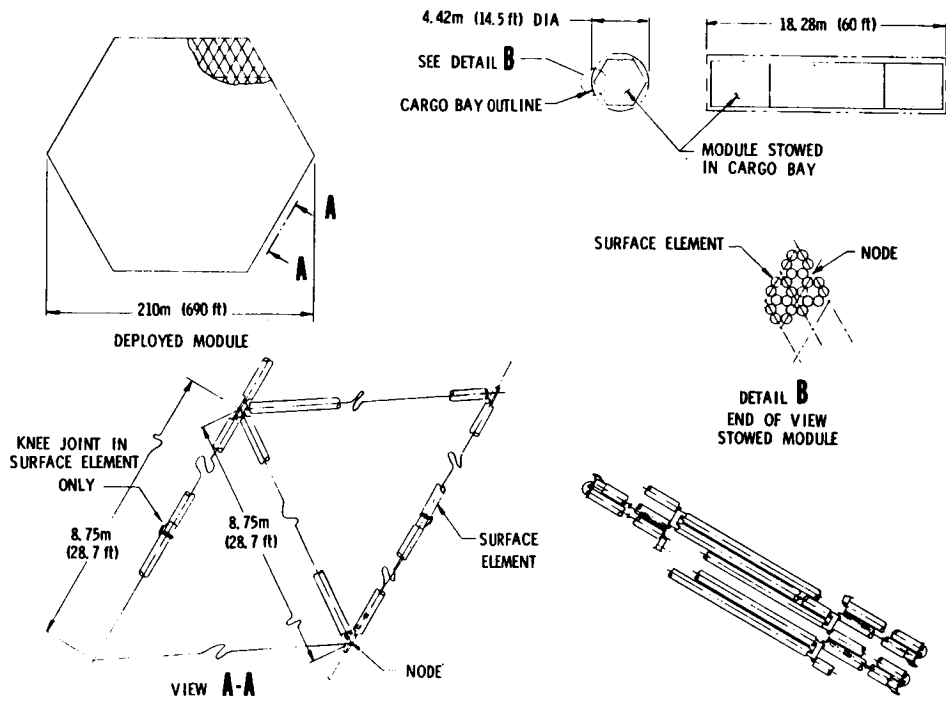
Figure 5.- Packaging for deployable concept.
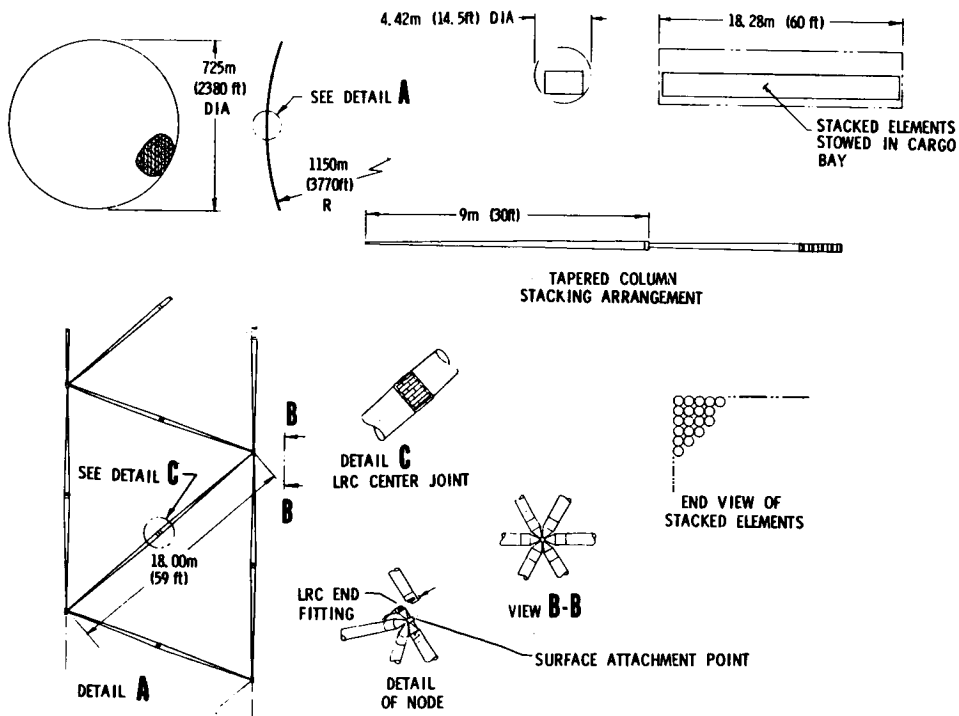
Figure 6.- Packaging for erectable concept.
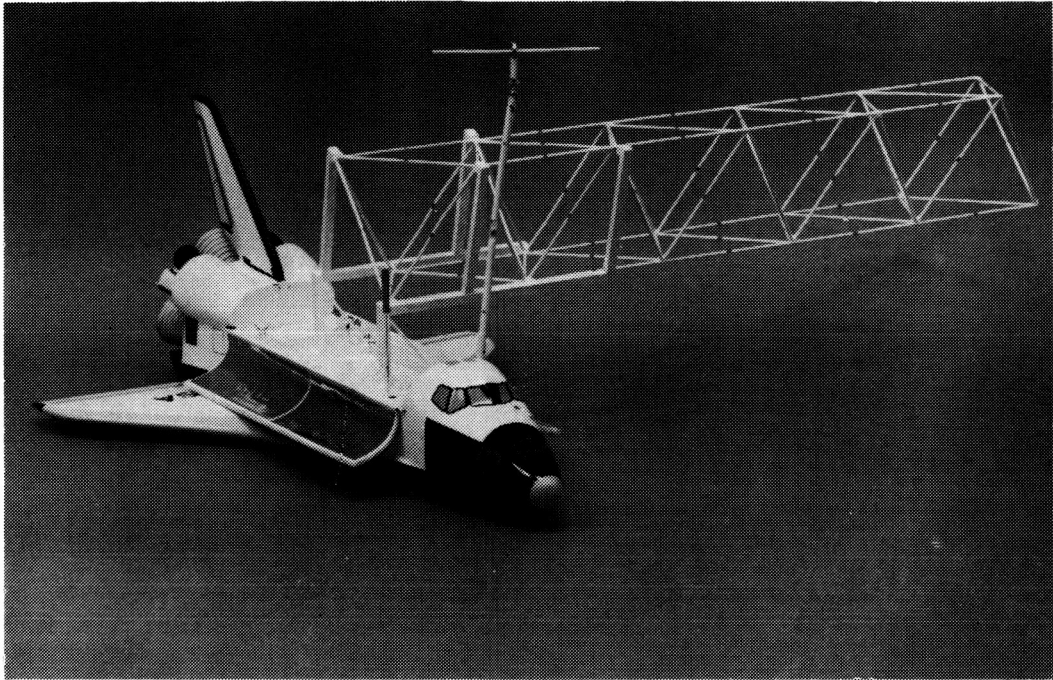
L-79-1597

Figure 7.- Erection of truss structure with remote
manipulator system.
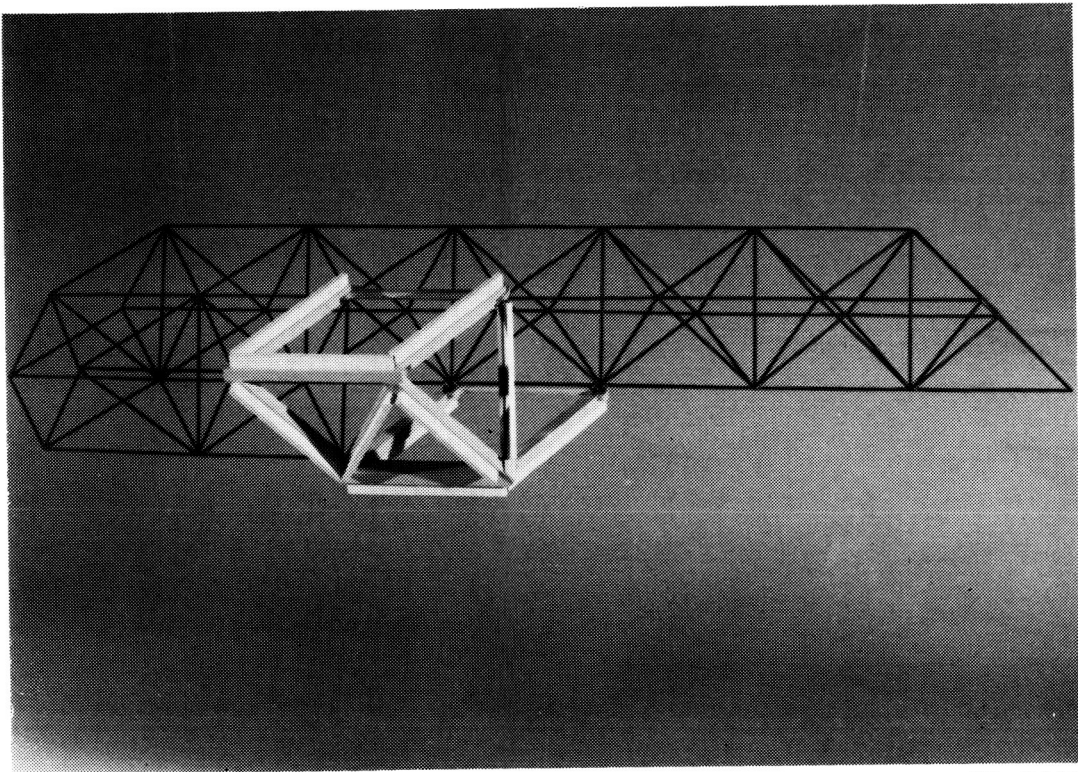
L-78-3642

Figure 8.- High-speed assembler.
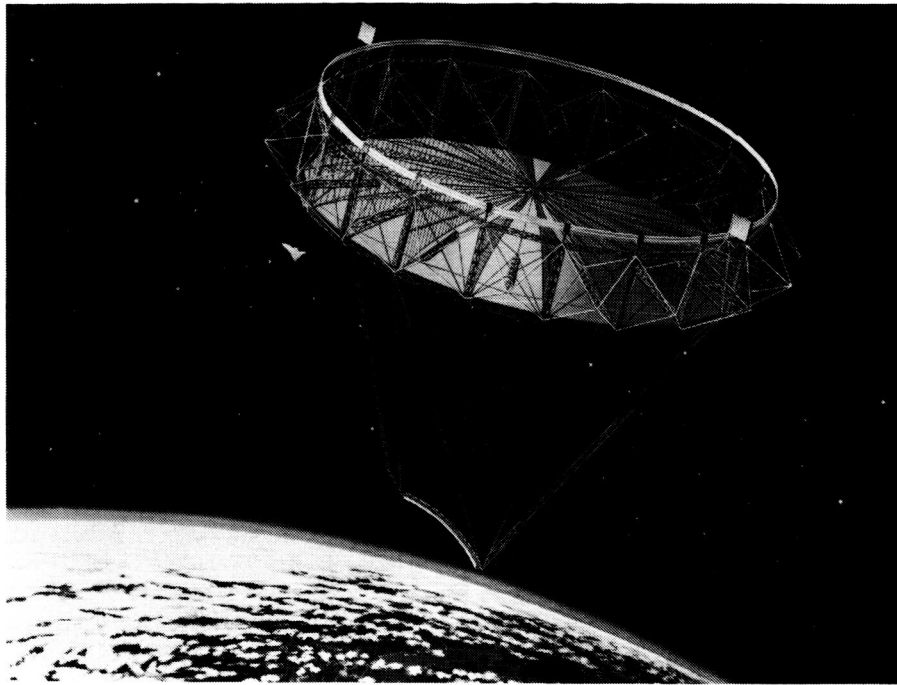
L-81-7540

Figure 9.- Tension rim concept.
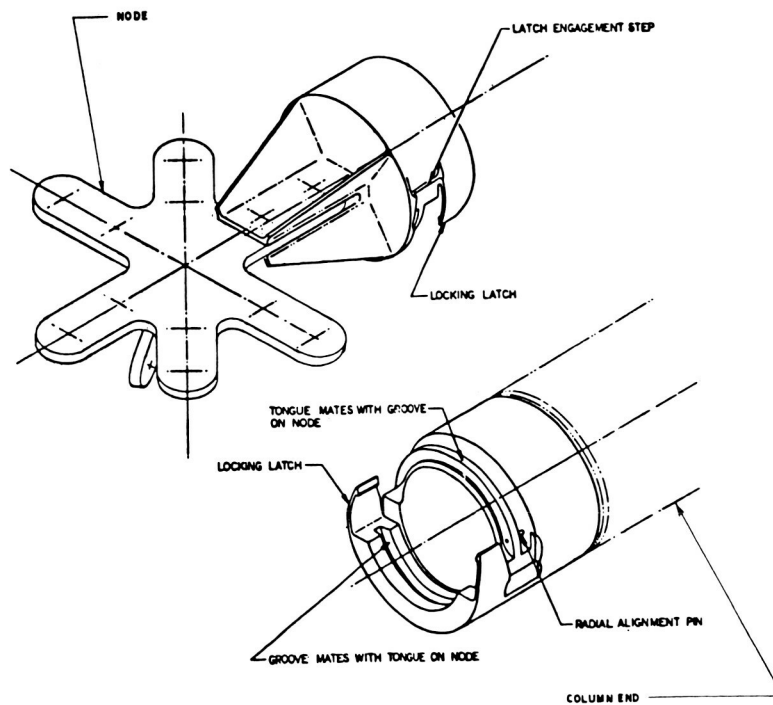
Figure 10.- Side-latching mechanical joint.
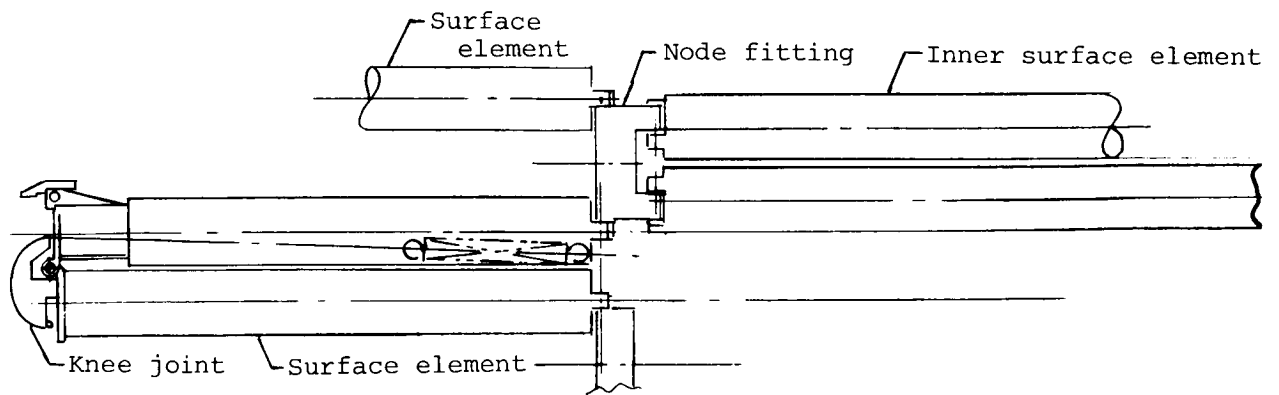
Figure 11.- Knee-joint fitting.
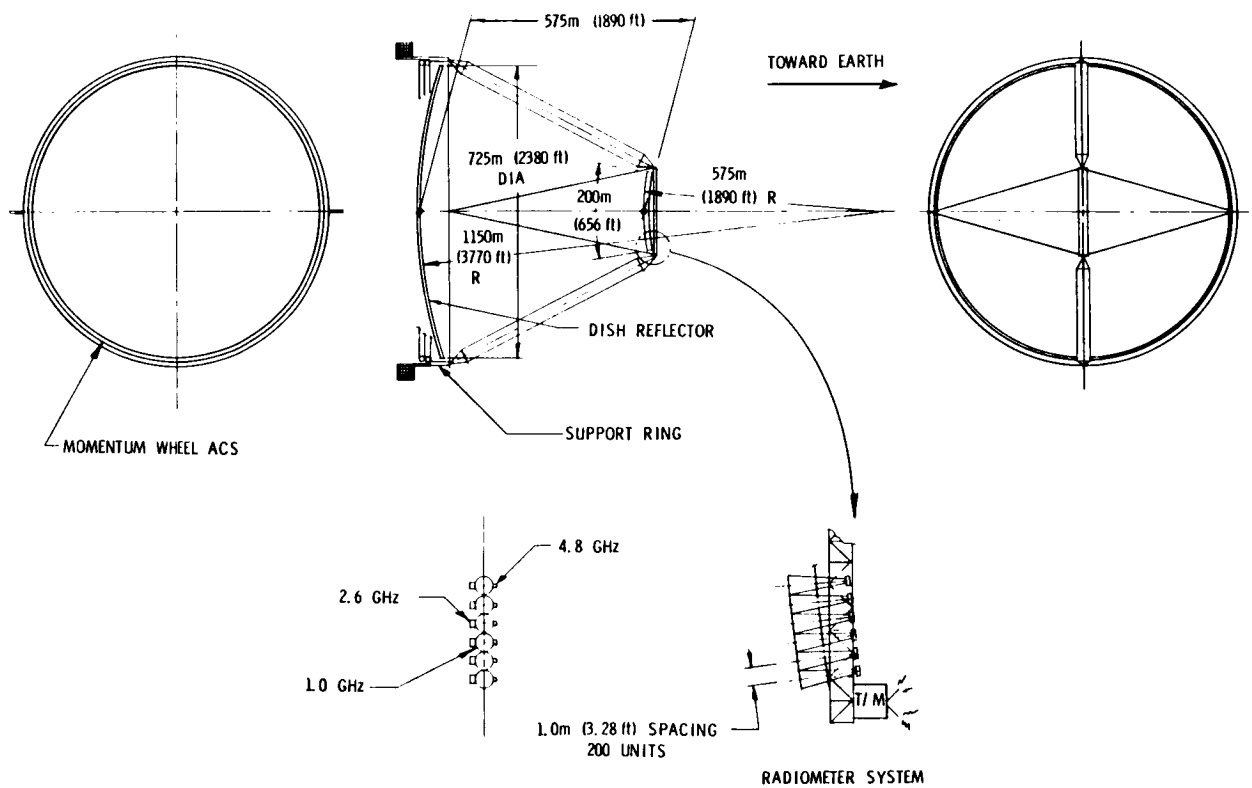
Figure 12.- Basic configuration of microwave radiometer
spacecraft (MRS).

PART II

DESIGN AND STRUCTURAL CONCEPTS

SYSTEMS DESIGN AND ANALYSIS OF

THE MICROWAVE RADIOMETER SPACECRAFT

L. Bernard Garrett
NASA Langley Research Center
Hampton, Virginia

SUMMARY

Systems design and analysis data were generated for a microwave radiometer spacecraft concept using the Large Advanced Space Systems (LASS) computer-aided design and analysis program. Parametric analyses were conducted for perturbations off the nominal-orbital-altitude/antenna-reflector-size and for control/propulsion system options. Optimized spacecraft mass, structural element design, and on-orbit loading data are presented. Propulsion and rigid-body-control systems sensitivities to current and advanced technology are established. Spacecraft-induced and environmental effects on antenna performance (surface accuracy, defocus, and boresight offset) are quantified and structured material frequencies and modal shapes are defined.

INTRODUCTION

The high spatial resolution requirement of passive microwave radiometry for moisture monitoring missions necessitates the use of large aperture systems in low Earth orbit. At the same time the launch vehicle is weight and volume limited, and the spacecraft weight and size must be kept to a minimum to reduce the number of launches required and hence the total cost of the mission. A systems analysis was conducted on the microwave radiometer spacecraft (MRS) configuration to determine an optimum combination of reflector size and orbital altitude which minimized the total mass of the spacecraft and met the resolution requirements of the mission.

The analysis was conducted using the Large Advanced Space Systems (LASS) computer-aided design and analysis program (refs. 1 to 3). Structural elements and spacecraft subsystems were sized for computed on-orbit environmental conditions to determine total spacecraft mass and size. Reflector surface distortions and dish/feed defocus and boresight offset statistics were generated for the spacecraft. Natural vibrational frequencies and mode shapes were calculated for the flexible structure.

The spherical reflector with multiple fixed beams was selected in reference 4, as the baseline concept for the study and is described in detail in reference 5. Figure 1 shows the basic MRS structure and supporting systems used in the systems analysis and evaluation. Subsystems were judiciously located to provide a reasonably balanced spacecraft (minimum cross products of mass inertia and minimum distance between center of gravity and center of pressure of the dish) and mass-efficient

control systems (large-diameter momentum control rings and maximum torque capabilities for the thrusters). The finite element model representation of the spacecraft used in the analysis is given in figure 2 with the nodal point numbering system noted.

LASS PROGRAM

Analytical results and design iterations were performed in the interactive Large Advanced Space Systems (LASS) computer-aided design program of references 1 to 3. The LASS program flow diagram depicting the basic program modules and functional capabilities is shown in figure 3. The Aerospace Vehicle Integrated Design (AVID) program (ref. 6) provides the executive-control and data-base/file-management capabilities of LASS. The overall capabilities of LASS are summarized in succeeding paragraphs.

In general, the Tetrahedral Truss Structure Synthesizer (TTSS) and the General Truss Synthesizer (GTS) modules allow the user to rapidly create the finite element model of the spacecraft structural elements, design the structural elements, add the spacecraft subsystems, and calculate the mass and inertia properties of the spacecraft. The Rigid-Body Control Dynamics (RCD) module calculates the on-orbit environmental forces and torques at user-specified circular orbital altitude and spacecraft orientation, determines the momentum storage and desaturation requirements, and iterates the masses of the annular momentum control device, propellant, and tankage to meet the orbit keeping, attitude control, and maneuver requirements of the spacecraft. Updated spacecraft mass, inertia, and centers of gravity and pressure are computed in the RCD module.

Actual on-orbit loads, individual element axial and bending-moment loads, stresses, and structural deflections are computed in the Static Loads Analysis (STLO) module and the Structural Analysis Program (SAP, ref. 7) for any combination of the following five loading conditions: (1) pretension, (2) thermal, (3) gravity gradient, (4) atmospheric drag, and (5) static thrust. If thermal loads are included, the Thermal Analysis (TA) module is used to compute radiation equilibrium temperatures for each structural element at a given position in the spacecraft orbit. Heat sources consist of solar radiation, Earth albedo, and Earth thermal radiation. STLO outputs summary data on the actual loads on the structural elements, compares them to the design loads, and permits the user to redesign the elements if the actual loads differ considerably from the design loads. The user can instruct the program to recycle through appropriate TTSS and/or GTS modules with the updated design loads and resize the elements. If the spacecraft mass and inertia properties are significantly modified, the RCD module can redefine the system requirements. Continuous iterations can be performed until the spacecraft design has been optimized for the actual environmental loads and torques. Deflections of the structure which are generated by SAP can be analyzed by the Surface Accuracy (SA) module for surface distortions in the reflective mesh and defocus boresight offset between the dish and feed.

SAP also performs a dynamic linear elastic analysis of the three-dimensional structural system and determines modal frequencies, mode shapes, and generalized internal forces for a specified number of modes. The Dynamic Loads (DYLO) module accepts the modal solution provided by SAP and computes the actual dynamic loads and stresses on the elements and structural amplitudes from user-specified time-varying force functions. It also permits the user to evaluate any reasonable advantage that might be obtained from gyroscopic dampers to increase the modal damping of the spacecraft structure in orbit.

Although the real MRS model consisted of 16 bays as shown in figure 4, an 8-bay analogous model corresponding to figure 2 was used in the analysis. The ANALOG module permits a large number of tetrahedral truss elements in a flat-platform or curved-dish truss to be replaced for analysis by a smaller number of equivalent elements. Element sizes, physical properties, and loads are transformed in such a manner as to retain the equivalent strength, stiffness, mass, inertia, and thermal characteristics of the original structure. Although the user interactive LASS program executes all the modules including SAP far more rapidly than any other with similar capabilities currently available in industry or government, the power of the analogous modeling capabilities to perform rapid parametric analysis is particularly noteworthy. For example, a single pass through the LASS modules (except DYLO) for the 8-bay case (121 nodes, 439 elements) required 5 minutes of central processing unit (cpu) time (including the SAP static and dynamic analyses, 15 modes with 700 degrees of freedom each, which required 62 and 259 sec of cpu time, respectively) and 1 1/2 clock hours of interactive processing time on the main frame computers during a relatively busy period of the day. In contrast the 16-bay case (421 nodes, 1723 elements) required about 30 min of cpu time (SAP static and dynamic times of 275 and 759 sec, respectively, were required) and would be difficult to complete in a single standard work day.

The Postprocessor (POST) module converts data from the analogous model form used for internal program computations to equivalent real model form. POST outputs summary data of overall spacecraft mass, size, and inertia, individual subsystem components (types, number, and masses required), and structural elements (types, number required, dimensions, and masses). The number and masses of fittings, pins, bearings, and connectors, mesh system masses, and spacecraft mass contingency are also output.

For typical cases the results for the real and analogous models are within 1 percent of mass and inertia projections. A thorough assessment of the effect of analogous modeling on dynamic analysis results has not yet been completed; however, preliminary results are encouraging. Comparisons of the 16-bay-real/16-bay-analogous case with the 16-bay-real/8-bay-analogous case yielded fundamental frequencies that are within 1 percent; however, it should be noted that the first elastic frequency results were influenced primarily by the feed and feed-support beams and not by the relatively stiff tetrahedral truss dish. The dish alone has a fundamental frequency about an order of magnitude higher than that for the total spacecraft.

SPACECRAFT DETAILS AND PROGRAM INPUTS

The structure consists of a relatively stiff double-layered tetrahedral truss dish (graphite composite) with an RF reflective mesh (aluminized Kapton with a unit mass of 0.03 kg/m^2) attached to offsets on the concave surface. Support beams (graphite composite) and tension cables (Kevlar) provide stabilization and boresight control for the feed horns mounted on a curved boom located at the focal point of the reflector. The dish is a spherical segment with focal-length-to-diameter ratio of 2. Attitude control is provided by a dual-ring annular momentum control device (AMCD) and eight 1-N liquid-oxygen/liquid-hydrogen thrusters. The AMCD rings are magnetically supported in races at the outer periphery of the convex surface of the dish (nodes 2003, 2010, 2031, and 2046). Node numbers are shown in figure 2. The eight gimballed thrusters are located at the six corners of the hexagonal convex surface. Six of the thrusters, one at each corner (nodes 1001, 1005, 1027, 1035, 1057, and 1061), fire in the direction of nadir. The other two thrusters (nodes 1005

and 1057) fire in the y-direction. Orbital velocity makeup is provided by four larger liquid-oxygen/liquid-hydrogen thrusters. Two are located on the dish structure (nodes 2001 and 2023) and provide 1500 N thrust each, and two are located at the extremities of the feed beam (nodes 3001 and 3002) and provide 500 N thrust each. Three propellant tanks are located on the convex side of the dish in a triangular arrangement at the three centermost points (nodes 2019, 2026, and 2027).

Two service modules with masses of 1500 kg each are attached at opposite extremes on the concave side of the dish (nodes 2004 and 2044) and a third service module with a unit mass of 75 kg/m is attached along the entire length of the feed beam (between nodes 3001 and 3002). Two solar panels weighing 200 kg each with collector areas of 25 m^2 each provide the estimated 10-kW power need of the MRS.

Two 500-kg gyros located at nodes 2044 and 3002 are available to damp the motions of the dish and the relative motions of the dish and feed system.

Three-year propellant resupply periods were assumed in the analysis. AMCD tip speeds of 200 m/sec were used which are within the strength capabilities of applicable materials. The spacecraft is assumed to undergo one maneuver every five orbits with maneuver rates and accelerations of 10^{-4} rad/sec and 10^{-6} rad/sec^2, respectively. The maximum duration is calculated internal to the RCD module. AMCD desaturation is once each orbit. The spacecraft dish points toward nadir with the long axis of the feed beam oriented normal to the spacecraft velocity vector.

RESULTS

Parametric Analysis

Three different combinations of spacecraft size and orbital altitude were analyzed as follows:

Case	Dish diameter, m	Orbital altitude, km
E-1	750	750
E-2	400	400
E-3	1000	1000

Case E-1 corresponds to the nominal baseline MRS. Case E-2 is for a smaller dish, requiring less structural mass but additional propellant for orbital velocity makeup and maneuvers because of higher atmospheric drag. Case E-3, while out of the sensible atmosphere and thus not subjected to any significant atmospheric drag, requires moderate quantities of propellant for AMCD momentum desaturation. The feed and feed-support beams, tension cables, and AMCD ring diameter for each case are linearly scaled with the antenna dish diameter.

Spacecraft mass summary data for each of the three size/orbital-altitude cases are given in table 1. Plots of cumulative mass as a function of antenna diameter and of orbital altitude are shown in figure 5. The optimum size/altitude combination which minimizes the total MRS mass occurs for the 750-m-diameter dish at about 750 km

altitude. At the lower altitudes the gross spacecraft mass is dominated by the propellant mass required to maintain orbital velocity in the high atmospheric drag environment. At the higher altitudes the structure and mesh masses become dominant.

A specific impulse I_{sp} for a state-of-the-art liquid-oxygen/liquid-hydrogen thruster system of 4000 N-sec/kg (408 sec) was baselined for this part of the study. Use of flight-qualified storable propellant thruster systems with I_{sp} between 2000 and 3000 N-sec/kg (204 and 306 sec) would bias the spacecraft mass minimization results toward the higher altitude, whereas the use of advanced electric thrusters with I_{sp} ranges between 30 000 N-sec/kg (3060 sec) and 100 000 N-sec/kg (10 200 sec) would favor a smaller spacecraft near the 400-km orbital altitude.

The mass advantage of a typical 8-cm electric ion thruster (I_{sp} = 30 000 N-sec/kg (3060 sec)) is shown in figure 6. The total mass of the 400-m-diameter spacecraft at 400-km altitude has been reduced by a factor of 3 below that of the same spacecraft using cryogenic liquid-oxygen/liquid-hydrogen thrusters (I_{sp} = 4000 N-sec/kg (408 sec)). Utilization of such electric thruster systems warrants further consideration. Not only does the electric thruster system yield a smaller spacecraft which translates into fewer shuttle flights (particularly in the volume-limited payload bay), but also its orbital altitude is potentially more accessible to the shuttle orbiter.

Since electric propulsion systems appear to hold such promise of significant size and mass reductions for the MRS, it was decided to examine an even smaller, lower altitude spacecraft, although it would not satisfy the repeat coverage requirements of the mission. A 200-m-diameter, 200-km-altitude case was run. For the 30 000 N-sec/kg (3060 sec) I_{sp} electric thrusters, the total spacecraft mass was 290 000 kg (a factor of 2 higher than the 750-m-diameter MRS baseline which used cryogenic propellants). The combined structure, mesh, and utilities masses were only 20 000 kg; however, the propellant and AMCD masses were 230 000 kg and 25 000 kg, respectively. The combinations of high drag and decreased moment arm for the thrusters and smaller diameter AMCD rings lead to prohibitive control system requirements at these altitudes. Obviously, higher I_{sp} systems (100 000 N-sec/kg (10 200 sec)) are required to permit these large structures to operate at lower altitudes for any reasonable period of time.

It is also enlightening to compare the mass advantage of the combination of the dual-ring annular momentum control device (AMCD) and reaction control system (RCS) thrusters with that of a control system using only RCS thrusters. The results of this comparison as computed in the Rigid-Body Control Dynamics module of the LASS program are shown in figure 7. The combined AMCD/RCS thruster system has a 2-to-1 mass advantage over the RCS thruster only for storable propellants with I_{sp} of 2000 N-sec/kg (204 sec). However, the advantage swings to the RCS thruster only system using electric propulsion at I_{sp} = 30 000 N-sec/kg (3060 sec). Again, the use of high I_{sp} electric propulsion systems, around 100 000 N-sec/kg (10 200 sec), would have a pronounced effect on the ability to maintain large structures in low Earth orbit, assuming that the electrical power requirements and the number and weight of the thruster system could be kept within reasonable bounds. (The eight ion thrusters are estimated to require a total of about 1 kW of power and are assumed to be powered by the 10-kW solar panels of the spacecraft.)

Static Loads Analysis and Structural Element Design

All structural elements were analyzed and designed in LASS to accommodate the on-orbit environmental loading conditions and the self-imposed loads created by the tension cables. The principal modules utilized in this part of the study were ANALOG, TTSS, GTS, STLO, and SAP (static). The dish elements were hollow rods, tension cables were solid rods, and feed-array/feed-support beams were triangular-truss struts. All members, except the tension cables, were sized to accommodate combined Euler buckling axial loads and bending moments. Loads created by bending moments were reduced to stress-equivalent axial forces in the analysis. The Kevlar tension cables were sized on the basis of tensile strength.

A summary of the combined maximum static loads (atmospheric drag, gravity gradient, thermal, static thrust, and pretensioning) on the various structural elements for the baseline case is given in table 2.

Loading distribution histograms for the front, rear, and diagonal elements of the dish are shown in figures 8(a) to (c), respectively. Although each generic class of elements in each part of the dish (i.e., front and rear surface elements and diagonal elements) was designed to carry the maximum load experienced by any of the individual elements in that class, it is apparent that the use of an individual design load for the lighter loaded elements would reduce spacecraft structural mass and control system requirements. By selectively designing the elements according to the loads histogram distribution, the masses of the dish structure and the control system are reduced to about 50 000 kg and 15 000 kg, respectively.

Additional spacecraft mass saving could be realized if alternative concepts from tension cables are developed to boresight the dish and feed beam. The results of the loads analysis revealed that the structure is loading itself by means of the tension cables and all environmental loads are relatively small in comparison (about 1 to 10 orders of magnitude lower). In descending order of importance, the net loads on the structural elements for the MRS case were

(1) Pretensioning

(2) Static thrust for orbital velocity makeup

(3) Thermal

(4) Gravity gradient

(5) Atmospheric drag

Change in orbital altitude, spacecraft orientation, and orbit location (for thermal) would change the relative ranking of these loads.

Thermal Analysis

Thermal loads on the individual elements will vary throughout the orbit and generally it is not known a priori at which points the loads reach a maximum. However, some insight on maximum thermal loading can be gained by calculating element temperatures and temperature differentials at selected orbital points. In this

study, heating rates and temperatures of each MRS structural element were calculated in the LASS Thermal Analysis (TA) module at four points in the orbit as follows:

(a) Orbit angle = 1.5 rad; Time ≈ 0.40 hr
    (just prior to spacecraft entry into Earth shadow)

(b) Orbit angle = 3.7 rad; Time ≈ 0.98 hr
    (just prior to spacecraft exit from Earth shadow)

(c) Orbit angle = 3.9 rad; Time ≈ 1.03 hr
    (just after spacecraft exit from Earth shadow)

(d) Orbit angle = 5.8 rad; Time ≈ 1.53 hr
    (midway in sunlit portion of orbit)

The start and end of Earth shadow were at orbit angles of 1.6 and 3.8 rad (time 0.4239 and 1.005 hr), respectively. The orbit period was 1.667 hr at the 750-km altitude. Summary results of the thermal computations for each point are given in table 3 where the maximum and minimum temperatures of the various elements are shown, along with the maximum temperature difference between any two elements.

Element temperatures for point c (just after exit of the spacecraft from Earth shadow) were selected for use in the static loads analysis discussed. This point was selected on the combined basis of near maximum temperature differential between elements and reasonably low temperatures for all the elements. Since the MRS is fabricated in an Earth ambient temperature thermal environment, it is expected that the low temperature of space (minimum of 198 K for point c) will introduce additional stress into the elements. Thermal loads for some of the individual elements were an order of magnitude less than the pretensioning loads and were not significant enough in this case to warrant a more detailed examination. However, for other spacecraft which are not self-loading, the thermal loads could become a significant design consideration.

Surface Accuracy

Contours of the rms surface distortions of the structural nodes on the mesh side of the dish are shown in figure 9(a). Positive displacements denote movement of the dish structure toward the feed. The distortions from a perfect spherical segment are caused principally by the structural loadings from the tension cables. The rms surface roughness of 6.6 cm exceeds the millimeters-of-accuracy requirement by an order of magnitude. However, since these distortions are principally affected by the cable tensioning (note the symmetry of contour patterns about the X- and Y-axes), it is expected that predesign of the surface to yield a spherical surface when under tension or calibration of the distorted tensioned surface will reduce the effective large distortion error to acceptable millimeter levels.

Defocus and boresight-offset data for the dish are also presented in figure 9. The dish surface is drawn inward (toward the feed) an average of 1.1 cm. More significantly, the center node in the feed is drawn toward the dish by 22 cm for an overall defocus distance of 23 cm. The boresight offset between the dish and feed is about 25 cm. This translates into a ground-track pointing location error for the dish of about 300 m which is within the 1-km resolution accuracy band. Again, proper

predesign of the antenna or calibration of the distorted tensioned surface should significantly reduce the defocus and boresight errors for the MRS. If the tension cables are eliminated, the structural surface distortions caused by the environmental effects (thermal, gravity gradient, and atmospheric drag) are reduced by more than an order of magnitude and meet the 6-mm surface accuracy requirements as shown in figure 9(b). Defocus and boresight errors are reduced commensurately.

Dynamic Analysis

Large advanced space structures are expected to have fundamental elastic frequencies that are 1 or 2 orders of magnitude lower than any substantial terrestrial or space-based structure built to date. For these systems the dynamicists and designers must assess the structural impact of a number of low-frequency transient forces which can excite the highly flexible spacecraft, whereas in the past these forces could be ignored in a dynamic analysis or considered to be of a static nature. Examples of the low-frequency forces which could trigger the vibrational modes of the structure may include propulsion system and other fluid flow system transients, solar array drive torques, attitude control system imbalances, and even thermal cycling between Sun and shadow. Shuttle orbiter release loads and resupply docking loads are other transient loading sources.

Lengthy analysis, design, and experimental processes are required to arrive at a quantification of the effects of time-variant forces on the spacecraft, and design and implementation of control systems to deal with the vibrational response of the structure. The first step in the process is to calculate the natural vibrational frequencies and mode shapes for the integrated spacecraft.

The lowest material vibrational frequencies for each of the three spacecraft designs range from 0.04 to 0.09 Hz and are listed in table 4. These frequencies are far below the design capabilities of current spacecraft controllers and actuators. Also shown is the fundamental frequency of 0.63 Hz for a 725-m-diameter tetrahedral truss dish only. The addition of the feed, feed-support beams, and tension cables reduce the fundamental frequency of the spacecraft by an order of magnitude. An examination of the first nine vibrational and mode shapes for the MRS baseline as shown in figure 10 reveals that the feed and feed-support beams are behaving as simply supported, free-free, or cantilevered beams whereas the truss dish structure is relatively stiff and does not appreciably control the lower modes. It should be noted that, whereas this part of the study did not address minimum vibrational frequency or flexible-body control system requirements for the MRS, it is possible that the triangular truss beams could be replaced with somewhat stiffer structural elements and modifications could be made to the tension cable concepts to raise the lower order frequencies somewhat. However, even with technology advances in stiff, lightweight materials and structural design concepts, it is likely that these low frequencies and possibly high amplitude vibrations will be typical for large future systems.

The calculation of natural vibrational frequencies and mode shapes is only the first step in a lengthy spacecraft analysis, design, and testing process. The next step in the effort requires an accurate definition and examination of the time-dependent environmental and spacecraft-induced disturbances and an assessment of flight-qualified and advanced-control systems capabilities to suppress any of the excited modes. These examinations were beyond the scope of the present study. However, these types of assessments warrant substantial efforts ranging from definition of the low-frequency forces, assessment of the influence of these forces on the

vibrational response of the structure covering several decades in frequency, quantification of the natural damping afforded in the design of joints and connectors, viscous damping due to low-altitude atmospheric density effects, and the design and placement of control systems (active or passive).

The capabilities and experimental data required to quantify the dynamic environment and structural-response/control-system requirements for large flexible structures such as the MRS are not presently available. Unlike worst-case static-loads and thermal-loads analyses which the designer can use to insure integrity of the overall spacecraft design, it is not clear how designs of the large flexible spacecraft structures and associated controls systems can be made with no real usable historical data to guarantee avoidance of resonant frequencies and high-amplitude vibrations. Either there will be a slow evolutionary process of growth in sizes of future spacecraft before large MRS become a reality or a focused effort on analysis, design, and Earth-based/on-orbit testing will be required to determine whether there are excessive vibrations and dynamic loads/stresses in the structure, to control reflective antenna surfaces to tight tolerances, and to maintain boresight control between the dish and feed.

CONCLUDING REMARKS

A parametric analysis of the MRS concept using the LASS computer-aided design program established approximately a 750-m diameter and a 750-km altitude as the optimum for a system with liquid-oxygen/liquid-hydrogen chemical thrusters. The use of advanced high specific impulse in thrusters systems in lieu of the state-of-the-art chemical thrusters for drag makeup could yield substantial reductions in spacecraft size and total mass and in the orbital altitude. However, in order to meet the 1-km-resolution requirement, it is unlikely (even with advanced subsystems) that the MRS antenna diameter would be less than 400 m. Multiple shuttle flights and on-orbit assembly of structural modules and subsystems will be required. If the resolution requirement can be relaxed, a significantly smaller microwave radiometer spacecraft can be developed and, possibly, a meaningful soil-moisture-measurement mission is achievable in a single shuttle launch. Future studies and analyses should be directed at meaningful compromises between mission requirements, spacecraft designs, and launch and operational costs.

The geodesic truss proves to be a relatively stiff, efficient structure. However, the inclusion of the less stable feed and support structures significantly modifies the elastic frequencies. Ultralow natural frequencies are a characteristic of this large spacecraft, ranging from approximately 10^{-2} Hz for the combined truss dish, feed array, and support system to 10^{-1} Hz for the truss dish only. The analysis has further provided detailed insight into the member loading and dish distortion with a definite recommendation for reexamination of the feed support cable tensioning.

The extension of analytical capabilities to predict low-frequency disturbances, the development of flexible-body control systems to suppress possible low-frequency, high-amplitude vibrations, and ground-test verification present special challenges to the analysts and designers.

REFERENCES

1. Leondis, Alex: Large Advanced Space Systems Computer-Aided Design and Analysis Program - Final Technical Report. NASA CR-159191-1, 1980.

2. Leondis, Alex: Large Advanced Space Systems Computer-Aided Design and Analysis Program - User Document. NASA CR-159191-2, 1980.

3. Leondis, Alex: Large Advanced Space Systems Computer-Aided Design and Analysis Program - Programmer Document. NASA CR-159191-3, 1980.

4. Keafer, Lloyd S., Jr.: Radiometer Design Concepts for a Large Aperture Microwave Radiometer Spacecraft. The Microwave Radiometer Spacecraft - A Design Study, Robert L. Wright, ed., NASA RP-1079, 1981, pp. 43-49. (Paper in this compilation.)

5. Wright, Robert L.: Evolution and Design Characteristics for the Microwave Radiometer Spacecraft. The Microwave Radiometer Spacecraft - A Design Study, Robert L. Wright, ed., NASA RP-1079, 1981, pp. 51-66. (Paper in this compilation.)

6. Wilhite, A. W.; and Rehder, J. J.: AVID: A Design System for Technology Studies of Advanced Transportation Concepts. AIAA Paper 79-0872, May 1979.

7. Cronk, M. J.: Solid SAP: User's Manual. CASD-CIH-74-008, General Dynamics/Convair Div., Oct. 1977 (revised Oct. 1978).

TABLE 1.— MRS PARAMETRIC STUDY MASS SUMMARY DATA

Case	Antenna diameter, m	Altitude, km	Mass data, kg					
			Gross	Structure	Mesh	Propellant (a)	AMCD	Other subsystems
E-1 (baseline)	750	750	131 510	70 051	19 075	16 960	2566	22 858
E-2	400	400	198 400	23 279	5 425	150 110	961	18 625
E-3	1000	1000	184 320	116 826	33 912	427	4800	28 155

a_{LOX/LH_2} propellant $I_{sp} = 4000 \frac{N\text{-sec}}{kg}$ (408 sec).

TABLE 2.- MRS STATIC LOADS SUMMARY

Load,ᵃ N

Case	Highest loaded elements in dish			Tension cables (b)	Feed-support beams (b)	Feed-array beams (b)
	Mesh side (b)	Back side (b)	Diagonal (b)			
E-1 (baseline) Diam. = 750 m Alt. = 750 km	+5934 −4065 (−6000)	+3530 −5847 (−6000)	+3075 −3162 (−4000)	3214 (+8000) ((+5000))	−6 279 (−10 000)	−21 250 (−25 000)
E-2 Diam. = 400 m Alt. = 400 km	+4254 −3142 (−5000)	+2754 −4366 (−5000)	+2192 −2324 (−3000)	2738 (+8000) ((+5000))	−4 142 (−5 000)	−9 612 (−15 000)
E-3 Diam. = 1000 m Alt. = 1000 km	+6419 −4318 (−7000)	+3761 −6234 (−7000)	+3314 −3383 (−4000)	+3447 (+8000) ((+5000))	−6 625 (−10 000)	−21 810 (−25 000)

ᵃThe structure is loading itself by means of the tension cables. Environmental loads are relatively small in comparison.

ᵇ+ represents tension, computed; − represents compression, computed; ( ) represent design loads; (( )) represent pretensioning loads.

TABLE 3.- MAXIMUM AND MINIMUM ELEMENT TEMPERATURES

Orbit point	Element temperatures, K										
	Dish elements						Feed beam	Feed support beams		Tension cables		Maximum temperature difference between elements
	Concave surface, mesh side		Convex surface		Diagonal							
	Max.	Min.	Max.	Min.	Max.	Min.		Max.	Min.	Max.	Min.	
a	312	232	312	237	312	236	313	312	308	310	286	79
b	191	183	184	183	179	176	191	179	179	180	180	12
c	251	201	264	196	255	214	267	261	256	262	227	71
d	332	324	328	324	325	300	321	298	271	301	275	30

TABLE 4.- LASS DYNAMIC ANALYSIS FIRST

NATURAL VIBRATIONAL FREQUENCY

Case	First elastic frequency, Hz
E-1	0.0560
E-2	.09019
E-3	.04191
Dish only (725-m diam.)	.6255
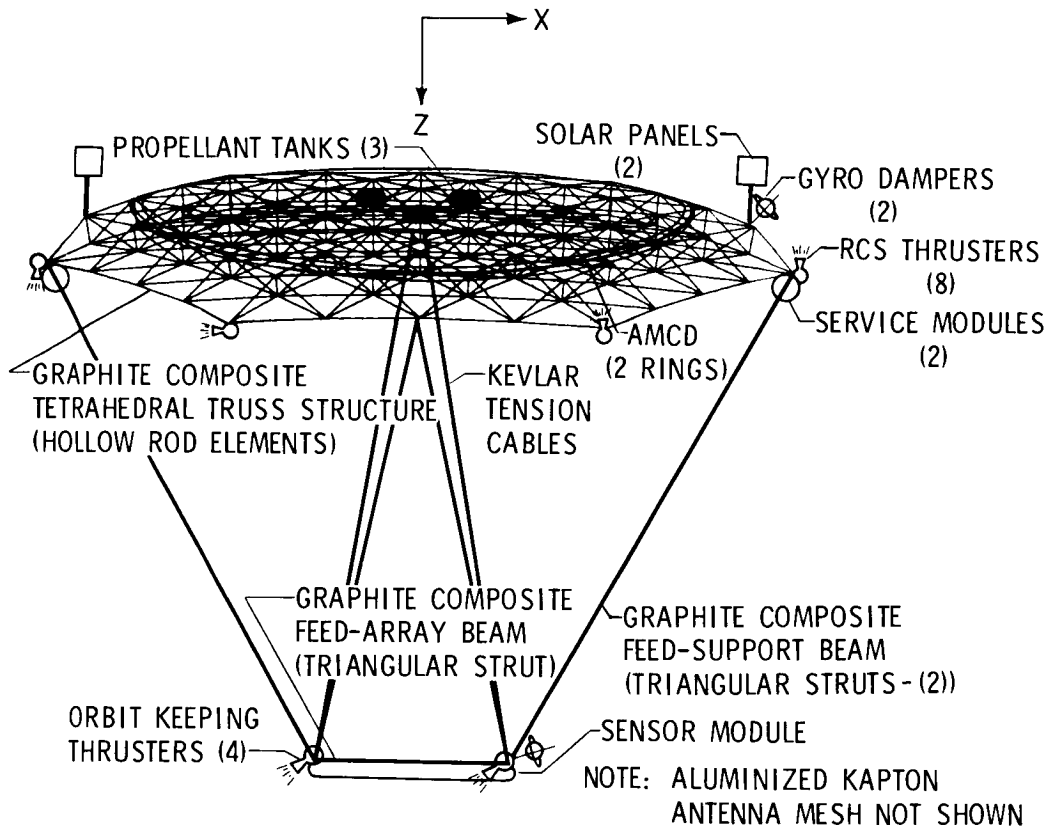
Figure 1. MRS schematic.
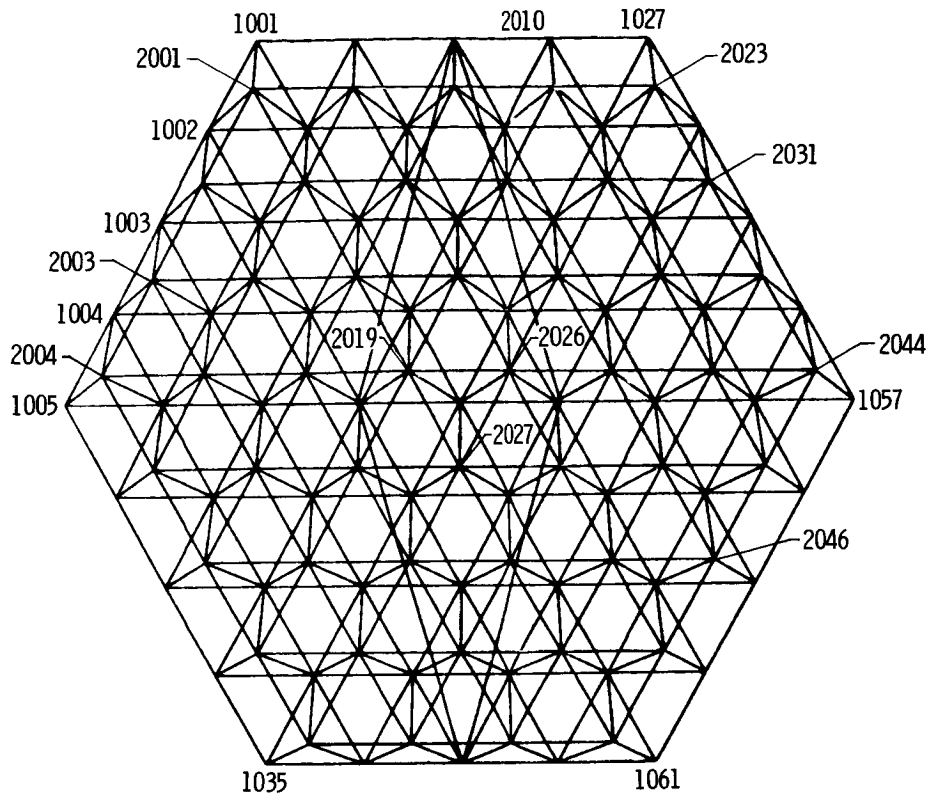
(a) Top view.
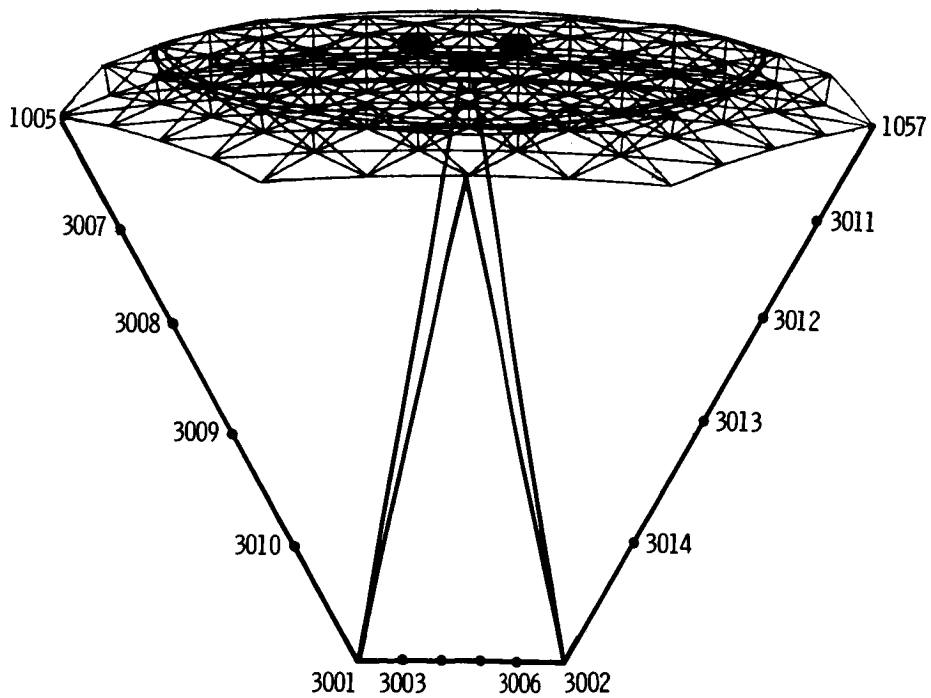
(b) Side view.

Figure 2.- MRS finite element model.
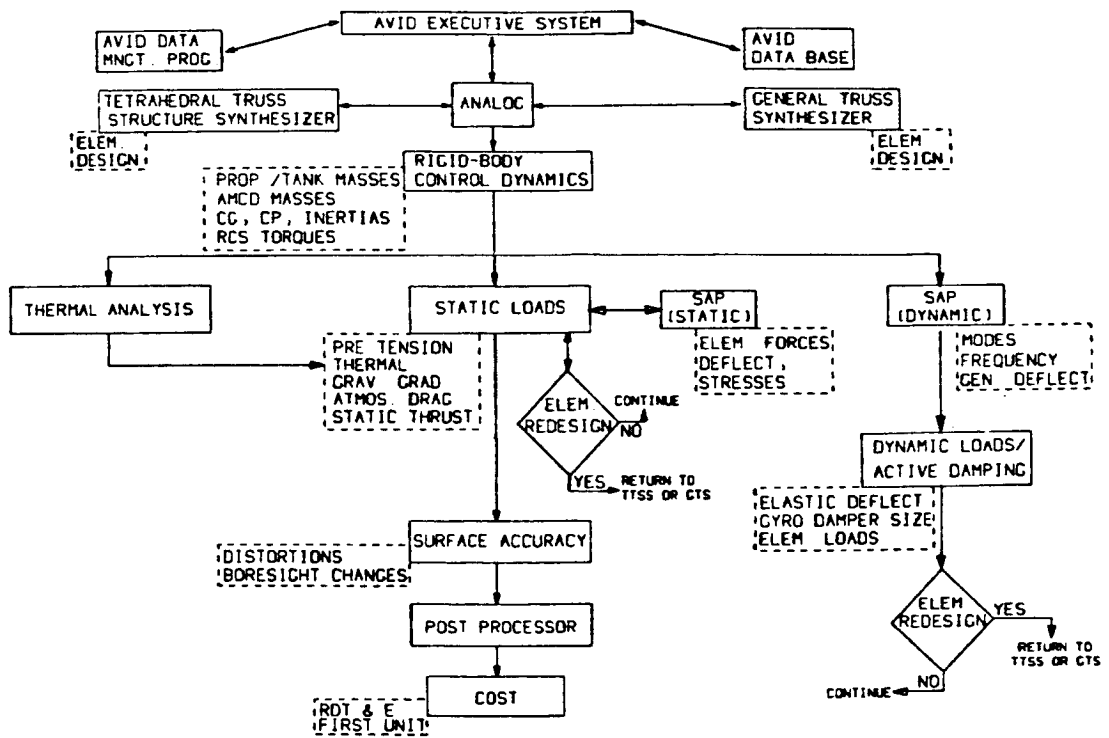
Figure 3.- Large advanced space systems (LASS)
computer program flow chart.
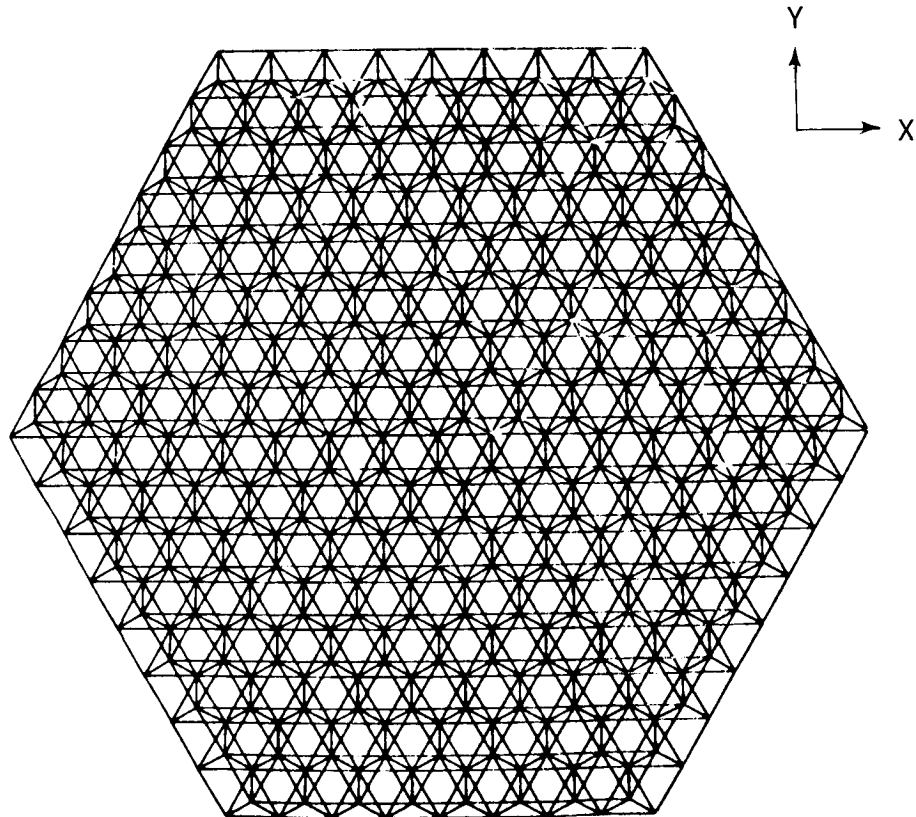
Figure 4.- Real dish model.
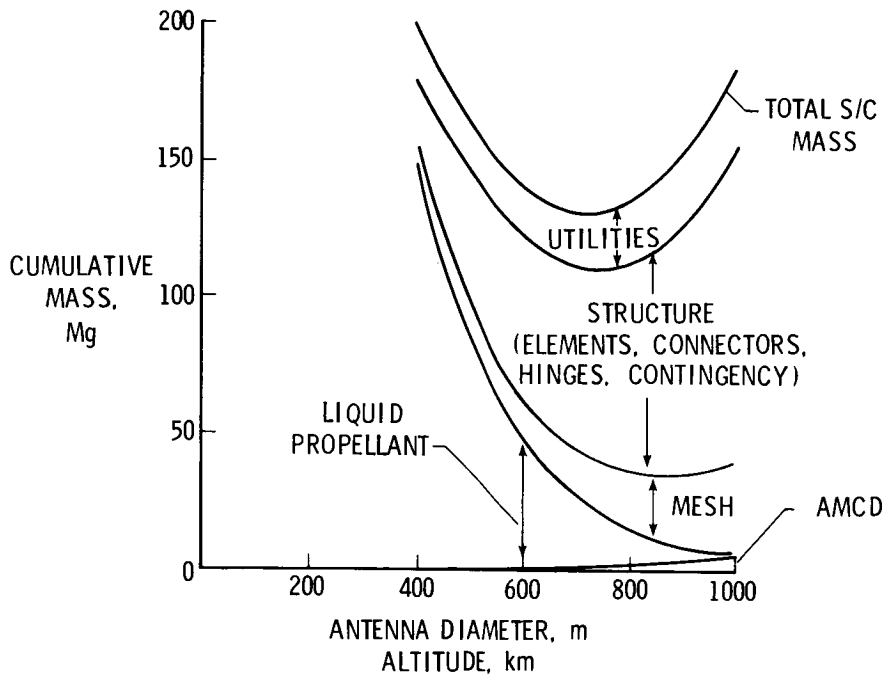
Figure 5.- Spacecraft mass as function of size and
altitude for baseline MRS.
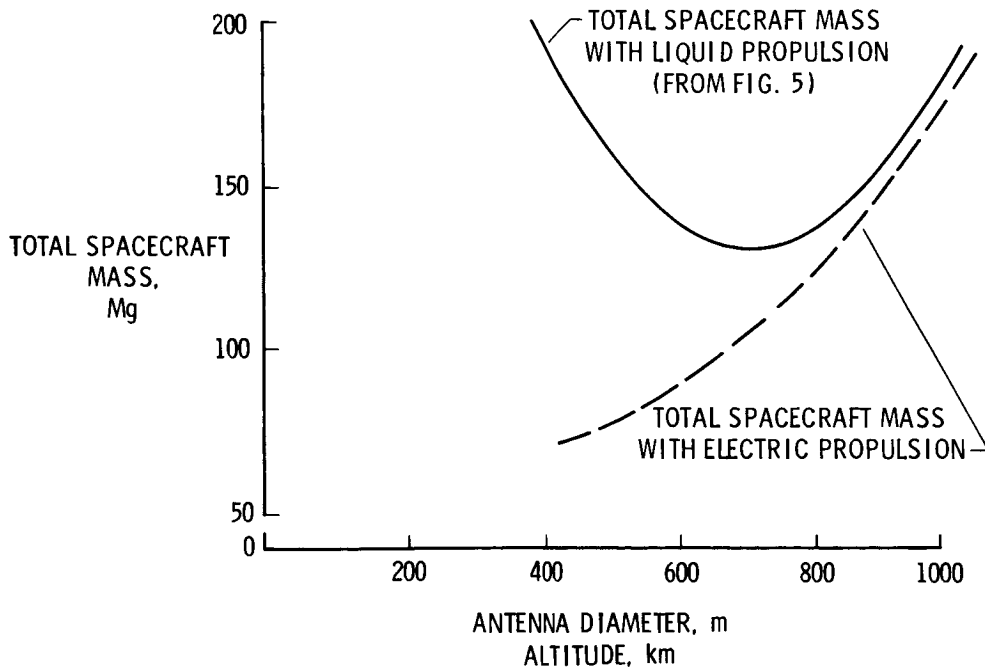
Figure 6.- Mass advantage of electric propulsion
for baseline MRS.
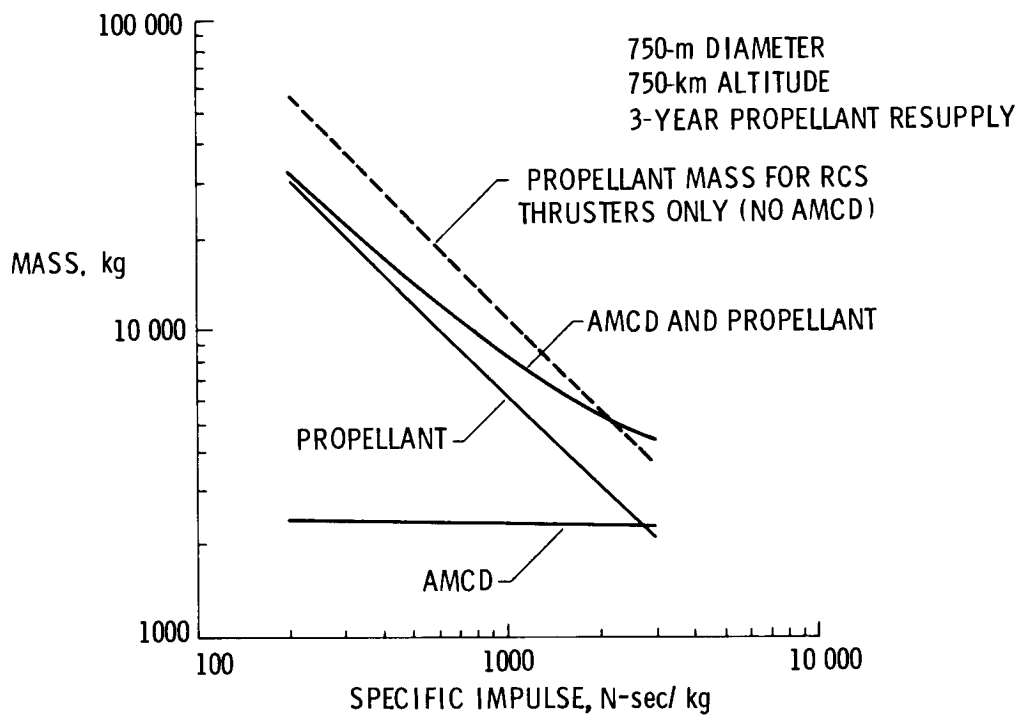
Figure 7.- MRS attitude/orbit-keeping control subsystems trade-off.

COMPRESSIVE DESIGN LOAD = 6000N

(a) Front elements.

COMPRESSIVE DESIGN LOAD = 6000N
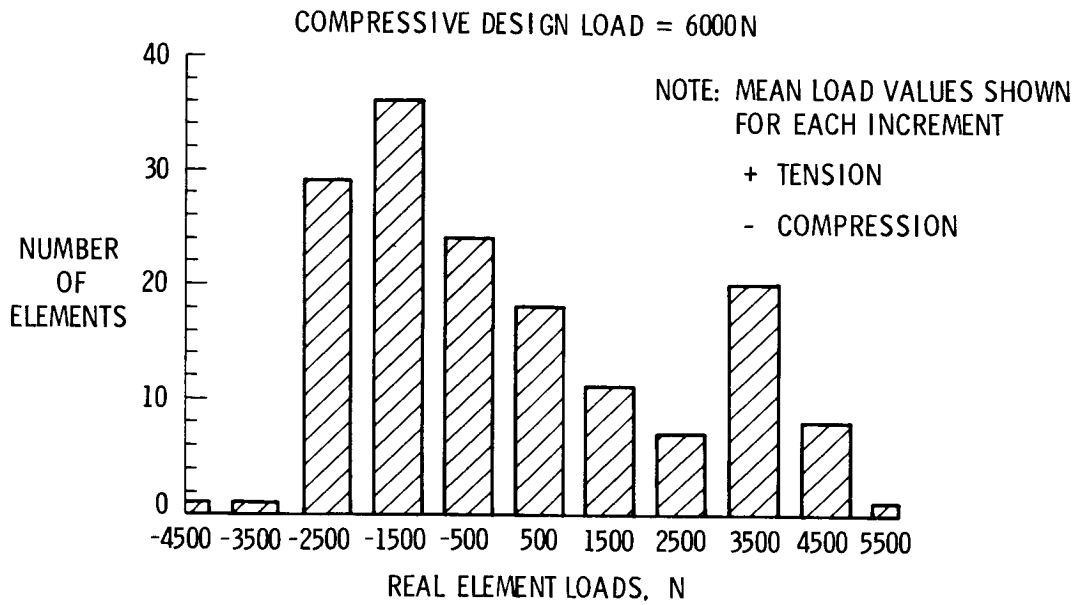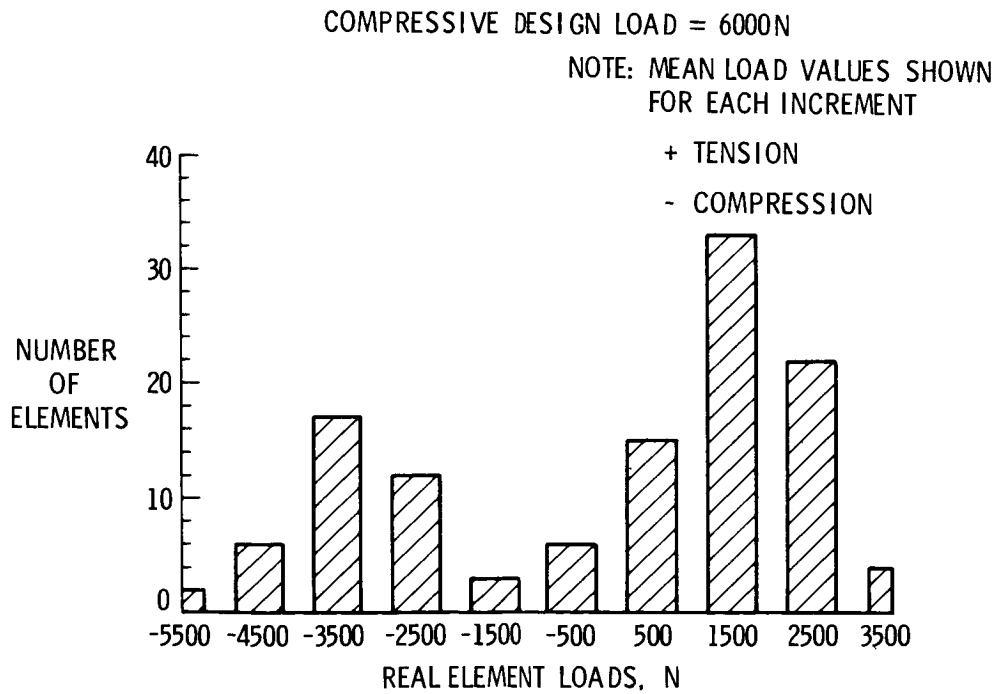
(b) Rear elements.

Figure 8.- Baseline MRS static loads.

COMPRESSIVE DESIGN LOAD = 4000N
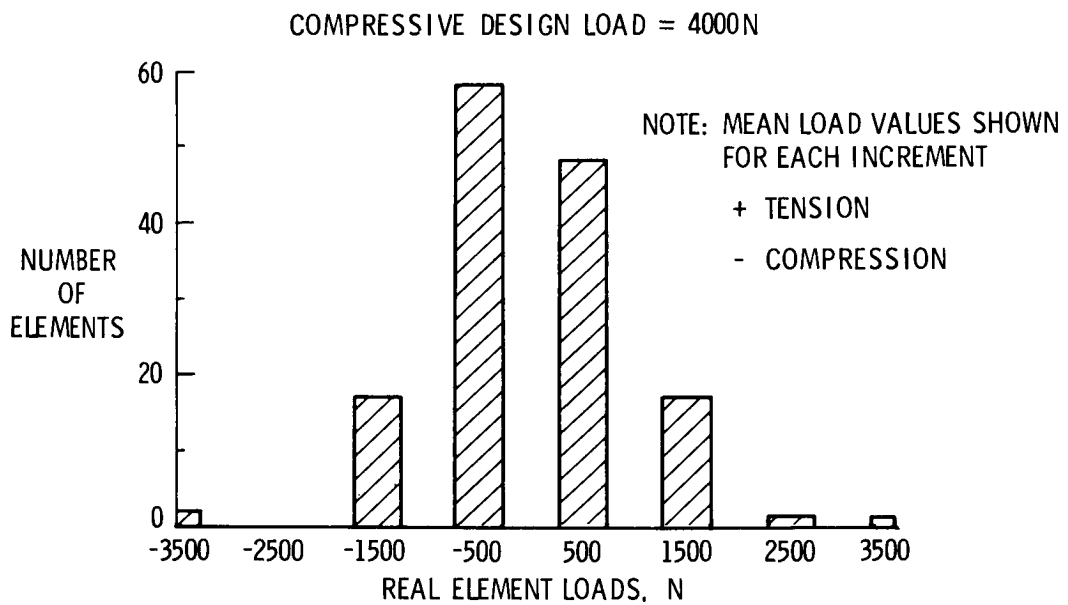
(c) Diagonal elements.

Figure 8.- Concluded.
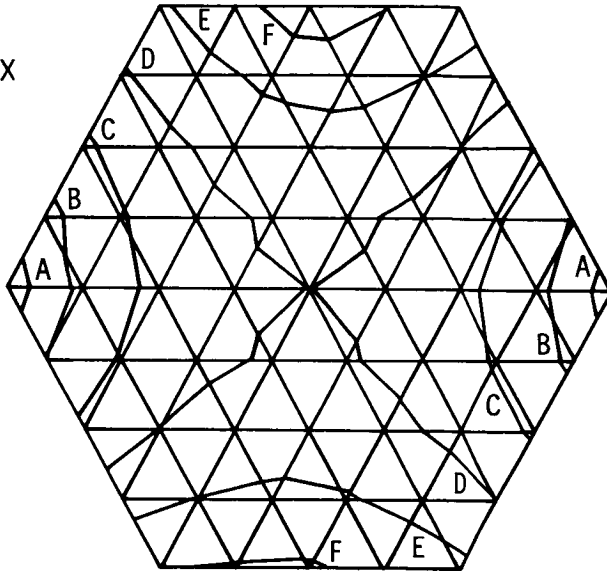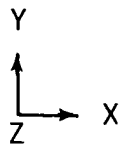
CONTOUR LEVELS, cm

A	-15	D	0
B	-10	E	+5
C	-5	F	+10

RMS ROUGHNESS

6.6 cm

Z-AXIS DISPLACEMENT

1.1 cm

ROTATION ABOUT X-AXIS

6.9×10^{-5} rad

ROTATION ABOUT Y-AXIS

-3.7×10^{-4} rad

(a) With tension cables.
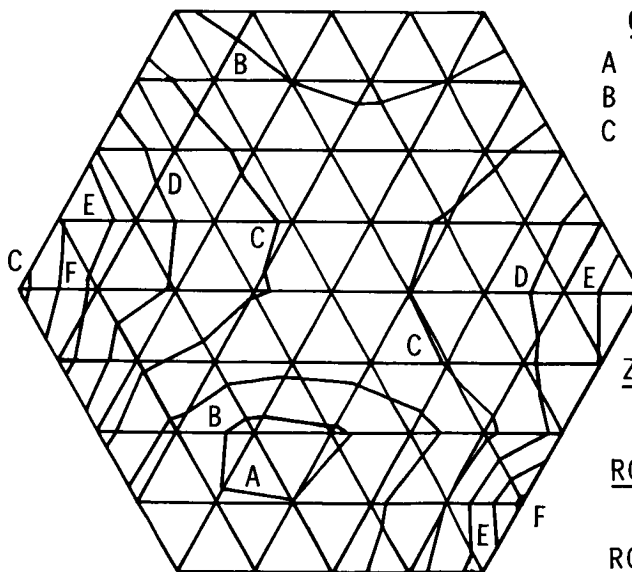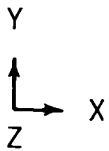
CONTROL LEVELS

A	-.050	D	+.025
B	-.025	E	+.050
C	0	F	+.075
		G	+.100

RMS ROUGHNESS

.035 cm

Z-AXIS DISPLACEMENT

.022 cm

ROTATION ABOUT X-AXIS

-7.5×10^{-7} rad

ROTATION ABOUT Y-AXIS

-1.3×10^{-6} rad

(b) Without tension cables (distortions from environmental loads only).

Figure 9.- Baseline MRS surface accuracy results.

DISPLACEMENT, cm

$\Delta X = 0.00642$
$\Delta Y = 0.000186$
$\Delta Z = 0.332$

(a) Mode 1; $f_1 = 0.05601$ Hz.

DISPLACEMENT, cm

$\Delta X = 0.000228$
$\Delta Y = 0.277$
$\Delta Z = 0.115$
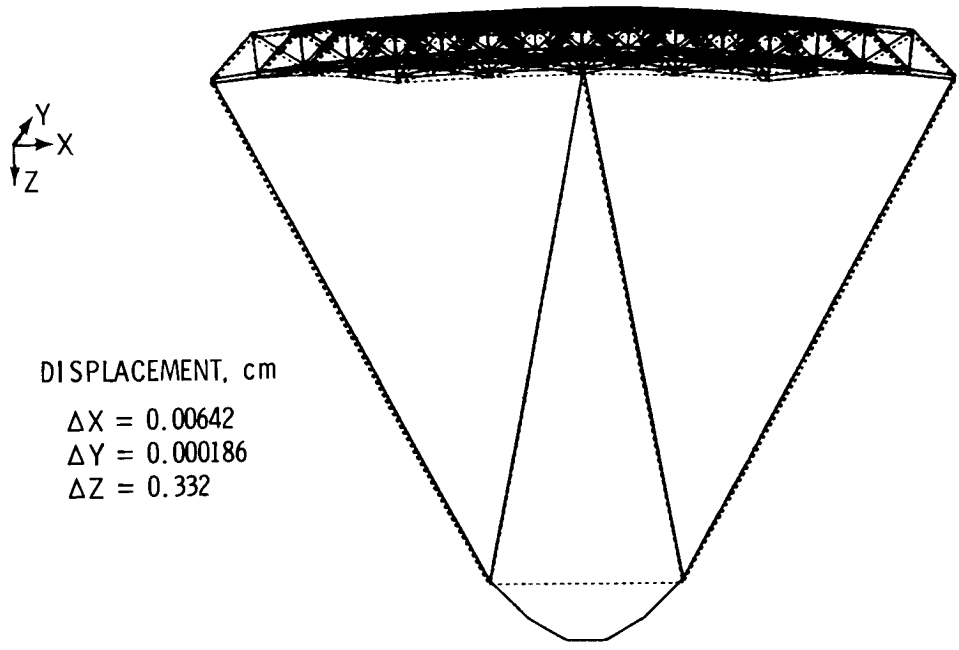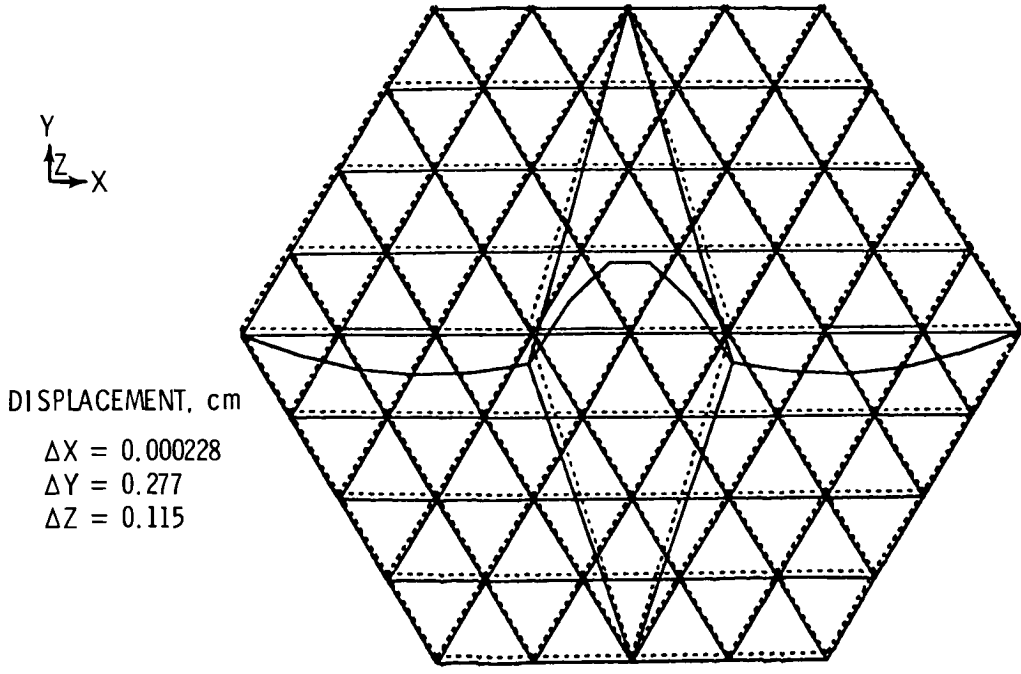
(b) Mode 2; $f_2 = 0.06935$ Hz.

Figure 10.- Mode shapes.

DISPLACEMENT, cm

$\Delta X = 0.0132$
$\Delta Y = 1.33$
$\Delta Z = 0.00248$

(c) Mode 3; $f_3 = 0.09979$ Hz.

DISPLACEMENT, cm

$\Delta X = 1.14$
$\Delta Y = 0.00511$
$\Delta Z = 0.674$
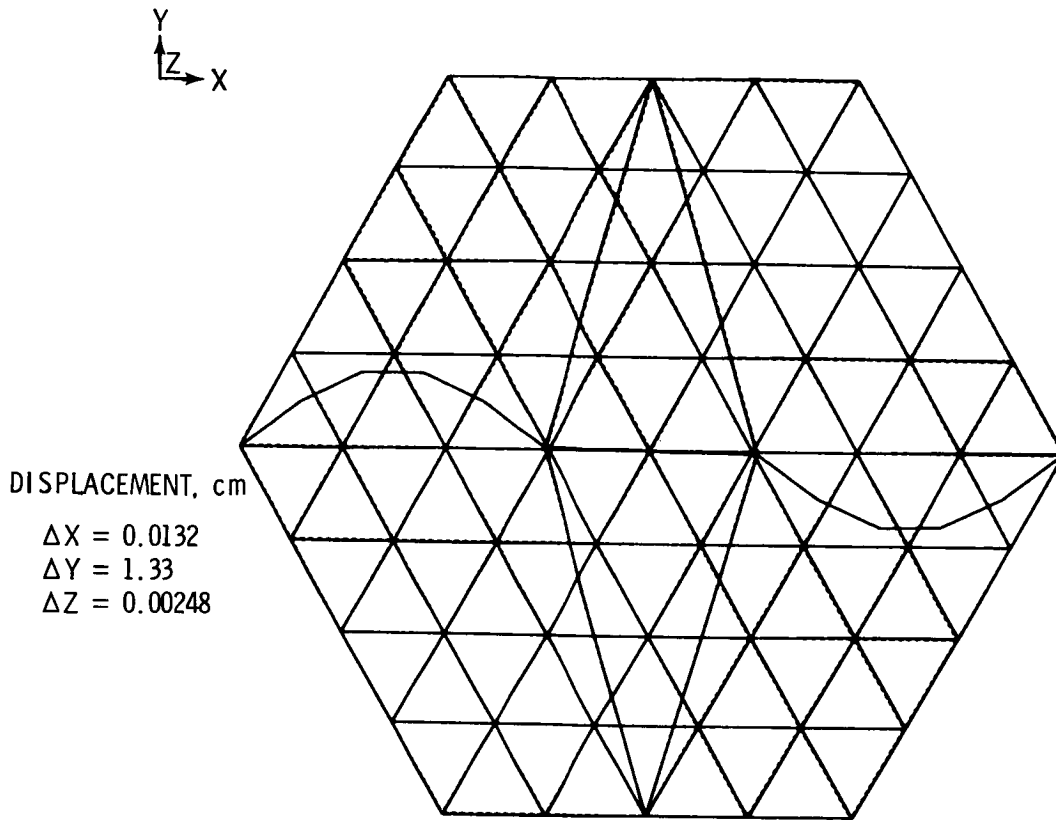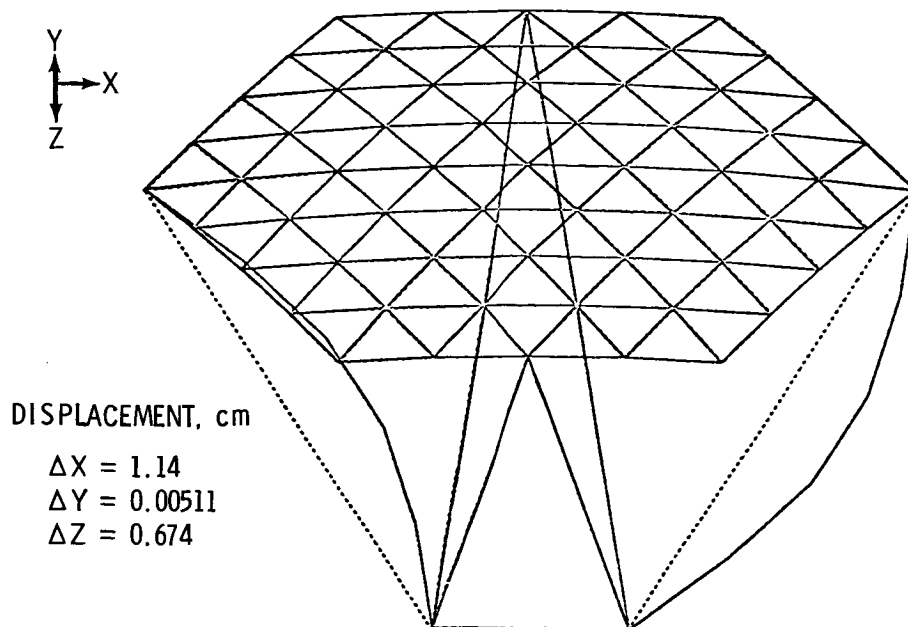
(d) Mode 4; $f_4 = 0.1000$ Hz.

Figure 10.- Continued.
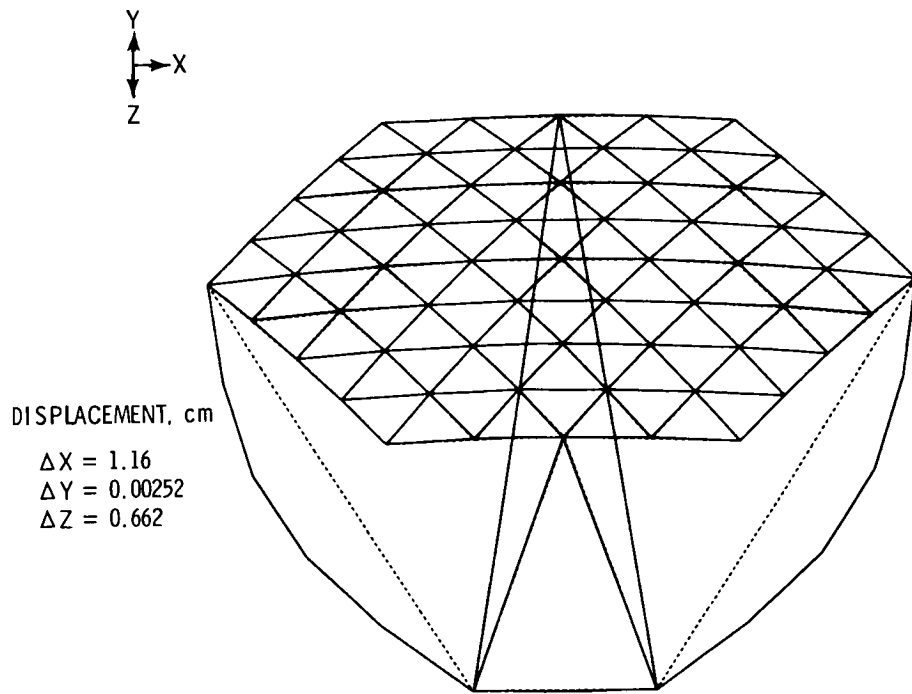
(e) Mode 5; $f_5 = 0.1003$ Hz.
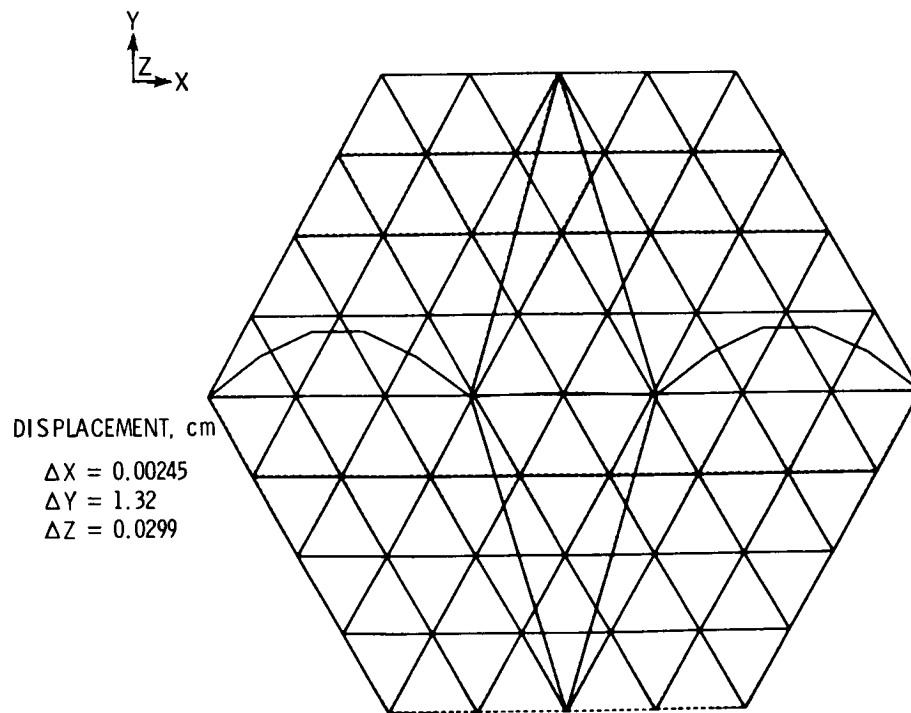
(f) Mode 6; $f_6 = 0.1011$ Hz.

Figure 10.- Continued.

Y
↑→X
Z

DISPLACEMENT, cm

$\Delta X = 0.0113$
$\Delta Y = 0.310$
$\Delta Z = 0.00248$

(g) Mode 7; $f_7 = 0.1461$ Hz.

Y
↑→X
Z

DISPLACEMENT, cm

$\Delta X = 0.186$
$\Delta Y = 0.00132$
$\Delta Z = 0.201$
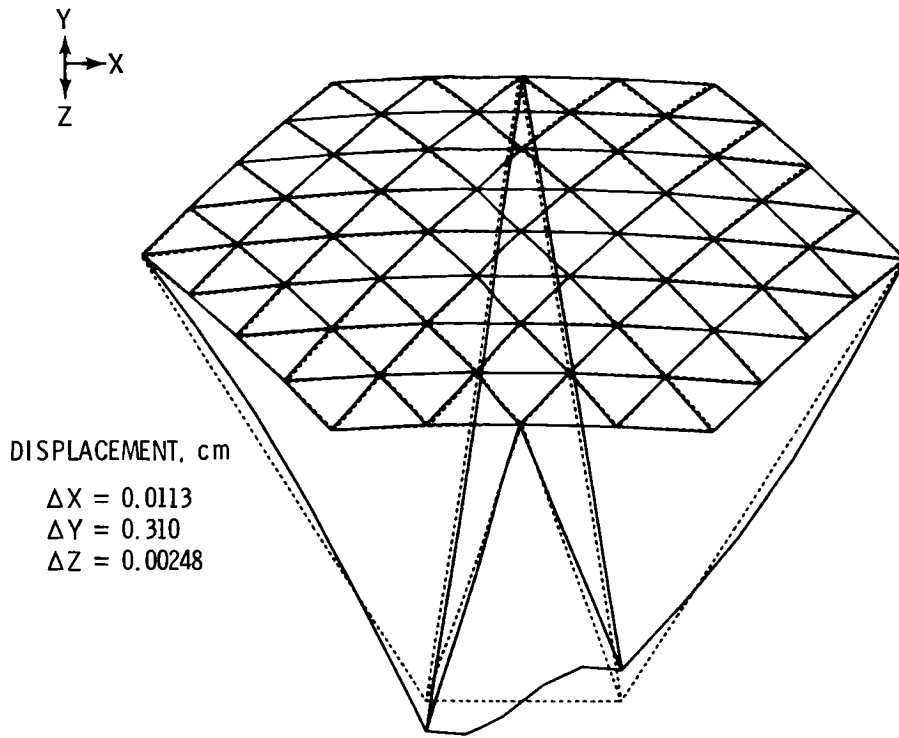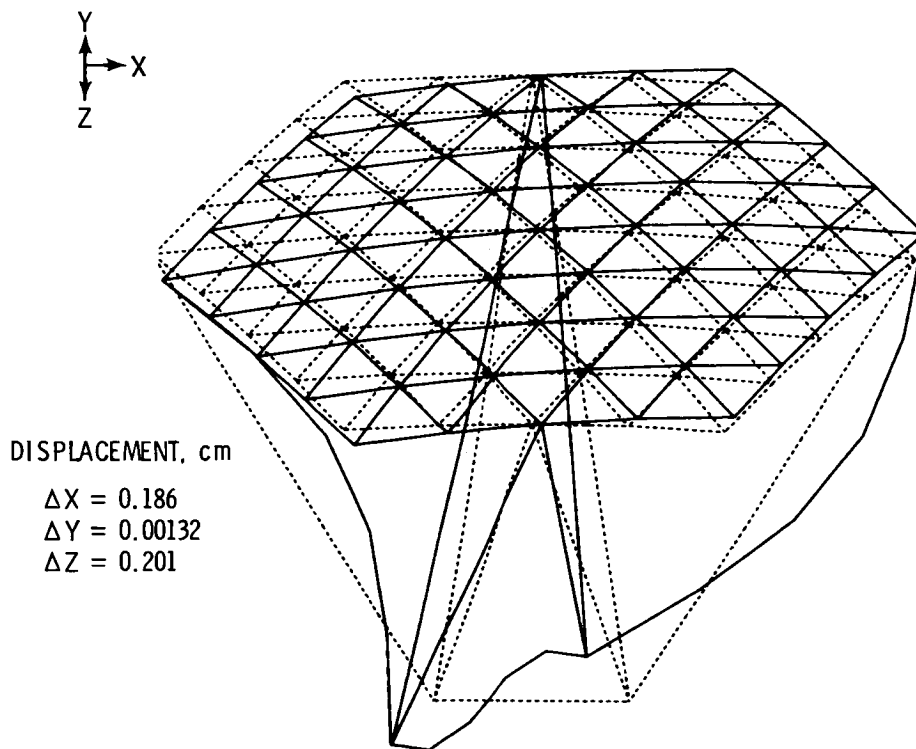
(h) Mode 8; $f_8 = 0.1472$ Hz.

Figure 10.- Continued.

DISPLACEMENT, cm

$\Delta X = 0.0769$
$\Delta Y = 0.00150$
$\Delta Z = 0.281$
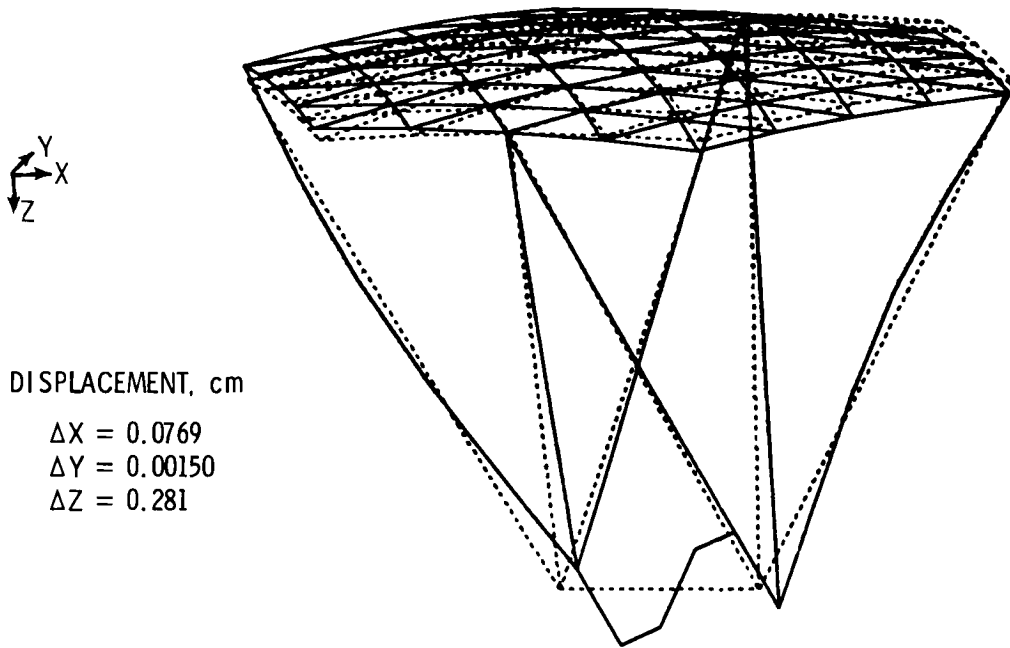
(i) Mode 9; $f_9 = 0.2264$ Hz.

Figure 10.- Concluded.

PRELIMINARY DESIGN OF TETRAHEDRAL TRUSS

REFLECTOR STRUCTURE

Michael F. Card
NASA Langley Research Center
Hampton, Virginia

and

J. Kermit Jensen
Kentron International
Hampton, Virginia

SUMMARY

A baseline structure proposed for the microwave radiometer spacecraft (MRS) reflector is a large graphite-epoxy truss. The truss structure was selected to provide adequate stiffness to minimize control problems and to provide a low-expansion "strong back" on which to mount and control reflector mesh panels. Details of the structural members, joints, and assembly concepts are presented, a concept for the reflector mesh surface is discussed, and preliminary estimates of the mass and structural natural frequencies of the reflector system are presented.

STRUCTURAL MEMBER/ASSEMBLY CONCEPT

Preliminary studies of relative masses and transportation volumes of deployable trusses indicated that space transportation requirements would be excessive for this structural approach (ref. 1). On the other hand, a concept for erectable truss structures in which structural elements are fabricated on Earth and assembled in orbit appears feasible. The nestable column (ref. 2) is an excellent element for erectable truss structures. As illustrated in figure 1, the nestable column consists of tapered tubes which are divided in the middle and nested like paper cups for transportation to orbit. Once on orbit the tubes are joined at their middle and used as long columns in an assembly operation.

Mechanical joining of the columns, first at the center to form a full-length column and then at the ends to attach the columns to the truss nodes, is accomplished by the use of one-piece, snap-locking joints. These joints, illustrated in figures 2 and 3, are lightweight, have a load path aligned with the column centerline, and quickly lock in place with a linear motion. Logistics are minimized because all joints of each type are identical. Design of these joints enables them to be made from metal or lightweight composite materials.

The center joints (fig. 2) assemble with an axial motion. Fingers deflect over an engagement site and latch the joint. End joints (fig. 3) latch in a similar manner but are sidelocking to simplify assembly and possible replacement of damaged

column members. Nodes at the tetrahedral apexes (shown in fig. 3) mate with the column end joints and are prefabricated out of graphite-epoxy or metal.

A concept for a high-speed assembler (refs. 3 and 4) is illustrated in figures 4 and 5. The nested half-column elements are transported to orbit in preloaded canisters. These elements are then dispensed and joined into full columns. The assembly machine is a large movable set of tools capable of shuttling back and forth to generate a large tetrahedral truss. The tools form a parallelogram device which "walks" from node to node of the previously formed structure and provides tools and machine arms for insertion of each element of the tetrahedral truss into the column-end-joint nodes. The assembler would be largely automated with man performing a limited maintenance function. A preliminary estimate of construction times suggests that an automated construction rate of less than 5.5 minutes per column may be feasible (ref. 3). Construction rates of 2 to 5 minutes per nested column have been achieved for short periods in tests at Langley Research Center using pressure-suited astronauts in MSFC's Neutral Buoyancy Chamber (ref. 5). Although the astronaut tests show the manual assembly to be faster than the automated, it should be noted that the astronaut cannot maintain this pace for extended periods of time. The automated assembler, however, can maintain its rate indefinitely.

REFLECTOR SURFACE CONCEPT/SIZING

A concept for designing a reflector surface is presented in reference 5. The idea of using flat facets to approximate a curved reflector surface is illustrated in figure 6. The basic approach is to stretch a flat membrane between the nodes of the tetrahedron truss structure. In figure 7, a laboratory demonstration of a stretched, reflecting membrane is shown in which optical flatness has been achieved on a stretched Mylar film. For the MRS, a mesh membrane is used and attached so that the flat stretched mesh facet is controlled as a rigid body.

Design information to size flat hexagonal and triangular facets is contained in reference 6. If equilateral triangular facets are selected, the length of the facet side ℓ is

$$\ell = 7.872 \sqrt{\delta_{rms} F}$$

where F is the focal length of the reflector and δ_{rms} is the surface accuracy defined as the root-mean-square deviation of the flat triangular surfaces from a shallow parabaloidal surface. For a 1-GHz reflector with focal length $F = 575$ m and a surface accuracy requirement of 6 mm ($\lambda/50$), the facet side length ℓ is 14.62 m. If the facet edges are supported by the triangular surface elements of the tetrahedral truss, then the column length ℓ of the truss is also 14.62 m.

REFLECTOR TRUSS-MEMBER SIZING

To size the reflector truss members, a condition to separate the overall frequency of the reflector from local frequencies of the individual column elements is used. This separation is desirable to avoid coupling between overall and local dynamic excitation and to simplify dynamic response and control of the vehicle.

To develop the sizing equations, assume that the lowest natural frequency of the reflector f_p can be approximated as the lowest frequency for a hexagonal truss plate with maximum width D, the overall diameter of the MRS reflector. From references 6 and 7, for a hexagonal tetrahedral truss plate:

$$f_p = \frac{25.93}{4\pi\sqrt{6}} \frac{\ell}{D^2} \sqrt{\frac{E_c}{\rho_c(1 + \lambda_m)}}$$

(1)

where ℓ is the column length, E_c is the column material modulus, ρ_c is the column material density, and λ_m is the ratio of nonstructural mass m_o to structural mass m_s.

If the truss columns are considered simply supported, thin-walled, cylindrical tubes, their lowest natural frequency is given by

$$f_c = \frac{\pi}{2\sqrt{2}} \frac{r_c}{\ell^2} \sqrt{\frac{E_c}{\rho_c}}$$

(2)

where r_c is the tube radius. To separate the column and truss plate frequencies by a ratio η, set

$$f_c = \eta f_p$$

(3)

Substitution of equations (1) and (2) into equation (3) yields

$$r_c = \frac{25.93}{2\pi^2} \frac{1}{\sqrt{3}} \frac{\ell^3}{D^2} \frac{1}{\sqrt{1 + \lambda_m}} \eta$$

(4)

The structural mass of the truss plate is

$$m_s = 6\sqrt{3} \frac{\rho_c A_c}{\ell} A$$

(5)

where A is the planform area of the tetrahedral truss and A_c is the tube cross-sectional area. If equation (4) is substituted into equation (5), structural mass m_s is

$$m_s = \frac{1}{2}\sqrt{m_o^2 + 4c^2} - \frac{1}{2} m_o$$

(6)

with

$$c = \frac{9\sqrt{3}(25.93)}{4\pi} \rho_c t_c^2 \ell^2 \eta$$

The sensitivity of structural and total mass to the choice of frequency ratio η is illustrated in figure 8. A value of $\eta = 10$ was selected for the baseline design. Using this value and material properties presented in table I, the lowest natural frequencies, column buckling strength, and structural masses are presented in table II.

DISCUSSION

Structural masses in table II are presented for five-ply minimum gage graphite-epoxy tubing with a thickness of 0.381 mm. The effects of including thicker tubing ($t_c = 0.57$ mm) with a Young's modulus identical to the five-ply configuration is also shown in table II. In both cases the parasitic mass was taken to be 17 500 kg. Included in parasitic mass are mesh and joint masses and a rude estimate of the mass of actuators required to provide rigid body pointing adjustments to individual reflector facets.

CONCLUDING REMARKS

A tetrahedral truss structure of tapered graphite-epoxy members provides the baseline structural concept for the microwave radiometer spacecraft reflector. Utilization of graphite-epoxy nestable structural members will enable the material necessary to construct a 725-m-diameter reflector to be transported to orbit in a single space transportation system flight. Preliminary studies have indicated that an automatic device to assemble these members on orbit is feasible and could significantly reduce the time required to construct a variety of space structures. The utilization of facets or modules to assemble a much larger structure has been advanced and would be worthy of additional study in the event that effort is continued.

REFERENCES

1. Heard, Walter L., Jr.; Bush, Harold G.; Walz, Joseph E.; and Rehder, John J.: Structural Sizing Considerations for Large Space Platforms. A Collection of Technical Papers, Part 1 - AIAA/ASME/ASCE/AHS Structures, 21st Structural Dynamics & Materials Conference, May 1980, pp. 147-158. (Available as AIAA-80-0680.)

2. Bush, Harold G.; and Mikulas, Martin M., Jr.: A Nestable Tapered Column Concept for Large Space Structures. NASA TM X-73927, 1976.

3. Jacquemin, Georges G.: Automatic In-Orbit Assembly of Large Space Structures. 13th Aerospace Mechanisms Symposium, NASA CP-2081, 1979, pp. 283-291.

4. Jacquemin, G. C.; Bluck, R. M.; Grotbeck, G. H.; and Johnson, R. R.: Development of Assembly and Joint Concepts for Erectable Space Structures. NASA CR-3131, 1980.

5. Bement, Laurence J.; Bush, Harold G.; Heard, Walter L., Jr.; and Stokes, Jack W.: EVA Assembly of a Large Space Structure Element. NASA TP-1872, 1981.

6. Agrawal, Pradeep K.; Anderson, Melvin S.; and Card, Michael F.: Preliminary Design of Large Reflectors With Flat Facets. NASA TM-80164, 1980.

7. Mikulas, Martin M., Jr.; Bush, Harold G.; and Card, Michael F.: Structural Stiffness, Strength and Dynamic Characteristics of Large Tetrahedral Space Truss Structures. NASA TM X-74001, 1977.

A   planform area of hexagonal plate

A_c column cross-sectional area

c   constant in equation (6)

D   maximum dimension of hexagonal plate (725 m for MRS)

E_c Young's modulus of column

E_x, E_y laminate Young's modulus in x-y direction

F   focal length of reflector

f_c column lowest natural frequency

f_p hexagonal-plate lowest natural frequency

G_{xy} laminate shear modulus in x-y plane

ℓ length of side of triangular facet; column length

m_c column mass

m_o parasitic mass of reflector (includes joint and mesh mass)

m_s structural mass of reflector truss structure (neglects joint mass)

m_t total reflector mass, $m_s + m_o$

P_{max} buckling strength of simply supported tubular column

r_c mean radius of tubular column

t   ply thickness, mm

t_c wall thickness of tubular column

α_c coefficient of thermal expansion of tubular column

α_x, α_y coefficient of thermal expansion of laminate in x- and y-directions, respectively

δ_{rms} surface accuracy, root-mean-square deviation of flat triangular surfaces from a shallow paraboloidal surface

η frequency spacing parameter, f_c/f_p

λ electromagnetic energy wavelength

λ_m mass ratio, m_O/m_s

ν_x Poisson's ratio

ρ_c column material density

TABLE I.- GRAPHITE-EPOXY COLUMN MATERIAL PROPERTIES

(a) Ply properties

Property	Laminate orientation angle, deg	
	0	90
E_x, GPa	131	10.9
E_y, GPa	10.9	131
G_{xy}, GPa	6.4	6.4
ν_x	0.32	0.027
α_x, K^{-1}	-0.54×10^{-6}	29×10^{-6}
α_y, K^{-1}	29×10^{-6}	-0.54×10^{-6}
t, mm	0.0762	0.0762

(b) Column-wall material properties

Laminate orientation, deg .... $(90/0_3/90)$

E_c, GPa 83.5

α_c, K^{-1} .... 1.5×10^{-6}

t_c, mm 0.381

ρ_c, kg/m^3 1520

TABLE II.- COLUMN TRUSS PROPERTIES

$[\eta = 10]$

Property	Thick tube	Minimum-gage tube
t_c, mm	0.57	0.381
r_c, mm	38.95	36.26
ℓ_c, mm	14.62	14.62
m_c, kg	3.10	1.93
p_{max}, N	408	220
m_o, kg	17 500	17 500
m_s, kg	51 500	32 000
m_t, kg	69 000	49 500
f_c, Hz	1.50	1.40
f_p, Hz	0.15	0.14

NESTED HALF-COLUMN ELEMENTS   ASSEMBLED COLUMN

L-79-7342
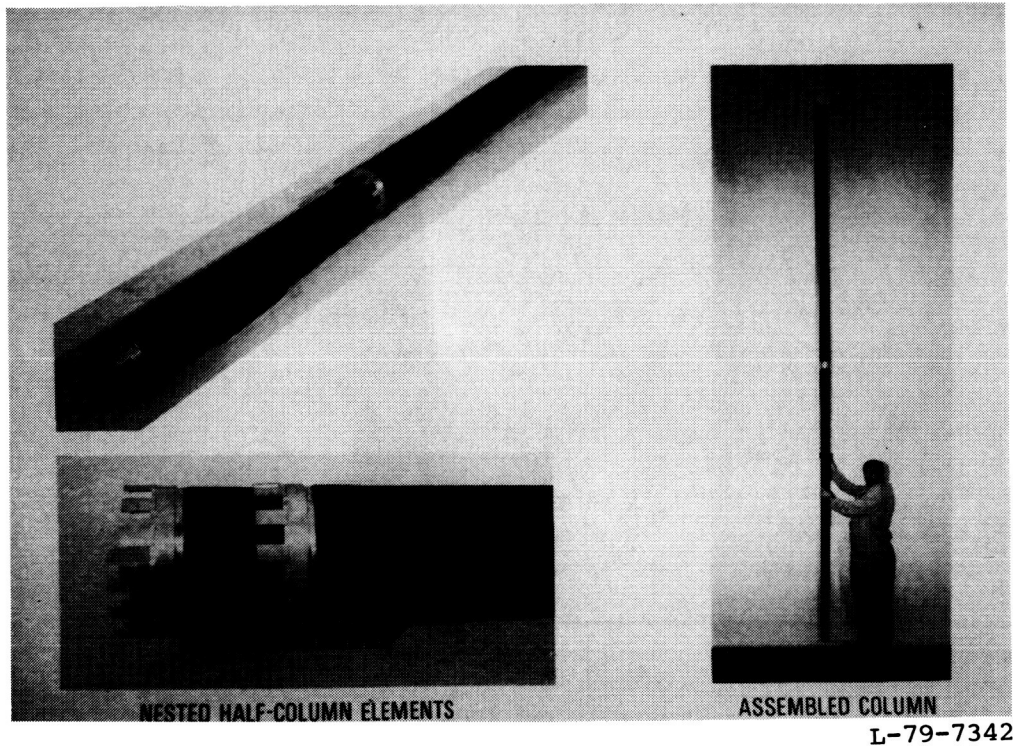
Figure 1.- Tapered column concept.

L-78-6466
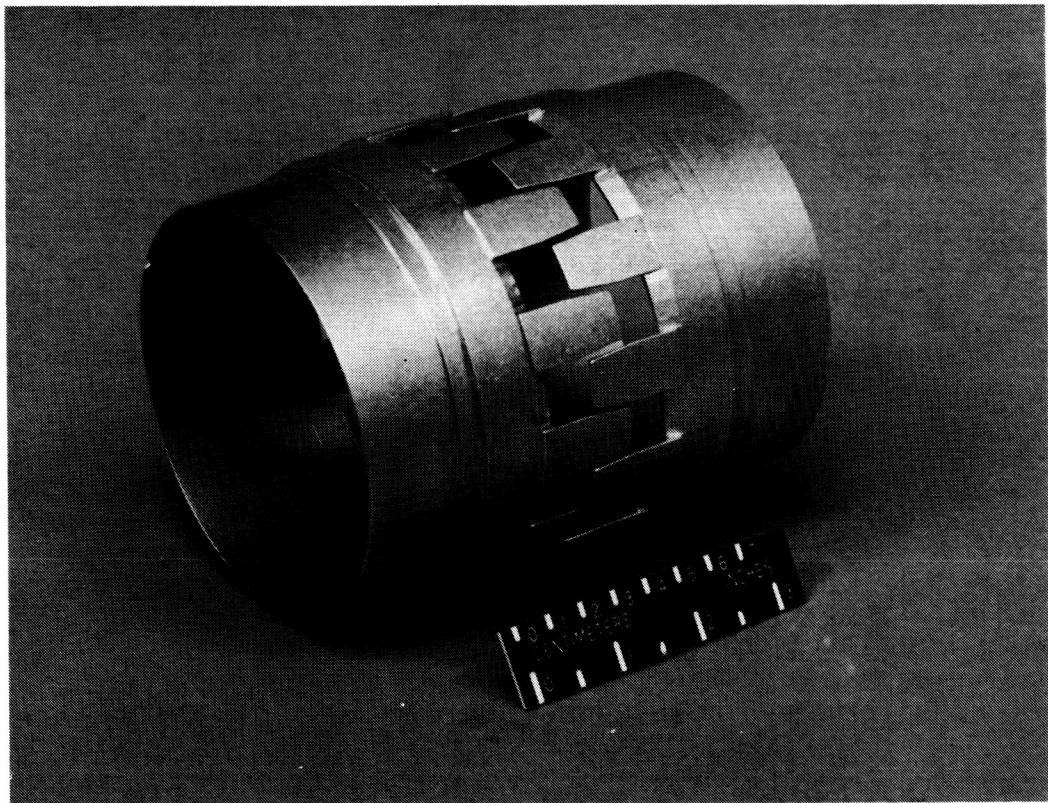
Figure 2.- Column center joint.
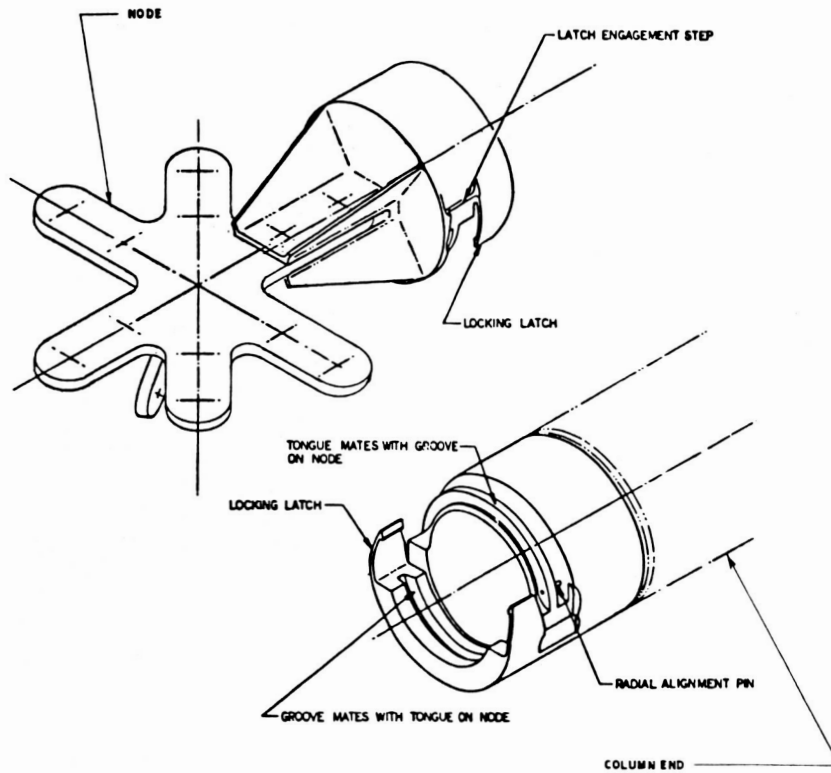
Figure 3.- Column end joint.

(a)

MOVABLE TOOL

CARTRIDGE OF
NESTABLE COLUMNS

(b)

(c)

(d)
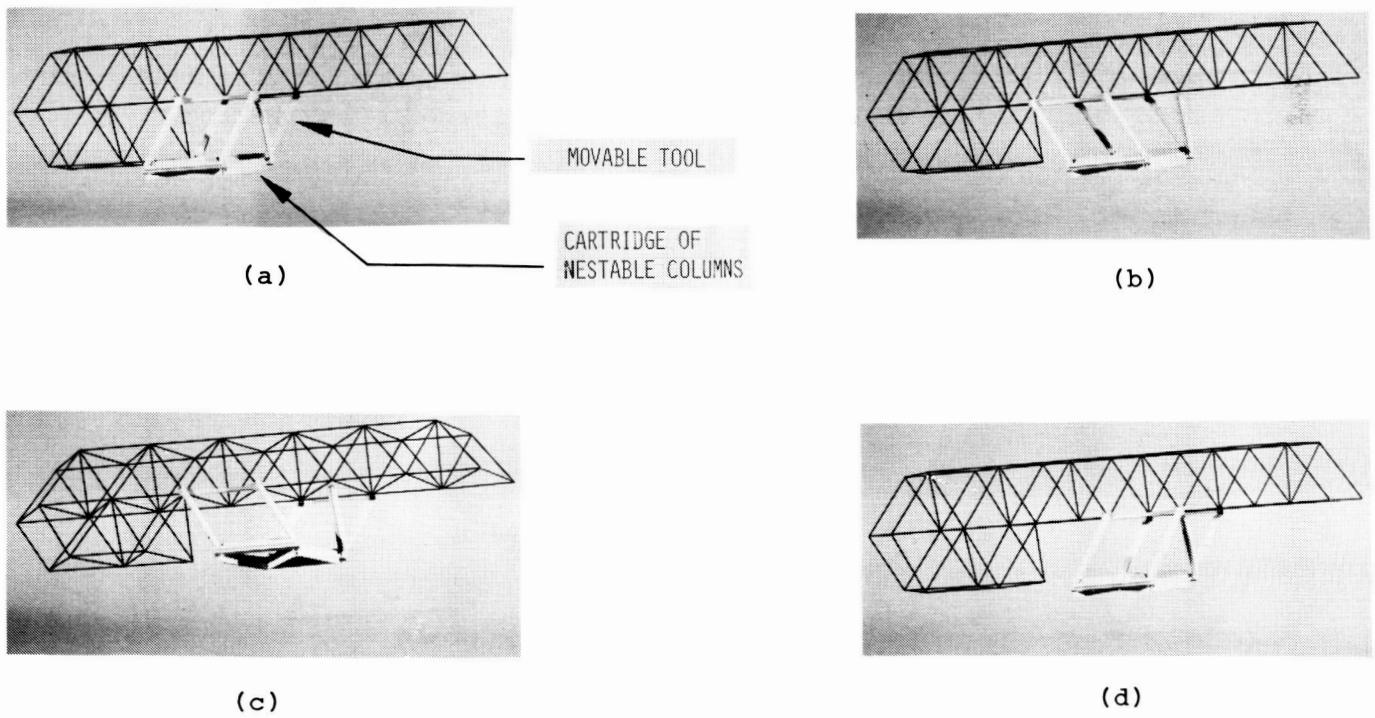
Figure 4.- High-speed assembler concept.
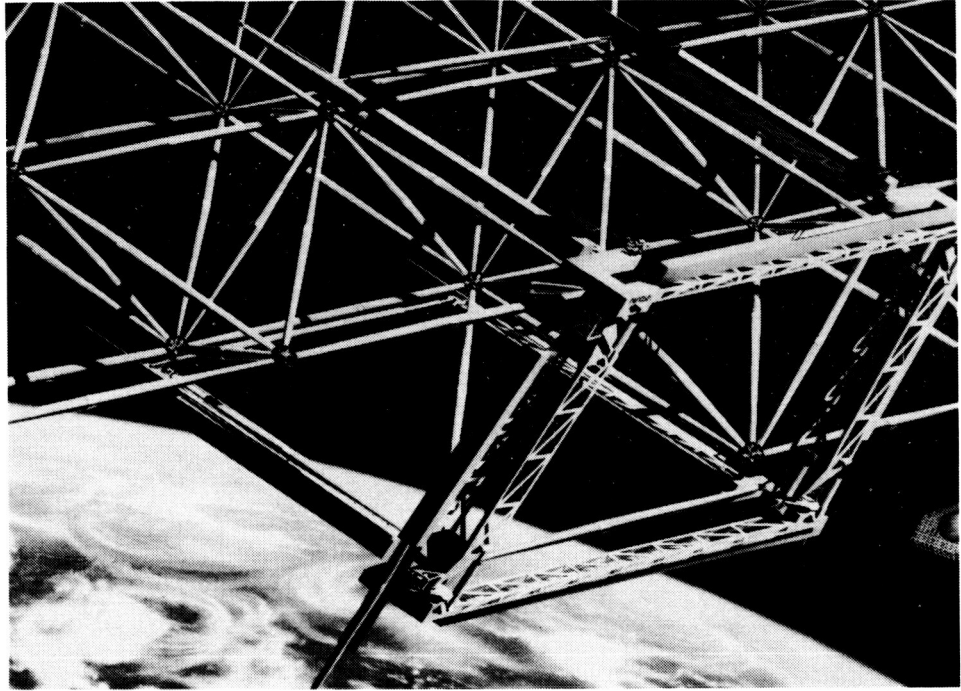
L-81-234

Figure 5.- Erector machine.
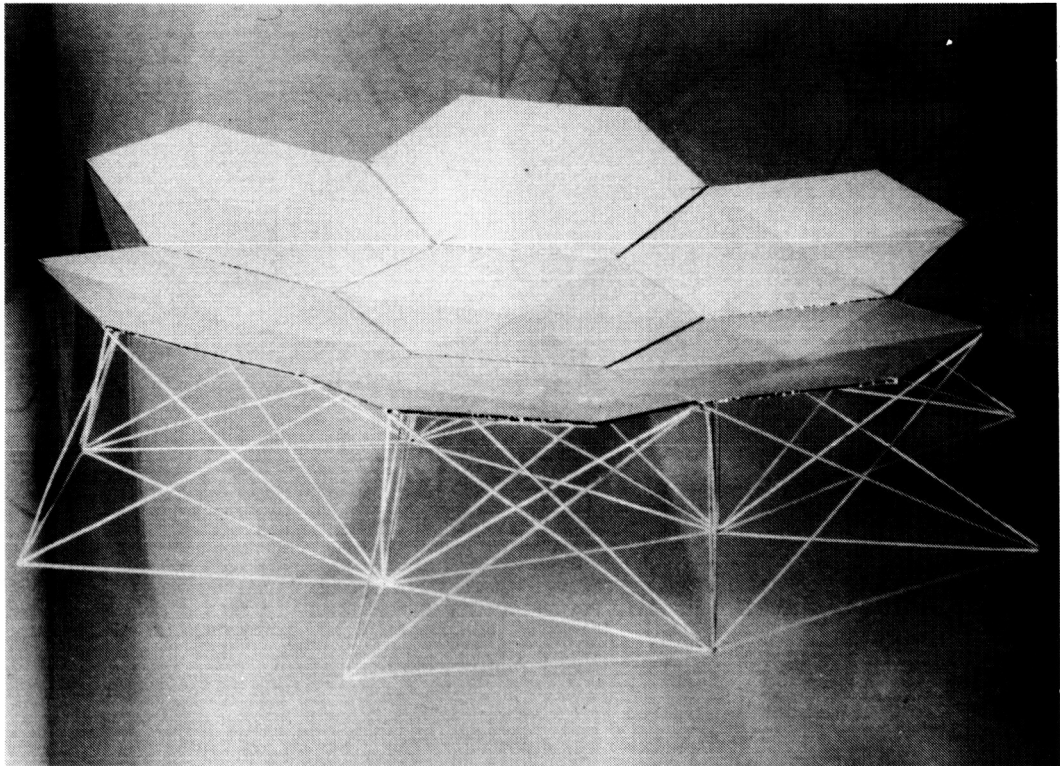
L-79-1347

Figure 6.- Flat-facet concept.
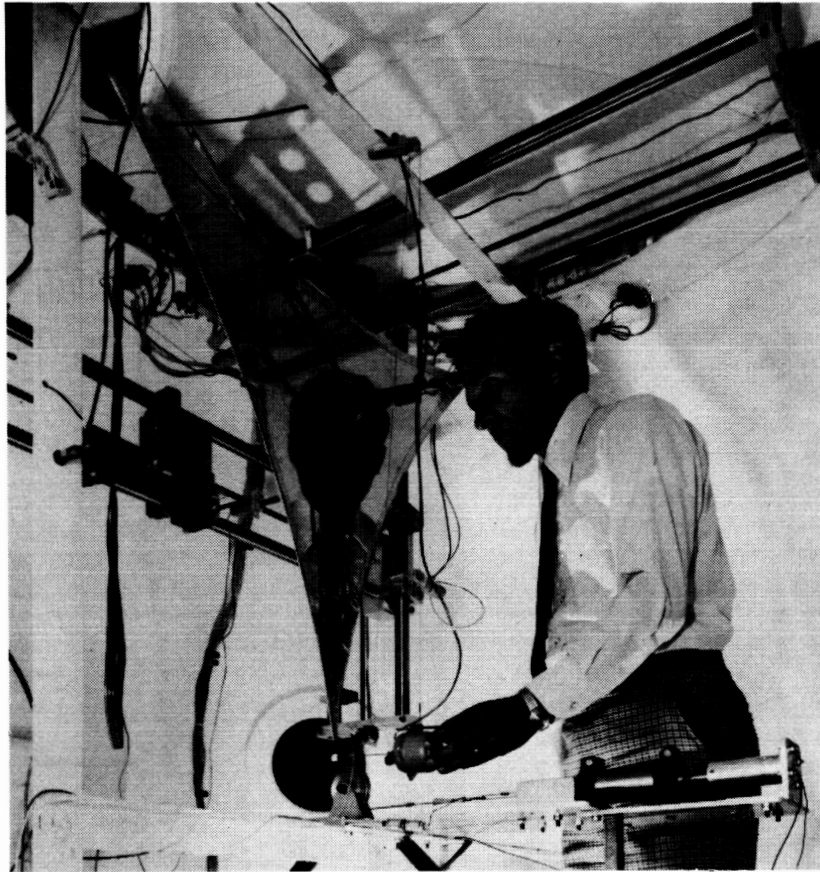
L-81-4382

Figure 7.- Tensioned triangular stretched membrane facet.
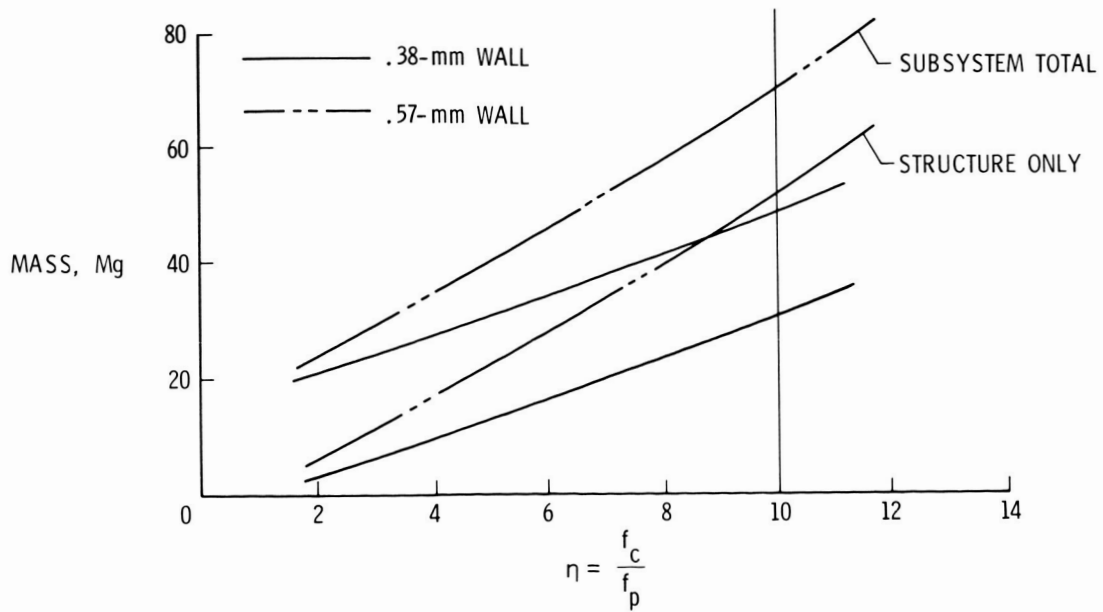
Figure 8.- Frequency separation factor.

WEIGHT ESTIMATES AND PACKAGING TECHNIQUES FOR THE

MICROWAVE RADIOMETER SPACECRAFT

J. Kermit Jensen
Kentron International
Hampton, Virginia

and

Robert L. Wright
NASA Langley Research Center
Hampton, Virginia

SUMMARY

Estimates of total spacecraft weight and packaging options have been made for three conceptual designs of a microwave radiometer spacecraft. Erectable structures were found to be slightly lighter than deployable structures but could be packaged in one-tenth the volume. The tension rim concept, an unconventional design approach, was found to be the lightest and transportable to orbit in the least number of Shuttle flights.

INTRODUCTION

One of the most important and least exact considerations in the design process is the estimation of weight and mass properties of an aircraft or space vehicle during the conceptual design phase. Although widely recognized mathematical prediction methods are used to calculate other design parameters, weight estimations are based largely on historical or empirical data. In recent years, these historical data have been compiled in computer programs which have saved many hours on proposals and conceptual design studies.

However, a new class of space vehicle, the very-large, low-mass space system such as the mirowave radiometer spacecraft (MRS), has been introduced in several long range space planning studies (refs. 1 and 2). Since these systems utilize the Space Shuttle for transportation to low Earth orbit (transfer to a higher orbit may be required), the system weight (and volume) is directly related to the number of Space Shuttle flights required and becomes a critical factor in the design. No historical weight data are available for these very large systems. This study was designed to provide weight comparisons of several technologically acceptable concepts of the microwave radiometer spacecraft and to develop weight estimates which would provide a baseline for estimating similar large platforms.

The microwave radiometer spacecraft (a passive antenna system) shown in figure 1 consists of three major structural components: a reflector and support structure; a radiometer array with its support structure; and support booms to position the radiometer array at the focal arc of the reflector. Weight estimates for these compo-

nents are determined for each of three structural concepts. Methods of assembly (deployable and erectable), packaging techniques, and number of Shuttle flights required are discussed.

WEIGHT ESTIMATES

Weight estimates are calculated from structural element estimates which, at the conceptual stage of the MRS design, are tentative because members are sized based on shape and configuration of the spacecraft and not on dynamic characteristics. Until detailed environmental criteria are available for the spacecraft, conceptual weight estimates will be used to assess the relative feasibility of the concepts.

The weight analysis was performed for the structural concepts involving single-layer geodesic truss, double-layer tetrahedral truss, and the tension rim; both erectable and deployable assembly methods were analyzed. Structural element lengths of 18 m, 8.75 m, and 6.43 m were considered in the weight analysis. The 18-m element, composed of two 9-m tapered tubes, was selected to provide maximum utilization of the Shuttle cargo bay. The 8.75-m element, used for deployable structures only, is sized to fit the length of the cargo bay. The 6.43-m element, which could be used for either deployable or erectable structures, is sized for a maximum surface area facet that could meet the surface accuracy requirements of the reflector without any mechanical adjustment or controls.

Weight estimates are determined for each of the major components (such as reflector strongback structure, support columns, and radiometer array) and summed to provide a total spacecraft weight for each concept. The total weights are used in a comparative analysis and in the development of packaging techniques which, in the final analysis, dictate the number of Shuttle launches required.

Reflector Strongback Structure

Three structural concepts were analyzed for the reflector strongback structure. The double-layer tetrahedral truss concept is based on the assembly of repeating tetrahedron shapes with the free apex of each tetrahedron connected to each of the surrounding apexes with columns of the same length (ref. 3). The resulting structure has two surfaces. The single-layer geodesic truss concept is a single-surface structure composed of planar triangular faces as the framework for the antenna. The tension-rim concept is a drastic departure from the rigid designs. The tension-rim concept does not use a strongback structure for support of the antenna membrane. Instead, the membrane is supported by a flexible bootlace catenary shaping system (ref. 4) attached to a large stiffening ring resembling a bicycle wheel.

Double-layer tetrahedral truss concept.- For the double-layer tetrahedral truss, calculations based on repeating geometric shapes (tetrahedrons) are made for the entire area. From reference 3, the number of elements, or columns, N_e is established by

$$N_e = \frac{6\sqrt{3}}{\ell^2} A \qquad (1)$$

where ℓ is the column length and A is the total area of the reflector (spherical segment). The number of nodes or joints connecting the columns N_j is

$$N_j = \frac{2}{9} N_e \tag{2}$$

For the 1-kN design load, the 6.43-m element will have a mass of 0.70 kg, the 18-m element will have a mass of 3.32 kg, and the mass of the node (cluster) fitting is 0.23 kg. Based on the column length of 6.43 m, the erectable double-layer strongback requires 106 497 elements and 23 666 node fittings for a total weight of 79 991 kg. Alternately, only 13 590 elements and 3020 node fittings with a total weight of 45 813 kg are required for the same structure with the 18-m-long columns.

The double-layer deployable tetrahedral truss concept uses hexagonal modules emanating radially from a central module, as shown in figure 2. The number of rings N_r in each deployable module is a function of the column outside diameter D_t and the packing diameter of the Shuttle cargo bay D_b (ref. 5). Although several packaging options are available, the densest package is obtained when both the primary and secondary surface members of the tetrahedral truss fold out. When the elements are fully nested, the number of rings is obtained from

$$N_r = \frac{D_b}{6D_t} \tag{3}$$

For the 8.75-m tapered column with a mean outside diameter of 0.058 m, deployable modules consisting of 12 hexagonal rings with a total area of 28 610 m^2 fit into the 4.57-m-diameter Shuttle bay. For the 6.43-m tapered column, the 12-ring module has an area of 15 470 m^2.

Each deployable module has the number of columns N_c calculated by (ref. 5)

$$N_c = 27N_r^2 - 3N_r \tag{4}$$

and the number of node (cluster) fittings N_j is

$$N_j = 6N_r^2 + 3N_r + 1 \tag{5}$$

A total of 3852 column elements (2556 primary members and 1296 secondary members) and 901 cluster fittings are required for each module. To construct a 725-m-diameter geodesic dome from deployable modules, 15 modules composed of 8.75-m tapered columns are required, whereas 27 modules are required if they are composed of 6.43-m tapered columns. (Additional columns would be required for joining the modules and would be determined in a detail design.)

For a design load of 1 kN, the 6.43-m element would have a mass of 0.70 kg and the 8.75-m element would have a mass of 0.95 kg. Knee joints in the primary elements would have a mass of 0.113 kg, and the cluster fittings a mass of 0.23 kg. With these masses, the deployable modules would have masses of 3190 kg with the 6.43-m elements and 4153 kg with the 8.75-m elements. Total reflector-structure masses would be 86 130 kg for the 6.43-m elements and 62 295 kg for the 8.75-m elements. These data are summarized in table I.

In all cases of the deployable modules, estimates are for flat plates, whereas the dish reflector has a spherical shape. The shape is not taken into consideration, nor are the edge anomalies where the basic hexagonal pattern approaches the structural outer ring. Dish curvature is estimated to have little effect on column count estimates (less than 2 percent). Edge fitting and module connectors were estimated to add about 5 percent to the weight.

Single-layer geodesic truss concept.- For the erectable single-layer strongback structure, calculations were made using the geodesic-dome mathematics of reference 6. From geodesic-dome mathematics, curvature of the dish necessitates columns of varying lengths. The number of columns of specified lengths was estimated and the values are listed in table II. A total of 4281 columns with lengths varying from 16.68 m to 21.14 m with a mean length of 18.91 m are needed. The number of node fittings for the single layer is 1490. The stiffener ring is defined by dividing the circumference of the spacecraft into 18-m increments with 9 structural elements required for each increment, for a total of 1143 elements. Total reflector structural weight, including the stiffener ring, is 18 351 kg (18 008 kg for elements and 343 kg for node fittings).

Tension-rim concept.- The erectable tension-rim concept (fig. 3) does not utilize a strongback structure. Instead, it uses a large stiffener ring and a cable and pulley system to support the antenna membrane.

The stiffener ring is constructed entirely of three-sided, 126-m-long beams with the 9-m-long graphite-epoxy tapered tube as the principal structural element. The three-sided beam is shown in figure 4. The stiffener ring consists of two 18-sided polygons separated by spacer beams, as shown in figure 3. A three-sided, 126-m long stabilization column, supported by quartz tension cables, is mounted at the centroid of, and perpendicular to, the plane of each of the 18 faces of the stiffener ring to reduce flexure in the ring. For the 1-kN design load, the beams have a mass of 105 kg for a structural weight of 7560 kg. The weight of the load-carrying tension cables must be included in the total weight of the stiffener ring. A design load of 26 688 N established a diameter of 0.476 cm for the Kevlar cables. Total length and weight for the beam tension cables, stabilization cables, and circumferential cables is 51 036 m and 821 kg. The total weight of the tension-rim reflector structure is 8381 kg.

Antenna Membrane

The antenna membrane must be lightweight, have high reflectivity characteristics to reduce RF losses, and high strength to maintain the required curvature (shape). Thin aluminum/Mylar membranes, laminated and vapor deposited, have long flight histories as lightweight reflectors (refs. 7 and 8). In the current application, a 423 700-m^2 antenna membrane composed of 0.0089-cm-thick aluminum/Mylar laminate would have a mass of 71 000 kg. Metallized membranes, such as the gold-plated molybdenum mesh of reference 9, are lighter than and equal in strength to the aluminum/Mylar

membrane. A typical metallized membrane with a density of 0.0826 kg/m^2 would have a mass of about 35 000 kg. Consequently, the metallized membrane is used as the reflector material in the weight analysis.

One critical problem area for flexible-membrane antennas involves the shape control of the membrane. The electrostatic technique of shape control (ref. 10) is applicable to the continuous aluminum/Mylar membrane. However, power losses due to transparency of the mesh material to plasma particles are a potentially serious problem (ref. 11) and further study is required.

Support Columns

Orientation between the reflector and feed horns is maintained by two support columns and four cables. Coarse alignment corrections are anticipated, so that provisions are made to control the relative location between the feed horns and reflector by activating the four cables. The columns have ball sockets on each end to allow relative motion between the major components.

Several concepts for the support-column design were investigated. The tension-stabilized column technique was determined to be lightest in weight and was selected as the basic concept for the study. The tension-stabilized concept minimizes buckling, the primary failure mode, by placing tension members at an effective radius of gyration and maintaining them in place with outriggers. A center shaft supports the outriggers at specified distances along its length, which causes the slender center shaft to act as a series of short columns. The basic tension-stabilized column is shown in figure 5. The center shaft is a 30.5-cm-diameter graphite/epoxy tube with a wall thickness of 0.076 cm, and the tension cables are Kevlar with a diameter of 0.157 cm. The outriggers are aluminum tubes 16.16 m long and 5.08 cm in diameter, with a wall thickness of 0.038 cm. The outriggers are mounted on aluminum hubs (collars) that mount on the graphite/epoxy shaft. The hubs are 10.16 cm long with a wall thickness of 0.305 cm.

Based on a total axial load of 2900 kg and a resultant stress of 39 010 kPa, the distance between outriggers is 39 m. This assumes that each column element (distance between outriggers) is a fixed-end column. A total of 16 outriggers is required along the 580-m support column.

The total weight of each support column is summarized in the following table:

Column component	Weight, kg
Center shaft (graphite/epoxy)	645
Cables (Kevlar)	10
Outriggers (aluminum)	85
Column total (approx)	740

Radiometer Array

A conservative approach was taken in sizing the feed horns of the radiometer array in that an identical configuration was selected for all three frequencies. An aperture diameter of 2 m is fixed for all three frequencies (1.08, 2.03, and

4.95 GHz) with the length, step location, and flare angle of the horn varying according to each frequency.

Techniques for decreasing the horn weight include reducing the size of the feed horns or modifying the horn construction. Standard state-of-the-art horns are constructed of thin metal with stiffener ribs that adversely affect the microwave properties. A new concept is to fabricate the horns from a composite of graphite and epoxy 0.04 mm thick with a 0.01-mm-thick aluminum sprayed inner surface to provide a ground plane (electrical continuity). As in the case of the tapered columns, 0.04-mm composites are pushing current technology (thickness is presently limited to 0.71 mm). Constructing the feed horns with a conductive mesh, or screen, supported by a frame would further reduce the weight. A 10-m-long horn constructed of metallized composites (density of 61.5 kg/m^2) weighs 23 kg, or 13 800 kg for the complete 600 horn array.

The feed beam supporting the horns is of tetrahedral truss construction. The 200-m beam is comprised of 15 bays (134 elements, 50 nodes, and 6 end elements) with a weight of 421 kg. Supports for mounting the feed horns to the feed beam, fabricated of graphite/epoxy, weigh 287 kg. Including 600 kg for electronics for the feed horns, the total weight of the radiometer array is 15 108 kg.

Auxiliary Equipment

Auxiliary equipment for the MRS includes the surface control system for the antenna, power system (solar panels), attitude control system (momentum wheels), and electronics for the radiometers and communications.

Surface control system.- Although power losses may pose a problem for the mesh material when using electrostatic shape control (ref. 11), the electronic tensioning concept is employed in the weight analysis of the surface control system. Results from the preliminary tests of reference 10 for a 1.83-m-diameter reflector were scaled to the full size reflector and the weight is estimated to be approximately 30 000 kg.

Solar panels.- A solar panel array of approximately 200 m^2 is needed to meet the power requirement of 20 kW. With state-of-the-art technology, this translates to a weight of 450 kg for the solar power system.

Attitude control system.- Laboratory tests (ref. 12) of a small prototype dual-momentum vector control system were used to scale the weight of the momentum wheels for the MRS. To keep the mass low, the control system would have a cross-sectional area of approximately 0.3 m^2 per wheel. The resulting wheel would be more flexible than the present laboratory specimen, probably taking the form of a rope or a fluid, and is currently beyond the state of the art of the technology. The attitude control system weight is estimated to be 2000 kg.

Electronics.- The weight of the electronics supporting the radiometer systems and the communications (data transfer) systems is estimated to be approximately 600 kg, based on corresponding weights of current spacecraft systems.

114

A number of new and innovative techniques have been developed for more efficient packaging of components of the microwave radiometer spacecraft. For the erectable concept for the strongback structure, tapered half-columns are used. The columns are stacked one inside the other, as shown in figure 6, and assembled in orbit by joining the larger ends together to form the 18-m structural member. In the deployable concept, the densest package is obtained when both the primary and secondary surface members of the tetrahedral truss fold out, as described in reference 5 and shown in figures 7 and 8. Also shown in figure 8 is the package arrangement for primary surface members folding in and secondary surface members folding out. For the feed horns, the stacking technique used for the tapered half-columns was found to be less efficient than splitting the feed horns along the longitudinal center line and stacking the half cones as shown in figure 9.

The goal of packaging the microwave radiometer spacecraft is to achieve the maximum weight allowed in each Space Shuttle launch. A cargo of up to 29 483 kg (ref. 5) is possible for launch only. A limit of 14 515 kg is the limit for landing (including an aborted launch). Location of the center of gravity of the cargo is also critical for landing. Attention must be given to distributing subsystem components within the cargo bay as well as throughout the system of launch vehicles to achieve optimum balance and packaging efficiency.

For the purpose of this study it was decided to use the high launch value of 29 483 kg and exclude the aborted launch condition. Nestable tapered columns were chosen for the basic structural member. All other components were either designed for maximum packing density or assumed to achieve minimum density when designed. Minimum packing density is

$$\frac{\text{Cargo capacity}}{\text{Volume of bay}} = \frac{29\ 483\ \text{kg}}{300\ \text{m}^3} = 98.3\ \text{kg/m}^3$$

Anything less than this density tends to make the cargo volume critical and is inefficient packaging. Ideally, all components will be packed in the "weight critical" condition.

For maximum efficiency, the minimum number of Shuttle flights is shown to be

$$\frac{\text{MRS weight}}{\text{Cargo capacity}} = \frac{139\ 951\ \text{kg}}{29\ 483\ \text{kg}} = 4.75$$

Although assembly equipment and orbit transfer systems are not accounted for, the MRS could be put into orbit with five Shuttle flights.

Based on this estimate of 5 Shuttle flights to transport the MRS components into orbit, a preliminary transportation plan was developed and is shown in figure 10. The antenna support structure would be transported in the first flight and assembled. The second flight's cargo would consist of the control system, the solar panels and supporting electronics systems, and a portion of the strongback structure for the double-layer tetrahedral truss. The third flight would be completely filled with

tapered columns, joints, and fittings for the major portion of the strongback struc-
ture. The remainder of the strongback structure, the support columns, the feed boom,
and the feed horns would be transported on the fourth flight. The fifth flight would
ferry the antenna mesh, the control activators, and the remaining electronics
systems.

DISCUSSION

The weight analysis of the three conceptual designs of the microwave radiometer
spacecraft is summarized in table III. Although detailed calculations were made of
the structural components of the spacecraft, the weights for the auxiliary equipment
(surface controls, solar panels, momentum wheels, and electronics) were estimated,
based on scaling weights of laboratory systems or comparisons with similar equipment
on existing spacecraft.

A comparison of the erectable and deployable double-layer tetrahedral truss
concepts for an element length of 6.43 m shows the deployable concept to be only
slightly heavier (less than 3 percent) than its erectable counterpart. However, the
erectable concept was 10 times more compact than the corresponding deployable concept
because of the packaging inefficiency of the deployable tetrahedral truss modules.
Each module weighs 3190 kg, yet it fills the cargo bay (weight capacity of 29 483 kg)
for a packaging efficiency of only 10.8 percent. Similar results would be found in a
comparison of the 8.75-m deployable and the 18.0-m erectable concepts.

The erectable single-layer geodesic truss concept is the lightest of the truss
structures, with a mass of 102 499 kg. The use of only a single geodesic truss layer
for the reflector strongback accounts for the weight reduction of this concept.
However, a detailed dynamic analysis of the flexures in the strongback has not been
performed and a stronger stiffener ring may be required to eliminate unwanted
flexures.

The unconventional tension-rim design is the lightest of all the concepts ana-
lyzed with a mass of 62 529 kg. An MRS spacecraft utilizing this concept could be
transported to orbit in only 2.1 Shuttle flights. Since this concept incorporates
technology that is at or beyond the state of the art, additional study is required
before it can be considered viable and carried beyond the conceptual design stage.

CONCLUSIONS

Total spacecraft weight for three conceptual designs of a microwave radiometer
spacecraft has been estimated and packaging options have been studied. Erectable
structures have been found to be 2.5 to 10 percent lighter than the comparable
deployable structure. Although the single-layer geodesic truss concept is about
30 percent lighter than the double-layer concept, no analysis was conducted on the
dynamics of the two concepts. The unconventional tension-rim concept was found to be
the lightest spacecraft and is transportable into orbit in the least number of
Shuttle flights. Erectable configurations were found to be 10 times more compact
than the corresponding deployable concept.

REFERENCES

1. Outlook for Space. Report to the NASA Administrator by the Outlook for Space Study Group. NASA SP-386, 1976.

2. Bekey, I.; Mayer, H. L.; and Wolfe, M. G.: Advanced Space System Concepts and Their Orbital Support Needs (1980-2000). Volume IV: Detailed Data - Part II: Program Plans and Common Support Needs. ATR-76(7365)-1, Vol. IV (Contract NASW-2727), Aerospace Corp., Apr. 1976. (Available as NASA CR-148708.)

3. Bush, Harold G.; Mikulas, Martin M., Jr.; and Heard, Walter L., Jr.: Some Design Considerations for Large Space Structures. AIAA/ASME 18th Structures, Structural Dynamics and Materials Conference, Mar. 1977, pp. 186-196. (Available as AIAA Paper No. 77-395.)

4. Ramsey, James H.; and Wright, Robert L.: Bootlace Catenary Concept for Antenna Shape Control. The Microwave Radiometer Spacecraft - A Design Study, Robert L. Wright, ed., NASA RP-1079, 1981, pp. 205-213. (Paper in this compilation.)

5. Barclay, D. L.; Brogren, E. W.; Fosth, D. C.; Gates, R. M.; and Straayer, J. W.: Large Space Structures - Configuration, Packaging, and Response Studies - Final Report. NASA CR-158928, 1978.

6. Tarnai, T.: Spherical Grids of Triangular Network. Acta Tech. Acad. Sci. Hung., vol. 76, nos. 3-4, 1974, pp. 307-336.

7. Coffee, Claude W., Jr.; Bressette, Walter E.; and Keating, Gerald M.: Design of the NASA Lightweight Inflatable Satellites for the Determination of Atmospheric Density at Extreme Altitudes. NASA TN D-1243, 1962.

8. Clemmons, Dewey L., Jr.: The Echo I Inflation System. NASA TN D-2194, 1964.

9. Sikes, L. D.; and Hower, T.: Effects of Antenna Blockage in Radio-Frequency Performance of the Microwave Radiometer Spacecraft. The Microwave Radiometer Spacecraft - A Design Study, Robert L. Wright, ed., NASA RP-1079, 1981, pp. 141-165. (Paper in this compilation.)

10. Hinson, William F.; Goslee, J. W.; McIlhaney, John R.; and Ramsey, James H.: Biaxial and Electrostatic Tensioning Effects on Thin Membrane Materials. The Microwave Radiometer Spacecraft - A Design Study, Robert L. Wright, ed., NASA RP-1079, 1981, pp. 189-204. (Paper in this compilation.)

11. Katz, Ira: Electrostatic Antenna Space Environment Interaction Study. Large Space Systems Technology - 1980, Volume 1 - Systems Technology, Frank Kopriver III, compiler, NASA CP-2168, 1980, pp. 271-278.

12. Groom, Nelson J.; and Terray, David E.: Evaluation of a Laboratory Test Model Annular Momentum Control Device. NASA TP-1142, 1978.

TABLE I.- SUMMARY OF WEIGHTS AND PACKAGING OF REFLECTOR STRUCTURE

[Total area of spacecraft is 412 825 m²]

Parameter	Double-layer tetrahedral truss			Single-layer geodesic truss	Tension rim
	Deployable		Erectable		
Element length, m	6.43	8.75	6.43	18.0	18.0
Element diameter, m	0.058	0.058	[a]0.1016	[a]0.1016	
Quantity of elements	104 004	57 780	106 497	[b]5424	
Module area, m²	15 470	28 610	13 590		
Module weight, kg	3190	4153			
Total weight, kg	86 130	62 295	79 991	45 813	18 351	[c]8381
Area density, kg/m²	0.2033	0.1470	0.1888	0.1081	0.0433	0.0198
Shuttle flights	27	15	2.7	1.6	0.6	0.3
Limiting criteria	Volume	Volume	Weight	Weight	Weight	Weight

[a]Mean diameter of tapered column.
[b]Includes stiffener ring.
[c]Includes cable weight.

TABLE II.- QUANTITY AND LENGTHS OF COLUMNS

FOR SINGLE-LAYER GEODESIC TRUSS CONCEPT

Number of columns	Length range, m (a)
222	20.90 to 21.14
708	20.46 to 20.78
735	20.08 to 20.35
639	19.72 to 19.73
597	19.25 to 19.57
426	18.93 to 19.16
399	18.46 to 18.74
291	17.89 to 18.19
165	17.35 to 17.64
69	16.99 to 17.29
30	16.68 to 16.75
4281	

[a]Values are ±0.15 m.

TABLE III.- TOTAL SPACECRAFT WEIGHT SUMMARY

Parameter	Double-layer tetrahedral truss				Single-layer geodesic truss	Tension rim
	Deployable		Erectable			
Element length, m	6.43	8.75	6.43	18.0	18.0	
Strongback structure, kg	86 130	62 295	79 991	45 813	b18 351	
Antenna membrane, kg	35 000	35 000	35 000	35 000	35 000	35 000
Surface controls,a kg	30 000	30 000	30 000	30 000	30 000	
Stiffener ring, kg	9990	9990	9990	9990		c8381
Actuators, kg	110	110	110	110	110	110
Support columns and cables, kg	1480	1480	1480	1480	1480	1480
Solar panels,a kg	450	450	450	450	450	450
Radiometer structure, kg	708	708	708	708	708	708
Radiometer horns, kg	13 800	13 800	13 800	13 800	13 800	13 800
Electronics,a kg	600	600	600	600	600	600
Momentum wheels,a kg	2000	2000	2000	2000	2000	2000
Total mass, kg	180 268	156 433	174 129	139 951	102 499	62 529

aEstimated values.
bIncludes stiffener ring.
cIncludes cables.

575 m

TOWARD EARTH

725 m· DIAM

200m

575 m

1150 m

DISH REFLECTOR

SUPPORT RING

MOMENTUM WHEEL ACS

4.95 GHz

2.03 GHz

1.08 GHz

1.0 m SPACING
200 UNITS

T/ M
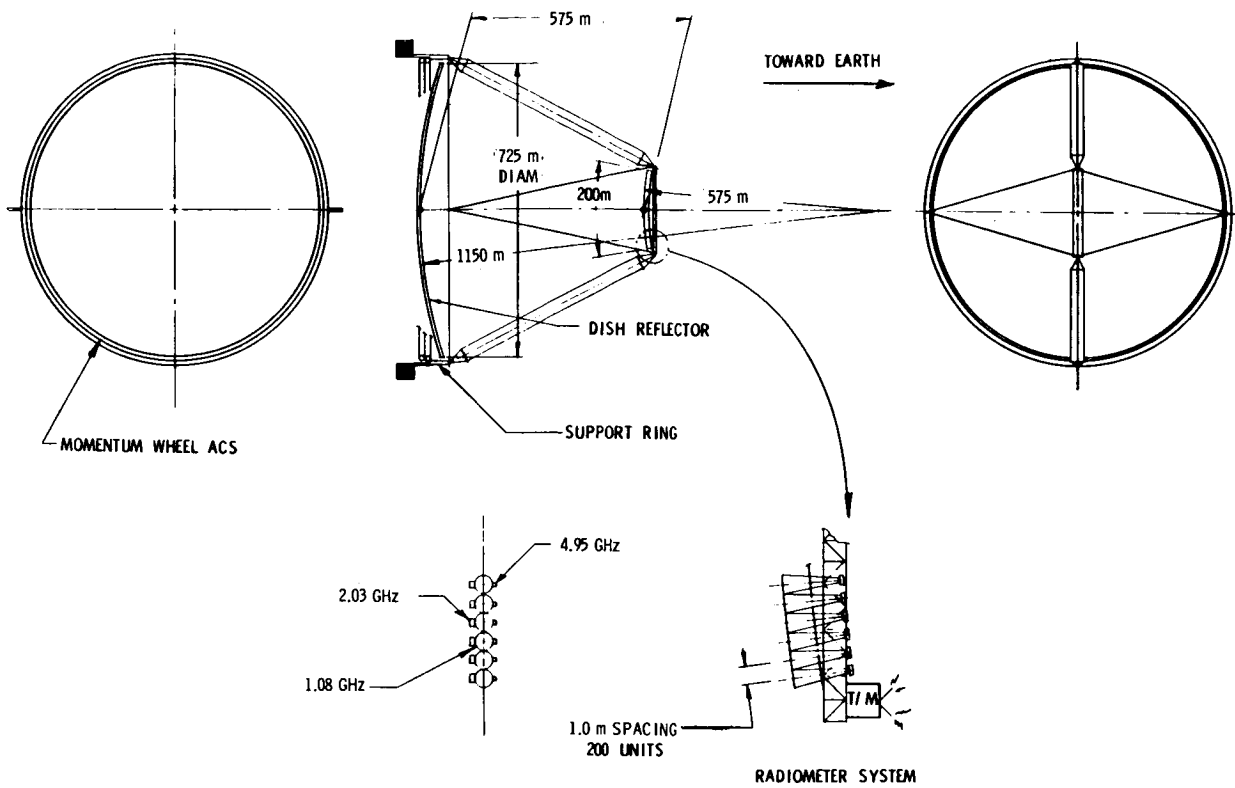
RADIOMETER SYSTEM

Figure 1.- Microwave radiometer satellite (MRS).

725 m DIA

1150 m R
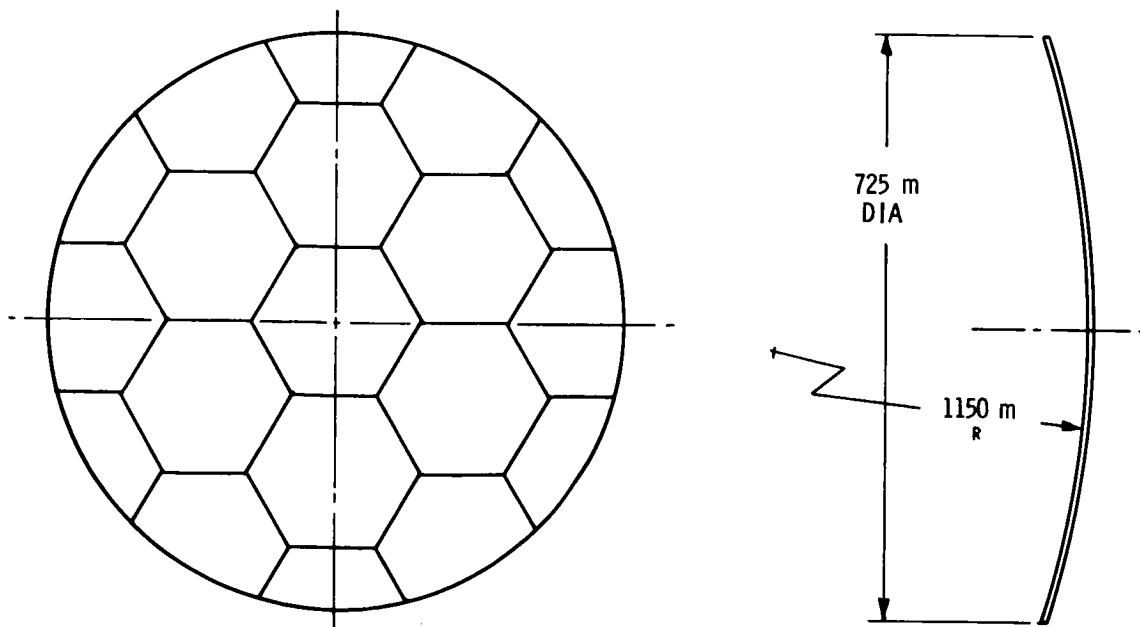
Figure 2.- Hexagonal modules for fully deployable
double-layer tetrahedral truss concept.
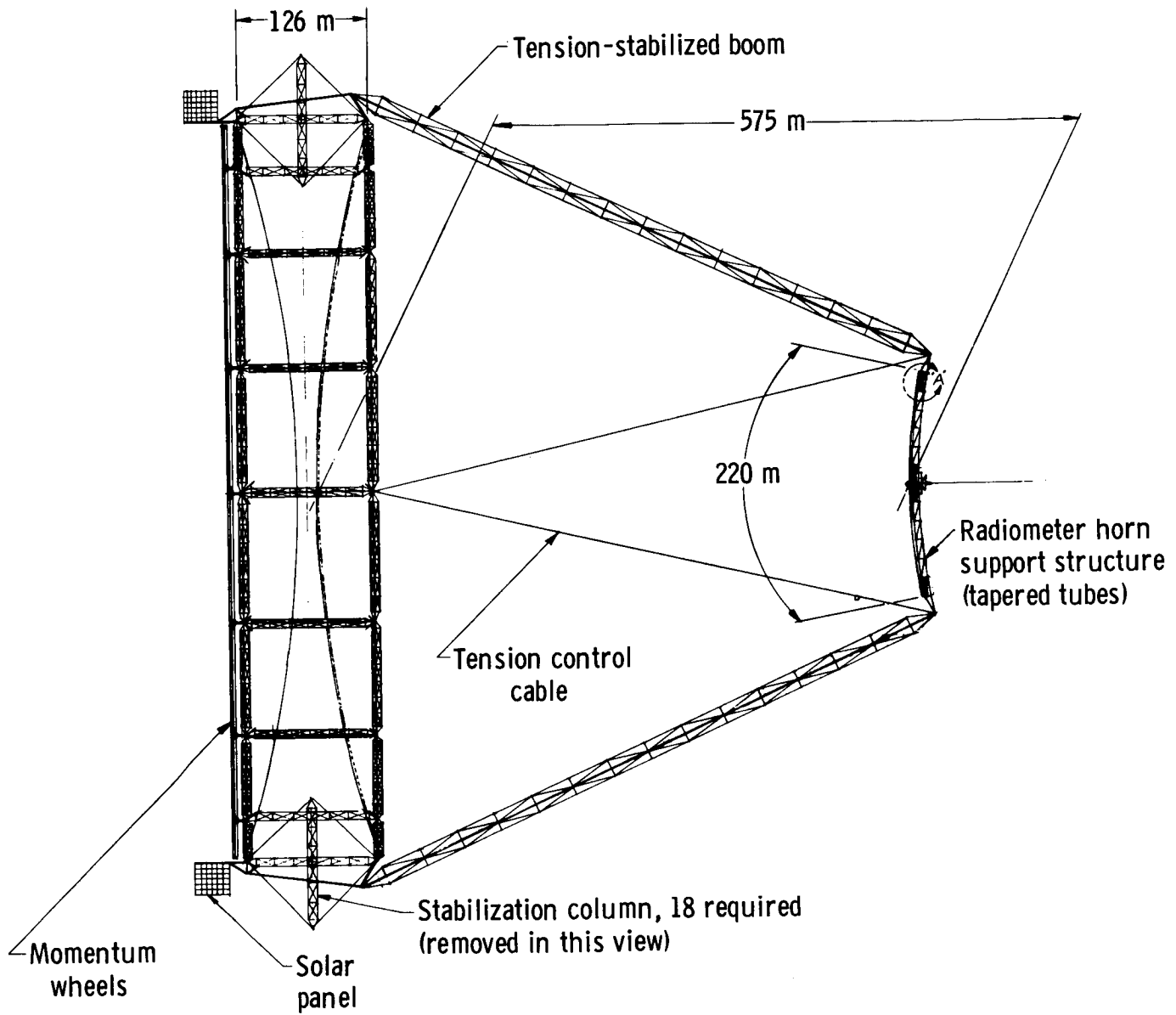
Figure 3.- Tension-rim concept.
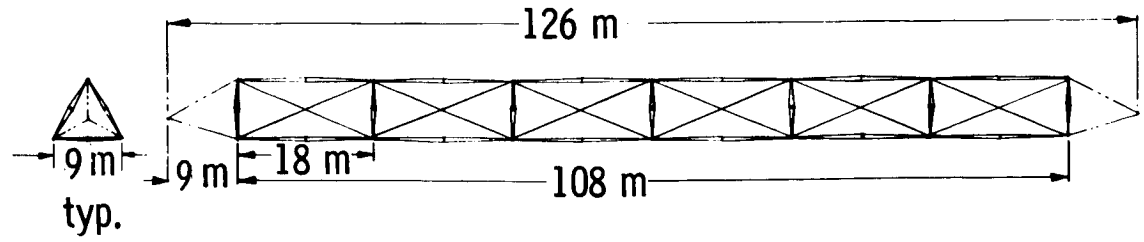
Figure 4.- Basic beam for stiffener ring
(tension-rim concept).
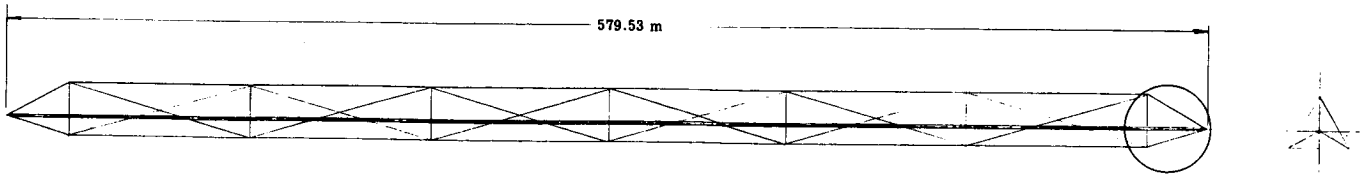
Figure 5.- Tension-stabilized column.

725 m DIAM

SEE DETAIL **A**

1150 m R

4.57 m DIAM

18.28 m

STACKED ELEMENTS STOWED IN CARGO BAY

9 m

TAPERED COLUMN STACKING ARRANGEMENT

SEE DETAIL **C**

18.00 m

DETAIL **A**

B

B

DETAIL **C**
LRC CENTER JOINT

LRC END FITTING

VIEW **B-B**

DETAIL OF NODE

SURFACE ATTACHMENT POINT

END VIEW OF STACKED ELEMENTS
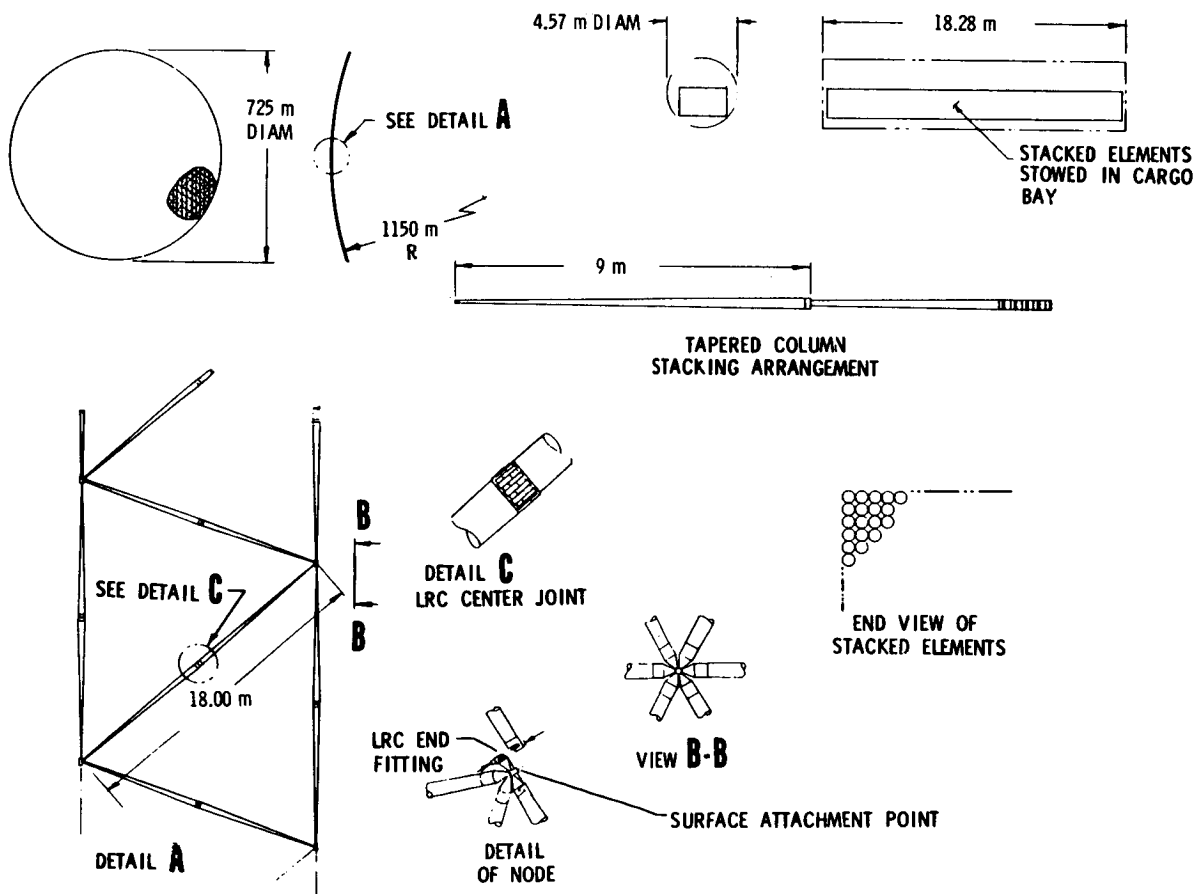
Figure 6.- Packaging of erectable concepts.
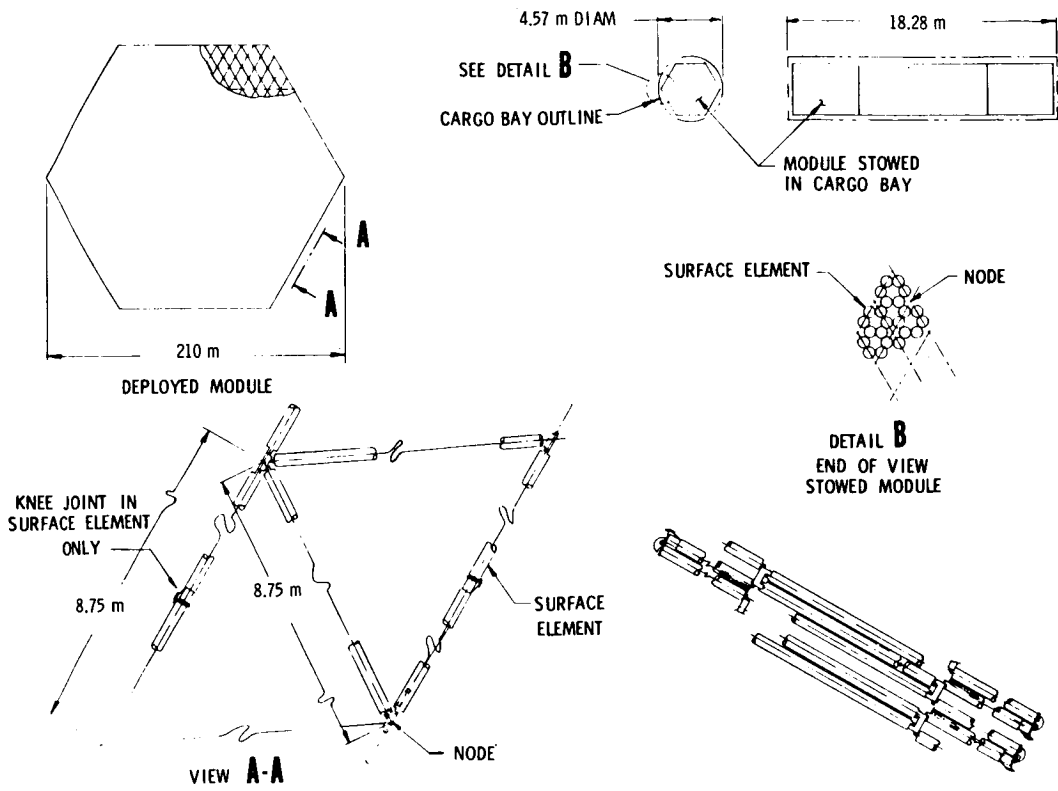
Figure 7.- Packaging of deployable concept.
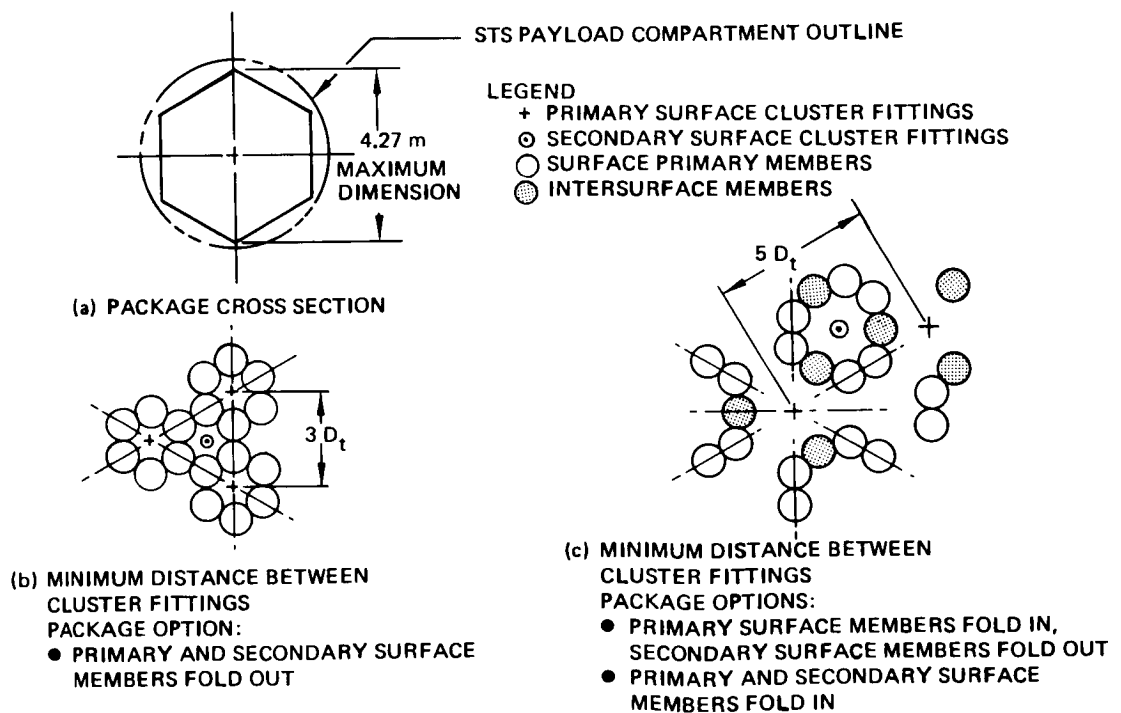
Figure 8.- Tetrahedral truss package arrangement.

Split horn packaging,
<1 Shuttle flight

4.57 m
diam.

Cargo bay

10 m

.15 m spacing

Cargo bay

Conical packaging,
3.8 Shuttle flights
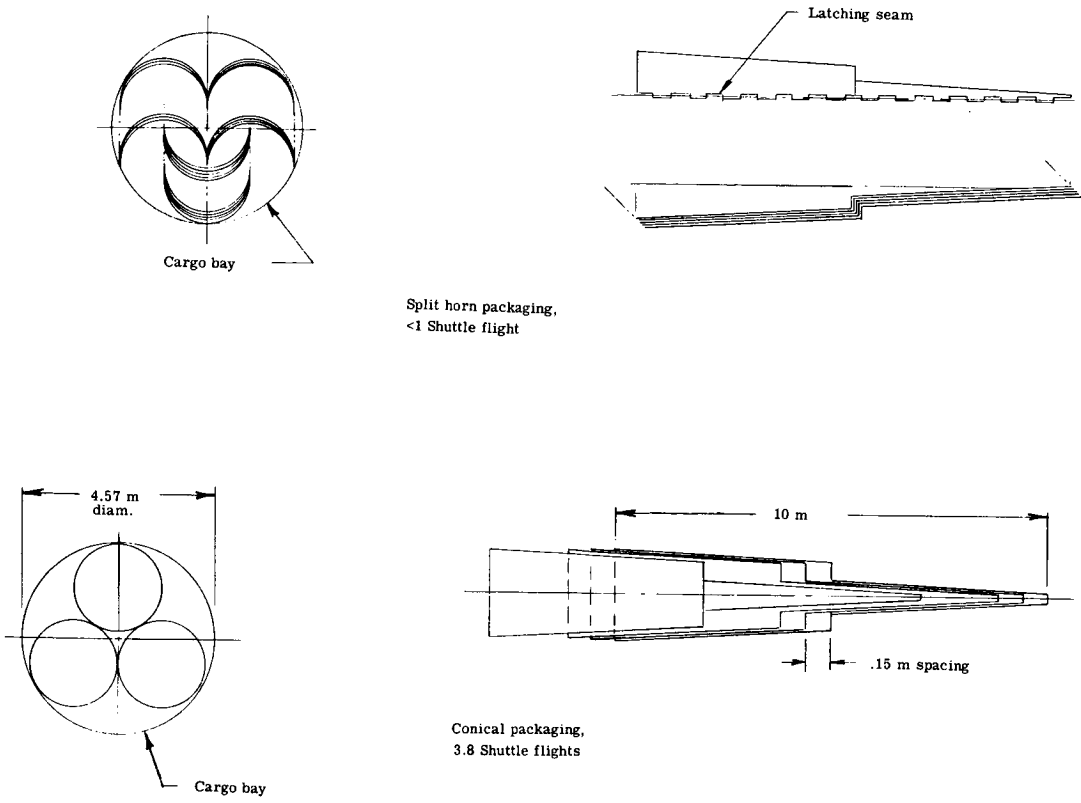
Figure 9.- Packaging of feed horns.

FLIGHT 1

FLIGHT 3

FLIGHT 4

FLIGHT 2

FLIGHT 5
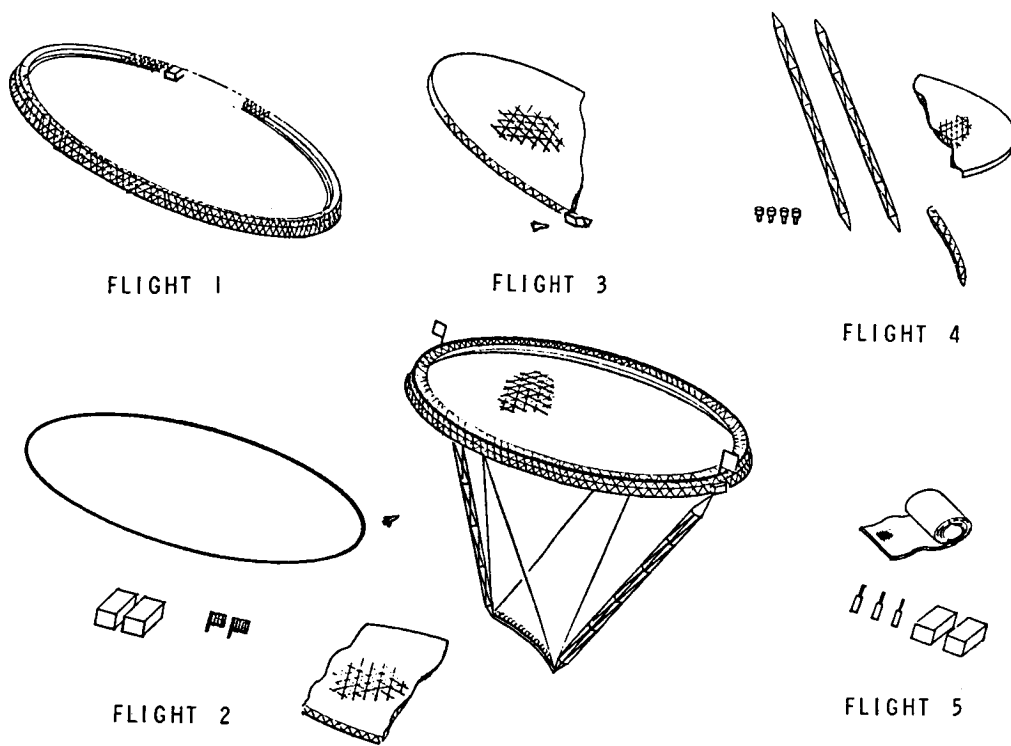
Figure 10.- Transportation and assembly plan of the MRS.

PART III

ELECTROMAGNETIC CONCEPTS

ELECTROMAGNETIC DESIGN OF A

MICROWAVE RADIOMETER ANTENNA SYSTEM

P. K. Agrawal*
RCA
Moorestown, New Jersey
and
C. R. Cockrell
NASA Langley Research Center
Hampton, Virginia

SUMMARY

A preliminary electromagnetic (EM) design of a radiometric antenna system has been developed for the microwave radiometer spacecraft mission. The antenna system consists of a large spherical reflector and an array of feed horns along a concentric circular arc in front of the reflector. The reflector antenna was sized to simultaneously produce 200 contiguous 1-km-diameter footprints with an overall beam efficiency of 90 percent, and the feed horns and feed-horn array were designed to monitor the radiation from the footprints.

INTRODUCTION

The soil-moisture radiometer mission of reference 1 requires a large reflector antenna system capable of simultaneously producing 200 contiguous, 3-dB, circular footprints on the ground while operating in a low Earth orbit. Th reflector must be large enough to operate at three frequencies: 1, 2, and 4 GHz. Designing the reflector for the lowest frequency of 1 Ghz produces a reflector size that will also accommodate the two higher frequencies. The 1-km-diameter footprints are required to be as identical to each other as possible. The single most important requirement of the system is that the overall beam efficiency for the copolarized component in each of the 200 beams be better than 90 percent within 2 1/2 times the 3-dB beam width. The cross polarization should be minimum (less than 25 dB).

REFLECTOR AND FEED-HORN DESIGN

A reflector and feed-horn design that meets the requirements of reference 1 is shown schematically in figure 1.[1] In this study, 200 beams are simultaneously obtained by stacking 200 identical feed horns along a concentric circular arc in

---

*Formerly with Joint Institute for Advancement of Flight Sciences, The George Washington University, Hampton, Virginia.
[1]The spherical reflector was selected because of its inherent geometrical properties which enable wide angle scanning of beams.

front of a spherical reflector such that each feed horn is pointing radially toward the spherical-reflector surface. Each feed horn is assumed to create its own independent footprint, and since each feed horn essentially "sees" an identical segment of the spherical reflector, the resulting 200 footprints are also practically identical. The angular separation θ between any two consecutive feed horns is the same as the angular separation between the centers of the two adjacent footprints. As an example, for an altitude of 650 km (measured at the center of curvature of the reflector) and a footprint size of 1 km, this angular separation turns out to be 0.088° and the 200 feed horns stacked along the feed arc thus subtend a total angle of 17.6° at the center of the spherical reflector. The geometry of the reflector antenna is presented in figure 2.

The angular separation between any two consecutive feeds depends only upon the altitude and the footprint size; the physical separation, however, is the product of the angular separation (θ = 0.088°) and the feed-arc radius of curvature. The radius of curvature of the feed arc, therefore, should be large enough to provide enough physical space for each of the 200 feed horns. It is assumed that each feed horn should have, on an average, a space of at least 88 cm, which leads to a feed-arc radius of curvature of 577 m. Since for spherical reflectors the feed arc is generally located about halfway between the reflector and its center of curvature, the radius of curvature of the spherical reflector is chosen to be 1150 m. Note there is no specific reason to choose 88 cm for feed-horn spacing except that the estimates of practical feed-horn size suggest that a space of about 1 m is needed for each feed horn. And, of course, whether or not a feed horn limited in size to 88 cm at 1 GHz feeding a reflector with the dimensions chosen herein can give a satisfactory secondary far-field pattern remains to be checked.

Consider an individual footprint which is caused by an individual feed horn located at the feed arc. Each feed horn illuminates a portion of the spherical reflector, and it is the far-field pattern of this illuminated-reflector aperture which must have (a) a 3-dB beam width of 0.088°, and (b) a beam efficiency of better than 90 percent within 2 1/2 times the 3-dB beam widths. The latter requires that the highest side lobe of the reflected pattern be less than -32 dB with wide-angle side lobes below -80 dB down from the main lobe. A study of various aperture distributions (ref. 2) indicates that for an operating frequency of 1 GHz, an aperture diameter of about 300 m (e.g., 305 m) with a rotationally symmetric cosine-squared field distribution produces both a 3-dB beam width of 0.088° and a side lobe at -32 dB, the side-lobe falloff being -18 decibels per octave.

As shown in figure 2, an illuminated aperture with a diameter of 305 m on the reflector corresponds to a cone of 15° half-angle emanating from each feed horn. Therefore, each feed horn whose nominal diameter has been fixed at 88 cm at 1 GHz has to be able to produce a rotationally symmetric cosine-squared far-field pattern over ±15°. The overall diameter of the spherical-reflector dish to produce 200 beams then turns out to be 660 m as shown in figure 2. Since the beams are scanned in one plane only, the spherical-reflector aperture dimension in the plane orthogonal to the scanned direction doesn't have to be 660 m but only 305 m (the illuminated-aperture diameter). These electromagnetic analyses, however, have treated the reflector as though it was uniformly spherical, so that its symmetrical properties could be utilized (if needed) in construction.

FEED CONSIDERATIONS

The EM design assumes that after reflection, each feed pattern gives rise to a rotationally symmetric aperture field which varies with cosine squared in the radial direction. For the reflector dimensions under consideration, the portion of the reflector illuminated by a feed is such a small fraction of the full spherical-reflector area that it is practically flat, and therefore a rotationally symmetric cosine-squared aperture distribution is easily achieved by a feed which also has a rotationally symmetric cosine-squared pattern.

A rotationally symmetric cosine-squared feed pattern can be generated by either a dual-mode horn or a corrugated horn. Since the antenna patterns of these horns are very similar, the secondary radiation patterns are similar. From the standpoint of construction and packaging, the dual-mode horn would be the choice, even though it is physically larger. The feed pattern used for the computations is shown in figure 3. The diameter of the horn is 2 m, which is larger than the 88-cm space designated for each feed horn at the feed arc. The feed horns, therefore, will have to be staggered around the feed arc so that they still average 88 cm, or 0.088°, of separation. The beam efficiency of the feed pattern within ±15°, which corresponds to the edge of the illuminated spot, is 98.3 percent. This value is important because the overall beam efficiency of the antenna system (required to be greater than 90 percent) is the product of this efficiency and the beam efficiency of the secondary pattern.

ELECTROMAGNETIC PERFORMANCE

For the reflector geometry of figure 2 and with the feed pattern of figure 3, the secondary pattern computed with the method of reference 3 is shown in figure 4. It has a 3-dB beam width of 0.08° and a very low maximum cross-polarization level. The beam efficiency of the secondary pattern at 2 1/2 times the 3-dB beam width is 93.4 percent. The overall beam efficiency, therefore, is better than 91 percent.

One of the concerns in spherical-reflector applications is the resulting spherical aberration. It is interesting that in the present case, such a small segment of the sphere is being used as a reflector that the maximum spherical aberration near the edge of the illuminated aperture (when the field strength is -26.7 dB) is equivalent to a phase error of only about 18°. Such a small phase error causes a negligible degradation in the antenna gain.

The performance of a reflector in space is sometimes not the same as that predicted by the initial design because the reflector undergoes severe distortions due to thermal variations. If the distorted shape of the reflector is quite different from the original spherical shape, the reflector performance may change significantly and may even become unsatisfactory.[2] Therefore, it is desirable to be able to predict the performance of even the distorted reflector. If the distortion of the reflector surface could be known analytically, then the reflector performance could, of course, be accurately predicted. It is not generally possible to know an analytic expression for the entire distorted reflector surface at all times. Alternatively, a sampling scheme can be implemented so that the coordinates of many discrete target points located along a rectangular grid on the reflector surface are known. Then, a

---

[2]Performance degradations, resulting from either surface distortions on irregularities, are discussed in reference 4.

smooth, tight cubic surface can be fitted through the four corners of each of the rectangular-grid patches so that the whole composite reflector surface is continuous and has continuous partial derivatives. By using this piecewise analytic expression for the reflector surface, the reflector performance can be computed. The target points on the reflector surface must be dense enough to sample the distortions and arranged so that the surface between the measured points could be assumed to be tightly stretched.

To demonstrate that the far-field radiation pattern can indeed be accurately computed even when the reflector surface is known only at certain discrete points, the following example is presented. Computations presented in figure 4 are made again. This time, though, instead of using a single analytic expression for the entire spherical-reflector surface, the x, y, and z coordinates of 45 equally spaced points are located on the reflector surface along a grid as shown in figure 5. The points are 40 m (133.3 wavelengths λ) apart. For computational purposes, the reflector surface over any rectangular patch is expressed as a bispline under tension (ref. 5). In figure 6, the far-field radiation pattern computed by using a single analytic expression for the entire spherical reflector surface (as in fig. 4) is shown by solid lines. On the same figure, the far-field radiation pattern computed by using the piecewise analytic composite surface through 45 target points on the reflector is also shown (as square symbols). The modifications in the computer program of reference 3 to make the present surface-fitting computation are given in reference 6.

For actual distorted-reflector conditions where the whole distorted reflector surface is not known analytically, accurate far-field pattern computations can be made with the computer programs of references 2 and 6, which will accept a set of discrete reflector-surface points for the reflector-surface geometry. The basic underlying assumption is that the surface is smooth between the target sample points. Although the sample-point program accurately computed the radiation pattern for the spherical reflector, more verification of the program is needed via experimental models.

CONCLUSIONS

A preliminary electromagnetic design of a radiometric antenna system has been developed for the microwave radiometer spacecraft mission. The reflector antenna and feed-horn array are designed to monitor radiation simultaneously from 200 contiguous 10-km-diameter footprints with an overall beam efficiency of 90 percent. Although the example chosen for illustration was for an orbit altitude of 650 km, the geometric relationships may be scaled for altitudes near this example. This analysis has indicated that an aperture with an overall beam efficiency of better than 90 percent is feasible; however, the analysis is for ideal surfaces, feeds, and illumination. Great care must be exercised to design systems that will allow analytical modeling and provide capability for control during orbital operations.

REFERENCES

1. Keafer, Lloyd S., Jr.: Mission Definition for a Large-Aperture Microwave Radiometer Spacecraft. The Microwave Radiometer Spacecraft - A Design Study, Robert L. Wright, ed., NASA RP-1079, 1981, pp. 17-32. (Paper in this compilation.)

2. Harris, Frederic T.: On the Use of Windows for Harmonic Analysis With the Discrete Fourier Transform. Proc. IEEE, vol. 66, no. 1, Jan. 1978, pp. 51-83.

3. Agrawal, Pradeep K.: A Computer Program To Calculate Radiation Properties of Reflector Antennas. NASA TM-78721, 1978.

4. Cockrell, C. R.; and Staton, Leo: Effects of Random Distortions on the Surface Accuracy of a Large Antenna. The Microwave Radiometer Spacecraft - A Design Study, Robert L. Wright, ed., NASA RP-1079, 1981, pp. 137-140. (Paper in this compilation.)

5. Cline, A. K.: Algorithm 476 - Six Subprograms for Curve Fitting Using Splines Under Tension [E2]. Commun. ACM, vol. 17, no. 4, Apr. 1974, pp. 220-223.

6. Agrawal, Pradeep K.: A Preliminary Study of a Very Large Space Radiometric Antenna. NASA TM-80047, 1979.
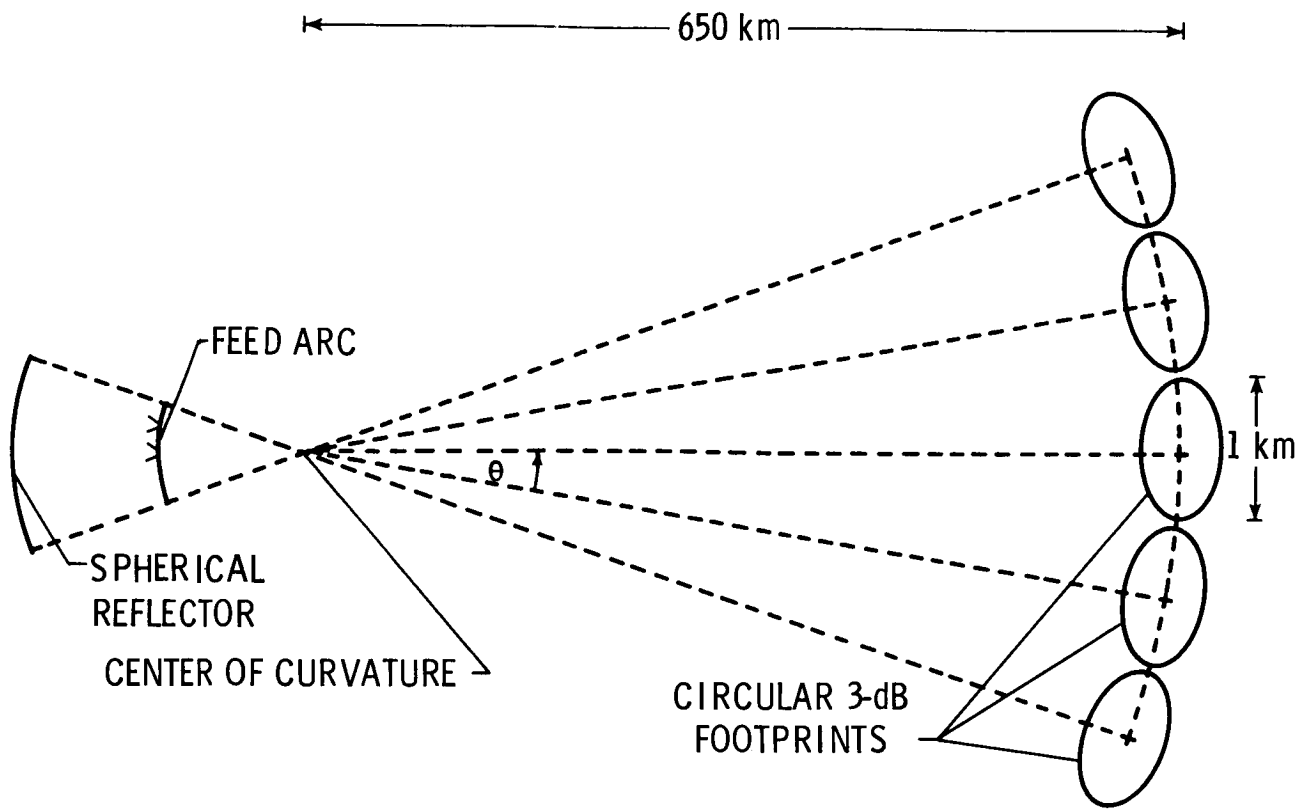
Figure 1.- Multiple-beam, spherical-reflector concept.
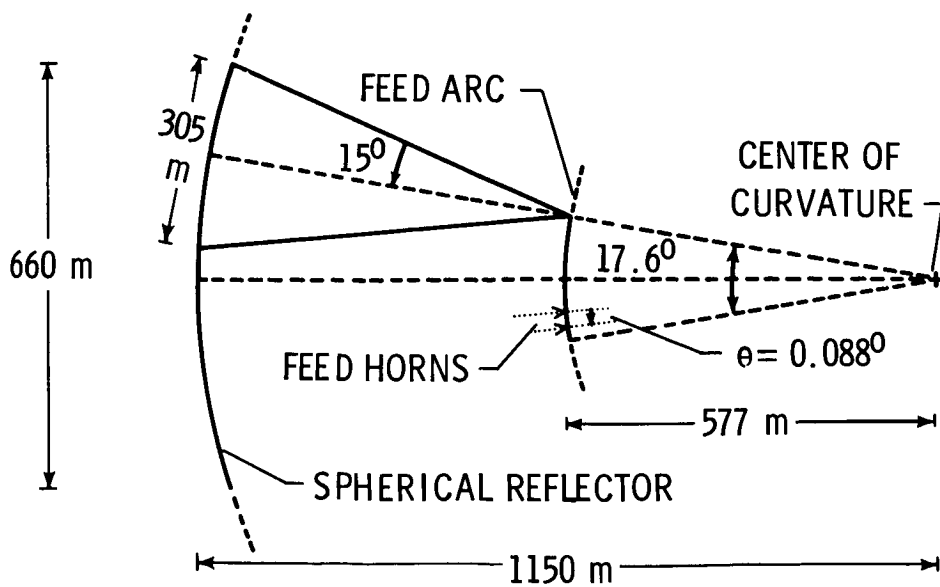
Figure 2.- Geometry of spherical-reflector antenna.

Figure 3.- Feed pattern.

ANGLE OFF THE REFLECTOR AXIS, deg
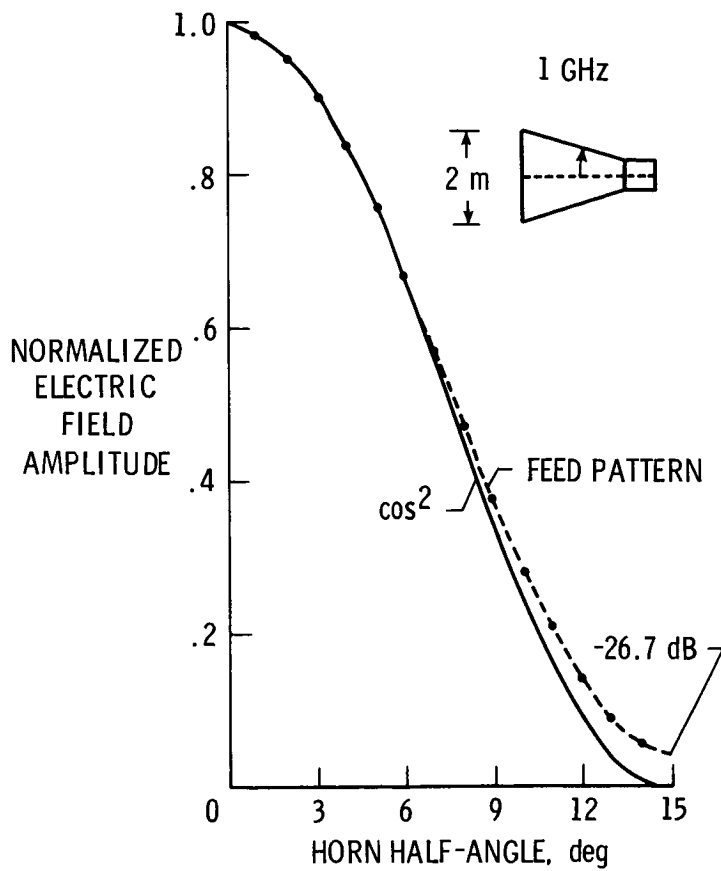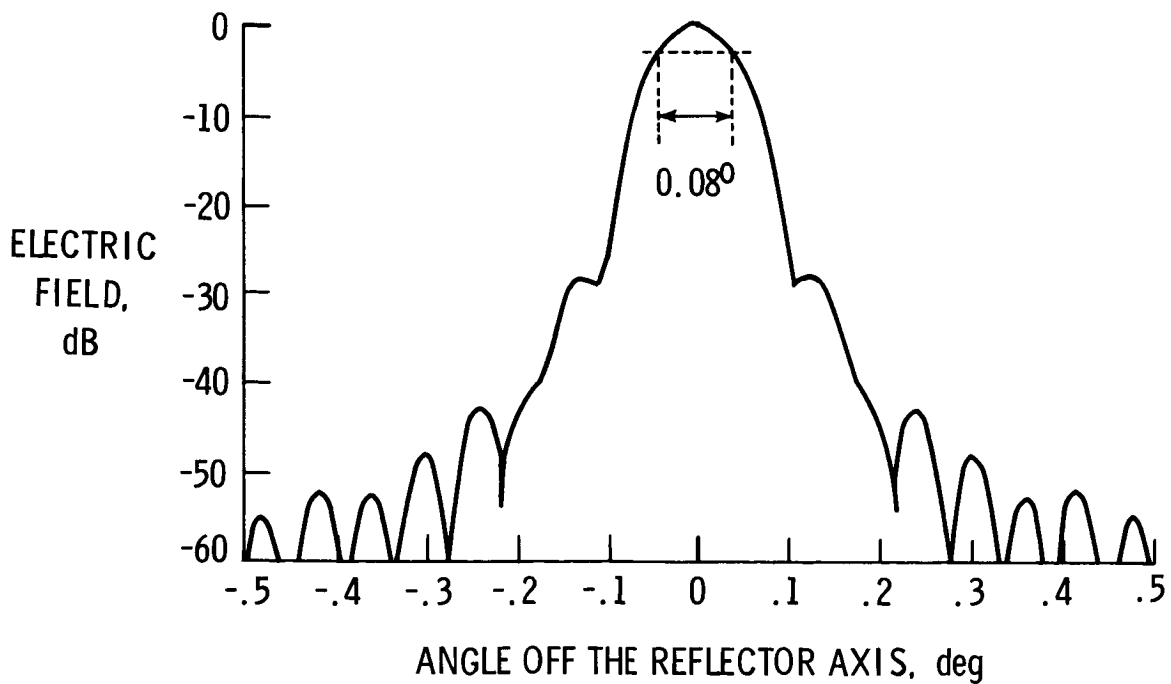
Figure 4.- Computed secondary pattern. Feed pattern was
used over ±16° with 1° increments.
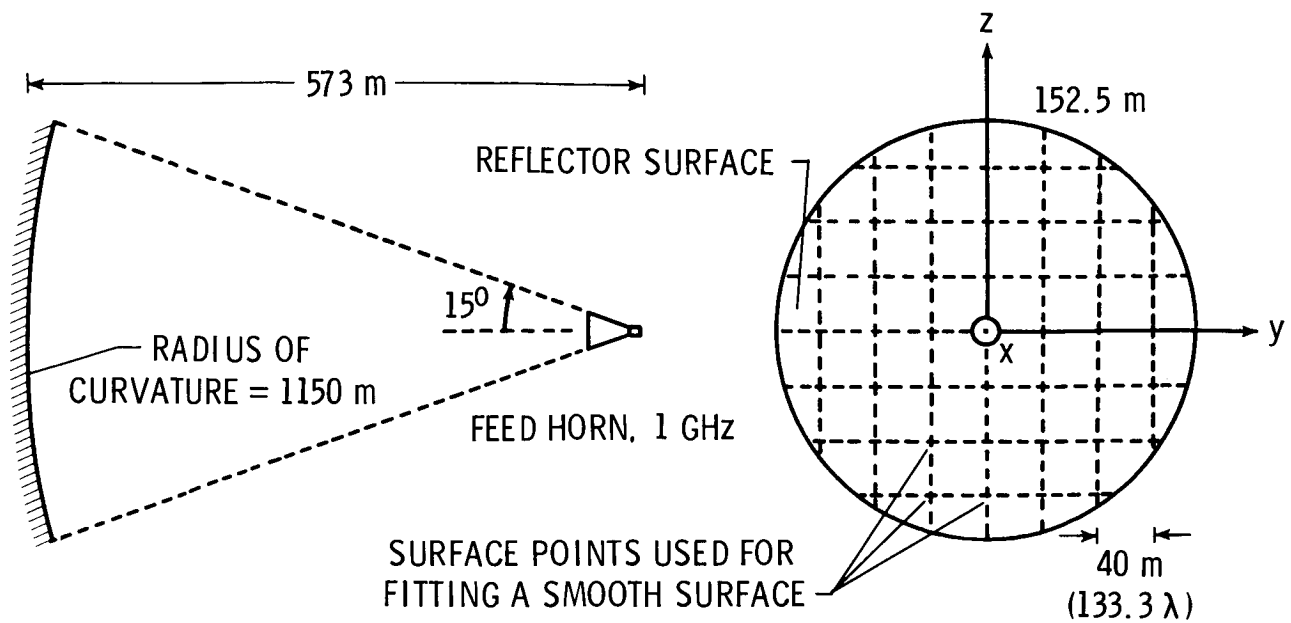
Figure 5.- Location of surface target points used for
surface-fitting calculations.
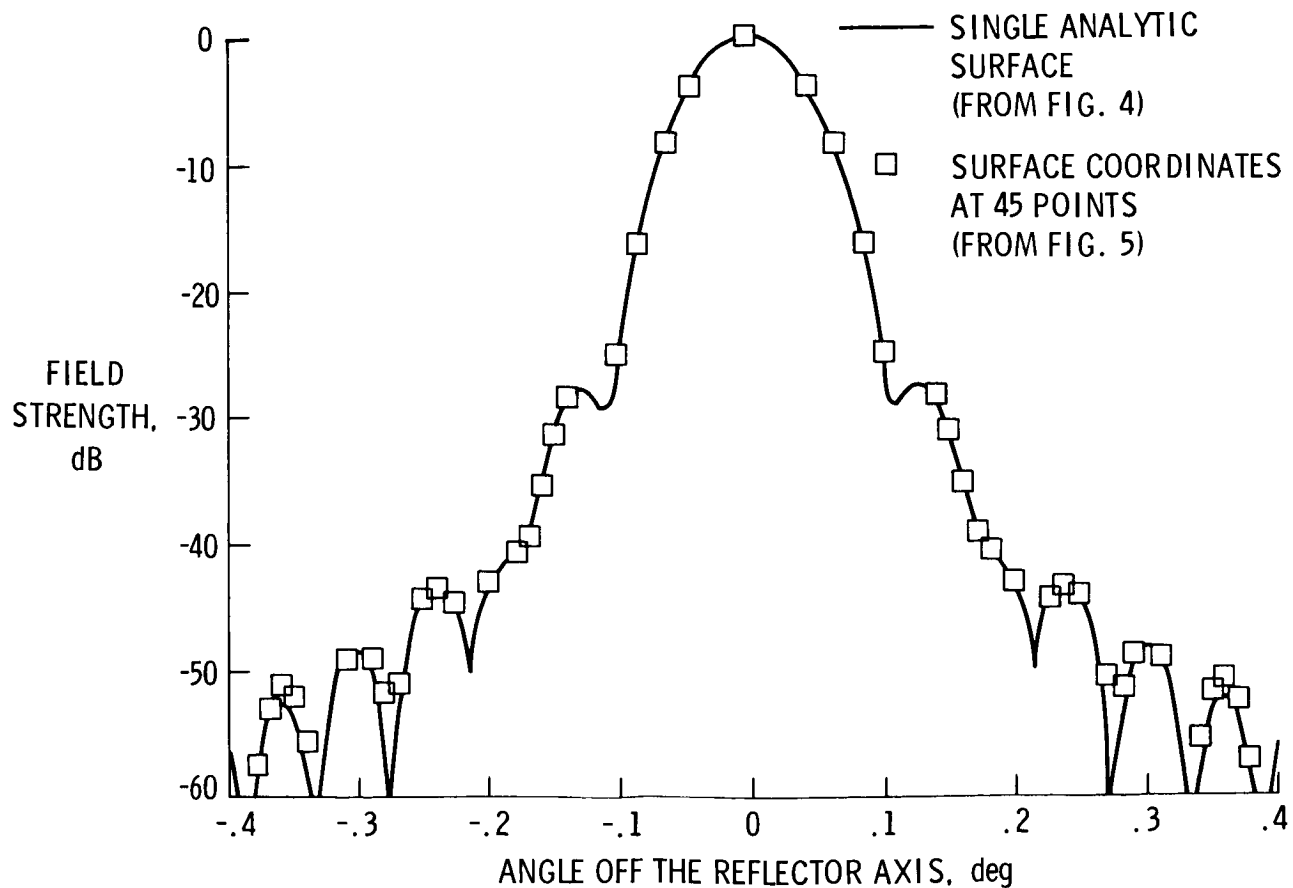
Figure 6.- Computed secondary pattern showing surface target-point data.

EFFECTS OF RANDOM DISTORTIONS ON THE SURFACE

ACCURACY OF A LARGE ANTENNA

C. R. Cockrell and Leo Staton
NASA Langley Research Center
Hampton, Virginia

SUMMARY

The effects of random reflector distortions or irregularities on a reflector's radiation pattern are discussed. The importance of such surface deviations with respect to a radiometric reflector antenna is addressed.

INTRODUCTION

Random irregularities or distortions in a reflector-antenna surface produce secondary radiation patterns that can differ significantly from those of perfectly smooth reflectors. The influence of these irregularities on the radiation pattern depends on their magnitude, shape, and location on the reflector surface. Depending on the location and magnitude of deviations from the desired pattern, it is necessary to examine these surface distortions in great detail.

DISCUSSION

When the application demands careful examination of only the main beam and immediate side lobes in the pattern, as is usually the case for communication antennas, the usual tolerance accepted for phase error is around $\lambda/16$ (corresponding to $\lambda/32$ for surface tolerance), where λ is wavelength (refs. 1 and 2). This tolerance limit is determined from gain consideration only; i.e., the allowable gain degradation dictates the tolerance to which a reflector surface must be held. For communication antennas, the other pertinent antenna-pattern characteristics such as half-power beam width and immediate side-lobe level are also generally satisfactory when the surface tolerance is on the order of $\lambda/32$.

In other applications, such as radiometry, when the absolute or the integrated values of wide-angle side lobes must be kept very low, a more severe restriction on the surface tolerance appears to be necessary. In addition, not only the magnitude of the surface deviations, but also their shape and distribution on the surface affect the amount of energy scattered in unwanted directions (wide-angle side lobes). This unwanted radiation lowers the effectiveness (i.e., the beam efficiency) of the antenna in concentrating its energy in and near the main beam. The seriousness of the change in wide-angle side-lobe level as a function of surface tolerance for a quasi-random roughness (distortion) is clearly demonstrated in reference 2 where surface tolerances of $\pm\lambda/100$ are suggested.

The effects of surface errors on the beam efficiency of a large aperture antenna can be illustrated by applying the theory developed by Ruze (ref. 3). In Ruze's work, the phase error (surface error) is chosen from a Gaussian population which is statistically uniform over the entire reflector surface such that the autocorrelation function on the phase is also of Gaussian form with a constant variance (square of the correlation length). Based on his work, the beam efficiency (assumed to be 100 percent for the unperturbed aperture) as a function of root-mean-square (rms) surface error, with the correlation length c as a parameter, is plotted in figure 1. Both rms surface error and correlation length have been normalized to wavelength. It is seen that the smaller c/λ values (i.e., more rapidly varying surfaces) give rise to more stringent requirements on surface rms error for high beam efficiency. For more slowly varying surfaces (large c/λ) the surface rms error can be relaxed and still allow relatively high beam efficiency. It should be reemphasized that these curves are based on the physically unrealizable assumption that the aperture has a beam efficiency of 100 percent in the absence of roughness. Practical application of Ruze's theory would thus require an even more severe tolerance requirement for acceptable beam efficiency.

Radiation patterns of large antennas are impossible to measure accurately on the ground because of antenna range limitations and/or ground interference. Pattern measurements in space would be very difficult, and accurate beam-efficiency calculations based on these measured patterns would be virtually impossible. Because of such deficiencies in measuring the performance of large antennas, the theoretically predicted performance is used. In order to verify predictions, the correlation interval must be greater than the operating wavelength but less than the diameter of the reflector antenna. If the predictions are based on surface point measurements, the correlation interval must contain many of these points.

The whole question of surface errors and their effects on antenna performance needs further investigation. Since a majority of the published work on surface errors is based on the early pioneering work of Ruze, his theory should be examined more carefully, particularly certain restrictive assumptions about the nature and distribution of the surface errors. Certain shortcomings in applying Ruze's statistical theory to specific antennas have already been reported. When the theory is used, along with electrical measurements, to describe the surfaces of a given antenna, it has been found (ref. 4) that the predicted surface errors exceed the mechanically measured surface errors. Thus, although useful as a guide, Ruze's theory may not be adequate for detailed calculations for narrow-beam, high-efficiency antennas. The general theoretical development is still comparatively primitive for the detailed prediction of large-antenna performance. Further theoretical work and computer simulation are required.

CONCLUSIONS

For radiometric applications, it has been shown that a more severe restriction than the usual $\lambda/32$ criterion appears to be necessary for the reflector's surface tolerance. In addition to the magnitude of the random surface deviations, their shape and distribution on the surface must be included in the analysis. The statistical treatment of random surface errors and their effects on antenna performance is an area of active research, and definitive predictions of performance must await further investigation.

REFERENCES

1. Silver, Samuel, ed.: Microwave Antenna Theory and Design. Dover Publ., Inc., 1965.

2. Dragone, C.; and Hogg, D. C.: Wide-Angle Radiation Due to Rough Phase Fronts. Bell Syst. Tech. J., vol. XLII, no. 5, Sept. 1963, pp. 2285-2296.

3. Ruze, John: Antenna Tolerance Theory - A Review. Proc. IEEE, vol. 54, no. 4, Apr. 1966, pp. 633-640.

4. Cogdell, John R.; McCue, J. J. Gerald; Kalachev, P. D.; Salomonovich, A. E.; Moiseev, I. G.; Stacey, Joseph M.; Epstein, Eugene E.; Altshuler, Eugene E.; Feix, Gerhard; Day, J. W. B.; Hein, Hvatum; Welch, William J.; and Varath, Frank T.: High Resolution Millimeter Reflector Antennas. IEEE Trans. Antennas & Propag., vol. AP-18, no. 4, July 1970, pp. 515-529.
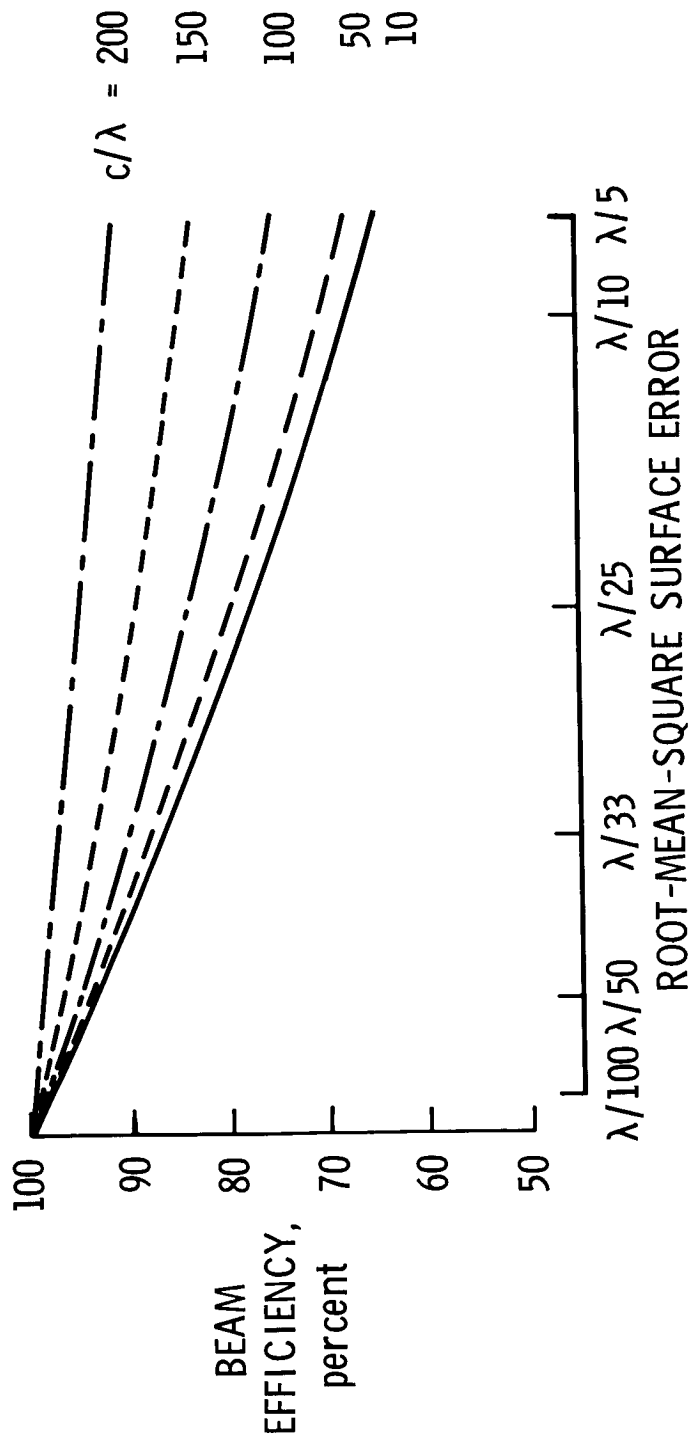
Figure 1.- Secondary-pattern beam efficiency versus rms surface error in wavelengths for diferent correlation lengths.

EFFECTS OF ANTENNA BLOCKAGE ON RADIO-FREQUENCY PERFORMANCE

OF THE MICROWAVE RADIOMETER SPACECRAFT

L. D. Sikes and T. Hower
The Harris Corporation
Melbourne, Florida

SUMMARY

Radio-frequency scaled models of the microwave-radiometer-spacecraft suspended-feed concept were tested to determine the effects of aperture blockage on the antenna radiation pattern. Contributors to the uncertainty of the test measurements were evaluated, and an estimate of the blockage effects was made for comparison with the test measurements. The gain loss budget associated with reflector performance characteristics (aperture blockage, surface reflectivity, reflector roughness, and defocus) was determined.

INTRODUCTION

Advanced antenna configurations have been studied for future communications, astronomy, and radiometer missions requiring large structural systems. Concepts, such as the suspended-feed configuration being considered for the microwave radiometer spacecraft (MRS), are subject to antenna aperture blockage. Increased side-lobe level and antenna gain reduction are possible results of aperture blockage which may adversely affect mission performance. The effects of aperture blockage on radio-frequency (RF) performance must be determined, and a performance evaluation of these particular blockage designs must be conducted to develop the proper RF/mechanical design trade-offs.

RF performance of the MRS suspended-feed configuration was investigated by fabricating and testing RF scaled models to determine the effect of aperture blockage on the radiation patterns. Detailed results of the tests are presented in reference 1 and summarized herein for the MRS configuration.

ANTENNA RANGE AND RF MODELS

RF measurements were made at the Harris Corporation antenna measurement range in Melbourne, Florida. The overall intent of the measurement program was to detect changes in the shape of the radiation patterns of the MRS antenna configuration due to aperture blockage. Anticipated pattern variations include changes in side-lobe levels, narrowing of main beam, and slight reduction in gain.

Range Description

The basic geometry of the antenna measurement range is given in figure 1. The 3.05-m-diameter test antenna is positioned atop a concrete structure elevating the reflector axis to approximately 13.7 m above ground level. The transmitting source antenna is 567 m down range and is mounted approximately 13.7 m above ground level. A 1.22-m, linearly polarized parabolic reflector antenna is used as a transmitting source. The range topography between the two towers consists of cleared, level ground.

RF Models

The model used for the MRS RF test was 3.05 m in diameter. The removable suspended feed (blockage model) consisted of two 7.37-cm-thick support booms and a simulated feed beam, 0.925 m long and 3.81 cm thick. A diagram of the RF model is presented in figure 2 and a photograph of the RF model mounted in test position is shown in figure 3. A feed support column consisting of styrofoam sheathed with fiberglass (a common lightweight feed support technique) holds the test feed horn (receiver) at the focal point of the antenna. In this way, the feed horn is mounted independently of the feed beam to eliminate feed defocusing with installation and removal of the blockage model.

Because of the extremely large diameter of the MRS reflector ($\approx$660 m), accurate down scaling of reflector diameter/wavelength and tension-control-cable diameter/wavelength ratios is not feasible. However, the primary blockage factor is the feed support boom and the geometry of the shadow it projects on the reflector aperture. This geometry is accurately modeled in the MRS RF model. No attempt is made to model the truss-type construction of the support boom, but rather it is modeled as a solid structure.

MEASUREMENT UNCERTAINTY AND BLOCKAGE ESTIMATE

Owing to the complexity of and the numerous contributors to the far-field pattern of a reflector antenna, a completely accurate analytic model is impossible to construct and, therefore, total correlation between measurements and predictions is unachievable. Additionally, instrumentation and reflection errors will further contribute to discrepancies. Therefore, it is necessary to evaluate uncertainty contributors to the test measurements and estimate blockage effects for comparison with the test measurements.

Gain Uncertainty

Gain of a test antenna is commonly measured by comparing the test antenna to a standard gain antenna. The presence of ground reflections can cause significant errors in the gain measurement. Ground reflection is a function of range geometry and is illustrated in figure 1. Energy from the source antenna reaches the antenna under test by direct (line-of-sight) radiation and by reflection from the ground or other objects. The primary reflection point occurs where incident and reflected angles with the ground are equal.

The calculation of the test antenna's gain measurement error is accomplished by assuming the worst possible phase condition for the reflected energy. The maximum (minimum) gain errors occur when the reflected energy E_R appears in (out of) phase with the direct energy E_D at the test antenna's terminals. This can be expressed as

$$E_{MAX} = E_D + E_R$$

$$E_{MIN} = E_D - E_R$$

The corresponding, antenna-gain measurement error, attributable to ground reflections in dB, is given by

$$\text{GAIN ERROR} = 20 \log \left(1 \pm \frac{E_R}{E_D}\right)$$

Magnitude of the reflected power is determined by consideration of the relative antenna gain for test and source antennas in the direction of the reflection point (fig. 1).

The expression for reflected power P_R reaching the test antenna terminals (in dB) can be written as

$$P_R = G_s + G_t/(P/dB)$$

where G_s is the relative gain, in dB, of the source antenna's pattern in the direction of the reflection angle compared to the gain in the direction of the test antenna; G_t is the relative gain of the test antenna's pattern in the direction of the reflection angle compared to the gain in the direction of the source antenna; and $1/(P/dB)$ is the relative magnitude of the reflection coefficient of the ground, assumed to be 0.

An additional ground reflection uncertainty is obtained from the feed backward radiation (side lobes of feed) towards the specular reflection point E_B. The side-lobe level from the test antenna feed was determined to be -30 dB at 7 and 10 GHz. The pertinent factors in determining antenna-gain measurement errors due to ground reflections are summarized in table I.

Additional contributors to gain uncertainty are attenuator/mixer and recorder/receiver errors, both of which were determined directly from calibration lab test curves. These performance specifications are for modern, state-of-the-art antenna measurement equipment. A list of the uncertainty contributors to gain measurements is given in table II, with the root-sum-square (rss) error.

143

Gain Loss to Aperture Blockage

Antenna gain reduction because of aperture blockage is determined by calculating the projected geometric shadows of all blockage contributors on the antenna aperture (reflector surface). The total blockage area is then modeled as center blockage and compared with the total aperture area to predict gain degradation.

Since the MRS blockage is all located behind the feed, there is no projection of this blockage and the blockage area is simply the cross-sectional area of the support columns and the feed beam. This area equals

$$A = 2(7.37 \text{ cm} \times 106.17 \text{ cm}) + (2.11 \text{ cm} \times 92.46 \text{ cm}) = 1760.04 \text{ cm}^2$$

An approximation for gain loss due to aperture blockage is given in reference 2, where

$$\text{Gain loss (9 dB)} = -20 \log (1 - a\beta^2) \simeq 8.7 \ a\beta^2$$

with $a \simeq (G_o/32)(F/D)^2$ for $a > 1.0$, β is the ratio of the area of blockage to the area of reflector, and G_o is the gain of the feed. Total gain loss because of blockage effects is

$$\text{Gain loss} = -0.21 \text{ dB at 7 GHz}$$

$$= -0.25 \text{ dB at 10 GHz}$$

Summarized in table III are the anticipated gain losses and range measurement errors. For the MRS concept, it is seen that range uncertainty (± 0.35 dB at 7 GHz and ± 0.34 dB at 10 GHz) exceeds anticipated gain reduction due to blockage effects (-0.21 dB at 7 GHz and -0.25 dB at 10 GHz).

RF MEASUREMENTS

Radio frequency tests were made on the MRS suspended-feed configuration to determine variations in the shape of the radiation patterns because of aperture blockage by the suspended-feed structure. Anticipated pattern variations such as gain reduction, main beam narrowing, and side-lobe level changes were investigated.

TEST TECHNIQUE

To determine the pattern variations, a series of three tests were conducted. Measurements were first made of the antenna without blockage to establish the base-line unblocked pattern. The suspended-feed blockage model was attached, and an identical set of pattern measurements were made to detect and define pattern variations. Then, the blockage model was removed and a second set of unblocked antenna measurements were made. Comparison of the unblocked patterns before and after the blockage

test ensured the time invariant performance of both the antenna and the range facilities. A typical comparison of two control patterns is presented in figure 4 to demonstrate the invariant behavior of the test set-up.

TEST MEASUREMENTS

The orientation of the spacecraft model for the pattern measurements is diagrammed in figure 5. Measurements (cuts) were made along horizontal and vertical planes. The horizontal plane is defined as the plane parallel to the suspended feed (electric vector E of 90°; magnetic vector H of 0°). The vertical plane is the plane perpendicular to the suspended feed (E of 0°, H of 90°). Test measurements were made at frequencies of 7 and 10 GHz. These frequencies were selected to permit use of a single, simple feed arrangement and for the sake of a practical test program. As discussed earlier, the blockage is accurately modeled (scaled to the reflector diameter) and the test data (7 and 10 GHz) can be directly correlated to the full-scale, operational MRS frequencies (1.0, 2.0, and 4.0 GHz). In addition, the blockage is modeled as a solid structure, whereas the actual support boom is a truss structure of graphite epoxy members (RF transparent). Consequently, the RF losses due to blockage are conservative.

Typical raw data plots of pattern measurements are presented in figure 6. Data are shown for the E-0° plane cut on the unblocked and blocked antenna at a frequency of 7 GHz.

The effects of aperture blockage on the RF patterns of the MRS antenna are shown in figure 7. Data are presented for both 7 and 10 GHz and for RF pattern cuts of E-0°, E-90°, H-0°, and H-90°.

Examination of patterns in figure 7 reveals the most significant impact of the aperture blockage is in the side-lobe structure. For pattern cuts parallel to the blockage strut (E-90° and H-0° cuts), an average -1.4 dB first-side-lobe level reduction was measured. In the perpendicular plane (E-0° and H-90° cuts), an average 2.8 dB first-side-lobe increase was measured. Effect of spar blockage was predicted using a geometric optics/FFT program in which the shape of the spar is superimposed upon the fast Fourier transform (FFT) grid. Comparison of measured and predicted data for the first-side-lobe level is shown in table IV. Measured and predicted relative voltage levels are shown and, in general, excellent agreement was achieved.

RF Analysis

Because of the simple geometry of the MRS suspended-feed structure, analysis of its blockage effects is simple. Since the suspended-feed structure is large compared to wavelength, the IFR factor equals unity and the aperture blockage is simply the geometric cross section of the suspended-feed structure. Also, since the feed does not directly illuminate the spar, there is no shadow projection onto the reflector surface.

Figure 8 is a diagram of projected blockage and blockage distribution in vertical and horizontal planes. Figures 9 and 10 are diagrams of the transformed blocked and unblocked distributions for the vertical and horizontal planes. No attempt was made to transfer the usual shape of the vertical and horizontal blockage distributions in figure 8, but rather a uniform distribution is assumed for the horizontal plane and a rectangular spike for the vertical plane.

In the horizontal plane, blockage effects are minor, decreasing main-beam gain by approximately 0.25 dB and each side lobe by approximately 0.5 dB. In the vertical plane, blockage effects are much larger. Since the blockage aperture distribution is quite narrow (approx. 1/40 of reflector diam), its transformed far-field pattern is very broad. As shown in figure 10, the first side-lobe level increases by approximately 3 dB, the second decreases by 6 dB, and the third increases by 5 dB. Main beam width is narrowed slightly.

MRS Prediction/Measurement Comparisons

Table V is a summary of the comparison between predicted and measured variations in the MRS far-field patterns. As mentioned previously, the vertical plane corresponds to E-0° and H-90° pattern measurement cuts and the horizontal plane corresponds to E-90° and H-0° cuts.

GAIN LOSS BUDGET

Estimated gain losses for the MRS 750-m antenna are presented in table VI. Only those components associated with reflector performance are presented. They include

- Aperture blockage

- Surface reflectivity

- Reflector roughness

- Defocus

The effect of aperture blockage by the support columns and feed beam has received considerable discussion in preceding sections and will not be analyzed here. However, specific detail which describes the loss mechanisms of the remaining reflector surface/structural effects will be given in support of the loss numbers provided.

Surface Reflectivity

Gold-plated molybdenum mesh is a strong, highly reflective antenna material, and its reflective characteristics have undergone considerable reflectivity measurements. The mesh geometry has been thoroughly investigated and a reflection-coefficient analytical model has been developed from the geometrical data. The correlation between measured and predicted reflection has been quite encouraging with the result that the mesh-reflection-coefficient analytical model has been adopted as the standard for analyzing mesh characteristics.

Reflector Roughness

The random roughness of the mesh reflector surface due to manufacturing uncertainties, surface pillowing, and thermal variations can be estimated and accounted for in the gain loss calculations. The root-sum-square (rss) of the roughness con-

tributors is used to calculate the root mean square (rms) roughness. This rms number is used in the following equation to compute the gain loss due to roughness:

$$\text{Roughness loss (dB)} = 10 \log \left[e^{-(4\pi k\sigma/\lambda)^2} \right]$$

where k is a number with range $0 < k < 1$. The value of k is a function of reflector focal-length-to-diameter ratio (F/D), where $F/D \equiv \infty$ gives $k = 1.0$. The parameter value $\sigma/\lambda \equiv$ rms roughness of the surface with respect to a free-space wavelength.

Defocus

The gain loss because of reflector-system axial defocus is computed by the following expression:

$$\text{Defocus loss} = 10 \log |A + jB|$$

$$A = 1 + (P/\beta^2)(1 + \cos \beta) + (P/\beta) \sin \beta$$

$$B = (P/\beta)(1 - \cos \beta) + 1 - (P/\beta^2)(\beta - \sin \beta)$$

where

$$\beta = (4\pi\Delta F/\lambda) \sin^2 \gamma$$

$$\gamma = \text{Arctan} \left[(1/4)(F/D) \right]$$

$$P = k(1 - r^2) \quad \text{the illumination function}$$

$\Delta F/\lambda$ is the defocus with respect to a wavelength

CONCLUSIONS

Radio-frequency (RF) performance degradation resulting from feed-support structure aperture was measured on scaled RF models of the microwave radiometer spacecraft configuration. Based on -6 dB edge illumination taper, the following conclusions were determined:

1. Gain degradation because of aperture blockage is approximately 0.2 dB.

2. In the plane perpendicular to the support boom, side-lobe effects are greatest. A -20-dB first side lobe is increased approximately 3.0 dB.

3. In the plane parallel to the support boom, near-in side-lobe levels are decreased by approximately 0.5 dB.

4. Variations in width of the main beam are insignificant.

REFERENCES

1. Harris Corp.: Assessment of Surface Accuracy and Aperture Blockage of Deployable Reflector Concepts. NASA CR-165783, 1980.

2. Rusch, W. V. T.; and Potter, P. D.: Analysis of Reflector Antennas. Academic Press, Inc., 1970.

TABLE I.- REFLECTION-ERROR SUMMARY GAIN UNCERTAINTY

	7.0 GHz	10.0 GHz
G_s, dB	12	15
G_t, dB	26	26
Total reflection isolation, dB	38	41
E_R	±0.0125	+0.0089
$E_{BLOCKAGE}$	±.0079	±.0056
E_R Total	±0.0204	+0.0145
Gain uncertainty due to range reflections, dB	±0.18	±0.13

TABLE II.- GAIN UNCERTAINTY CONTRIBUTORS

Contributor	7.0 GHz	10.0 GHz
Reference standard, dB	±0.25	±0.25
Range reflections, dB	±.18	±.13
Attenuator/mixer error, dB	±.10	±.10
Recorder/receiver error, dB	±.15	±.15
rss error, dB	±.35	±.34

TABLE III.- ANTICIPATED GAIN DEGRADATION AND MEASUREMENT UNCERTAINTY

	7.0 GHz	10.0 GHz
Total gain measurement uncertainty, dB	±0.35	±0.34
Anticipated gain reduction of MRS, dB	-.21	-.25

TABLE IV.- MRS GAIN LOSS BUDGET

Contributor	Frequency, GHz		
	1.0	2.0	5.0
Support boom blockage,[a] dB	-0.21	-0.21	-0.21
Surface reflectivity,[b] dB	-.003	-.001	-.07
Reflector roughness,[c] dB	-1.11	-4.46	
Defocus,[d] dB	-.1	-.38	-2.5
Total loss, dB	-1.423	-5.051	-2.78

[a]Assumes uniform aperture illumination.
[b]Assumes 14 openings per 2.54-cm mesh.
[c]rms roughness = 1.45 cm.
[d]Defocus = 12.7 cm.

TABLE V.- MRS MEASUREMENT/PREDICTION COMPARISONS

	Measured	Predicted
Variation in width of main beam	Insignificant	Insignificant
First side-lobe levels, dB Vertical plane Horizontal plane	+2.9 (avg.) -.87 (avg.)	+3.0 -.50
Second side-lobe levels, dB Vertical plane Horizontal plane	[a]-2.0 [a]-1.0	-6.0 -.50
Third side-lobe level, dB Vertical plane Horizontal plane	[a]+2.5 [a]+1.4	+5.0 -.5

[a]Changes in side-lobe structure make precise comparisons difficult.

TABLE VI.- MRS SIDE-LOBE ANALYSIS PREDICTED VS MEASURED DATA

Antenna model orientation	Measurement frequency, GHz	Without support, first SLL,[a] dB		With booms, first SLL,[a] dB		Relative blockage, Voltage - Measured, volts		Relative blockage, Voltage - Predicted, volts
		Left	Right	Left	Right	Left	Right	
E-0°	7.0	20.5	18.5	16.0	16.25	0.107	0.05	0.06
	10.0	21.0	20.0	19.0	17.5	.03	.05	.06
						Avg.	.059	
E-90°	7.0	20.5	19.0	21.5	21.0	-0.01	-0.01	-0.005
	10.0	20.5	20.5	20.0	21.5	-.005	-.01	-.005
						Avg.	-.008	
H-0°	7.0	22.5	21.0	23.5	22.0	-0.008	-0.010	-0.005
	10.0	20.0	20.5	22.0	24.0	-.025	-.02	-.005
						Avg.	.015	
H-90°	7.0	18.00	19.25	15.5	16.25	0.042	0.045	0.06
	10.0	18.25	18.25	14.75	16.25	.061	.032	.06
						Avg.	.045	

[a]SLL - side-lobe level.

151
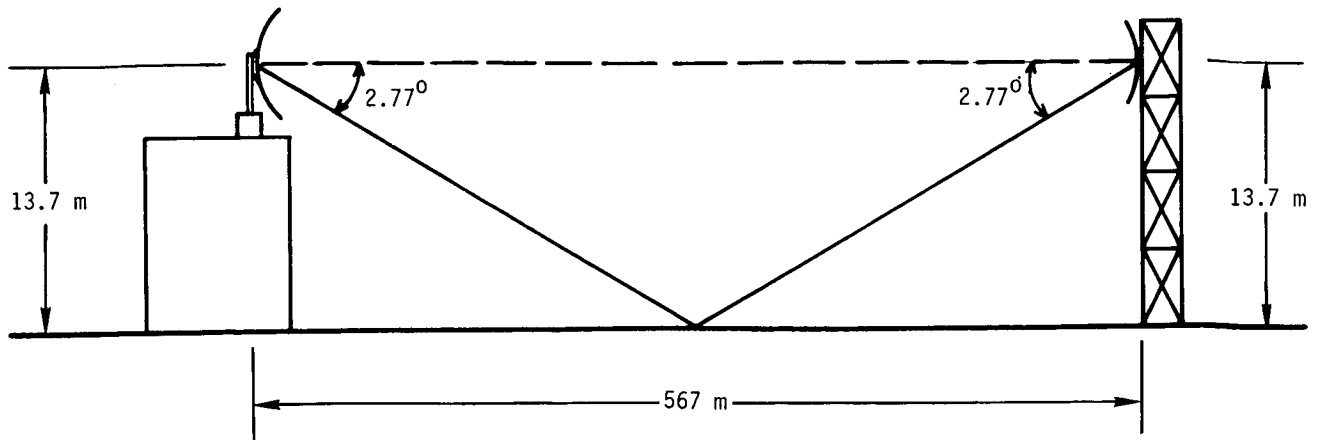
Figure 1.- Antenna range.
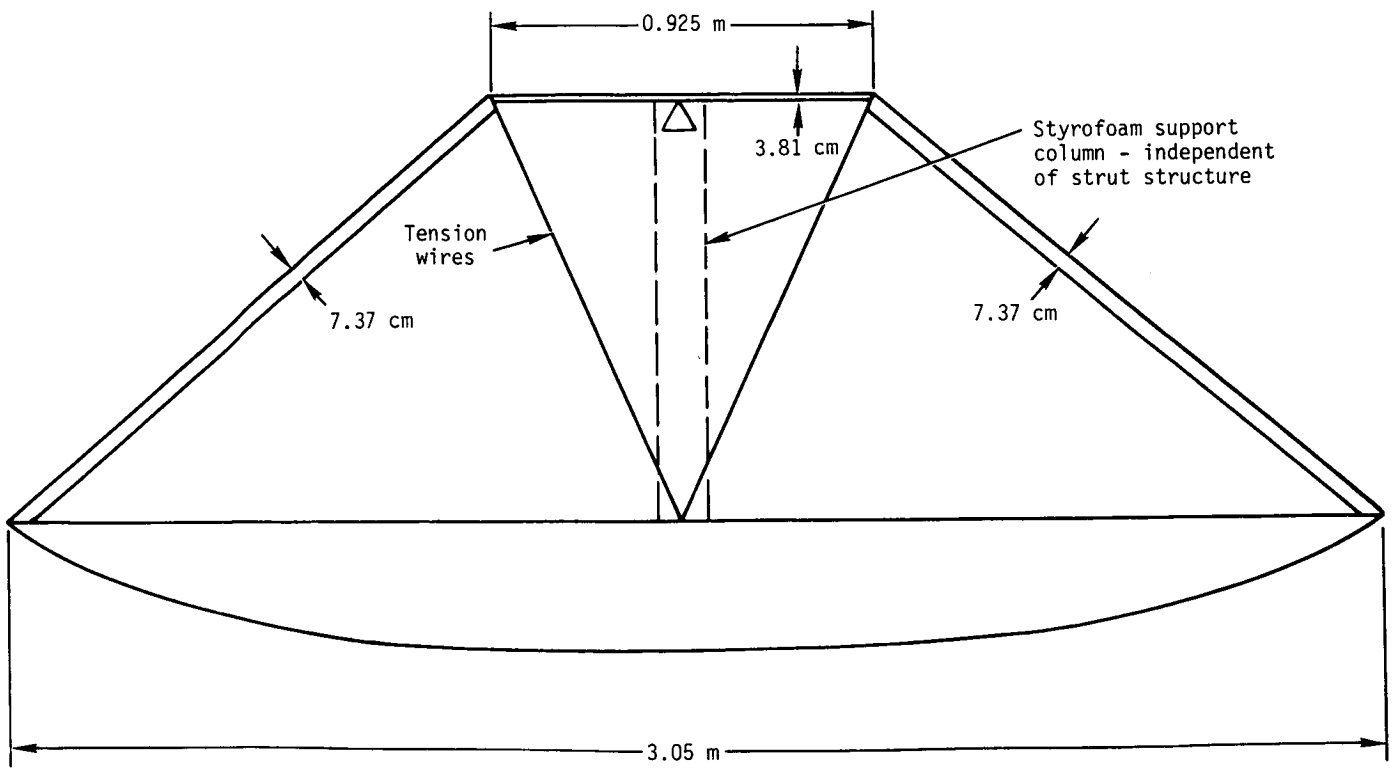
Figure 2.- MRS test model dimensions.
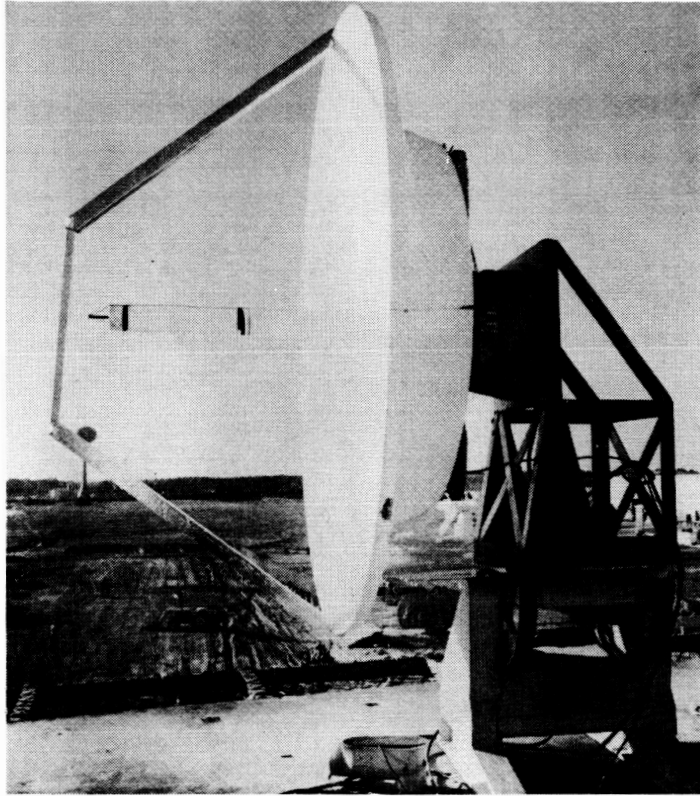
Figure 3.- MRS test model.
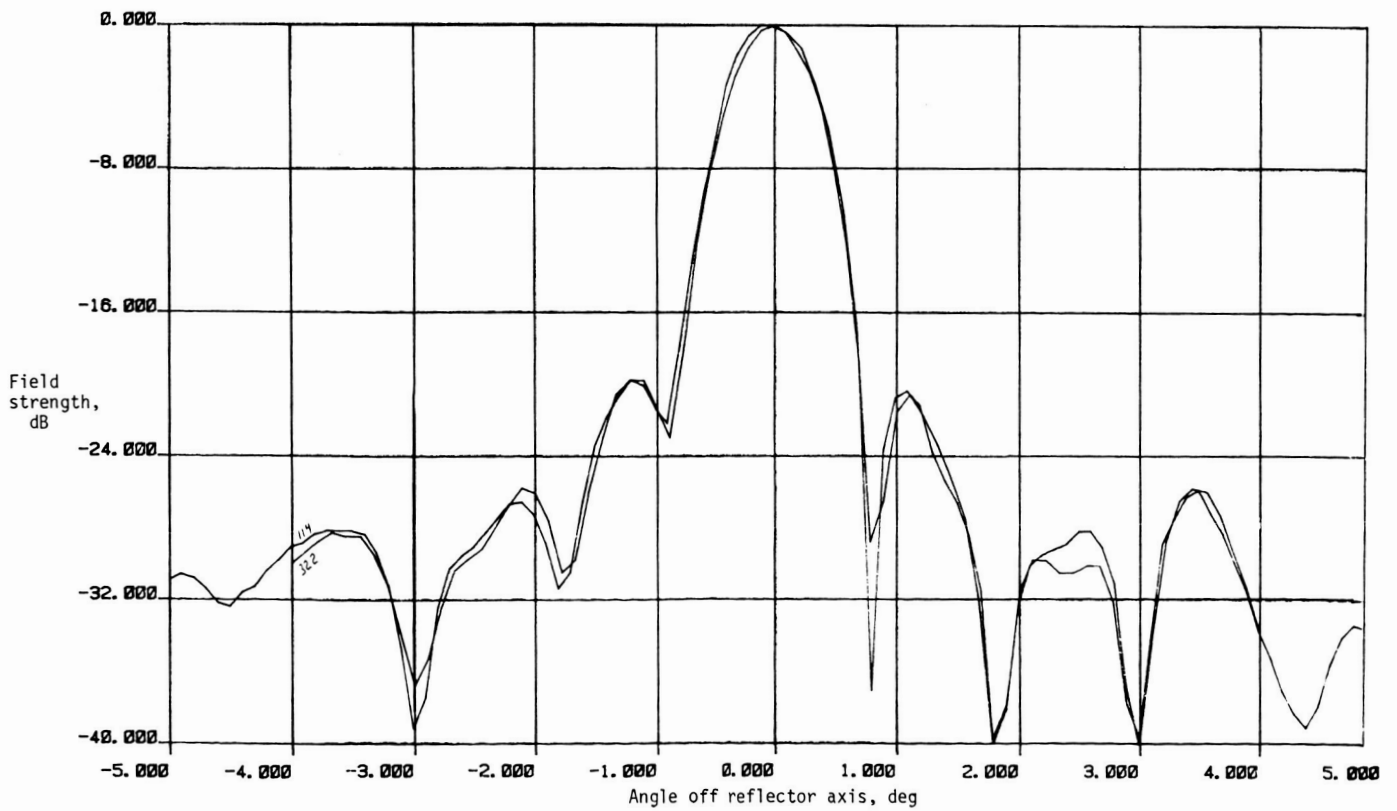
Figure 4.- Control patterns measured before and after blockage measurements.
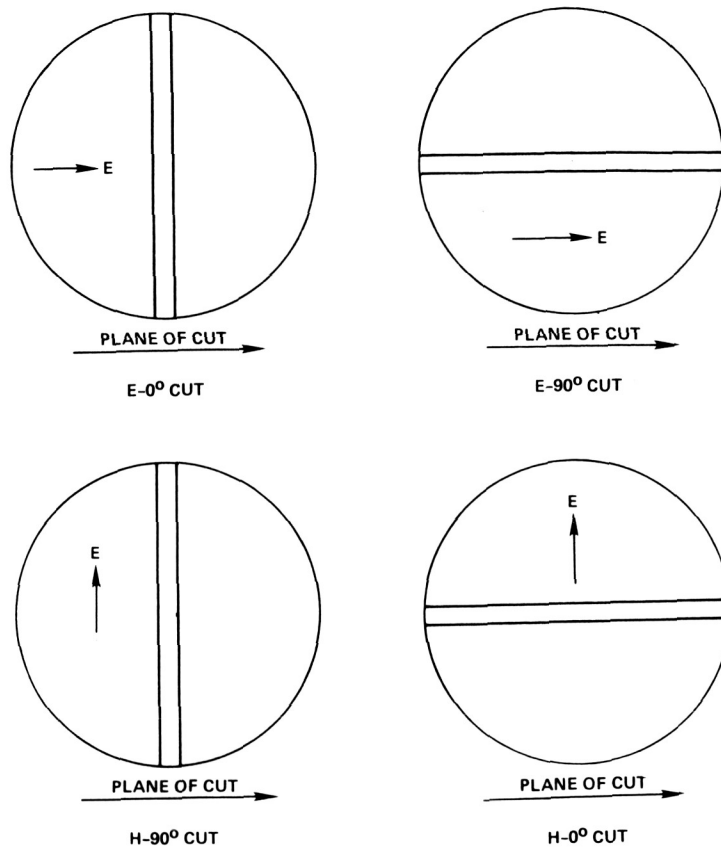
Figure 5.- MRS measurement orientations.
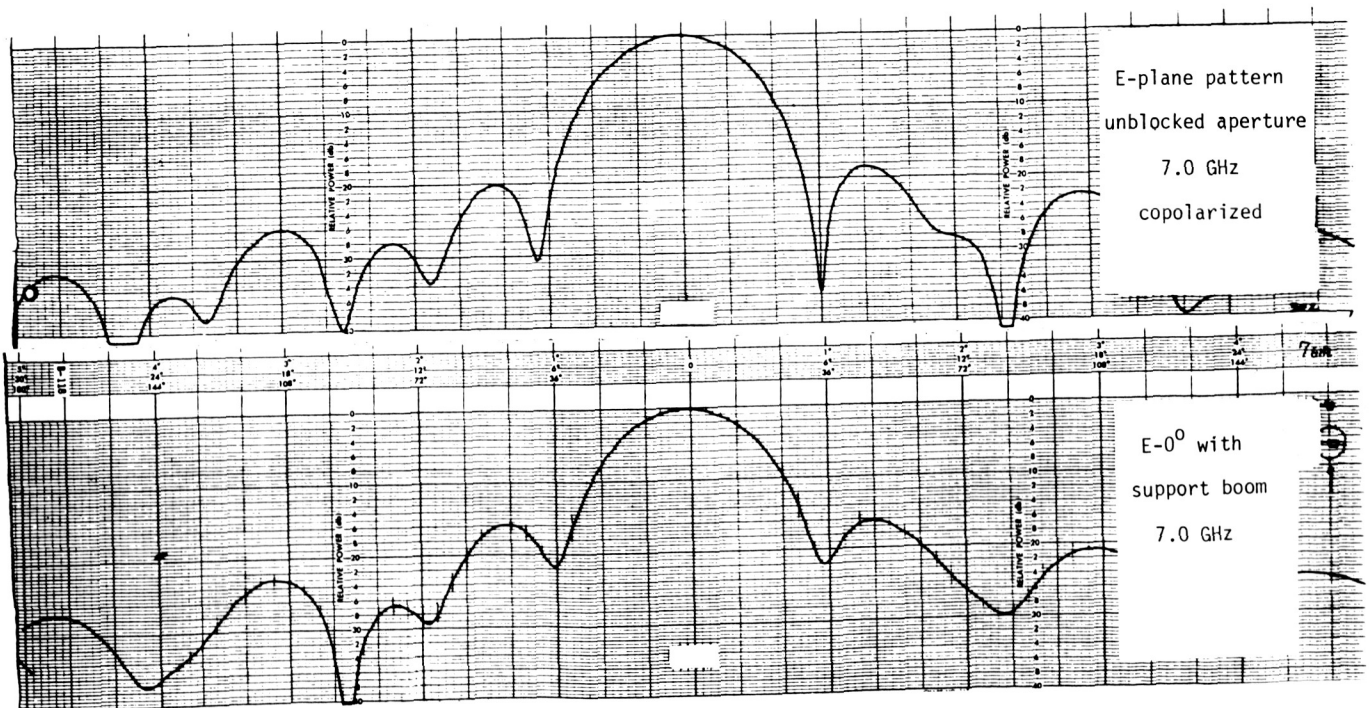
Figure 6.- Typical RF pattern measurements.

154
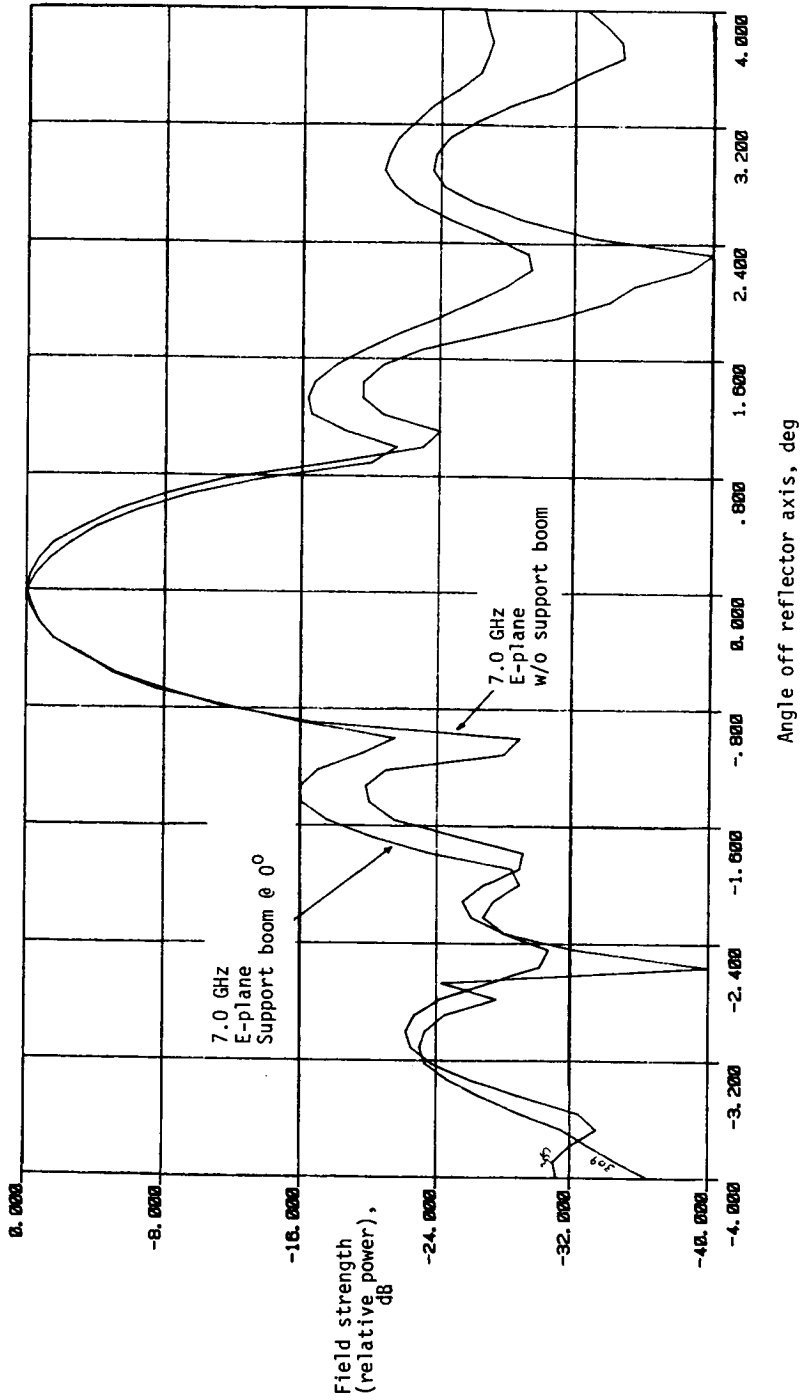
(a) E-plane, 7.0 GHz, support boom at 0°.

Figure 7.- Test measurements.
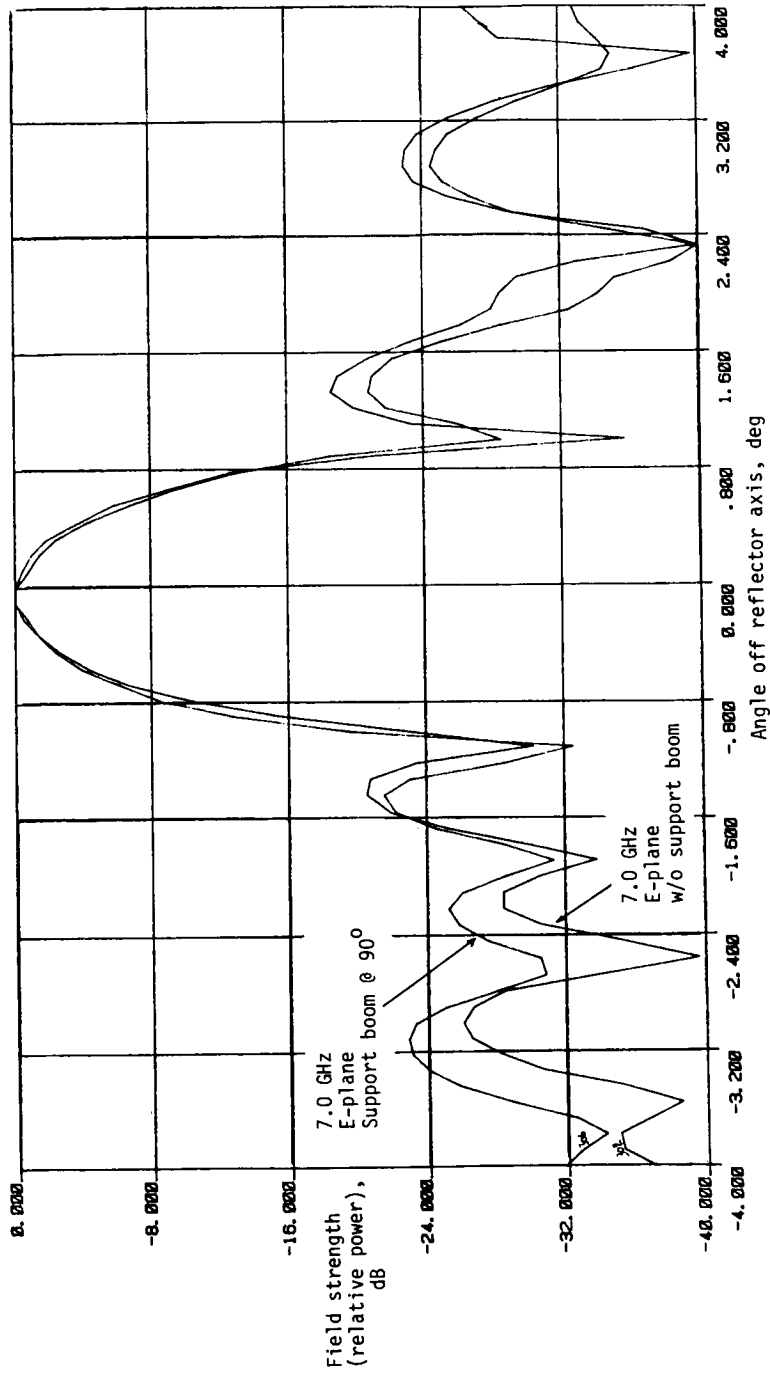
(b) E-plane, 7.0 GHz, support boom at 90°.
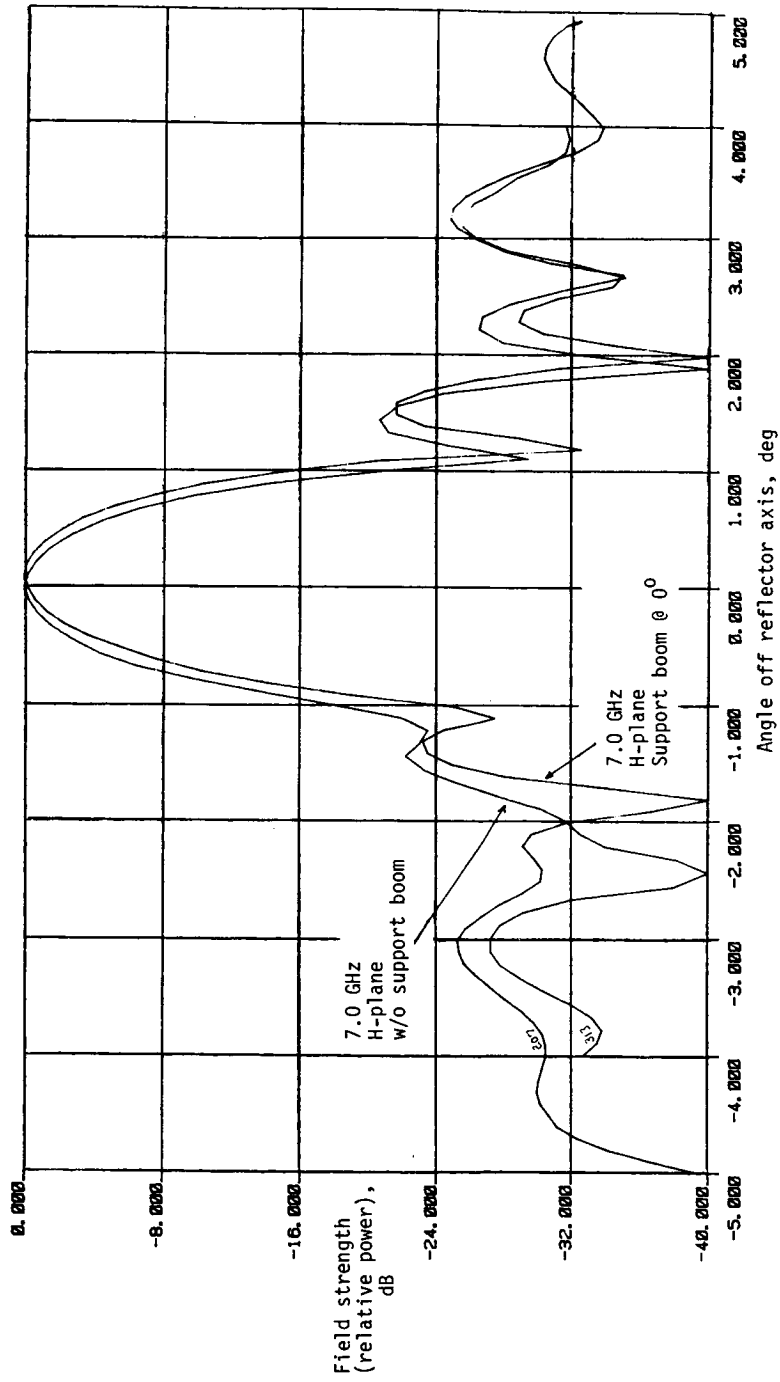
Figure 7.- Continued.

(c) H-plane, 7.0 GHz, support boom at 0°.
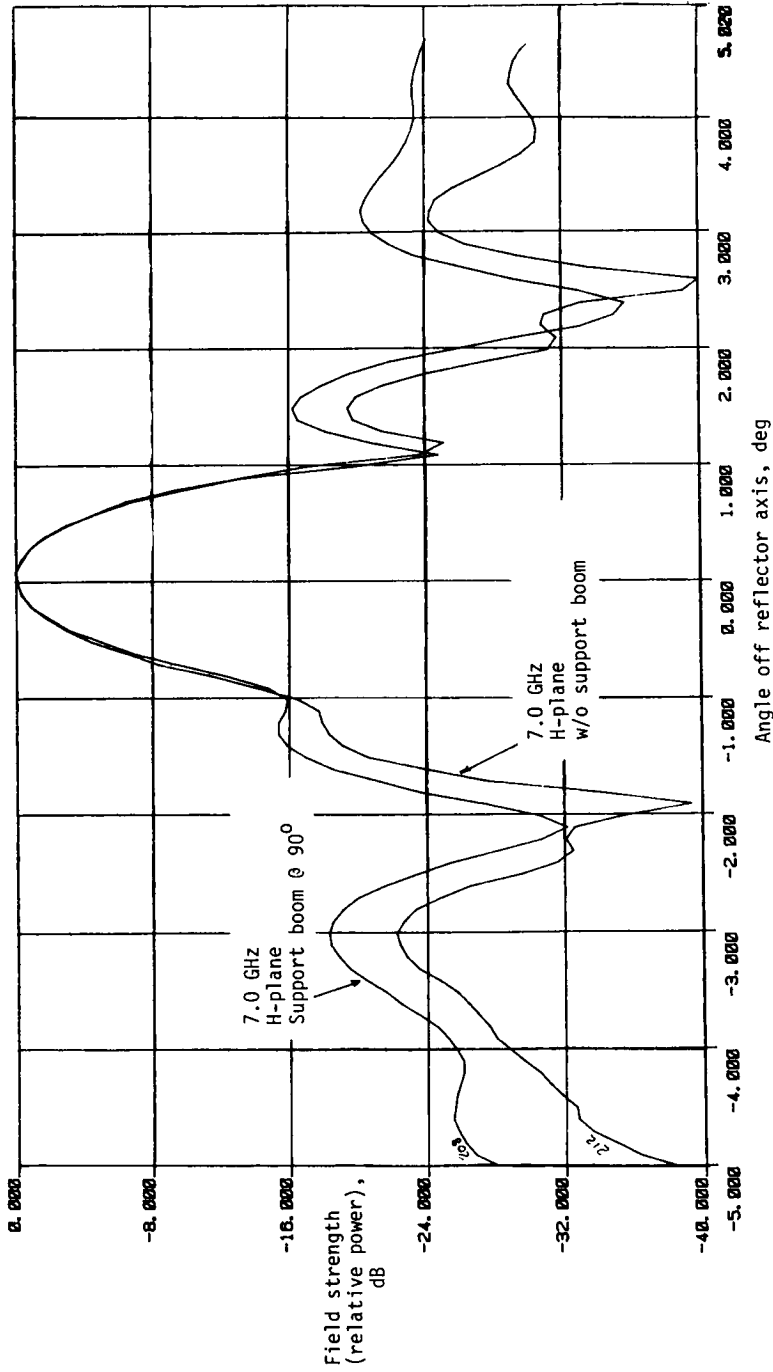
Figure 7.- Continued.

(d) H-plane, 7.0 GHz, support boom at 90°.
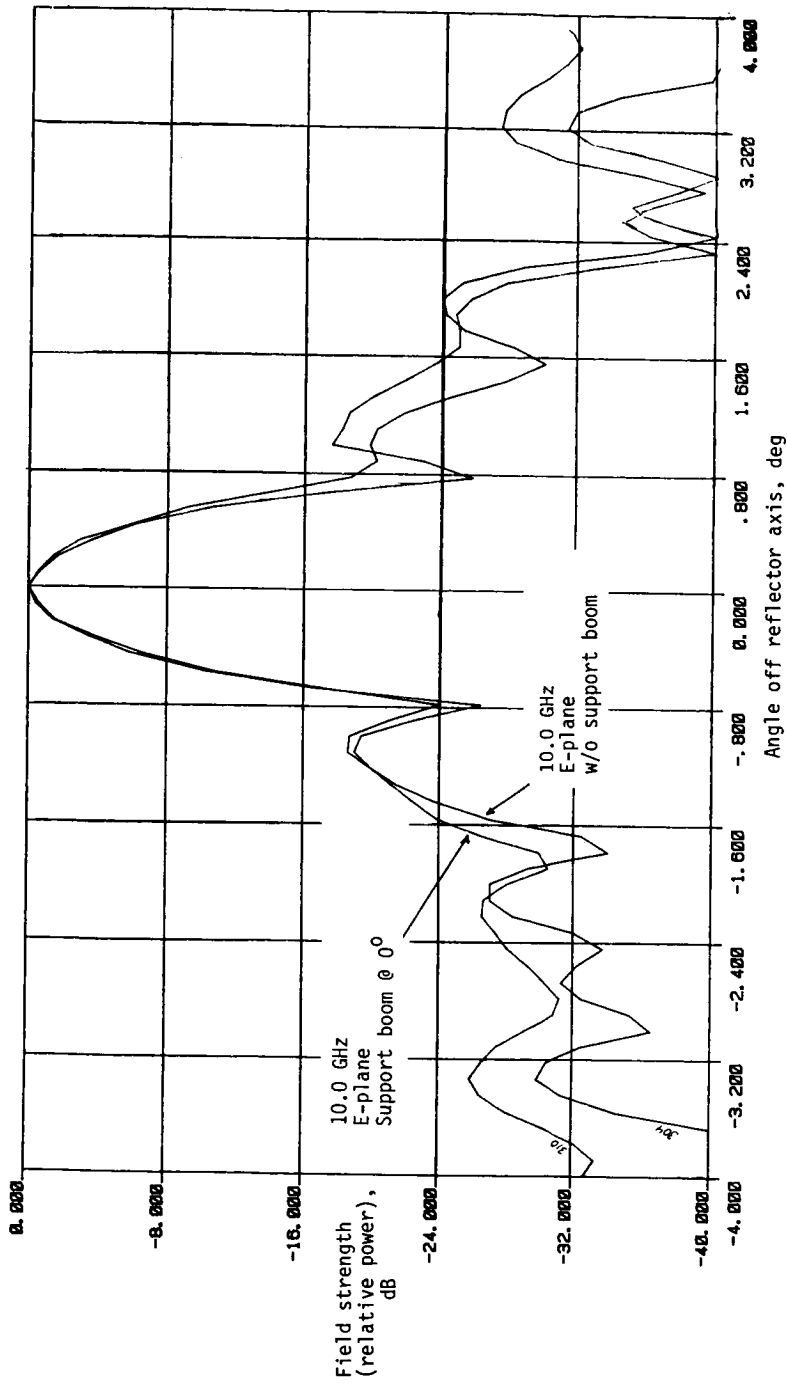
Figure 7.- Continued.

(e) E-plane, 10.0 GHz, support boom at 0°.
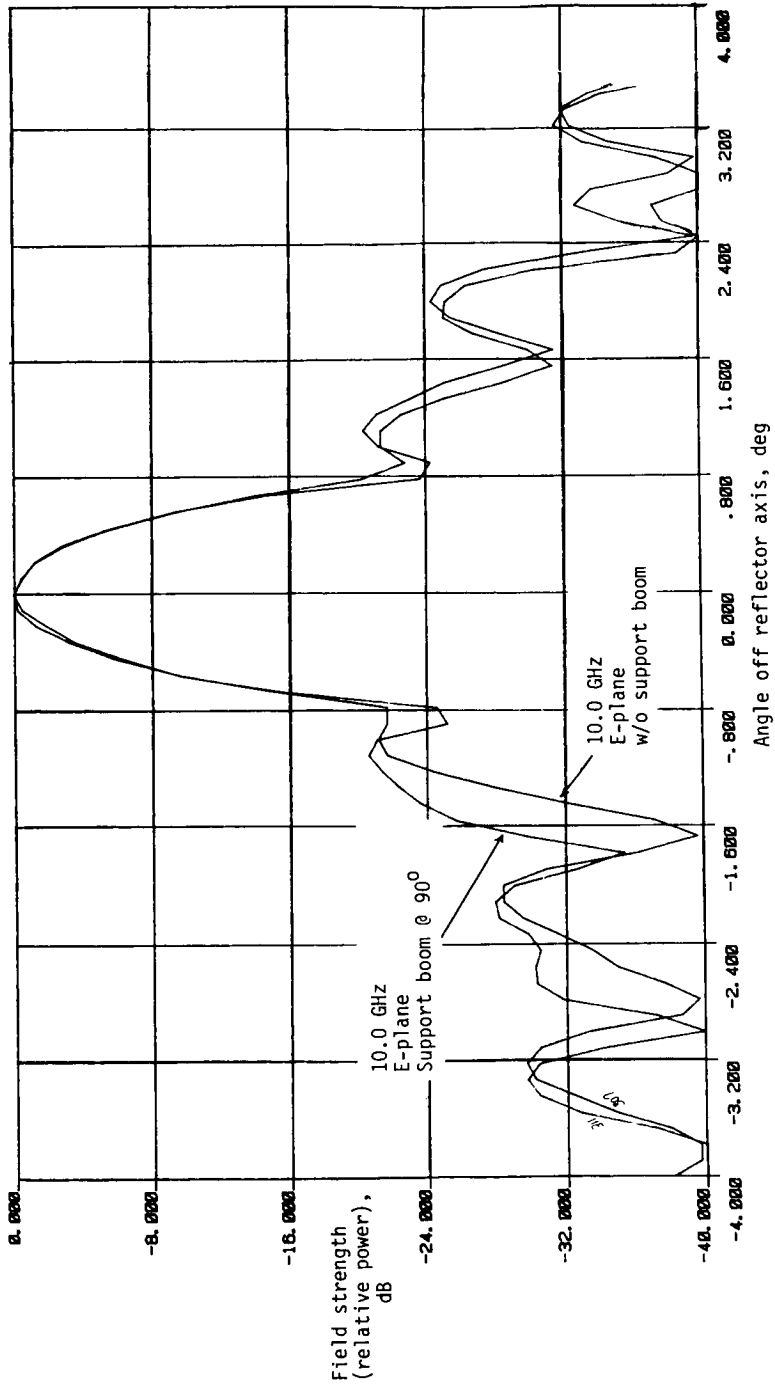
Figure 7.- Continued.

(f) E-plane, 10.0 GHz, support boom at 90°.
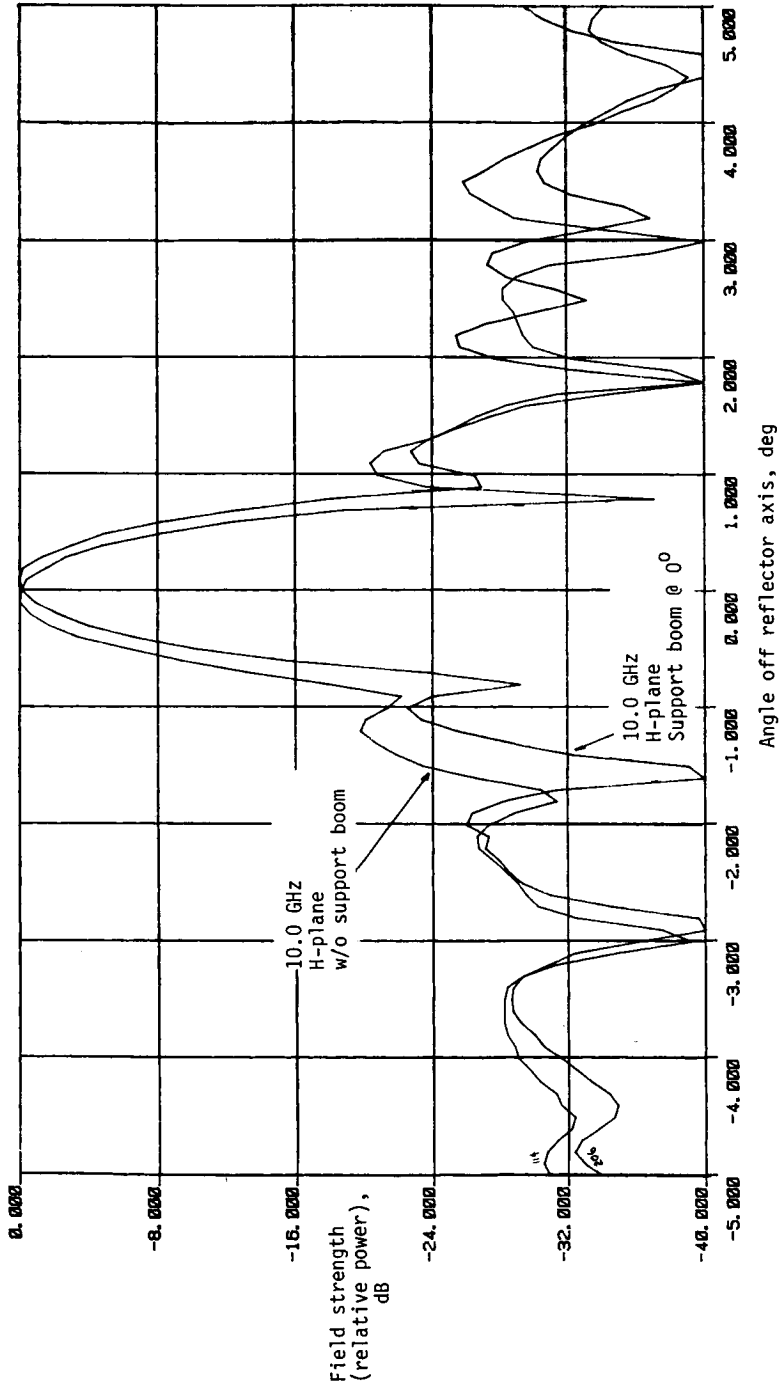
Figure 7.- Continued.

(g) H-plane, 10.0 GHz, support boom at 0°.
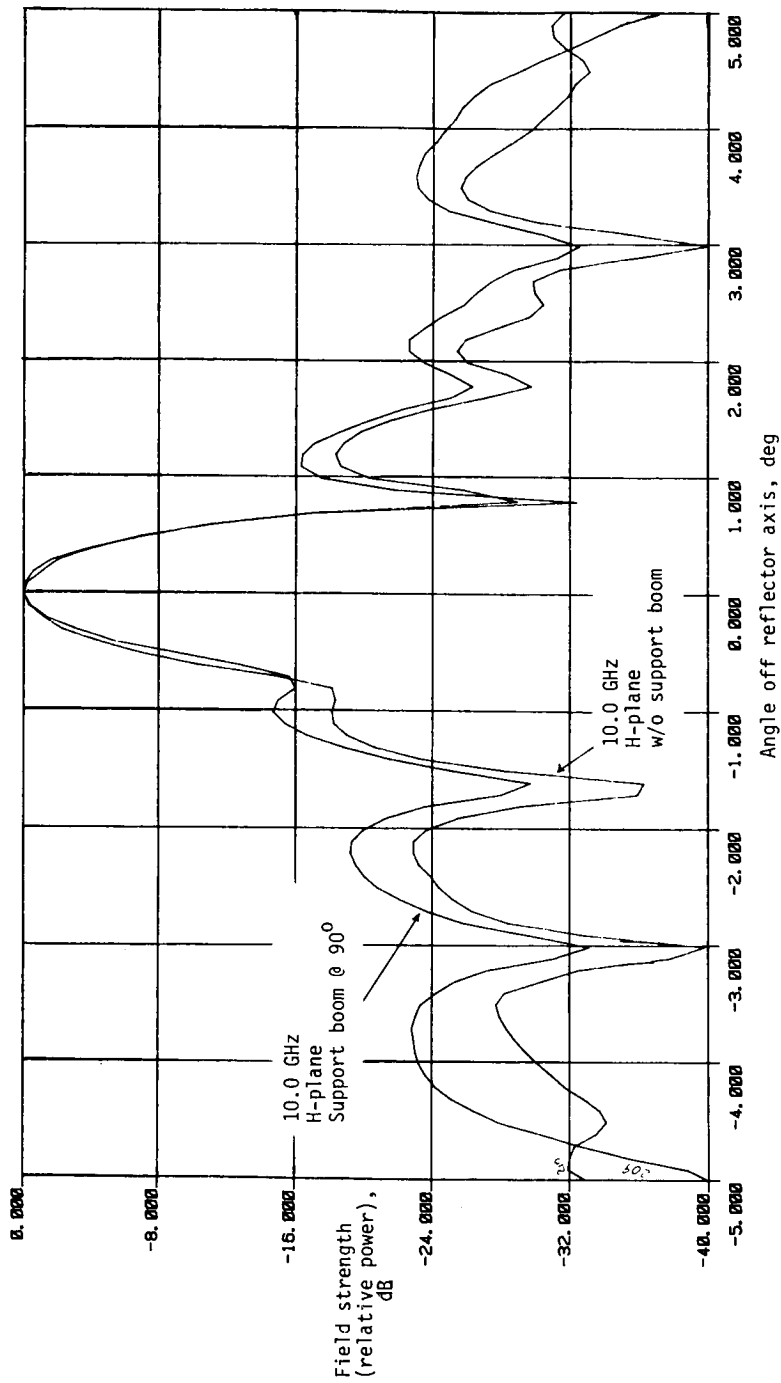
Figure 7.- Continued.

(h) H-plane, 10.0 GHz, support boom at 90°.

Figure 7.- Concluded.

Vertical blockage
distribution

Blockage distribution
w/o support boom

Blockage distribution
w/support boom

Horizontal blockage distribution
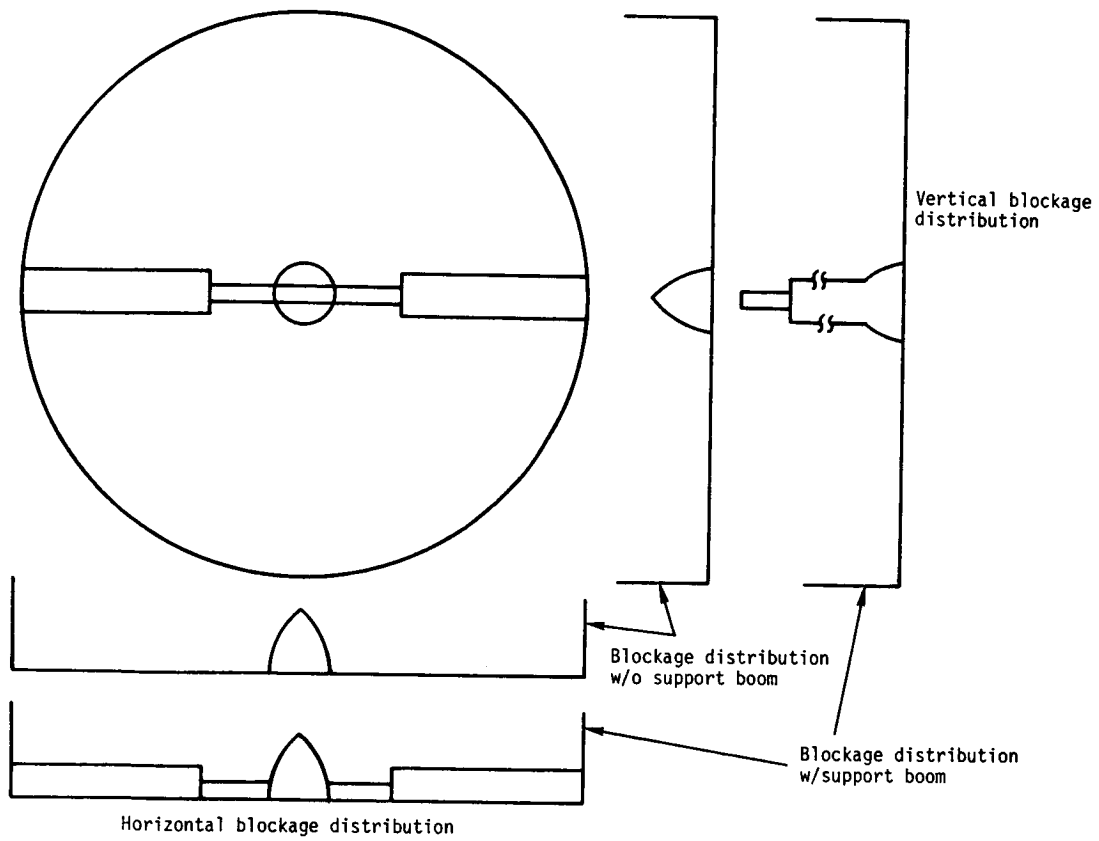
Figure 8.- Projected blockage distributions.
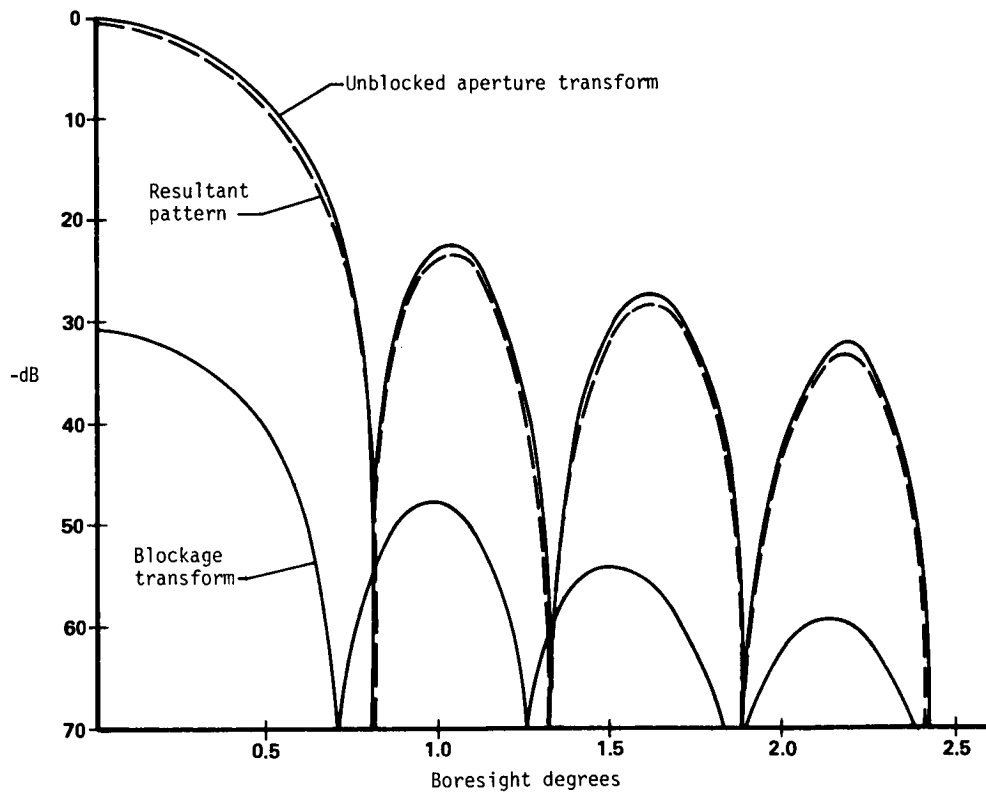
Figure 9.- MRS blockage effects, horizontal plane.
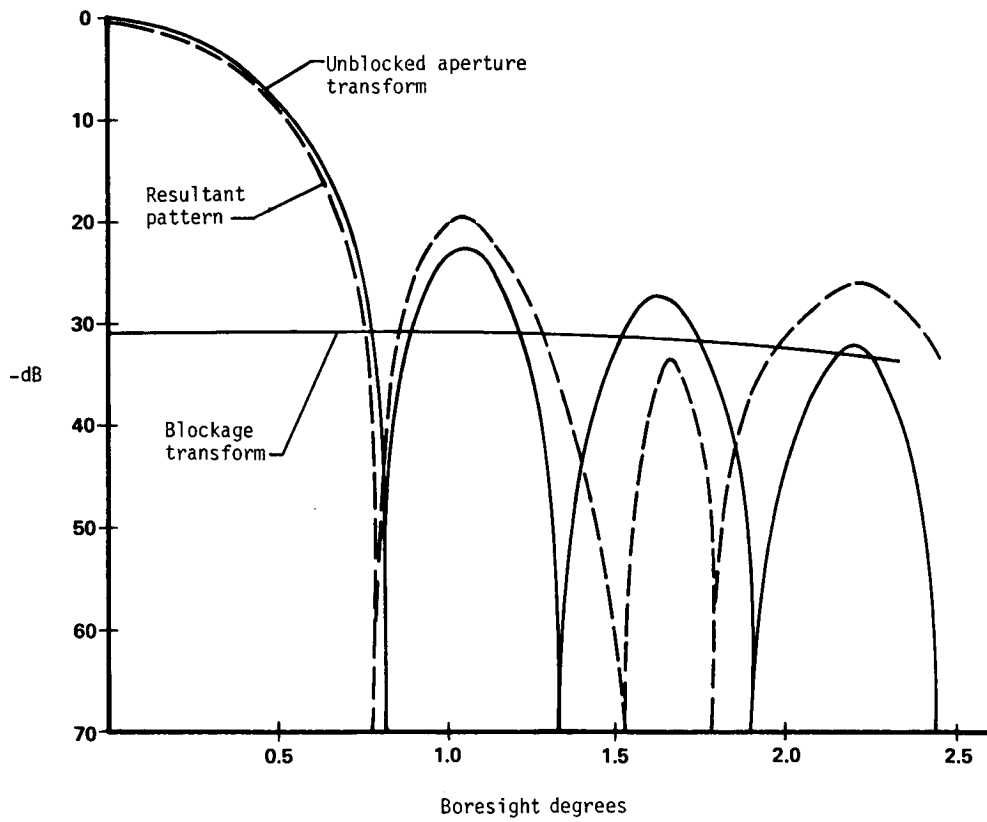
Figure 10.- MRS blockage effects, elevation plane.

PART IV

CONTROL CONCEPTS

ADAPTIVE CONTROL SYSTEM FOR LARGE ANNULAR

MOMENTUM CONTROL DEVICE

Raymond C. Montgomery
NASA Langley Research Center
Hampton, Virginia

and

C. Richard Johnson, Jr.
Virginia Polytechnic Institute and State University
Blacksburg, Virginia

SUMMARY

A dual-momentum vector control concept, consisting of two counterrotating rings (each designated as an annular momentum control device), has been studied for pointing and slewing control of large spacecraft. In a disturbance-free space environment, the concept provides for three-axis pointing and slewing capabilities while requiring no expendables. The approach utilizes two large-diameter counterrotating rings or wheels suspended magnetically in many race supports distributed around the antenna structure. When the magnets are energized, attracting the two wheels, the resulting gyroscopic torque produces a rate along the appropriate axis. Roll control is provided by alternating the relative rotational velocity of the two wheels. Wheels with diameters of 500 to 800 m and with sufficient momentum storage capability require rims only a few centimeters thick. The wheels are extremely flexible; therefore, it is necessary to account for the distributed nature of the rings in the design of the bearing controllers. Also, ring behavior is unpredictably sensitive to ring temperature, spin rate, manufacturing imperfections, and other variables. This paper deals with an adaptive control system designed to handle these problems.

INTRODUCTION

Large space antennas will require establishing and maintaining a fixed attitude over long periods of time. Reaction control systems are unsuitable for this application because of the severe logistics problem associated with fuel resupply. Furthermore, many large space structures are inherently flexible, and the motions set up by the on-off activity of reaction control systems result in acute structural dynamic problems. An approach which provides the necessary control forces while avoiding these problems is to magnetically couple a pair of very large, flexible counterrotating rings to the spacecraft that is to be controlled. The rings nominally spin in the plane of a large area; this spin makes the dual-momentum vector device particularly suitable for large-area structures. The dual-momentum vector control concept, shown schematically in figure 1, provides three-axis pointing and slewing capabilities. The resupply problem is largely alleviated since the primary requirement is for electric power which can be obtained from a solar cell array in combination with long lifetime batteries. Reaction jets required for desaturation of the rings after

long periods of use would involve small quantities of fuel. A noncontacting magnetic or electrostatic suspension provides for control smoothness not obtainable from reaction jets.

An early analysis of this dual-momentum vector control concept for attitude control about all axes was presented in reference 1. The concept involves independently orienting the spin axes of two identical wheels. The wheels nominally have a zero net angular momentum. This is in contrast to the control moment gyro concept which uses a single wheel or a cluster of nominally orthogonal wheels to achieve attitude control. The dual-momentum vector control process can be visualized in the following way. (See fig. 2.) Suppose that the spin axes of the two identical wheels are aligned and that the wheels are spinning with equal but opposite spin rate as shown in figure 2(a). The net angular momentum of the pair is zero, and if they are constrained (by bearings and a gimbal assembly) to maintain the same net angular momentum condition, any applied external moment will cause the pair to tumble as if the wheels had no individual momentum. If the momentum vectors are skewed by some mechanical means without applying any external momentum as in figure 2(b), then, as conservation of momentum demands, there exists a momentum component, $h_c = -h_1 - h_2$, called the control momentum. Therefore, the assembly (the wheels, suspension, and spacecraft) must rotate with an angular velocity ω_c. A large maneuver may be accomplished by skewing the momentum vector about an appropriate axis to create a control angular velocity. When the assembly has rotated to the desired orientation, the momentum vector is unskewed to stop the rotation as shown in figure 2(c).

Large-area space systems are expected to be relatively flexible and have large inertias. For the application of a dual-momentum vector control device to a large antenna (e.g., 800 m diameter), the wheel momentum required is huge, and careful design of the wheels must be made to optimize the ratio of momentum to mass and lower the ultimate cost of the device. Concentrating the mass of the wheels at the periphery leads to the most efficient ratio of momentum to mass (ref. 2). Also, it is desirable to maximize the speed of rotation of the wheels to maximize momentum storage. The speed is limited by allowable material stresses but is still quite large (about 400 m/sec); therefore, the use of mechanical bearings is inappropriate. Hence, the wheels should be rings as large as the spacecraft can accommodate and should be attached to the spacecraft with a suspension that is noncontacting. For space control applications, the first noncontacting annular device was the annular momentum control device (AMCD) described in reference 2. The device is a spinning ring that is magnetically suspended. In concept, the ring can be of arbitrary size. However, at this time, the technology has been studied only for rings of about 2 m in diameter. Very large rings of 800 m in diameter (e.g., needed for controlling large platforms) behave like lariats and problems exist in stabilizing the ring during spin-up and during spacecraft maneuvers. Also, problems exist in the a priori modeling of the dynamics of a spinning ring. They are the uncertain influences of spin rate, temperature, unknown material characteristics, and a host of other factors related to the dynamics of the ring. For these reasons, an adaptive control system is required for ring stabilization and maneuvering. An original adaptive control methodology for distributed parameter systems is presented and applied to AMCD stabilization in reference 3.

ADAPTIVE STABILIZATION OF A SPINNING RING

The adaptive control methodology presented in reference 3 is followed in this paper for the development of an adaptive stabilizer for the large AMCD ring of the microwave radiometer spacecraft.

The preactivation analysis steps are as follows:

(1) Because of the spatial repetition caused by ring closure, the linearized out-of-plane deformation w of a spinning, flexible ring can be decomposed as a function of s, a variable describing the particles of the ring, and t, time, using an infinite sine/cosine series.

(2) If the higher spatial frequency deformations are assumed to exhibit lower amplitudes due to the resilience of the ring material, this frequency series can be truncated with arbitrary accuracy at a finite number of modes N_{MS} (number of modes simulated) so that

$$w(s,t) = W_1(t) + \sum_{j=1}^{N_{MS}} [W_{j+1}(t) \cos (js) + W_{j+NMS+1}(t) \sin (js)] \tag{1}$$

where W_j represents the modal deflection amplitudes and s the angular location in a ring particle reference frame. Note that W_1 corresponds to the translational mode in figure 3, W_2 and W_{NMS+2} to the rotational mode, and W_3 and W_{NMS+3} to the deformation mode.

(3) Assume that NS (number of sensors) measures the instantaneous deflection of the ring normal to a desired inertially fixed reference plane and that all sensors can be interrogated simultaneously. This could be accomplished by a single rapidly rotating scanner located at the ring center. The sensor measurements are to be taken at a number of sensor points located along the periphery of the ring at angles $s = L_{si}$ (location of sensor point i), i = 1, 2, . . ., N_S, which do not change with respect to the reference plane. At time t, therefore, deflection measurements are made at particles $\{s = (S_i)_{Ls}\}$, i = 1, 2, . . ., n_S. The decomposition of these deflection measurements into a modal representation W_j can be made by using a multiple formulation of equation (1) as follows:

$$\begin{bmatrix} w((S_1)_{Ls},t) \\ w((S_2)_{Ls},t) \\ \cdot \\ \cdot \\ \cdot \\ w((S_{NS})_{Ls},t) \end{bmatrix} = \begin{bmatrix} 1 & \cos (S_1)_{Ls} & \cdots & \cos N_{MM}(S_1)_{Ls} & \sin (S_1)_{Ls} & \cdots & \sin N_{MM}(S_1)_{Ls} \\ 1 & \cos (S_2)_{Ls} & \cdots & \cos N_{MM}(S_2)_{Ls} & \sin (S_2)_{Ls} & \cdot & \sin N_{MM}(S_2)_{Ls} \\ \cdot & \cdot & \cdot & \cdot & \cdot & \cdot & \cdot \\ \cdot & \cdot & \cdot & \cdot & \cdot & \cdot & \cdot \\ \cdot & \cdot & \cdot & \cdot & \cdot & \cdots & \cdot \\ 1 & \cos (S_{NS})_{Ls} & \cdots & \cos N_{MM}(S_{NS})_{Ls} & \sin (S_{NS})_{Ls} & \cdots & \sin N_{MM}(S_{NS})_{Ls} \end{bmatrix} \begin{bmatrix} W_1(t) \\ W_2(t) \\ \cdot \\ \cdot \\ \cdot \\ W_{2NMM+1}(t) \end{bmatrix} \tag{2}$$

where N_{MM} (number of modes measured) is the number of modes used by the controller to represent the measurement data. Clearly, an exact representation of the N_S measurements may exist only if $N_{MS} \leq N_{MM}$. Note that no assumption has been made concerning the values of $(S_i)_{Ls}$ (sensor i at location s) which may differ from sample to sample. The inertia reference frame location of the measurement can be related to the spinning particle reference frame by using the equation $(S_i)_{Ls} = L_{Si} - \Omega t$, $i = 1, 2, \ldots, N_S$, if $(S_i)_{Ls} = L_{Si}$ at $t = 0$. This relation is required since the ring particles move with angular velocity Ω with respect to the reference frame.

(4) Assume each actuator is located in the reference plane at angles $s = L_{Ai}$ (location of actuator i), $i = 1, 2, \ldots, N_A$ (number of actuators) along the periphery of the ring and instantaneously produces a magnetic force constant over the sample interval on the ring at the inertially fixed point location of the magnet. The modal forces F are functions of both the mode shapes and the actual forces f applied to the ring for a point distribution of magnetic actuators. These are the Fourier series components for the distributed force in the spatial domain. Thus,

$$
\begin{bmatrix} F_1(t) \\ \cdot \\ \cdot \\ \cdot \\ \cdot \\ F_{2NMS+1}(t) \end{bmatrix} =
\begin{bmatrix}
1 & 1 & \cdots & 1 \\
\cos (f_1)_{Ls} & \cos (f_2)_{Ls} & \cdots & \cos (f_{NA})_{Ls} \\
\cos 2(f_1)_{Ls} & \cos 2(f_2)_{Ls} & \cdots & \cos 2(f_{NA})_{Ls} \\
\cdot & \cdot & \cdot & \cdot \\
\cdot & \cdot & \cdot & \cdot \\
\cdot & \cdot & \cdot & \cdot \\
\cos N_{MS}(f_1)_{Ls} & \cos N_{MS}(f_2)_{Ls} & \cdots & \cos N_{MS}(f_{NA})_{Ls} \\
\sin (f_1)_{Ls} & \sin (f_2)_{Ls} & \cdots & \sin (f_{NA})_{Ls} \\
\sin 2(f_1)_{Ls} & \sin 2(f_2)_{Ls} & \cdots & \sin 2(f_{NA})_{Ls} \\
\cdot & \cdot & \cdot & \cdot \\
\cdot & \cdot & \cdot & \cdot \\
\cdot & \cdot & \cdot & \cdot \\
\sin N_{MS}(f_1)_{Ls} & \sin N_{MS}(f_2)_{Ls} & \cdots & \sin N_{MS}(f_{NA})_{Ls}
\end{bmatrix}
\begin{bmatrix} f_1(t) \\ \cdot \\ \cdot \\ \cdot \\ f_{NA}(t) \end{bmatrix}
$$

$$= (AMFCM) \ f(t) \tag{3}$$

where $(f_i)_{Ls}(t) = L_{Ai}(t) - \Omega t$ denotes the location of the ith actuation force $f_i(t)$.

(5) For this ring stabilization problem, an appropriate control objective is to damp the motions of the ring. This damping will be attempted by individual modal

difference equation pole placement achieved via dynamic output feedback. The low order of the modal difference equations allows a closed-form solution for the controller parameters from the plant parameter estimates.

The second-stage or real-time processing steps are as follows:

(1) The N_S by $(2N_{MM} + 1)$ matrix of equation (2) relates the N_S measurements $w((S_i)_{Ls},t)$, $i = 1, 2, \ldots, N_S$, and the $(2N_{MM} + 1)$ modal amplitudes W_j, $j = 1, 2, \ldots, (2N_{MM} + 1)$. It will be denoted MADCM (modal to actual deflection conversion matrix). There are three situations which may occur: $N_S < 2N_{MM} + 1$, $N_S = 2N_{MM} + 1$, and $N_S > 2N_{MM} + 1$. For $N_S < 2N_{MM} + 1$ there are an insufficient number of measurements to determine the $2N_{MM} + 1$ modes and the problem must be cast as a simultaneous identification and estimation problem requiring an estimator or observer to track the modal amplitudes W_j with inputs w_i. The estimator or observer is not well defined since the parameters of the model are not known. Hence, the problem is a simultaneous identification and estimation problem and will not be explored further in this paper. For $N_S = 2N_{MM} + 1$, the matrix MADCM is square and, provided there is no duplication of measurements, is invertible, and one can solve for the W_j modal amplitudes corresponding to a measurement set w_i uniquely. If $N_S > 2N_{MM} + 1$, then there are more measurements than modal amplitudes and a least-squares fit using $2N_{MM} + 1$ modal amplitudes can be used. The resulting detected modal amplitudes are

$$\left\{ W_j(t) \right\} = \text{DMACM} \left\{ w \left[(S_i)_{Ls}, t \right] \right\} \tag{4}$$

where

$$\text{DMACM} \equiv (\text{MADCM})^T (\text{MADCM})^{-1} (\text{MADCM})^T$$

Note that equation (4) covers the cases where $N_S \geq 2N_{MM} + 1$.

(2) If the number of modes controlled (N_{MC}) is less than that measured (N_{MM}), then some modes will have to be deleted from consideration. However, at the current state of this work, N_{MC} and N_{MM} have been chosen equal.

(3) For large, lightweight rings, $W_j(t)$ of equation (1) is effectively undamped such that, for a small amplitude motion,

$$\frac{d}{dt^2}[W_j(t)] + \omega_j^2(\Omega, t) \; W_j(t) = \left(\frac{1}{M_j} \right) F_j(t) \tag{5}$$

where ω_j represents the modal time frequency, which can be a function of both time and ring spin rate Ω. For measurements of W_j taken at uniform sample intervals of T seconds, the discrete equivalent of equation (5) can be written as

$$W_j(k) = A_{1j}W_j(k - 1) + A_{2j}W_j(k - 2) + B_{1j}F_j(k - 1) + B_{2j}F_j(k - 2) \tag{6}$$

where $A_{1j} = 2 \cos(\omega_j T)$, $A_{2j} = -1$, and $B_{1j} = B_{2j} = (1 - \cos \omega_j T)/(M_j \omega_j^2)$. The assumption here requiring adaptivity is that the modal frequencies ω_j (and perhaps the actual damping coefficient assumed to be zero) have unknown infrequently varying values. Identifying the difference equation descriptions of equation (6) via an equation error formulation yields an adaptive algorithm of the following form (ref. 4):

$$
\begin{bmatrix} \hat{A}_{1j}(k) \\ \hat{A}_{2j}(k) \\ \hat{B}_{1j}(k) \\ \hat{B}_{2j}(k) \end{bmatrix} = \begin{bmatrix} \hat{A}_{1j}(k-1) \\ \hat{A}_{2j}(k-1) \\ \hat{B}_{1j}(k-1) \\ \hat{B}_{2j}(k-1) \end{bmatrix} + e_j(k-1) \begin{bmatrix} (W_a)_{1j} W_j(k-2) \\ (W_a)_{2j} W_j(k-3) \\ (W_a)_{3j} F_j(k-2) \\ (W_a)_{4j} F_j(k-3) \end{bmatrix}
\tag{7}
$$

where e_j is the modal output prediction error defined by

$$
e_j(k-1) = W_j(k-1) - \hat{A}_{1j}(k-1)\, W_j(k-2) + \hat{A}_{2j}(k-1)\, W_j(k-2)
$$

$$
+ \hat{B}_{1j}(k-1)\, F_j(k-2) + \hat{B}_{2j}(k-1)\, F_j(k-3)
\tag{8}
$$

If each adaptive step-size weight, $(W_a)_{ij}$, is positive and appropriately bounded, for example,

$$
(W_a)_{1j} W_j^2(k-2) + (W_a)_{2j} W_j^2(k-3) + (W_a)_{3j} F_j^2(k-2) + (W_a)_{4j} F_j^2(k-3)] < 2
\tag{9}
$$

and W_j and F_j are "persistently exciting" then convergence of

$\hat{A}_{1j}(k)\ \hat{A}_{2j}(k)\ \hat{B}_{1j}(k)\ \hat{B}_{2j}(k)$ to $A_{1j}\ A_{2j}\ B_{1j}\ B_{2j}$ as $k \to \infty$ can be guaranteed. This

identifier can be used even if the assumption of no damping is violated since equation (7) assumes only the second-order form of equation (6). During actual operation, some modes may not possess sufficient excitation to guarantee the consistency of the parameter estimates required for appropriate controller parameterization. Identifiable tests could be incorporated in the mode selection procedures, if used, of processing step (2).

(4) The modal pole placement objective corresponding to a specific fourth-order characteristic equation

$$
z^4 + (C_{dce})_{1j} z^3 + (C_{dce})_{2j} z^2 + (C_{dce})_{3j} z + (C_{dce})_{4j} = 0
\tag{10}
$$

(with C_{dce} signifying desired characteristic equation coefficient) can be achieved by utilizing the parameter estimates of equation (7) in a second-order, dynamic output feedback element as illustrated in figure 4. This controller does not explicitly require rate information, a quantity anticipated to be difficult to sense because of extremely low modal frequencies inherent in such large structures. Equating the coefficients in equation (10) and the characteristic equation corresponding to figure 4, permits the following solution for the controller parameter estimates:

$$\hat{D}_{1j}(k) = -(C_{dce})_{1j} - \hat{A}_{1j}(k) \tag{11}$$

$$\hat{C}_{1j}(k) = \{\hat{D}_{1j}(k) \, \hat{A}_{2j}(k) - (C_{dce})_{3j} + [\hat{D}_{1j}(k) \, \hat{A}_{1j}(k)$$

$$- \hat{A}_{2j}(k) - (C_{dce})_{2j}] [\hat{A}_{1j}(k) - \hat{A}_{2j}(k) \, \hat{B}_{1j}(k)/\hat{B}_{2j}(k)]$$

$$+ (C_{dce})_{4j} \, \hat{B}_{1j}(k)/\hat{B}_{2j}(k)\} [\hat{B}_{1j}(k) \, \hat{A}_{1j}(k) + \hat{B}_{2j}(k)$$

$$- \hat{A}_{2j}(k) \, \hat{B}_{1j}(k)/\hat{B}_{2j}(k)]^{-1} \tag{12}$$

$$\hat{D}_{2j}(k) = \hat{A}_{1j}(k) \, \hat{D}_{1j}(k) - (C_{dce})_{2j} - \hat{B}_{1j}(k) \, \hat{C}_{1j}(i) - \hat{A}_{2j}(k) \tag{13}$$

$$\hat{C}_{2j}(k) = \frac{\hat{D}_{2j}(k) \, \hat{A}_{2j}(k) - (C_{dce})_{4j}}{\hat{B}_{2j}(k)} \tag{14}$$

The modal forces provided by decentralized dynamic output feedback as in figure 4 can be calculated given equations (11) through (14) via

$$F_j(k) = \hat{C}_{1j}(k) \, W_j(k - 1) + \hat{C}_{2j}(k) \, W_j(k - 2)$$

$$+ \hat{D}_{1j}(k) \, F_j(k - 1) + \hat{D}_{2j}(k) \, F_j(k - 2) \tag{15}$$

(5) The selection of actual forces to be applied to the ring once desired modal forces have been selected requires pseudoinversion of the $(2N_{MS} + 1) \times N_A$ actual to modal forces conversion matrix (AMFCM) (eq. (3)) resulting in a desired modal to actual forces conversion matrix (MAFCM)

$$MAFCM = [(AMFCM)^T(AMFCM)]^{-1}(AMFCM)^T \tag{16}$$

with N_{MC} replacing N_{MS} in AMFCM, which can only exist if N_{MC} is not less than half of one less than the number of actuators, that is, $N_{MC} \nless (N_A - 1)/2$ or $2N_{MC} + 1 \nless N_A$. Note, however, that since N_{MC} is typically less than N_{MS}, forces entering "uncontrolled" modes need not be zero thereby exciting uncontrolled modes. This undesirable effect has been designated "control spillover" (ref. 5).

Therefore, simultaneous identification and control of a flexible ring is achieved by (a) using DMACM to convert an instantaneous spatial disturbance distribution to modal amplitudes, (b) performing the correction of the estimates of the A_{ij} and B_{ij} coefficients of equation (6) via equation (7) to overcome uncertainty in ω_j, (c) solving for the controller parameters in equation (6), via equations (11) through (14), (d) inserting them in equation (15) to select the desired modal forces, and (e) utilizing MAFCM to determine the actual forces to be applied. Note that the current modal control effort $F_j(k)$ can be calculated entirely from past measurements of modal amplitudes and forces. A control calculation is performed during the sample interval; therefore, no degrading delay between deflection measurement and control application (which could be appreciable due to the necessary pseudoinversions) is required. Furthermore, only the matrix operations in (a) and (e), which can be quickened by exploiting their special structure, cannot be computed in parallel making the objective of a multiple microcomputer based implementation possible.

SIMULATION STUDIES

A digital computer program has been written (ref. 6) to simulate out-of-plane motions of a ring and the adaptive controller described in the preceding section. Figure 5 is a block diagram indicating the ring control simulator flow and capability. To observe the behavior of the ring alone, the uncompensated step response and uncompensated step torque response of an initially unperturbed spinning, flexible ring with

$$
\begin{aligned}
& N_{MS} - N_{MM} - N_{MC} = 4 \\
& \omega_j^2 = 9,\ 1,\ 4,\ 5,\ 10,\ 1,\ 4,\ 5,\ \text{and } 10 \\
& M_j = 1,\ 1,\ 1,\ 1,\ 1,\ 1,\ 1,\ 1,\ \text{and } 1 \\
& \Omega = 60 \text{ deg/sec} \\
& N_S = 8 \\
& L_{Si} = 0,\ 45,\ 90,\ 135,\ 180,\ 225,\ \text{and } 315 \text{ deg} \\
& N_A = 9 \\
& L_{Ai} = 0,\ 20,\ 60,\ 90,\ 135,\ 180,\ 225,\ 270,\ \text{and } 315 \text{ deg} \\
& T = 0.1 \text{ sec}
\end{aligned}
\tag{17}
$$

are illustrated in figures 6 and 7, respectively. Note that, as expected, the response to a single step input includes translation while the response to a balanced

torque does not. The triangles on the displacement curves mark measurement points. The arrowheads along the spatial coordinate axis show actuator locations with the length of the arrowshaft proportional to the applied force according to the right-hand scale. The plots are based in the ring particle reference frame so the sensor and actuator locations appear to regress for a progressing ring. Note the movement of the two actuator locations 20° apart. For the large scale rings currently under consideration, the X-axis covers over 2 km. Therefore, the out-of-plane deflections, approximately 100 times smaller, are well within the region of linear behavior. More realistically, the modal frequencies are divided by 1000 for the structures involved; therefore, the stated times are multiplied by 1000. The uncompensated response to magnetic force inputs of only 20 N produces severe excitation of the flexible modes in addition to the rigid body modes. This situation implies a requirement for damping the flexible modes.

The undamped behavior of the same ring is illustrated in figure 8 by release from the initial deformation disturbance of

$$w(L_{Si},0) = 3.7, -0.96, 0, 0.23, -2.7, 1.16, 2.6, \text{ and } -0.37 \text{ m} \tag{18}$$

The predictable oscillatory behavior occurs as the ring appears near-flat at 0.8 sec but near-maximum deflection only 0.4 sec later. The damping chosen for each mode implicit in

$$\left.\begin{array}{ll} (C_{dce})_{1j} = -1.7 & (C_{dce})_{2j} = 1.06 \\[2mm] (C_{dce})_{3j} = -0.272 & (C_{dce})_{4j} = 0.024 \end{array}\right\} \tag{19}$$

removed the disturbance within 1.3 sec as shown in figure 9. The required modal forces were calculated by using equation (15) with the difference equation parameter estimates equaling their actual values. They remain within the ±50-N range. For computational simplicity, the applied forces from solution of equation (3) were assumed spatially fixed with respect to the ring during the same interval; that is, ring movement was inappropriately modeled to occur instantaneously at the sample instants. Correction of this procedure can be achieved by appropriate actuator windowing; therefore, the generality of these simulation results was not affected. Since $N_{MS} = N_{MC} = N_{MM}$, both AMFCM and MADCM are square and invertible, with control and observation spillover avoided in these simulations.

If the modal difference equation parameter estimates are assumed to be less than 10 percent in error for A_{1j}, exact for A_{2j}, and within 20 percent for B_{1j} and B_{2j} (which corresponds to a 20-percent estimate error in M_j and 50 to 350 percent overestimation of the structural frequencies), that is,

$$\left.\begin{array}{l} \hat{A}_{1j} = 2, 1.8, 1.8, \ldots, 1.8 \\[2mm] \hat{A}_{2j} = -1, -1, \ldots, -1 \\[2mm] \hat{B}_{1j} = \hat{B}_{2j} = 0.004, 0.004, \ldots, 0.004 \end{array}\right\} \tag{20}$$

an unstable controller results unless adapted. Fixed use of these erroneous plant parameter estimates leads, as shown in figure 10, to an over 20-m (and growing) maximum disturbance within the desired damping interval. Alternatively, adaptive identification with

$$(W_a)_{ij} = 1[W_j^2(k - 2) + w_j^2(k - 3) + F_j^2(k - 2) + F_j^2(k - 3)]^{-1}$$

in satisfaction of equation (9) and controller recalculation via equation (15) bounds the deformation within the ±8-m maximum deflection range within the same interval in figure 11. Maximum forces are applied by the adaptive controller at 2.5 sec and the deformation has disappeared within 5 sec. By convergence to proper time-invariant parameter values from initial errors in the model plant parameters, the superiority of the adaptive scheme is demonstrated in this instance.

CONCLUDING REMARKS

An original adaptive control methodology applicable to the control of distributed systems has been presented. It has been applied to the stabilization of the flexible modes of a spinning ring. Simulation studies presented confirm the need for active stabilization of rings if they are to be used to conduct spacecraft maneuvers. A fixed point controller design that gives desirable damping if the ring dynamics are as prespecified was shown to be unstable when the assumed parameter values are in error. The adaptive controller, however, did produce stable results by quickly identifying the plant parameters and simultaneuosly adjusting feedback controller gains. Further efforts should be directed at evaluation of controller objective specifications and requirements, sensor noise effects, criteria for selection of the modes to be controlled, and robustness despite control and observation spillover. A long-range goal should be to conduct studies evaluating the proposed adaptive control philosophy for distributed systems having more than one spatial coordinate.

REFERENCES

1. Kennedy, H. B.: A Gyro Momentum Exchange Device for Space Vehicle Attitude Control. AIAA J., vol. 1, no. 5, May 1963, pp. 1110-1118.

2. Anderson, Willard W.; and Groom, Nelson J.: The Annular Momentum Control Device (AMCD) and Potential Applications. NASA TN D-7866, 1975.

3. Montgomery, Raymond C.; and Johnson, C. Richard, Jr.: The Dual-Momentum Control Device for Large Space Systems. A Collection of Technical Papers - AIAA/NASA Conference on Advanced Technology for Future Space Systems, May 1979, pp. 366-374. (Available as AIAA Paper 79-0923.)

4. Mendel, Jerry M.: Discrete Techniques of Parameter Estimation. Marcel Dekker, Inc., 1973, pp. 180-223.

5. Balas, Mark J.: Active Control of Flexible Systems. Dynamics and Control of Large Flexible Spacecraft, L. Meirovitch, ed., AIAA, June 1977, pp. 217-236.

6. Montgomery, Raymond C.; and Johnson, C. Richard, Jr.: The Dual Momentum Control Device for Large Space Systems: An Example of Distributed System Adaptive Control. Conference Record - Twelfth Asilomar Conference on Circuits, Systems & Computers, 78CHI369-8, IEEE, Nov. 1978, pp. 59-68.

AMCD   angular momentum control device

AMFCM   actual to modal forces conversion matrix

$A_{ij}, B_{ij}, C_{ij}, D_{ij}$ coefficients in difference equations

C_{dce} desired characteristic equation coefficient

e_j modal output prediction error

F   force, N

f   actual force

$f_i(t)$ ith actuation force

$\left(f_i\right)_{Ls}$ force at location s

h_c control momentum

h_1 control momentum component for ring 1

h_2 control momentum component for ring 2

k   constant

L_{Ai} location of actuator i

L_{Si} location of sensor point i

MADCM   modal to actual deflection conversion matrix

MAFCM   modal to actual forces conversion matrix

N_A number of actuators

N_{MC} number of modes controlled

N_{MM} number of modes measured

N_{MS} number of modes simulated

N_S number of sensors

$\left(s_i\right)_{Ls}$ sensor i at location s

s   variable describing angular location of particle in ring

T   uniform sample time interval

t   time, sec

W   deflection, m

$\left(W_a\right)_{ij}$ adaptive step-size weight

W_j modal deflection amplitudes

w linearized out-of-plane deformation

w_i input for modal amplitude

Ω ring spin rate

ω_c angular velocity

ω_j modal time frequency

      Caret over symbol indicates estimated value.
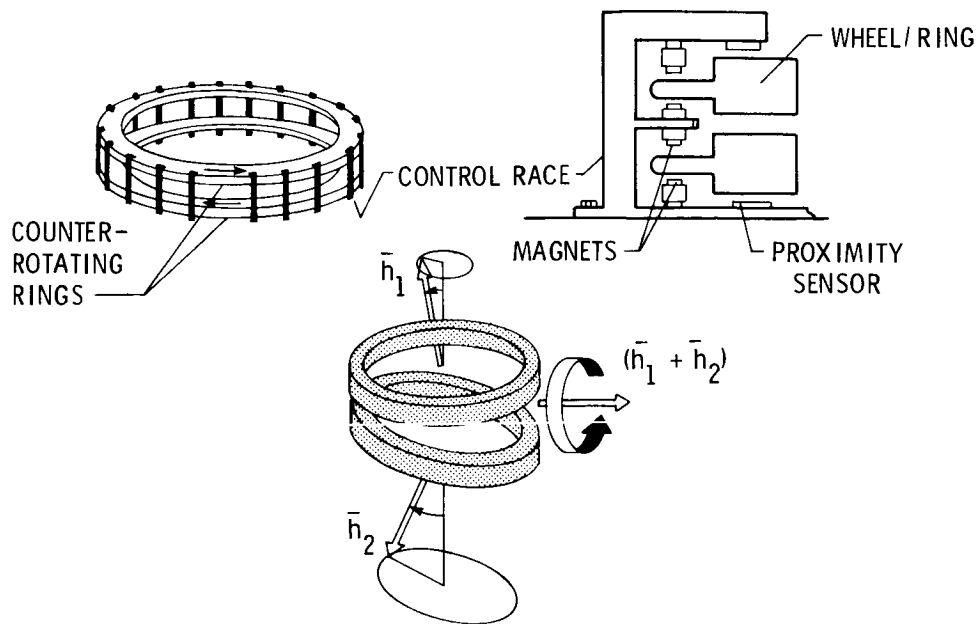
Figure 1.- Schematic of dual-momentum
vector control concept.
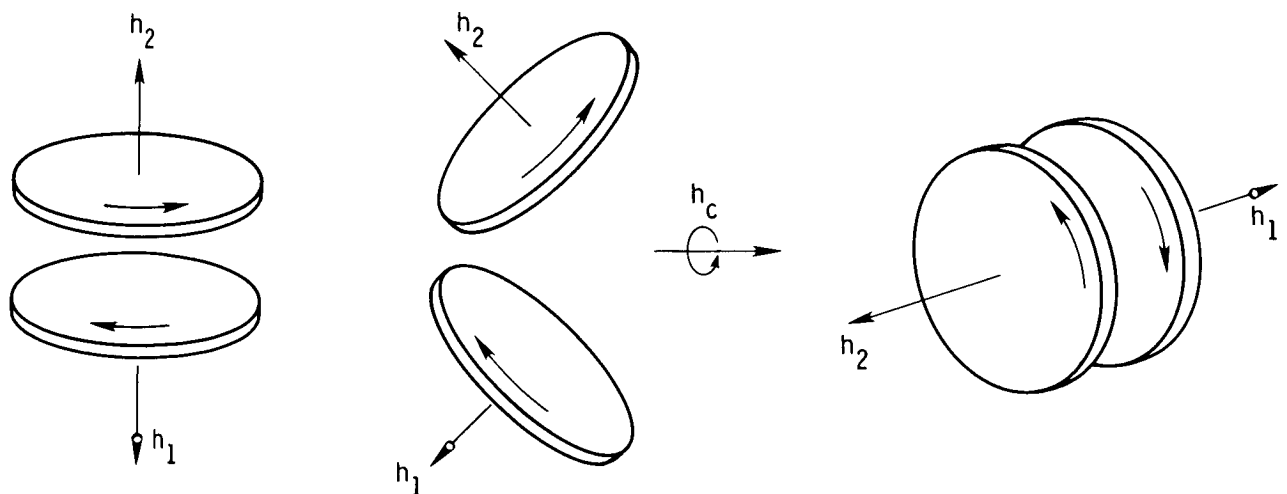
(a) Initial orientation. (b) Maneuvering orientation. (c) Orientation after
maneuver.

Figure 2.- Dual-momentum vector control concept.

TRANSLATION   ROTATION   FLEXIBLE MODE
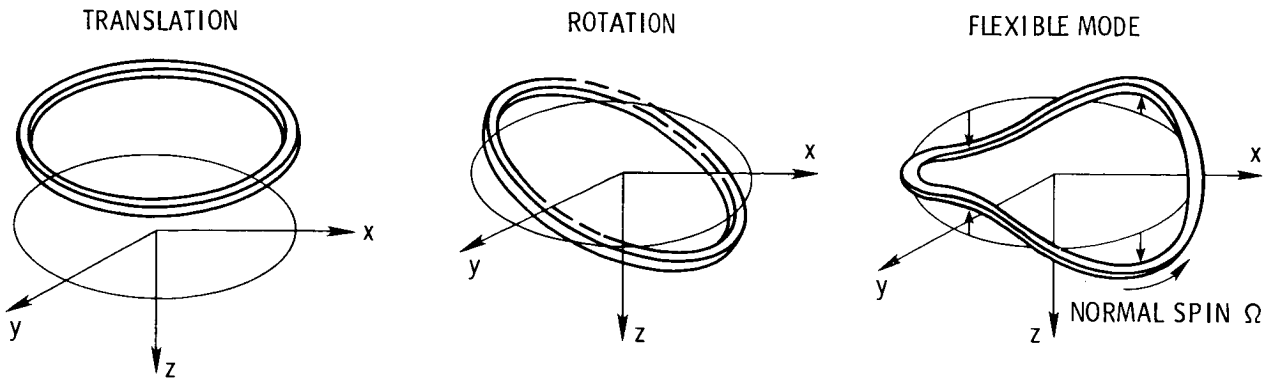
Figure 3.- Modes of motion of spinning ring.
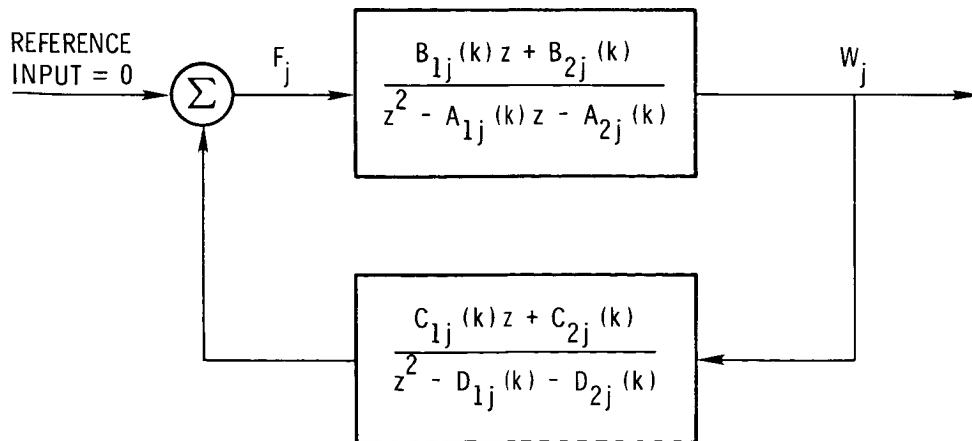
Figure 4. Dynamic output feedback configuration.
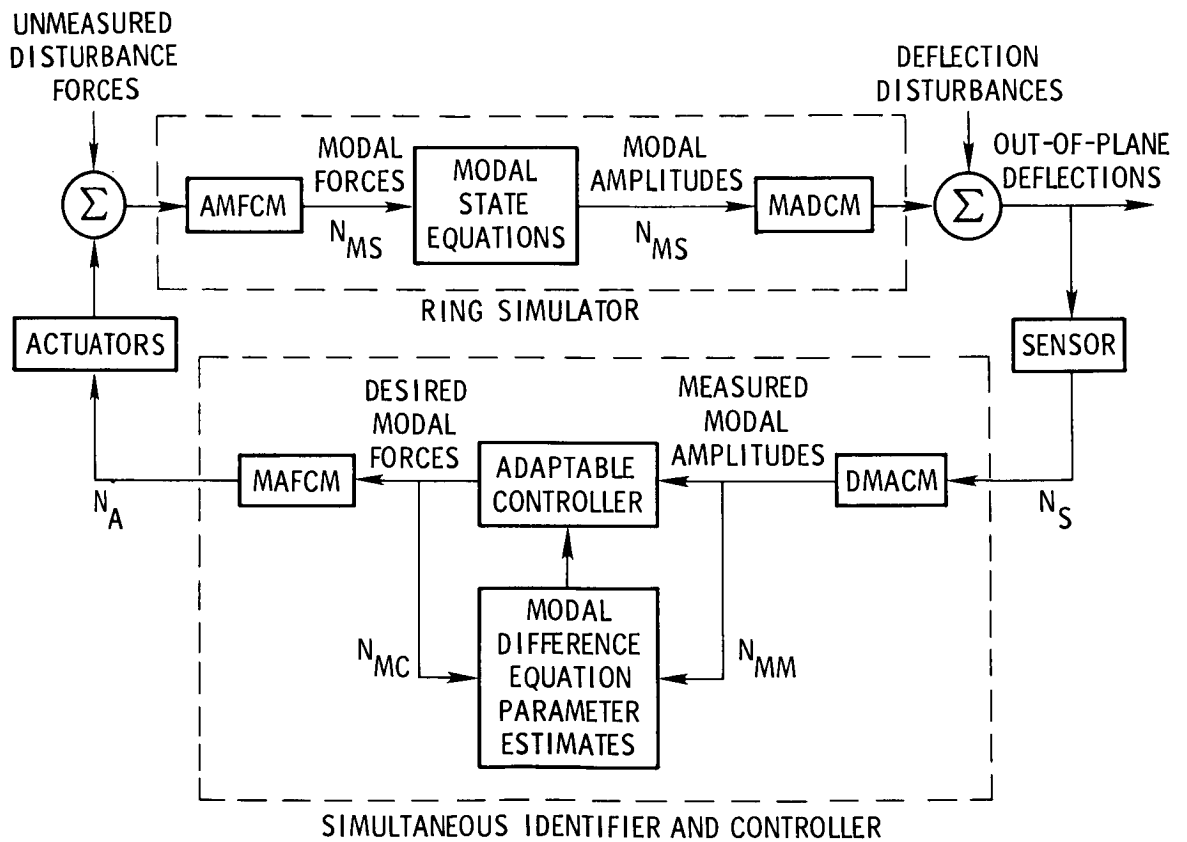
Figure 5.- Ring control simulator.

Figure 7.– Uncompensated step torque response.

Figure 6.– Uncompensated step response.

185
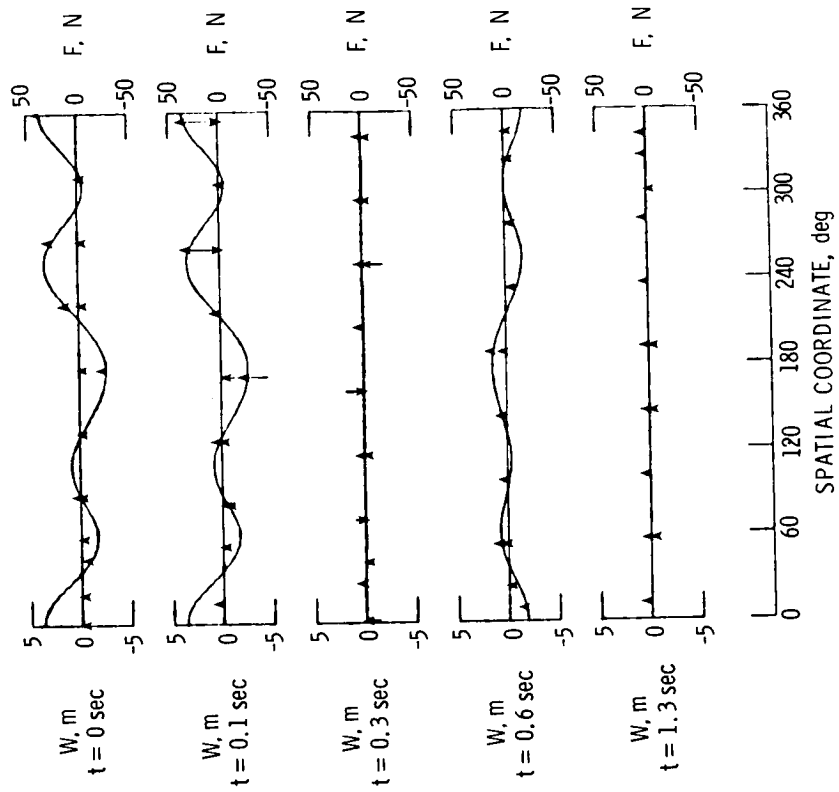
Figure 8.— Free response to initial deformation.
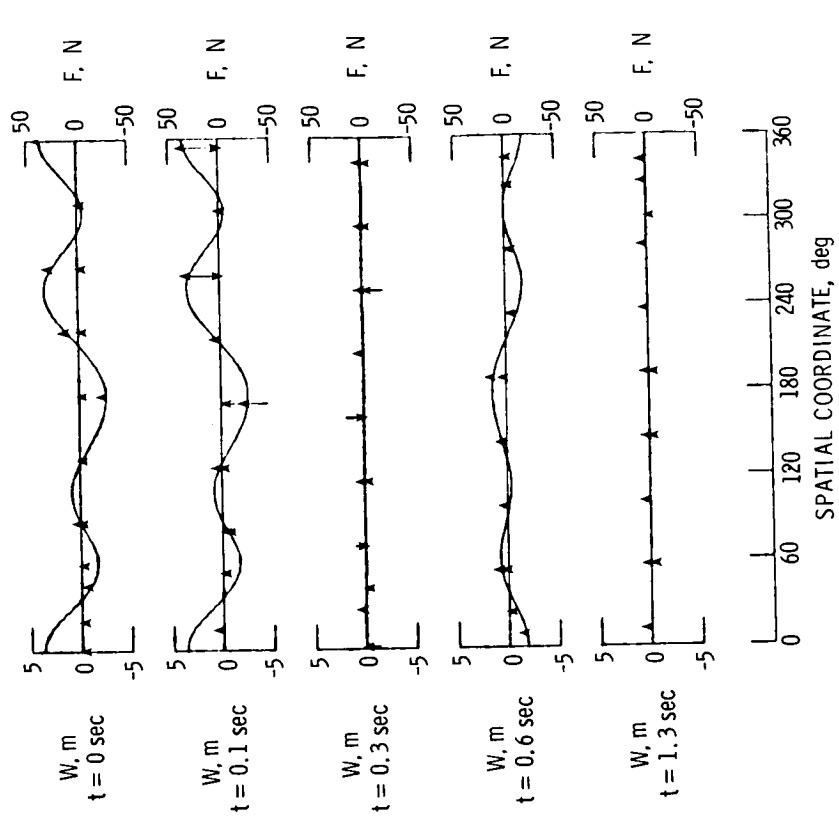
Figure 9.— Desired damping of initial deformation.
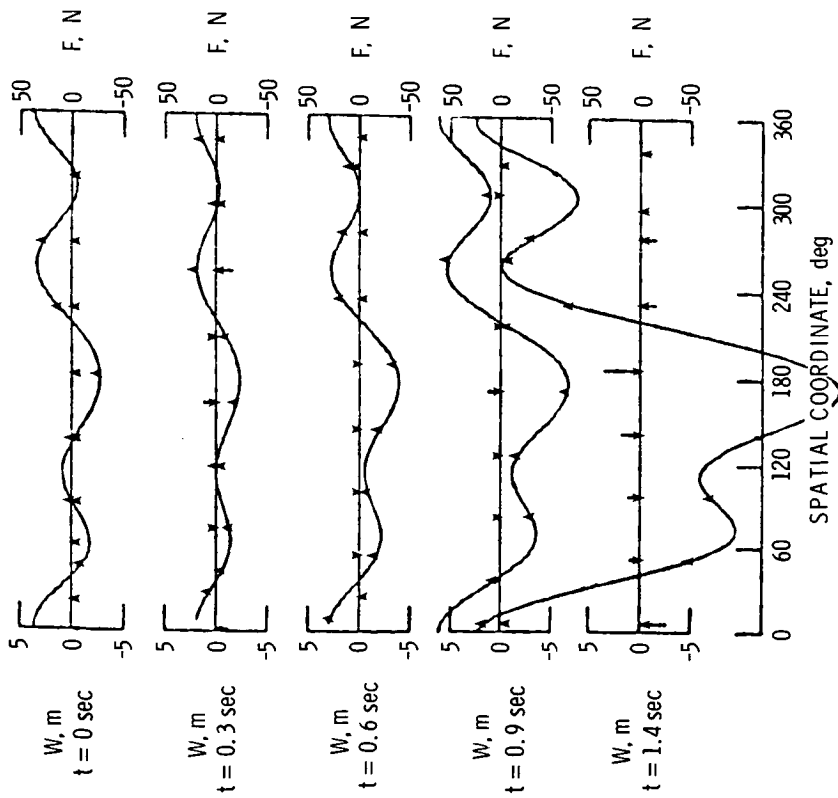
Figure 10.- Fixed incorrect parameter control response.
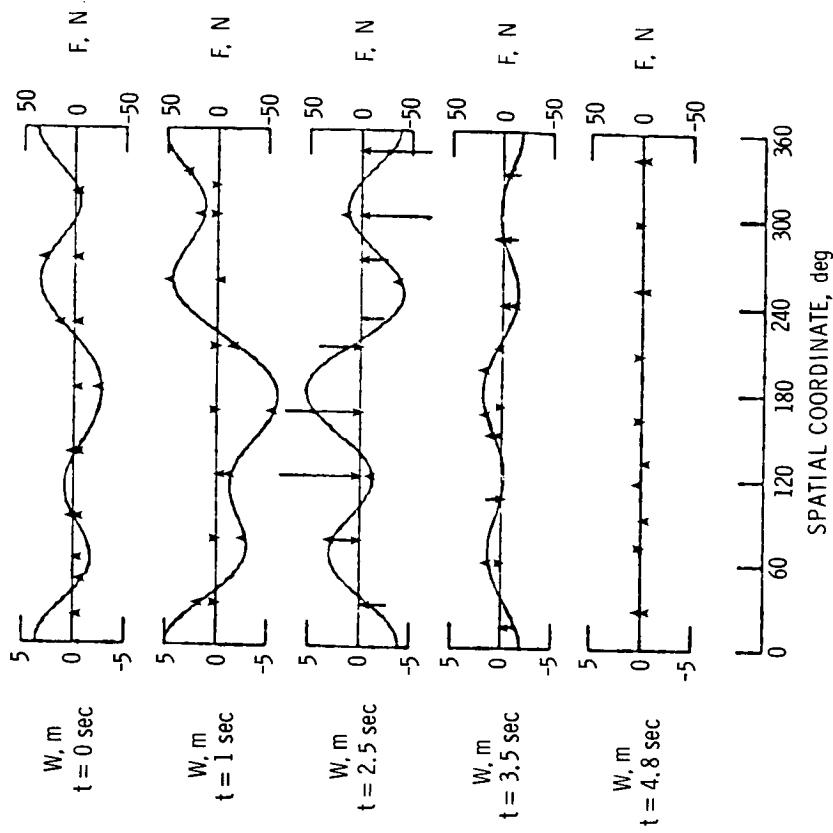
Figure 11.- Adaptive control response despite initial control law instability.

187

BIAXIAL AND ELECTROSTATIC TENSIONING EFFECTS ON

THIN MEMBRANE MATERIALS

William F. Hinson and J. W. Goslee
NASA Langley Research Center
Hampton, Virginia

and

John R. McIlhaney and James H. Ramsey
Kentron International
Hampton, Virginia

SUMMARY

Thin-membrane materials were subjected to biaxial and electrostatic tensioning loads to study techniques for maintaining surface smoothness of a thin-membrane antenna. The basic mechanical and electrical setup for the tests is described and preliminary measurements of surface smoothness and surface deviation are presented.

INTRODUCTION

Thin membranes are being considered for various surface applications on future large space structures such as the microwave radiometer spacecraft. The membrane would be stretched across or between structural members or frames with the requirement that the membrane be maintained within specified limits of smoothness that are dictated by the particular application, such as a reflective antenna or solar collector. Methods of applying tension and the tension required to maintain smoothness in the membrane need to be determined for use in the structural design loadings of the space structure. Two membrane-tensioning methods, biaxial load and electrostatic forces, are being investigated (ref. 1), and the purpose of this paper is to present preliminary results.

During the biaxial-load test, the flatness deviation of the material surface was measured as a function of increasing load. In the electrostatic-forces test, the membrane was installed on a circular frame and electrostatic forces were applied to form a "dish" surface. The smoothness of the membrane surface was measured by hand and by a laser-beam instrument. The membrane material was Mylar (polyester film) coated with vacuum-deposited aluminum (≈ 1 μm thick) ranging in total thickness from 0.00122 cm (0.0005 in.) to 0.00508 cm (0.002 in.).

Numerous investigators have used biaxial-load test equipment with thin-sheet specimens to determine the mechanical behavior of various materials (refs. 2 to 6). One of the major problems discussed in these investigations has been how to support the specimen so that the forces applied can be evenly distributed along the sides.

The specimens were supported by hooks, clamps, rings, eyelets, and/or strings. The force in reference 2 was applied with a whiffletree test fixture. To generate biaxial stress in reference 3, a small specimen was attached to a pressurized cylinder. In reference 4, weights were attached to several pull points around the circular membrane. In reference 5, individual strain-gage load cells were attached to several eyelets around the sides of the membrane. These load cells were fastened to a pair of right-angle, L-shaped, interconnected frame assemblies which were designed to move apart biaxially when pulled uniaxially by a tensile testing machine.

In the present investigation, the biaxial force loading and support procedures resembled the methods in references 5 and 6, respectively. The membrane was supported by seven eyelets on each of the four sides. The eyelets were attached to adjustable rods which were in turn attached to the test frame. On two sides of the specimen, an electrical strain-gage load cell was mounted to measure force loads at each pull point. These load cells could be set individually for the specified static-load conditions. As in reference 5, it is believed that applying force over small segments of the specimen and being able to measure that segment force results in a more uniform force distribution and biaxial stress condition in the thin membrane.

The electrostatically controlled membrane-tensioning concept is a new approach to achieving large, very light reflectors for various space applications. To achieve and control the membrane tension requires a controllable pressure field on the membrane. Electrostatic pressures appear usable because (1) they appear readily controllable, (2) they can be an integral part of the control system, (3) they can be maintained with insignificant power or current flow even though the voltages required are large, and (4) even though the pressures on the membrane are small, they appear adequate to contour membranes of a thickness that can be reasonably handled and manufactured.

Reference 7 presents technology developed by the General Research Corporation (GRC) for the forming of an antenna or reflector using electrostatic or Coulomb forces. The system is essentially a charged capacitor with the deformable reflector as one of its electrodes. When a voltage is applied between the unstressed membrane and the back electrode, the electrostatic attractive force draws the membrane inward. An electrical network is used to generate the required high field strength between the supported back electrode and the deformable membrane. A membrane acted upon by such a pressure loading naturally forms a concave surface of the sort required for most antenna reflectors. The fixed back control electrode can be segmented into electrically isolated elements, each supplied with a different control voltage and thus exerting a different field strength and pressure on the membrane. GRC has built, tested, and analyzed several small breadboard models in the initial stages of this new technology. The next logical step is to construct and test larger models to demonstrate the concept applicability. Therefore, a reflector, 1.83 m (6 ft) in diameter, has been constructed for exploratory tests. Materials used in this investigation are commercially available production-run materials.

The uniqueness of the present investigation over previous work is the measurement of the material surface deviation as a function of increasing biaxial load and the formation of a relatively large antenna reflector by electrostatic forces. All test equipment used was designed, constructed, and operated at the Langley Research Center.

APPARATUS, TESTS, AND MATERIALS

The basic mechanical and electrical setup for the biaxial tests is shown in figure 1 and schematics are given in figures 2 and 3. A typical biaxial sample is shown in figure 3(a). The number of load application points was determined from the theoretical curve shown in figure 4. This curve represents the fractional region of the test sample at constant stress (a/b) as a function of the number of load application points. Each sample had 24 eyelets for mounting to the biaxial tension fixture. However, to prevent wrinkling of the sample material in the corners due to biaxial loading, the corner eyelets were used to load in both the X- and Y-directions. Therefore, the total number of loading points was considered to be 28 which results in an a/b ratio of 0.57. Thus, for the 25.4-cm (10-in.) square sample, the area considered to be at constant stress is shown in figure 3(a) as the inner dotted square. This region was therefore considered the test area, across which surface deviations were measured.

Tensioning of the test sample was accomplished by the apparatus shown in the schematic in figure 3(b). A coarse load was applied through a cable and pulley arrangement to a slide bar which had seven load cells attached to it. The cells were attached to the test sample through threaded turnbuckles, rods, and clamps. The turnbuckles allowed a fine adjustment of the load. The load was applied to two adjacent sides of the test sample, in the plane of the edge and perpendicular to the test sample. A support structure supported the weight of the turnbuckles, adjustment rods, clamps, and load cells. Teflon tape was used between sliding surfaces to reduce friction.

The load measuring system is shown in figure 2(b). The load cell output signal was conditioned by the balance box, amplified, and displayed on the digital voltmeter.

The material surface deviations were measured by the noncontacting capacitance probe and associated equipment shown in figure 2(c). The capacitance probe (gage) is based upon the principle that a voltage applied across two plates which are electrically isolated from each other permits a charge to accumulate within the plates, causing the formation of an electric field. The change accumulation, i.e., the capacitance, is determined by the physical parameters of the system; it is directly proportional to the area of the plates and the dielectric constant of the intervening medium, and inversely proportional to the distance between the plates. Therefore, in order to measure capacitance changes due to displacement, it is necessary to fix the probe diameter (area) and dielectric constant in a manner that permits variance only in the separation distance between the probe (one plate) and the material test sample (the other plate).

In the present investigation, the dielectric medium was air and the probe sensing diameter was 0.53 cm (0.21 in.) with a nominal spacing for zero at 0.057 cm (0.0225 in.) above the material surface; the measuring range was ± 0.0254 cm (± 0.01 in.) about the zero spacing. The output of the capacitance probe (surface deviations) and the probe position (fig. 3(a)) along the test sample surface were recorded by the X-Y plotter.

The electrostatically controlled membrane concept is shown in figure 5. A compression rim is shown constructed with three interconnected circular rings. The membrane was draped over the front ring and fastened rigidly to the second ring. The third ring was used for mounting an electrode which is shown as curved and segmented with controlled voltages to each segment. A simple, single, flat electrode with a

voltage of 35 kV was used for the initial design and tests reported in this paper. Voltage applied to the electrode resulted in the generation of an electrostatic pressure which caused the membrane to be drawn toward the electrode resulting in the membrane forming a concave surface. A laser sensor located at the radius of curvature of the formed reflector measured concavity and surface smoothness.

Surface materials used in all these tests consisted of Mylar coated with vacuum-deposited aluminum (≈ 1 μm thick), with a total thickness ranging from 0.00122 cm (0.0005 in.) to 0.00508 cm (0.002 in.).

DISCUSSION OF RESULTS

Biaxial Tensile Tests

Figures 6(a) and 6(b) show the effect of increasing biaxial stress on material surface deviations. Each curve represents the surface deviations corresponding to a specific load or stress condition as a function of probe travel across the test sample (fig. 3(a)). Two sets of data are presented, one set without and one set with fold points as marked in figure 6(b). The material surface deviations shown by the curves without folds represent perturbations caused by general handling of the material such as was needed to prepare the test samples. The second data set represents the surface deviations due to the material handling plus man-made deviations (folds). The fold points were generated by wrapping the material tightly by hand around a wire 0.16 cm (0.062 in.) in diameter, thus generating surface deviations with a bend radius. As shown in the figures, increasing the biaxial stress results in a reduction in the material surface perturbations, man-made or natural, to a near smooth condition.

It must be emphasized that the data presented in figure 6 are illustrative only. The wire size was chosen to represent probable folds which would be inherent in packaging the material for flight. Such perturbations or folds would depend heavily on material properties, preparation, handling, and memory properties. However, the trend of reducing the perturbation height by increasing the biaxial stress should remain the same. Only the stress level needed to reduce the perturbations would change.

Electrostatic Tensile Tests

The initial tests of a thin membrane, 0.00122 cm (0.0005 in.) thick, are shown for a flat or untensioned condition in figure 7 and for a tensioned condition in figure 8. A flat electrode was used with a voltage of 35 kV in relatively dry air. Test conditions were designed to form a reflector with a focal length to diameter ratio (f/D) of 4.4. As can be seen, the material surface at the center of the reflector appears very smooth but some surface perturbations occur near the rim. The electrostatic pressure field generated by the flat electrode design and voltage used did not have sufficient strength and uniformity to smooth the total material surface. Figure 9 shows manual and laser instrument measurements of the reflector maximum concavity shown in figure 8. Deviations from the calculated concavity curvature varies from about 1 to 6 mm. The goal is to be able to control the formation of the total reflector surface to within approximately 1 mm, as developed and discussed in reference 8. An error analysis of the laser instrument measurement technique indicated that a 50-percent error in surface deviations is likely (see ref. 9).

192

These tests were not extensive enough to make major conclusions, however, the tests do indicate the possibility of using electrostatic forces to shape reflectors such as discussed herein. Reference 9 presents tests using smaller models (approximately 1 m in diameter) with a discussion of various methods of obtaining a more uniform reflector shape and surface smoothness by controlling the electrostatic pressure and strength. These methods include using a curved segmented electrode, variation in rim design, voltage variation, different membrane types, and variation in the membrane attachment procedure. A proposed layout, design, and test program for a 4.88-m (16-ft) diameter ground-test electrostatic system is included in reference 9. Plans are underway at the Langley Research Center to construct this system for further testing of the electrostatic concept.

CONCLUDING REMARKS

Thin membrane materials were subjected to biaxial and electrostatic tensioning loads to study techniques for maintaining surface smoothness of a thin-membrane antenna. The data presented were not extensive enough to generate major conclusions, but were adequate to define requirements for further study.

The results indicate that the biaxial test equipment appeared to load the aluminum-coated Mylar uniformly and that perturbations in the specimen were smoothed with increasing biaxial load.

The electrostatic pressure field generated was not adequate in strength and uniformity to smooth the total surface of the reflector; however, the tests do indicate the possibility of using electrostatic forces to shape reflectors. These tests have been redesigned to include the construction and tests of a 4.88-m (16-ft) diameter reflector.

REFERENCES

1. Hinson, W. F.; and Goslee, J. W.: Uniaxial and Biaxial Tensioning Effects on Thin Membrane Materials. NASA TM-81812, 1980.

2. Jerke, John M.; Heath, Atwood, R., Jr.; and Bond, Victor R.: The Geometric Properties of an Expandable Whirling-Membrane Solar-Energy Concentrator. NASA TN D-4532, 1968.

3. Niccum, R. J.; Munson, J. B.; and Rueter, L. L.: Investigation of Kevlar® Fabric-Based Materials for Use With Inflatable Structures. NASA CR-2724, 1977.

4. Mikulas, Martin M., Jr.: Behavior of a Flat Stretched Membrane Wrinkled by the Rotation of an Attached Hub. NASA TN D-2456, 1965.

5. Arenz, R. J.; Landel, R. F.; and Tsuge, K.: Miniature Load-Cell Instrumentation for Finite-Deformation Biaxial Testing of Elastomers. Exp. Mech., vol. 15, no. 3, Mar. 1975, pp. 114-120.

6. San Miquel, Anthony: An Automated Biaxial Sheet Tester. Exp. Mech., vol. 12, no. 3, Mar. 1972, pp. 155-157.

7. Mihora, D. J.; Redmond, P. J.; Crawford, R. F.; and Mortz, M. S.: Electrostatically Formed Antennas (Test Concept). NASA CR-159068, 1979.

8. Keafer, Lloyd S, Jr.: Radiometer Design Concepts for a Large Aperture Radiometer Spacecraft, The Microwave Radiometer Spacecraft - A Design Study, Robert L. Wright, ed., NASA RP-1079, 1981, pp. 43-49. (Paper in this compilation.)

9. Spiers, Robert B., Jr.: Surface Measuring Technique. Large Space Systems Technology - 1979, NASA CP-2118, 1980, pp. 193-198.

BIAXIAL TENSION
TEST FIXTURE

Figure 1.- Photograph of biaxial tension test equipment.

L-78-5726.1

195
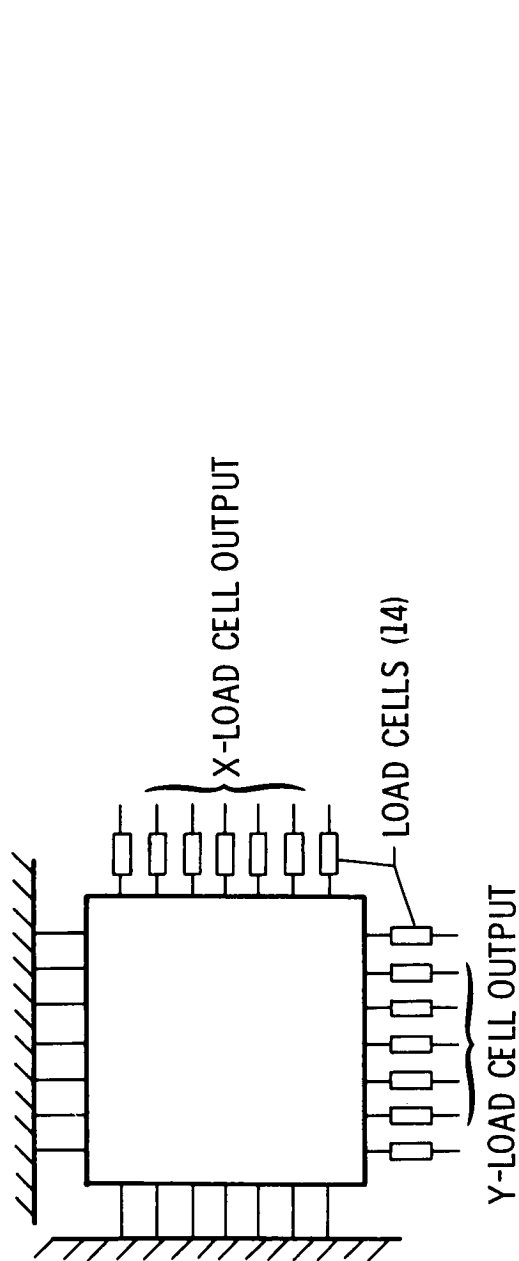
(a) Typical test sample.
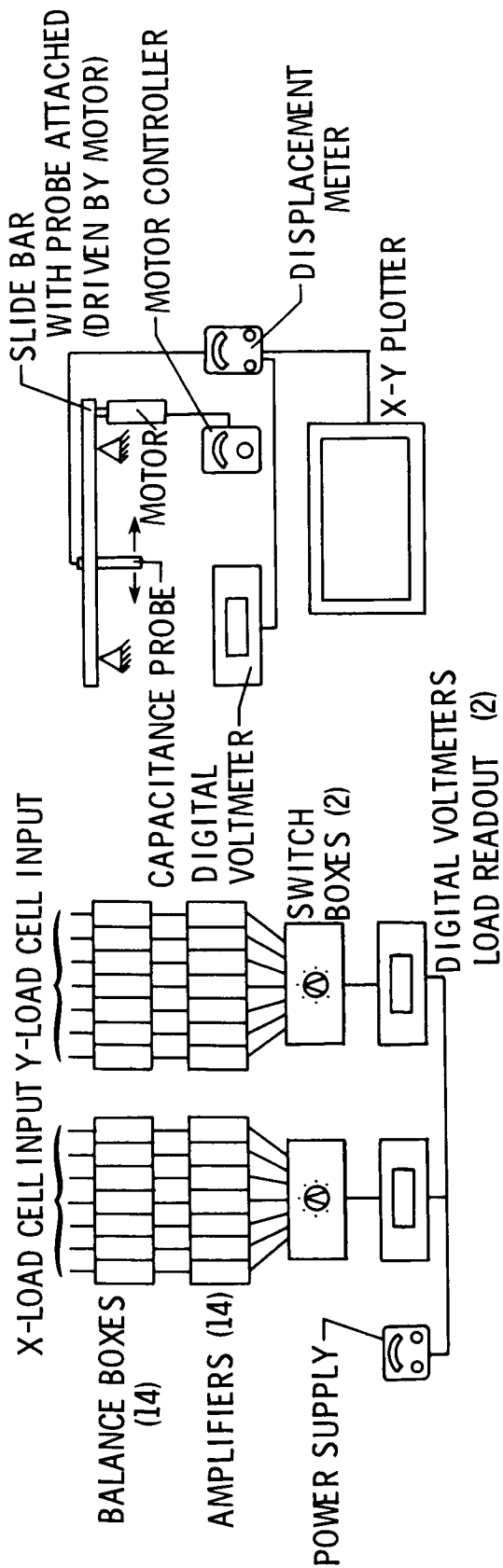
(b) Force measuring system.

(c) Material flatness measuring system.

Figure 2.- Schematic of biaxial tension test equipment.
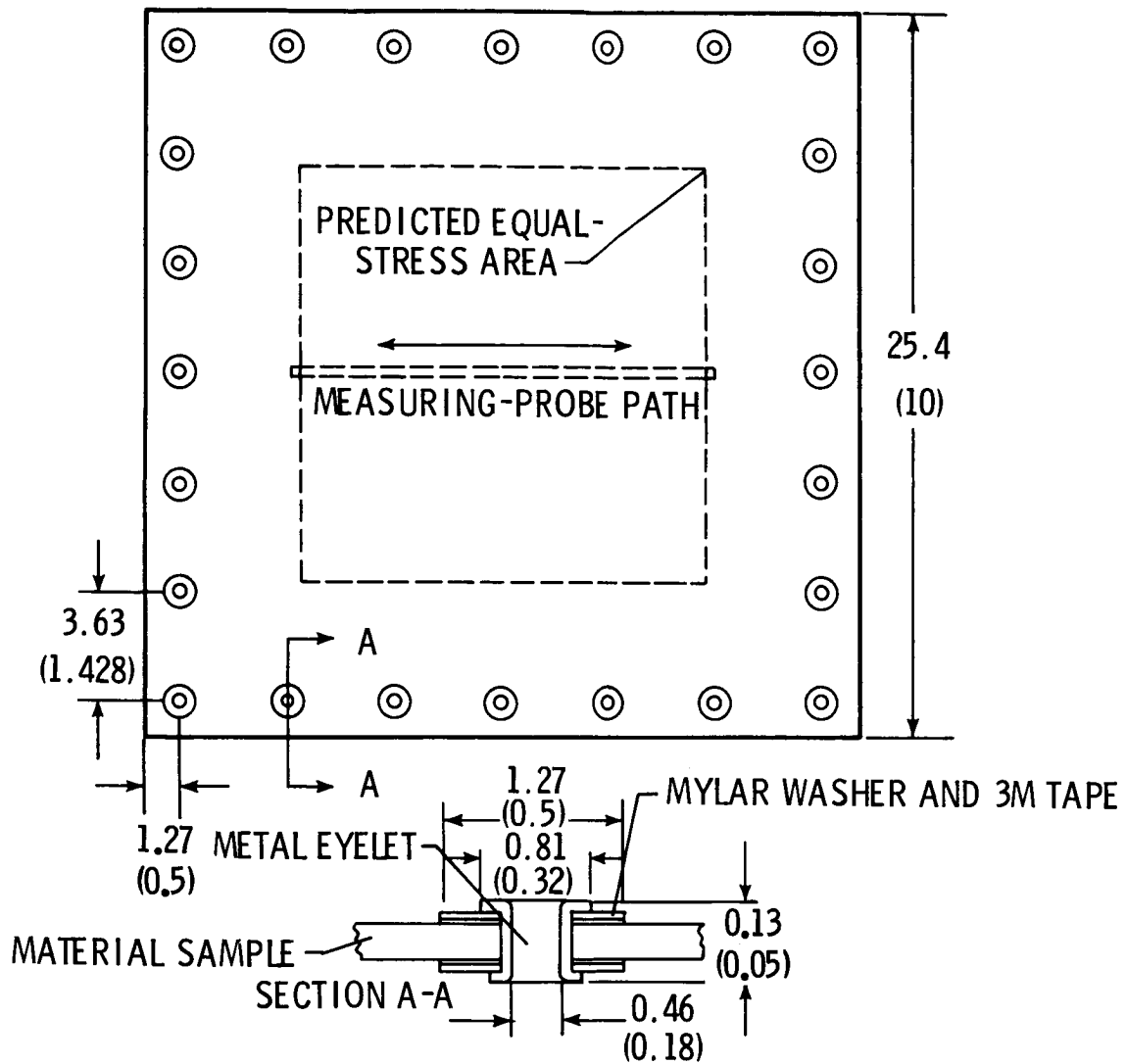
(a) Test sample.
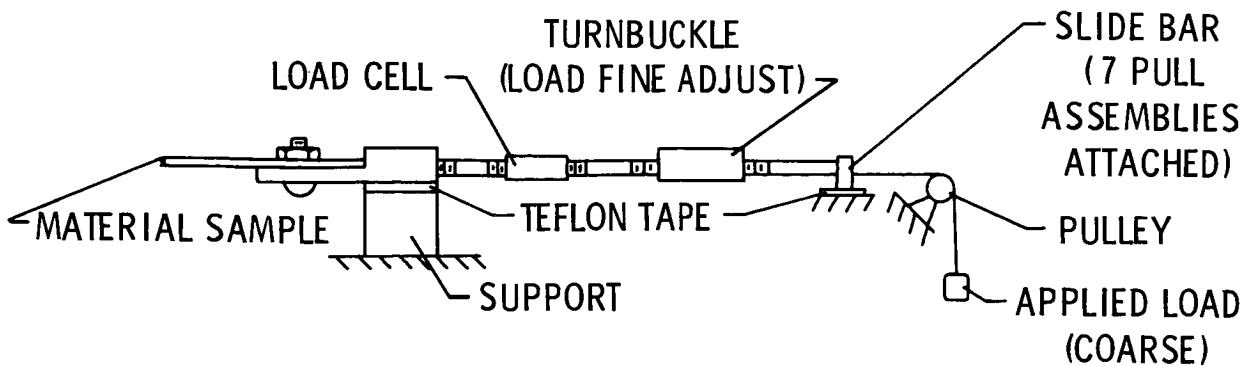
(b) Typical loading apparatus.

Figure 3.- Typical test sample and loading apparatus. Dimensions are in cm (in.).
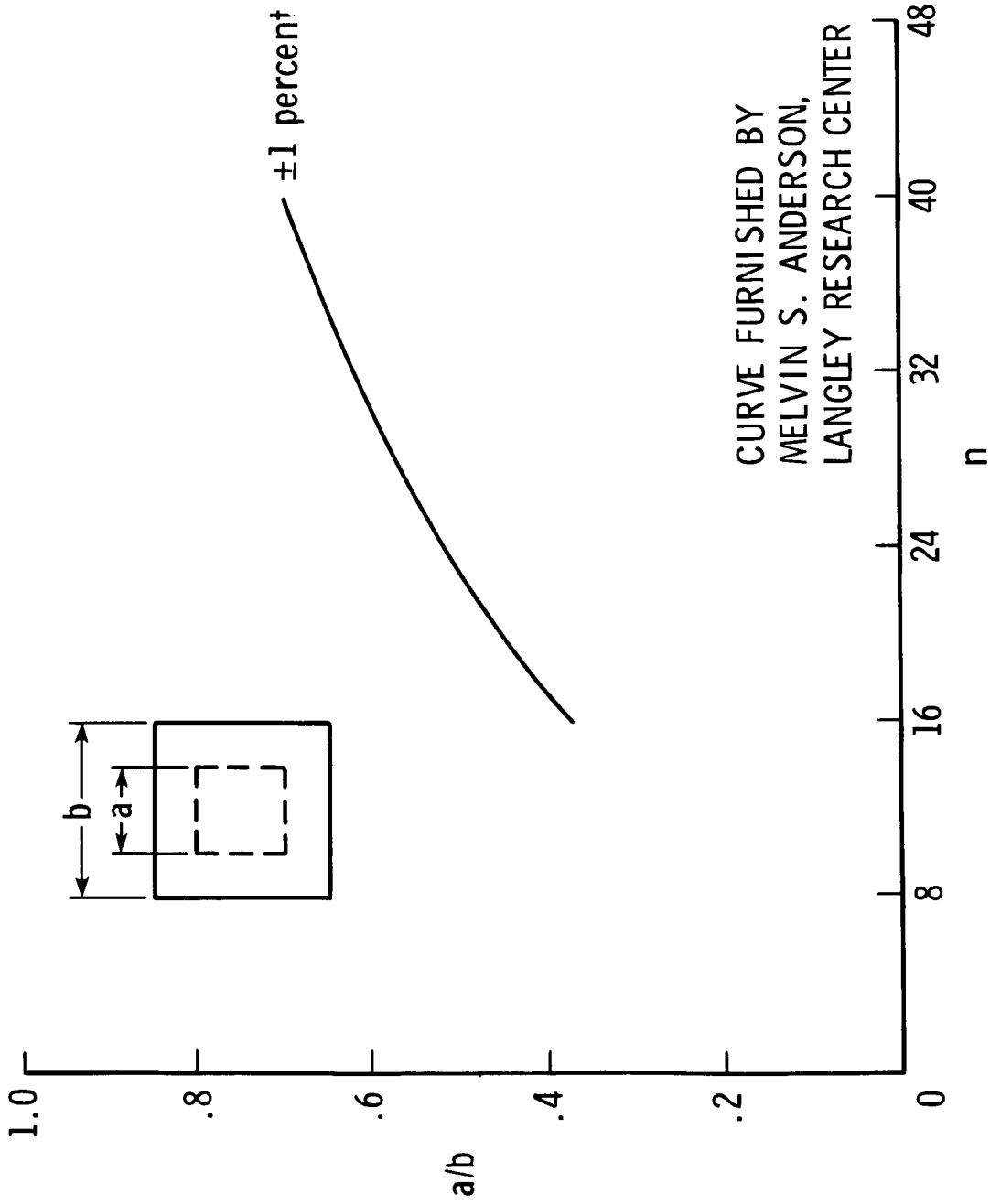
Figure 4.- Fractional region a/b at constant stress versus
number of load application points n.
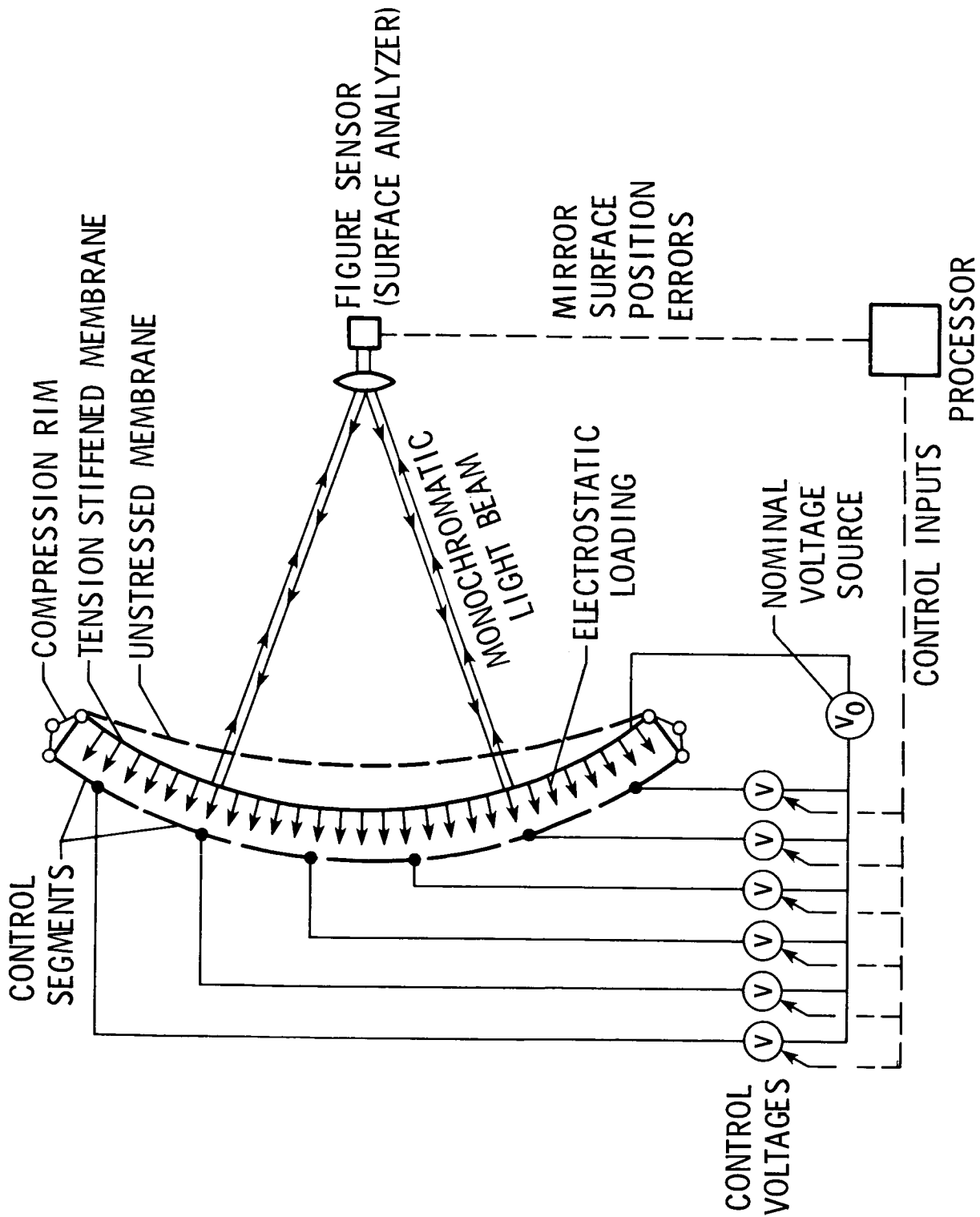
Figure 5.- The electrostatically controlled membrane concept.
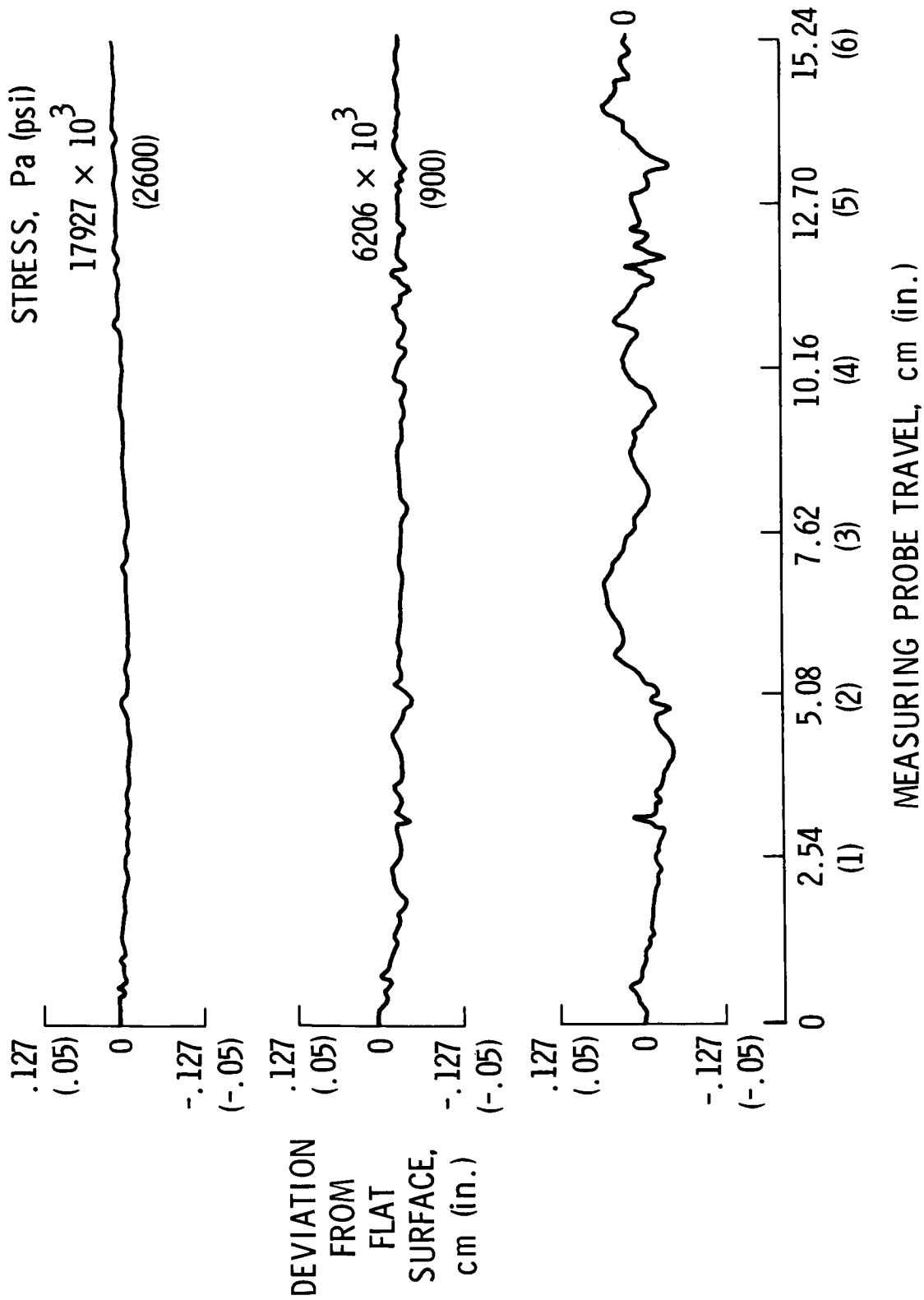
(a) Aluminized Mylar, 0.0025 cm (0.001 in.) thick.

Figure 6.- Surface flatness measurements. Dimensions are in cm (in.).
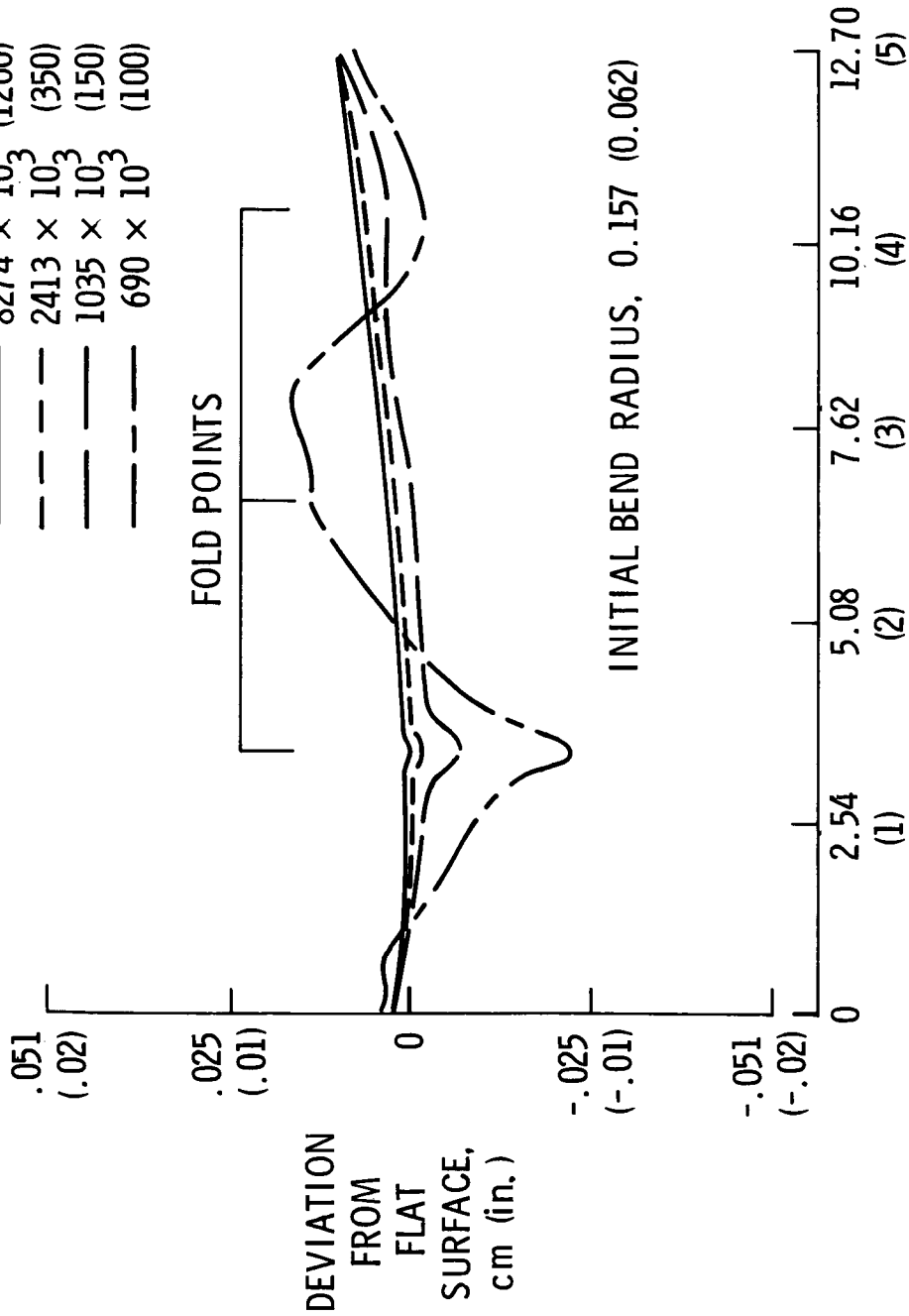
(b) Aluminized Mylar, 0.0051 cm (0.002 in.) thick.

Figure 6.- Concluded.
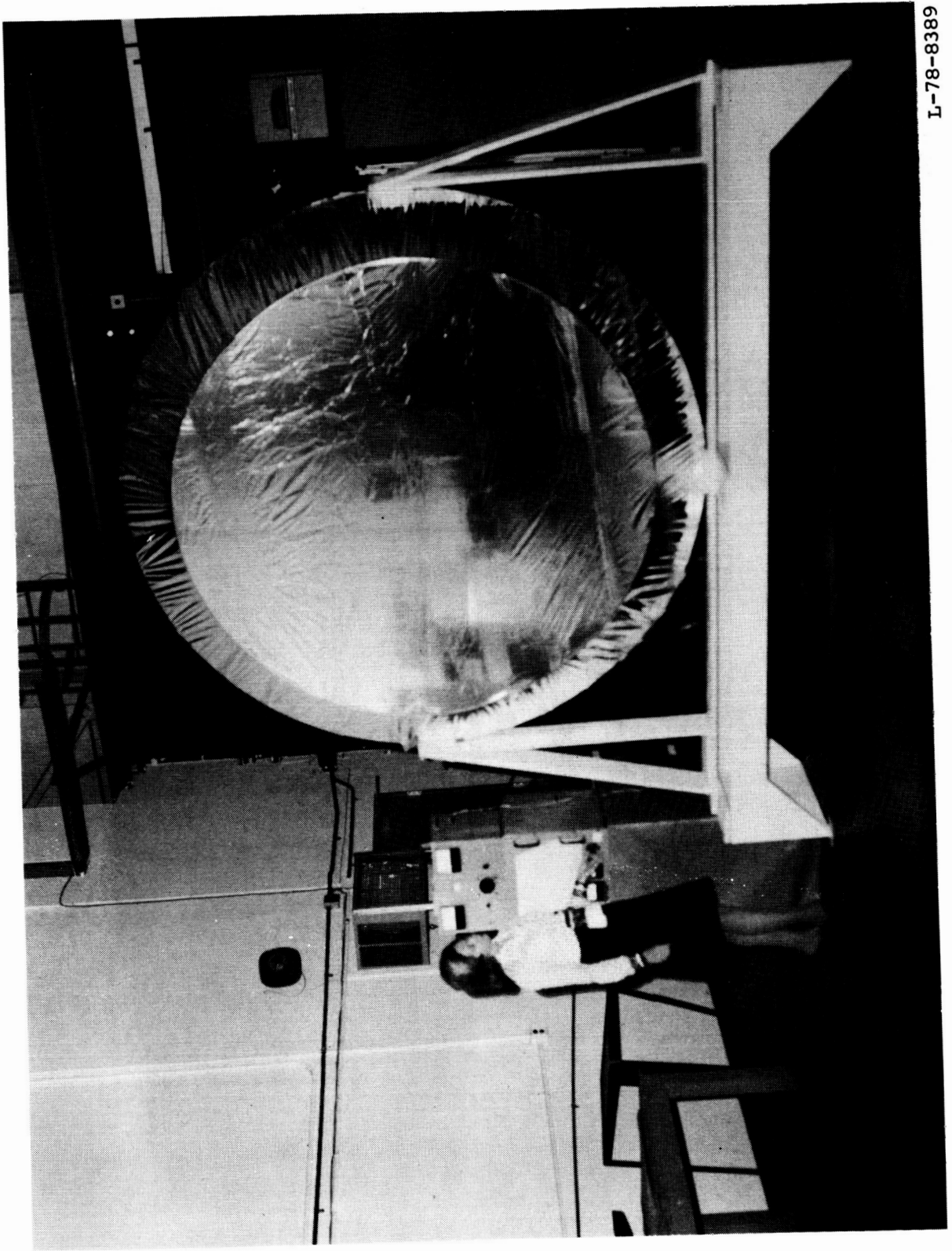
Figure 7.- Untensioned 1.83-m (6-ft) diameter membrane.

L-78-8389
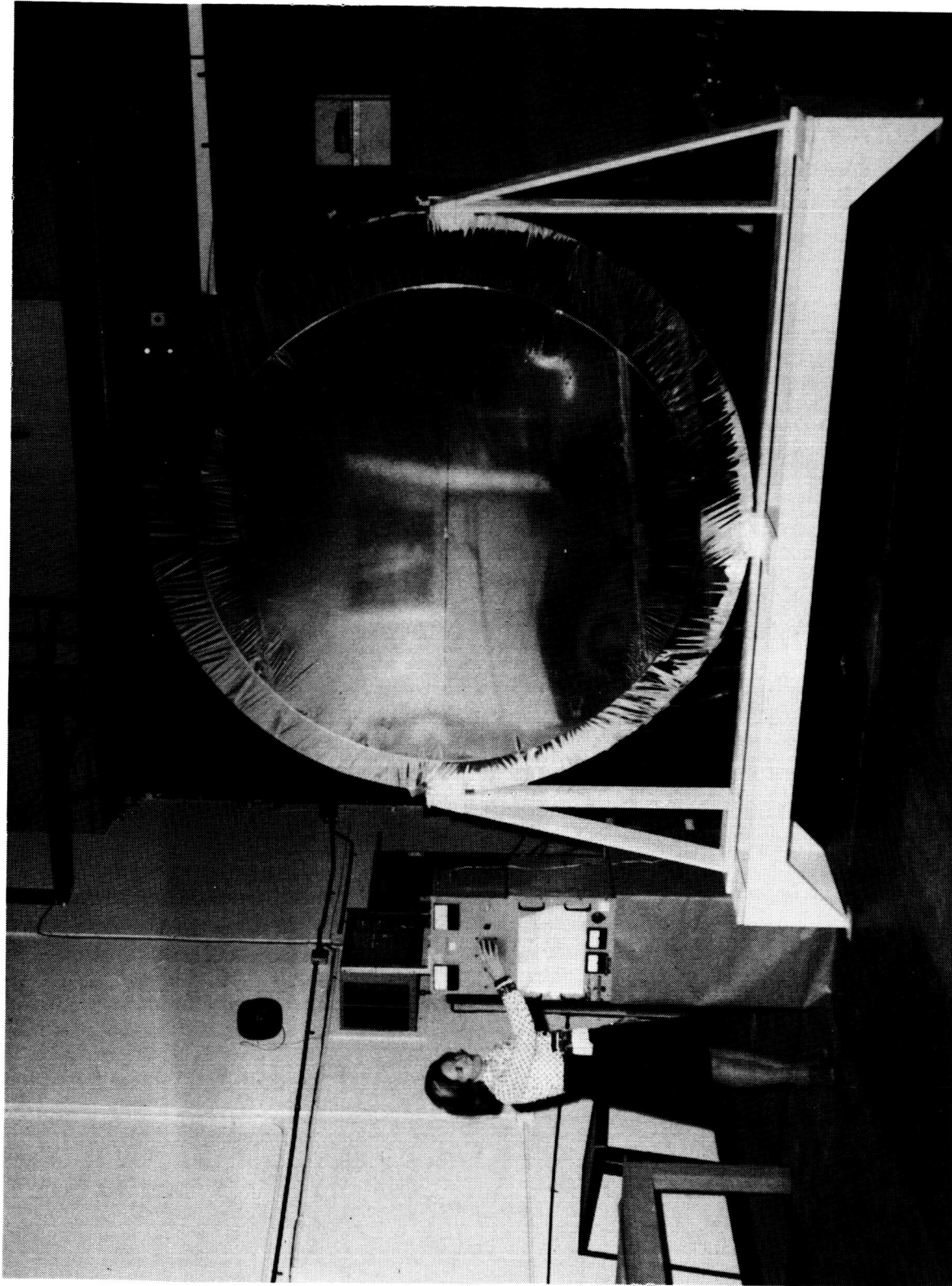
L-79-8388

Figure 8.- Tensioned 1.83-m (6-ft) diameter membrane.
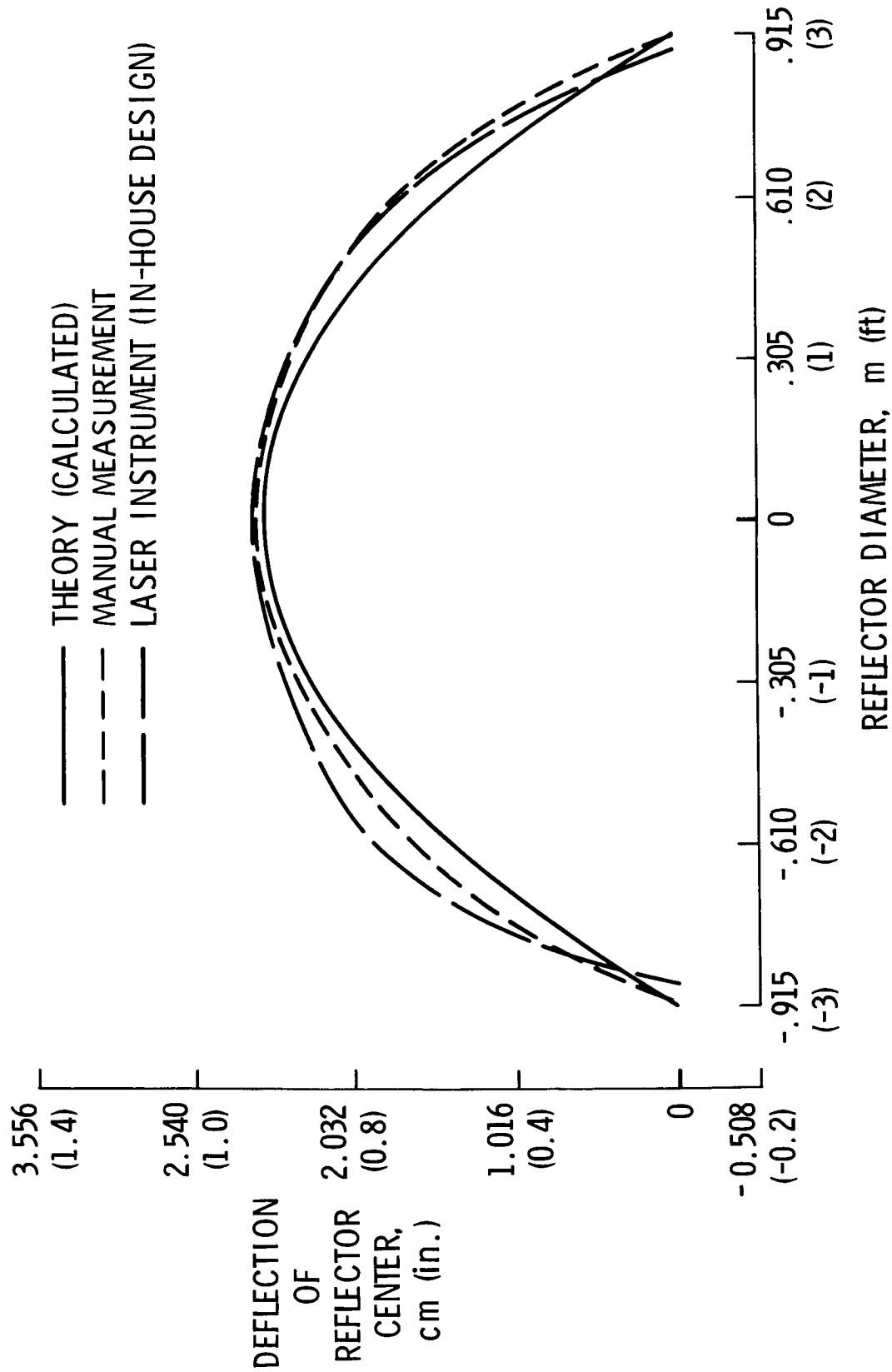
Figure 9.- Material surface deflection measurements of electrostatically formed reflector. Focal length/diameter = 4.4.

BOOTLACE CATENARY CONCEPT FOR ANTENNA SHAPE CONTROL

James H. Ramsey
Kentron International, Inc.
Hampton, Virginia

and

Robert L. Wright
NASA Langley Research Center
Hampton, Virginia

SUMMARY

A preliminary design of the microwave radiometer spacecraft (MRS) using the bootlace catenary shaping concept was developed. The application of this radically different design for shape control of the antenna membrane was assessed and possible sources of inaccuracies and errors were investigated.

INTRODUCTION

Large-diameter antennas (diameter greater than 100 m) are susceptible to distortions resulting from a combination of effects from the space environment (e.g., temperature extremes, solar pressure, and micrometeoroid impacts) and materials behavior (e.g., graphite microcracking and moisture dry out and creep of pretensioned elements). Performance requirements for these antennas dictate the use of in-orbit surface adjustments to control and minimize the distortions.

The use of a stretched membrane in a tensioned structure (without any strongback support) has been proven as an effective approach for lightweight, precision antennas in the smaller sizes up to 20 m in diameter. The typical construction of this design uses a balanced pair of membranes (upper and lower) which are supported on a rigid hoop, as shown in figure 1. The two membranes are drawn together into the desired shape by a number of tension lines between the two surfaces. The contour of the reflecting surface is set by exact tailoring of each tension line.

The potential accuracy and weight benefits of the stretched membrane offer a promising approach for the 750-m-diameter MRS antenna, for which both of these factors are critical. However, in scaling this design to the MRS application, several problems are encountered. Thermal ranges and gradients, which are more controllable in a smaller antenna size, will present severe problems of reflector distortion in any fixed design such as the typical configuration of figure 1. The contour of the smaller antenna is exactly tailored to shape during construction on the ground, but the gravity effects on a 750-m-diameter antenna would preclude any accurate shaping in the Earth's gravity field. Even if a 750-m-diameter antenna could be accurately constructed on the ground, it would be virtually impossible to launch into orbit.

Furthermore, with tension lines normally spaced at intervals of 4 to 5 m, the number of lines to be trimmed becomes enormous on a 750-m system. Because of these problems, a radically different approach was investigated for shape control of the unsupported stretched membrane on the microwave radiometer spacecraft.

BOOTLACE CATENARY SHAPING CONCEPT

The bootlace catenary shaping concept is based on the fact that a stretched line with uniform loading at equal increments will assume a curve which is a precise parabolic curve (see fig. 2) defined by the formula

$$y = \frac{F}{2t_o} x^2$$

where y is deflection, F is loading (uniform), t_o is tension at attachment, and x is axial length from attachment. As dictated by this formula, the curve is defined solely by the ratio of forces. The curve is unaffected by the characteristics of the material or other external conditions so long as the ratio of forces is maintained constant. This relation indicates a method which can compensate for thermal changes and which is not primarily dependent on the uniformity of material to maintain accuracy of the curve.

Surface height is modified at specified radial boundaries (adjustment planes) by changing the tension in a crisscross, single-cord/multiple-pulley arrangement (shown schematically in fig. 3), which has the appearance of a "laced" boot when viewed in the plane of the reflector surface.

Control of the curve along a ring diameter is achieved by the combination of vertical adjustments at each end plus the curvature control. With these three controls, it is possible to achieve essentially complete control of the whole curve along a ring diameter.

Because of the comparatively light forces and thin lines required, the chances of control-line breakage from internal or external factors is very slight. However, a redundancy may be included if necessary by inclusion of more radial elements than specifically required for surface accuracy.

The advantages of this bootlace catenary design include (1) simple shape adjustment in orbit, (2) inherent thermal compensation, and (3) use of shape control for final accuracy to eliminate precision construction operations.

By changing the tension t in the common bootlace line, the amount of shaping tension f may be varied simultaneously in each load line. The vertical force on each load line is a direct function of tension and the angle of forces ϕ at each pulley so that $f = 2t \cos (\phi/2)$. The vertical lines (splining elements) are cut so as to put all pulleys in straight lines at the desired curvature, with the result that all loading forces are identical. The system will accommodate an appreciable deviation from design curvature since the differential force Δf in each line is only $\Delta f \approx t \sin \Delta\phi$ where $\Delta\phi$ is normally quite small. For the same reason, the surface-shape accuracy is comparatively insensitive to errors in the vertical line lengths, so precision on-site trimming is not necessary.

206

To achieve a spherical rather than a parabolic shape, it is only necessary to taper the interval between loading lines across the diameter. The amount of taper (i.e., the interval decrement) to convert from parabolic to spherical is quite small and can be easily computed (although the computation was not done in this preliminary study).

MRS DESIGN

The bootlace catenary concept was investigated as an alternate design concept for surface-shape control of the MRS antenna. A detailed view of a radial adjustment element of the bootlace catenary system and one gore of the antenna surface are shown in figure 4. The antenna surface is composed of a fine metallic mesh. The assembly of 18 gores and associated radial adjustment elements defines the MRS antenna shown in figure 5. The structure of this alternate design is identical to the basic MRS design of reference 1, with the exception of the rim supporting the antenna system.

BOOTLACE CATENARY CONCEPT ASSESSMENT

A preliminary assessment of the application of the bootlace catenary concept for surface-shape control of the MRS antenna was conducted under contract and is reported in reference 2. Numerous possible sources of inaccuracies and errors were identified and are discussed hereinafter.

Radial Adjustment Elements

Surface-shape control adjustments are made at the intersection (boundary) of antenna-surface gores. The increased (or decreased) tension in the cords will tend to be partially dissipated in the mesh adjacent to the cords. Thus the effects of the height adjustments are localized. For the large spans (i.e., distances between boundaries) which exist on this antenna, this adjustment coarseness is not sufficient. Surface sensitivity analyses using a detailed finite-element model could determine the required number of adjustment boundaries. However, even a tenfold increase in the current number (from 18 to 180) would still result in tip spans greater than 12 m.

Friction between the pulley groove and the quartz-cord drawstring, particularly in a vacuum, could be quite large. The friction forces would generate a nonuniform tension in the drawstring with the maximum tension being adjacent to the take-up spool/winch drive on the rim and the minimum tension being at the hub of the spacecraft. If the friction forces are large enough, the original tension in some parts of the drawstring would be unchanged by an adjustment.

Thermal effects on the pulleys and/or the drawstring could produce undesirable results, particularly when the thermal environment is not uniform (e.g., side Sun condition and shadowing).

The adjustment forces react against a rear surface, which is a net or metallic-mesh material. Previous work with a double-mesh concept and breadboard models revealed the relative instability of this approach. The mesh material is nonlinear and is not as predictable or as controllable as pretensioned cords or other "rigid" members (e.g., graphite strips or beams). Hence, a better approach would be to have the drawstring tension changes react into a stiffer outer trusswork, or rim.

The same structure at the surface center (hub) reacts to tension changes in opposite adjustment boundaries, that is, boundary number 1 is connected to boundary number 10, boundary number 2 is connected to boundary number 11, and so on. Since the tension changes (adjustments) in all 18 boundaries will be different, the possibility exists that entire boundaries will be translated laterally (relative to the antenna centerline) in order to achieve static equilibrium. If the movement is large enough, appreciable mispointing will result. Each boundary should react independently and adjustments in one boundary should not affect any other boundary.

Pillow Roughness

Pillowing of the antenna surface as a result of the spacing of the quartz-cord drawstring produces a roughness effect on the metallic-mesh membrane. Pillow roughness can be approximated with the following formula (ref. 3):

$$\text{Roughness} = \frac{1}{4}\left[\left(\frac{1}{\cos\theta}\right)\frac{PL^2}{8N_c} + \frac{L^2}{16f}\right]$$

where

θ $= \tan^{-1}(r/2f)$

r radius to the pillow

f focal length

L cord-to-cord spacing

P equivalent mesh pressure, $\frac{1}{2f}(N_c \cos\theta + N_R \cos^3\theta)$

N_R radial mesh tension

N_C circumferential mesh tension

By assuming $N_c = 35.0$ N/m, $N_R = 17.5$ N/m, and that a pillow located at 2/3 of the tip radius represents a nominal pillow, the pillow roughness effect was computed to be 0.673 cm for the proposed 10-m spacing. This is an unacceptable value. Figure 6 is a graph showing pillow roughness as a function of cord spacing. Recognizing that other parameters will also contribute to the total surface roughness (e.g., manufacturing inaccuracies and thermoelastic effects), the recommended cord spacing should be on the order of 4 m with a pillow roughness effect of about 0.127 cm.

Drawstring-Temperature Controllers

Each gore (the metallic-mesh antenna surface between radial-adjustment elements) is maintained in an "as set" condition by using drawstrings to connect the two surfaces and properly shape the contour. Thermal shading of portions of the antenna surface would produce thermal gradients in the mesh material and the attached drawstrings. The resulting effect of thermal expansion on the drawstring length would be a change in the drawstring tension, and therefore a drawstring-temperature controller

is required to compensate for the resulting force imbalance. The temperature controllers must be capable of accurately compensating for temperature excursions of 200° to 260°C.

For the gore design of figure 4, as many as 222 drawstrings and temperature controllers would be required per gore, resulting in a total of 3996 for the entire antenna. As shown in the pillow roughness/cord spacing curve of figure 6, a more realistic spacing would require 2 to 3 times as many drawstrings and temperature controllers.

In-Orbit Distortion

The desired surface accuracy (ref. 4) of 1/50 of a wavelength ($\lambda/50$) translates into a total roughness of 0.610 cm at 1 GHz and 0.122 cm at 5 GHz. (The accuracy is assumed to apply over the entire operational bandwidth.) These values should be examined from a physical standpoint to fully appreciate the surface-accuracy requirements. Even using the larger of the two roughness values (0.610 cm), the rms of the distortions from the desired contour is approximately the thickness of 3 nickels for an antenna diameter of almost 1 km. This is less than 10 ppm. By comparison, the tracking and data relay satellite system (TDRSS) antenna has a roughness-to-diameter ratio which is over 100 ppm. Extrapolation of the current technology would yield a roughness prediction of over 5.08 cm for the proposed MRS antenna, and this does not account for an added complexity factor associated with antenna size.

Achievement of the goal of $\lambda/50$ is integrally related to state-of-the-art advancements in manufacturing techniques, analysis techniques, surface-set capabilities in 1g, and in-orbit surface-adjustment methods. The latter is probably the driving force in achieving high-accuracy antennas of extremely large diameter. Assuming tremendous advancements in all of the areas mentioned, the desired $\lambda/50$ is conceptually possible at the lower frequency spectrum of 1 GHz. However, this same roughness value (0.610 cm rms) translates into a $\lambda/10$ surface accuracy at 5 GHz. Therefore, a surface accuracy of $\lambda/50$ for the higher frequencies does not appear possible. A "sliding scale" accuracy requirement is thus recommended for the MRS mission, with accuracies ranging from the two extremes ($\lambda/50$ at 1 GHz and $\lambda/10$ at 5 GHz).

More realistic distortions for a 750-m-diameter antenna are presented as follow. These distortions lie between the desired accuracy of $\lambda/50$ at 1 GHz and current-technology extrapolations. It is recommended that radio-frequency (RF) performance predictions and budgets reflect these values.

$$\text{Roughness} = \sqrt{\left(\begin{array}{c}\text{surface}\\\text{set}\end{array}\right)^2 + \left(\begin{array}{c}\text{thermoelastic}\\\text{distortions}\end{array}\right)^2 + \left(\begin{array}{c}\text{measurement}\\\text{errors}\end{array}\right)^2 + \left(\text{uncertainties}\right)^2}$$

$$= \sqrt{(0.76)^2 + (0.99)^2 + (0.51)^2 + (0.51)^2}$$

$$= 1.44 \text{ cm}$$

This roughness translates into an accuracy of approximately $\lambda/20$ at 1 GHz and $\lambda/4$ at 5 GHz. Also, defocus distortions of 12.70 cm and mispointing distortions of 0.05° can be expected with the current state of the art.

These summary distortions represent a projection of technology advancement and an appreciation of the overall complexity due solely to the size of the antenna. They may, in fact, be overly optimistic. However, the values are believed to be more achievable than current estimates, and therefore they should be used for future mission-performance assessments until better data become available.

CONCLUSIONS

The bootlace catenary concept was assessed for shape control of the stretched-membrane antenna system of the MRS and a preliminary design was developed. The assessment included possible sources of inaccuracies and errors in the concept that require further study. The major conclusions of the investigations are:

1. The bootlace adjustment technique is feasible. However, there are several areas where the design is deficient or can be improved upon. Most notable are the cord/pulley friction effects and the reaction of the drawstring tension into a non-linear material (mesh) on both the front and rear surfaces. Reacting this tension into the outer rim is a preferable approach.

2. If the drawstring approach is perfected, the number of adjustment boundaries must be increased significantly. The number required is related to the desired surface accuracy.

3. The current cord spacing of 10 m should be reduced at least to 4 m to reduce pillow effects to reasonable magnitudes.

4. Publicized and currently expected surface accuracies are not possible for the 5 GHz application and are questionnable for the low-frequency regime (1 GHz). A range of $\lambda/10$ to $\lambda/20$ seems to be a more realistic value for mission planning purposes.

REFERENCES

1. Wright, Robert L.: Evolution and Design Characteristics of the Microwave Radiometer Spacecraft. The Microwave Radiometer Spacecraft – A Design Study, Robert L. Wright, ed., NASA RP-1079, 1981, pp. 51-66. (Paper in this compilation.)

2. Harris Corp.: Assessment of Surface Accuracy and Aperture Blockage of Deployable Reflector Concepts. NASA CR-165783, 1981.

3. Harris Corp.: AAFE Large Deployable Antenna Development Program, NASA CR-159013, 1976.

4. Lovelace, Uriel M.: Executive Summary. The Microwave Radiometer Spacecraft – A Design Study, Robert L. Wright, ed., NASA RP-1079, 1981, pp. 1-14. (Paper in this compilation.)

20-m TENSION REFLECTOR

SHAPING TENSION LINES

SHAPED REFLECTOR SURFACE
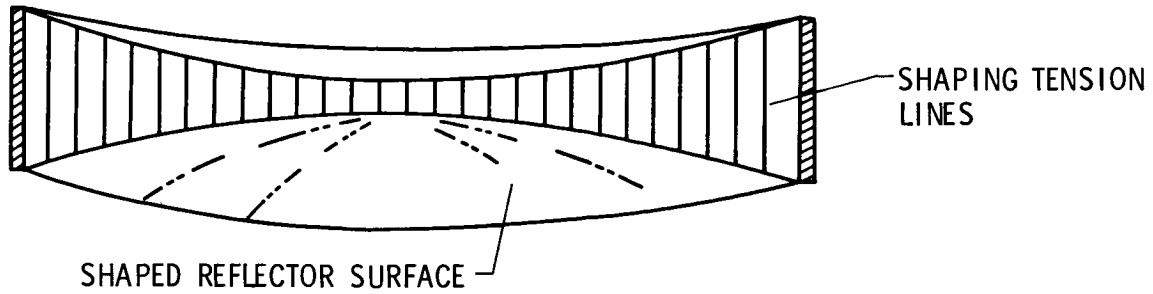
SCALING PROBLEMS FOR 100-TO 750-m-DIAMETER ANTENNA

      - THERMAL DISTORTION

      - TRIM ACCURACY AT ZERO g

      - CONSTRUCTION COMPLEXITY

Figure 1.- Stretched membrane in a tensioned structure (reflector) with shaping tension lines.

UNIFORMLY LOADED LINE

MATHEMATICALLY DEFINED CURVE,

$$y = \frac{F}{2t_0} x^2$$
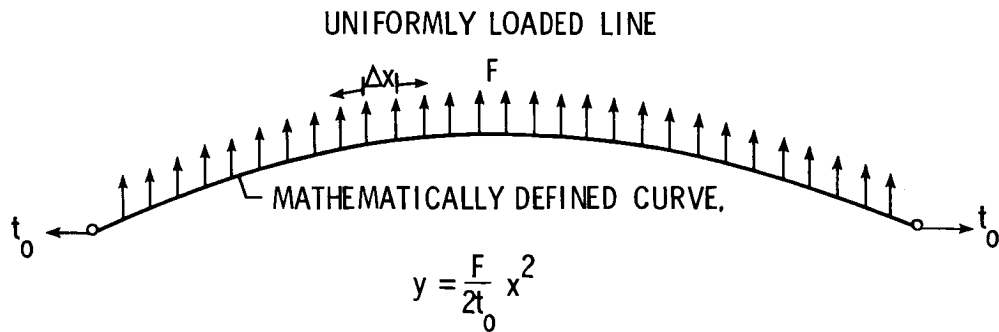
BOOTLACE CONCEPT

    — UNIFORMLY VARIABLE FORCE SYSTEM
    — FLOATING-PULLEY ARRAY

$$F = 2t \cos (\phi/2)$$
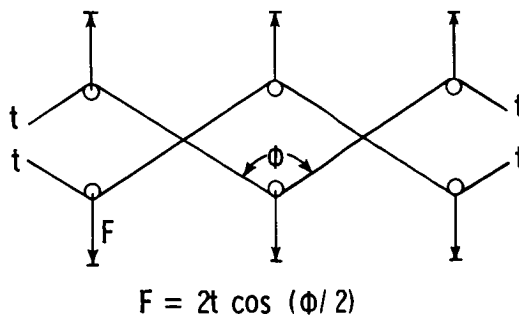
Figure 2.- Stretched membrane in a tensioned structure (reflector) with floating-pulley array.

211

RADIAL ANTENNA ELEMENT

FEATURES:

THERMAL COMPENSATION
TENSION CONTROL

ERROR TOLERANCE
FLOATING PULLEY

$\Delta F \approx t \times \sin \Delta\Phi$
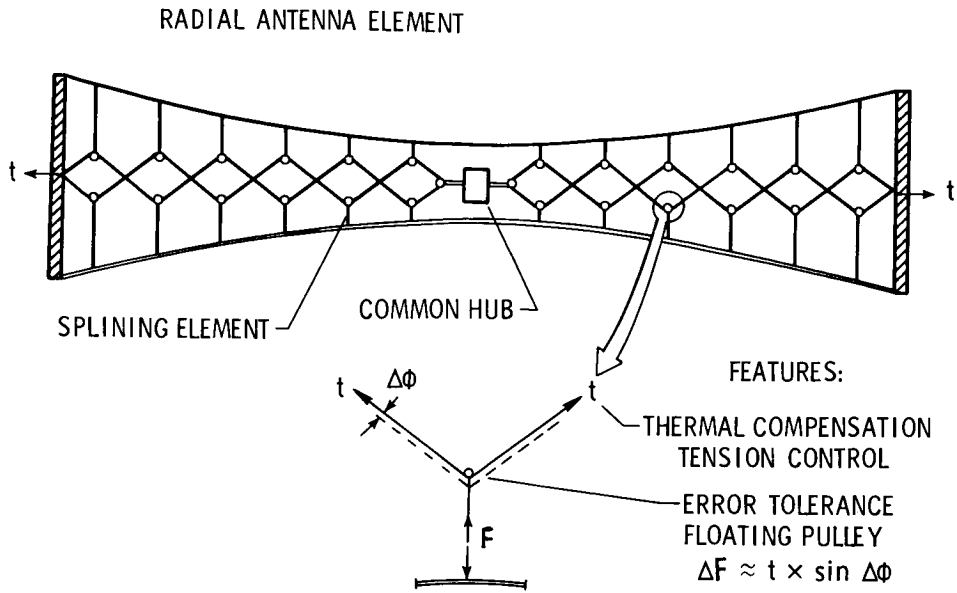
Figure 3.- Bootlace catenary shaping concept.

TOP VIEW

TENSION SPOKE

METALIZED MESH
(ON THIS SURFACE ONLY)

1150-m RAD.

SIDE VIEW

DISTANCE BETWEEN
PULLEYS WILL VARY

RIM

PULLEYS ATTACHED
TO MAIN GORE

REVERSE TORQUE
DRIVE

WINCH DRIVE

NO METALIZED MESH ON THIS
SURFACE; NET ONLY
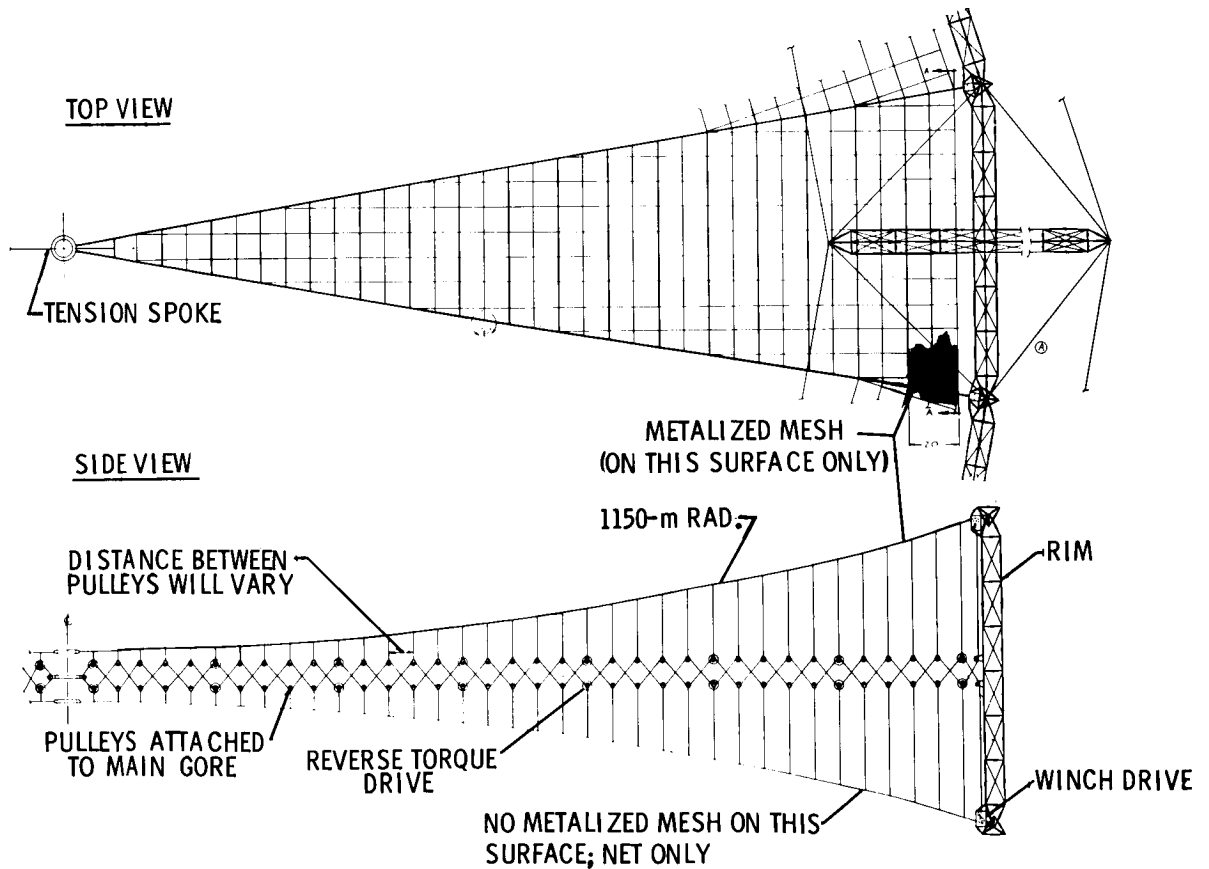
Figure 4.- Antenna gore showing radial adjustment element.
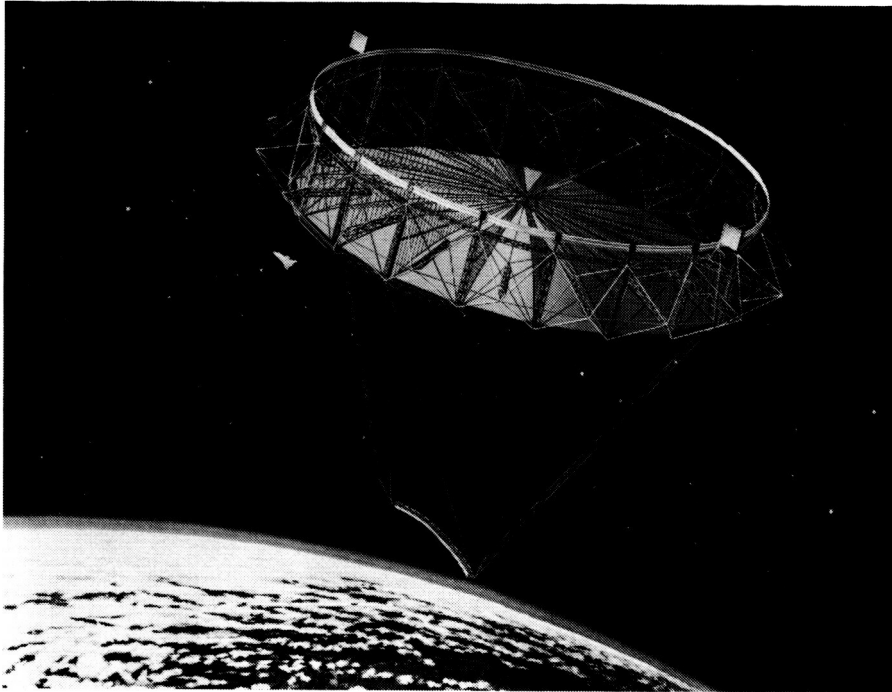
L-81-7540

Figure 5.- Pictorial representation of MRS antenna configuration using bootlace catenary shaping concept.
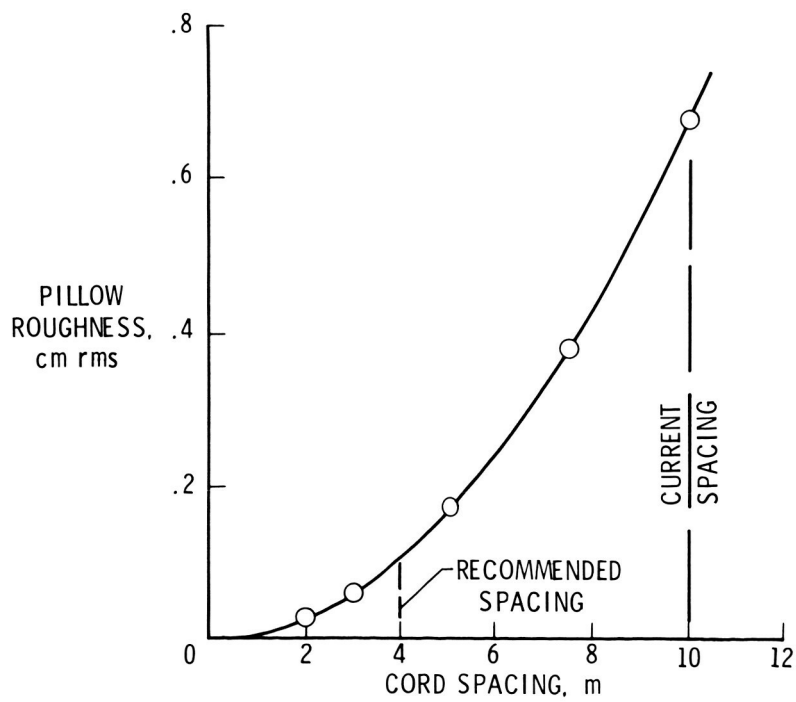
Figure 6.- Pillow roughness as a function of cord spacing (from ref. 2).
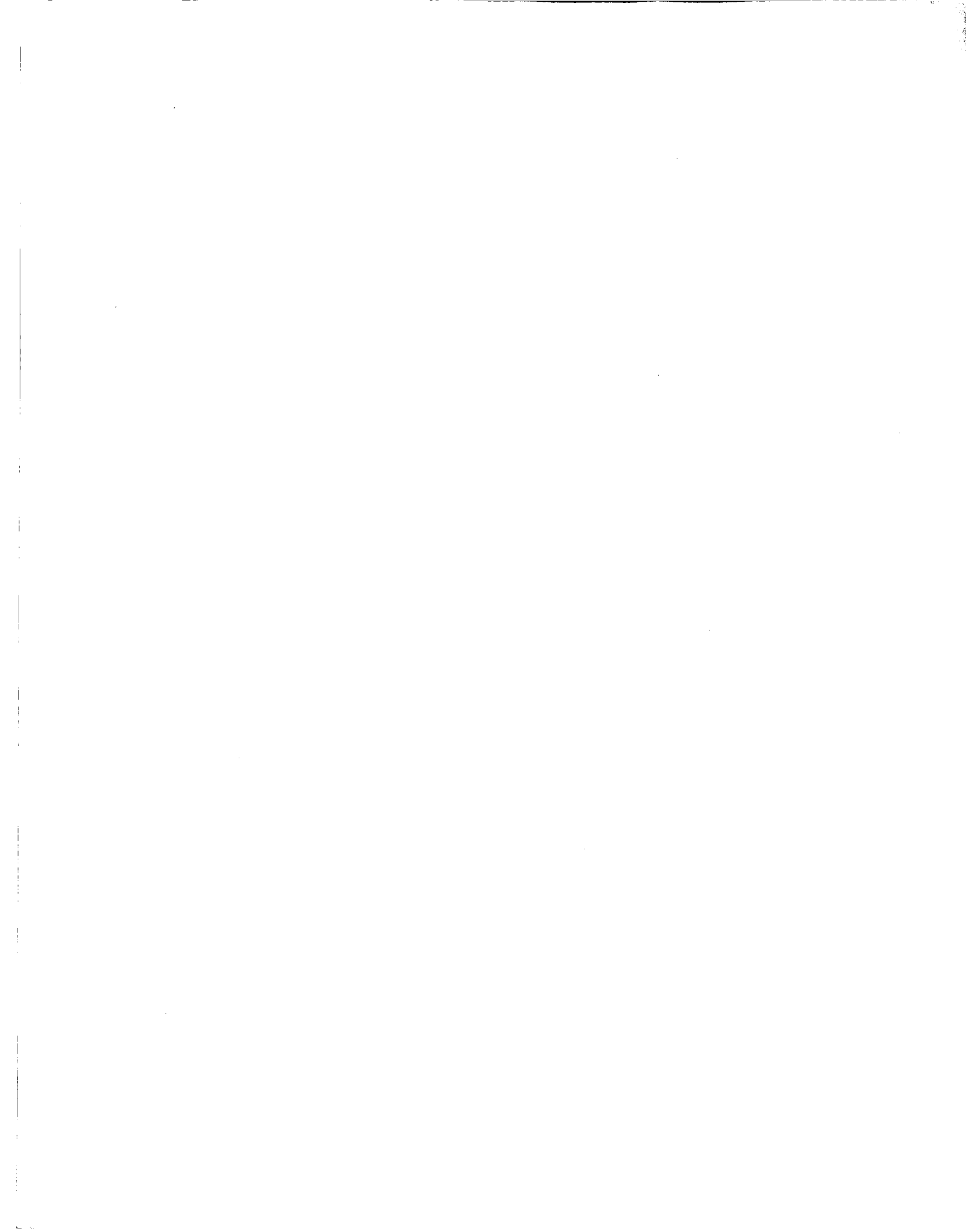
APPENDIXES

APPENDIX A

GLOSSARY OF TERMS AND ACRONYMS

Terms

Bay - The number of tetrahedrons arranged in a straight line to form the maximum diameter of a structure

Bootlace catenary - Shaping concept using pulleys and cords to provide uniform loading which produces a precise curvature to a stretched line or membrane

Brightness temperature - A measurement of radiated energy from the surface of the Earth, the product of soil ambient temperature and emissivity

Cluster fitting - A fitting interconnecting the surface elements with the intersurface elements

Contiguous mapping - Mapping without gaps in the coverage (each mapped segment is adjacent to another mapped segment)

Deployable structure - A structure that is manufactured, assembled, and packaged on Earth, transported in the packaged condition to orbit, and deployed

Double layered - A structure with primary and secondary surfaces separated by intersurface elements

Erectable structure - A structure whose members are manufactured on Earth, packaged, and transported to orbit where they are removed and assembled by means of EVA and/or RMS

Facet - A small plane surface

Feed beam - Support structure for feed horns

Geodesic - Defined by the shortest line on a mathematically derived surface between two points on the surface

Intersurface elements - Elements connecting the primary and secondary surface of a double-layered structure

Kapton* - Polyimide film

---

*Registered trade name of E. I. DuPont de Nemours & Co., Inc.

Kevlar* - Organic film within the family of aromatic polyamids

Measurand - A physical quantity or condition which is to be measured

Microwave sensing - Sensing in the wavelength region of approximately 250 μm to 1 m

Near all-weather - All weather except for conditions of extremely heavy clouds or rain

Nestable column - A column composed of two tapered half-columns which nest like plastic cups for transportation to orbit and are assembled in orbit by joining together the larger ends

Node - A terminal of any branch of a network or a terminal common to two or more branches of a network, junction

Optical sensing - Sensing in the wavelength region of approximately 0.25 μm to 250 μm

Passive microwave sensing - Sensing of natural microwave radiation (no irradiation by sensing system)

Phased array - An array of antennas electronically phased to provide cross-track scanning

Push broom - A concept of using multiple receivers mounted in a cross-track fashion to provide continuous cross-track scanning

Repetition factor - Number of orbits per day required for the orbiting spacecraft to revisit the same location on the Earth in a given time cycle (1, 3, 7, 14 days)

Resolution element - Assigned field of view at the Earth's surface during a single measurement sequence

Scatterometer - A device that illuminates a distributed target and measures the back-scattered electromagnetic radiation

Strongback - Support structure for the antenna

Support column - Structural column that supports the feed beam at the focal arc of the reflector

Swath - Observed path of the spacecraft on the Earth's surface during an orbital transit

Synthetic aperture - A technique using timing and Doppler frequency shift of the return signal to obtain better spatial resolution than that normally obtained with the actual antenna aperture

Temporal repeat - Time required for the spacecraft to revisit a specified target or scene on the Earth

_____

*Registered trade name of E. I. DuPont de Nemours & Co., Inc.

Tension rim - A structural concept resembling a bicycle and using a flexible catenary for support of the antenna membrane

Tessera - In mosaic mapping, segments cut in square or rectangular shapes and fashioned into the mosaic

Tetrahedral truss - A truss consisting of an array of repeating tetrahedral modules

Acronyms

AMCD	Annular momentum control device
AMFCM	Actual to modal force conversion matrix
ANALOG	Preprocessor (LASS module)
ASMR	Advanced Scanning Microwave Radiometer
AVID	Aerospace Vehicle Integrated Design (computer program)
DYLO	Dynamic Loads (LASS module)
EM	Electromagnetic
ESMR	Electronically Scanned Microwave Radiometer
EVA	Extravehicular activity by astronauts
FEM	Finite-element model
FOV	Field of view
G/E	Graphite epoxy
GTS	General Truss Synthesizer (LASS module)
IFOV	Instantaneous field of view
ITOS	Improved Tiros Operational Satellite
LASS	Large Advanced Space Systems (computer program)
LOX/LH2	Liquid-oxygen/liquid-hydrogen
LSST	Large space systems technology
MADCM	Modal to actual deflection conversion matrix
MAFCM	Modal to actual force conversion matrix
MRS	Microwave radiometer spacecraft
POST	Postprocessor (LASS module)

RCD   Rigid-Body Control System (computer subroutine)

RCS   Reaction control system

RF   Radio frequency

RMS   Remote manipulator system

rms   Root mean square

rss   root sum square

SA   Surface Accuracy (LASS module)

SAP   Structural Analysis Program (LASS module)

SIMS   Shuttle Imaging Microwave Spectrometer

SMMR   Scanning Multichannel Microwave Radiometer

SMMRE   Shuttle Multiple-Function Microwave Radiometer Experiment

STLO   Static Loads Analysis (LASS module)

STS   Space Transportation System

TA   Thermal Analysis (LASS module)

TTSS   Tetrahedral Truss Structure Synthesizer (LASS module)

APPENDIX B

SPACECRAFT DRAWINGS

J. Kermit Jensen
Kentron International
Hampton, Virginia

Detailed drawings of the microwave radiometer spacecraft (MRS) and subsystems that were developed during the design study are presented in this appendix. The spacecraft configuration is distinguished by a large (725-m-diameter) passive reflecting dish attached by two long support columns and four tension cables to a feed boom supporting a bank of 600 horn antennas. Although three concepts for the structure of the reflecting dish were studied, detailed layouts are presented only for the double-layered tetrahedral truss concept. The remaining structural components (support columns, feed boom, and feed horns) and subsystems (actuators, cables, etc.) are common to all the reflector configurations.

An assembly drawing of the MRS is shown in drawing 1. Systems, subsystems, and components for which detailed drawings are presented are noted on the assembly drawing. The following drawings are included in this appendix:

+X
-Z   +Z
-X

Momentum wheel,
attitude control system

Data management, communication,
and guidance equipment

Drawing 1

Solar power panels
(shown rotated 90°)

View J-J

4.08 m

Section H-H

J

J

575 m rad.
spherical

725 m
diam.

575 m

A

Radiometer controls
and telemetry

H

H

+Y

A

Drawings 16 and 17

Active control cables

Feed horn array,
drawing 4

1150 m rad.
spherical

See detail D,
drawings 8, 9, and 10

Reflector
surface

See detail K,
drawing 2

Main columns,
drawing 13

See detail E,
drawings 11 and 12

725-m-DIAMETER DOUBLE-LAYER
DOME ASSEMBLY

Momentum wheel
attitude control system

See detail C,
drawing 7

Drawing 1

See detail M,
drawing 3

18.00 m
Basic column
length

See detail L,
drawing 3

Location of dish
reflector surface

14.70 m

DETAIL K - DOUBLE-LAYER GEODESIC DOME

Drawing 2

DETAIL M
TRUSS MEMBER CENTER JOINT

Tapered column

Surface
attachment
point
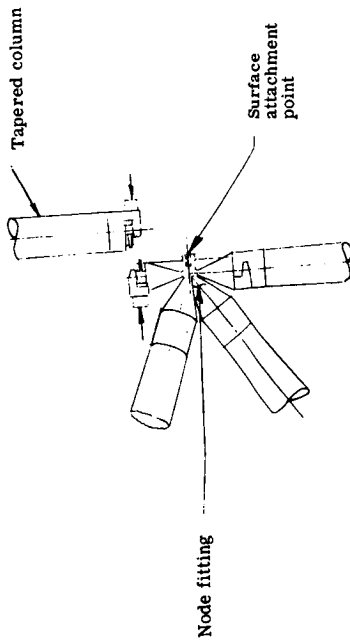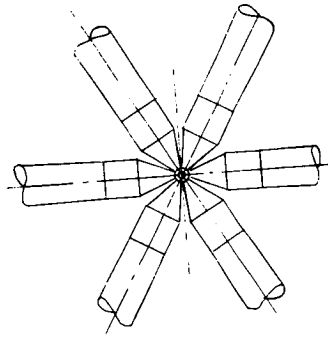
DETAIL L
END FITTING

Node fitting
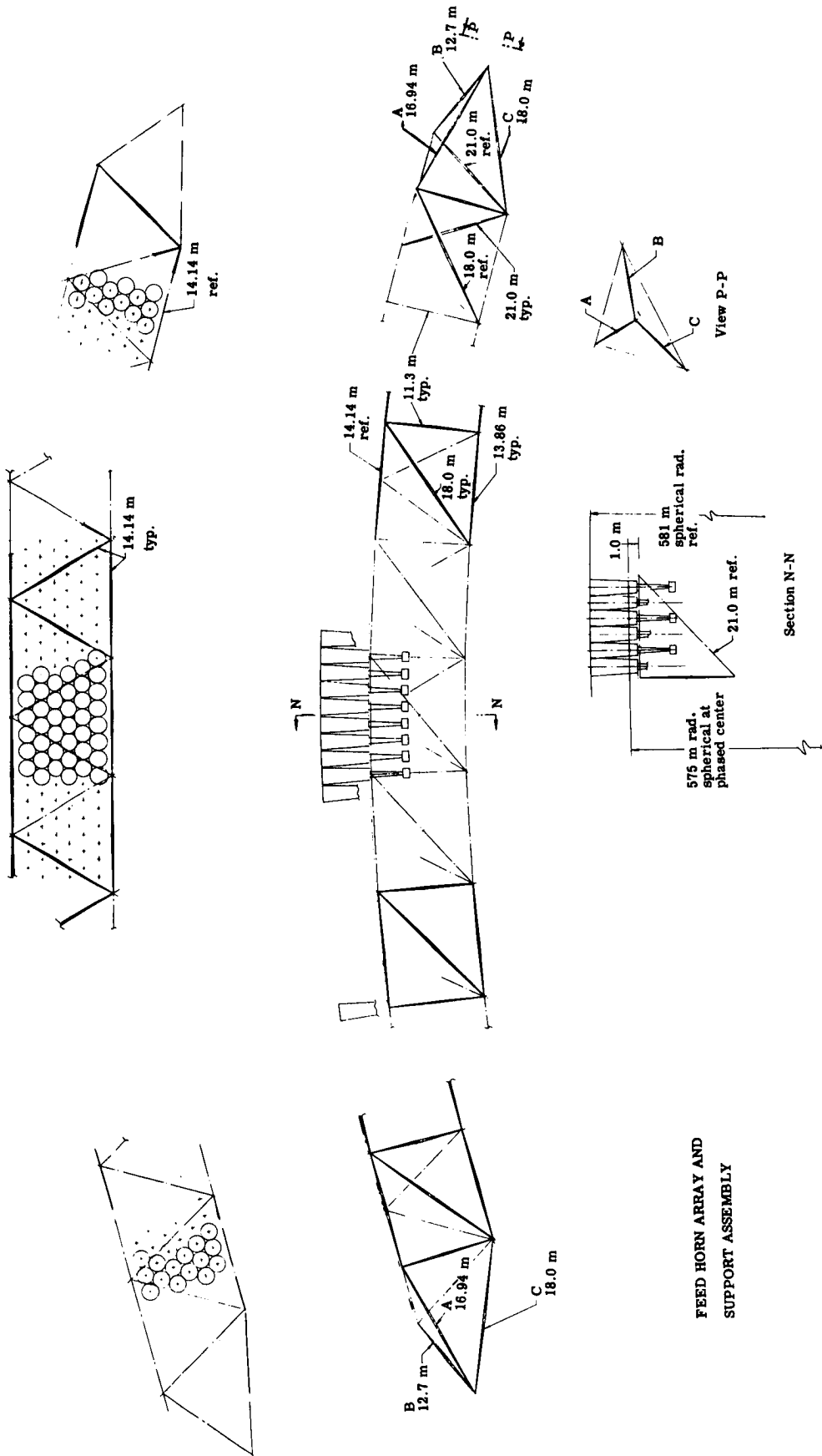
Drawing 3

FEED HORN ARRAY AND
SUPPORT ASSEMBLY

Drawing 4

A 16.94 m
B 12.7 m
C 18.0 m
21.0 m ref.
18.0 m ref.
21.0 m typ.
14.14 m ref.
11.3 m typ.
18.0 m typ.
13.86 m typ.
14.14 m typ.
14.14 m ref.

View P-P

1.0 m
581 m spherical rad. ref.
21.0 m ref.
575 m rad. spherical at phased center

Section N-N
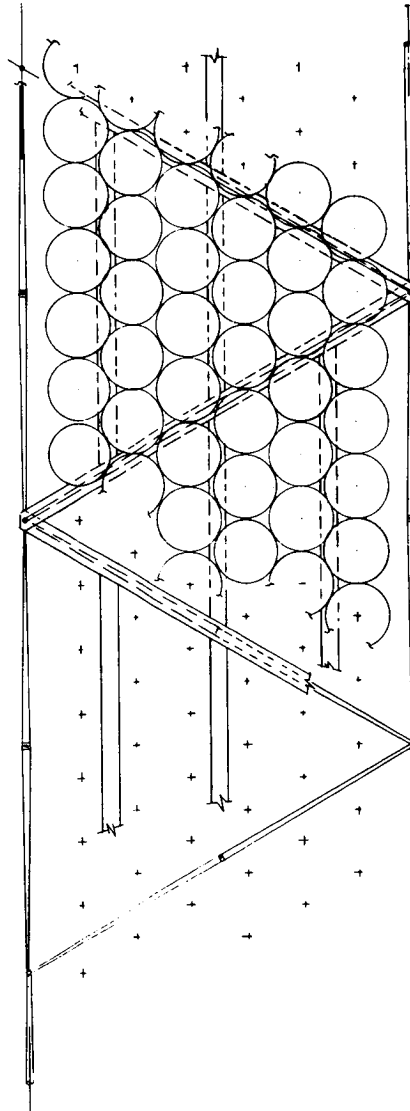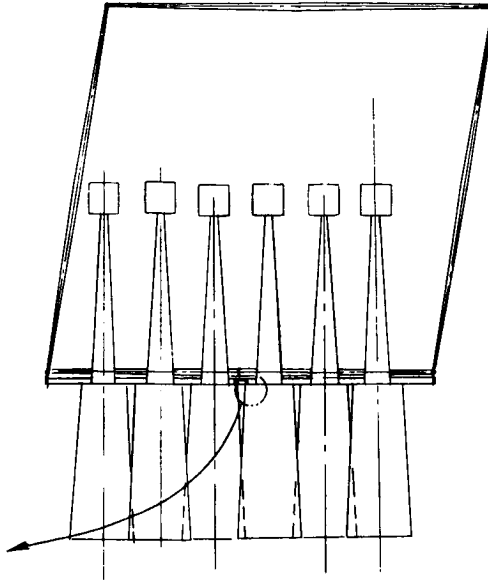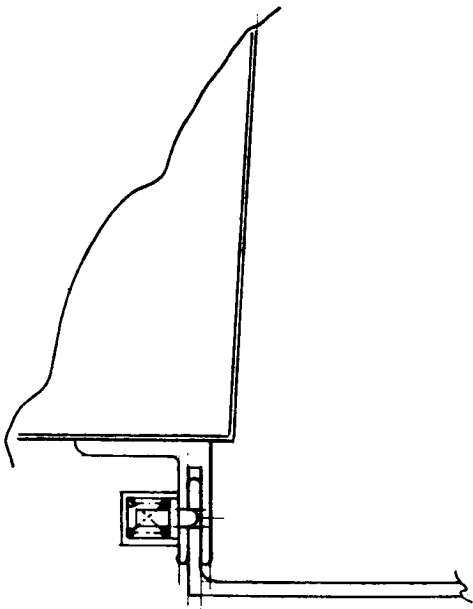
FEED HORN ATTACHMENT

Drawing 5
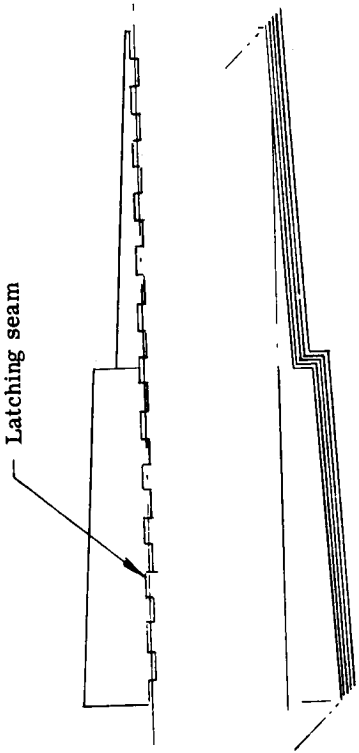
Latching seam

Split horn packaging,
<1 Shuttle flight

Cargo bay

10 m

.15-m spacing

Conical packaging,
3.8 Shuttle flights

4.57 m
diam.

Cargo bay

FEED HORN PACKAGING

Drawing 6

See node detail,
drawing 18

Dish
reflector

Attachment elements

Juncture similar
to detail D,
drawings 8, 9, and 10

Main column

Support ring
tapered column
construction
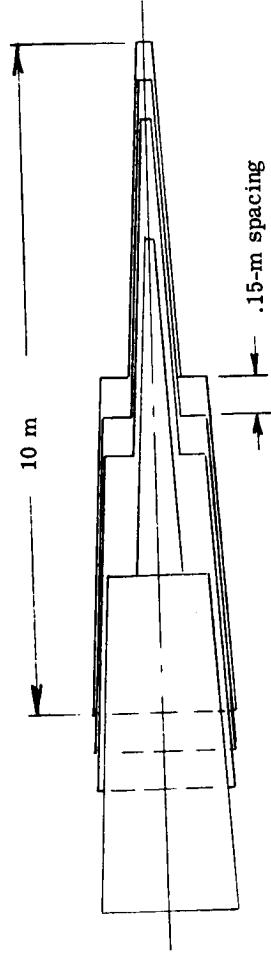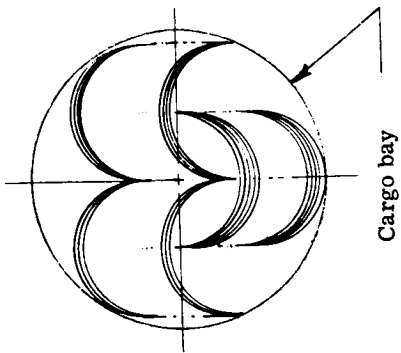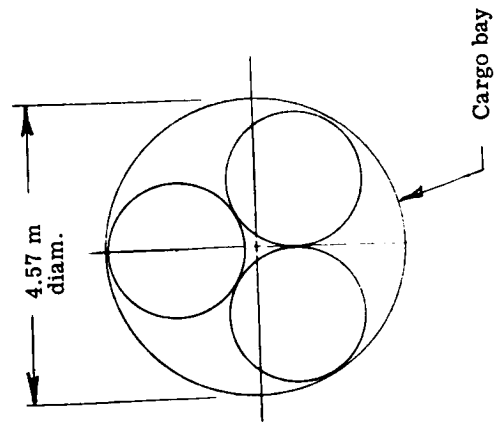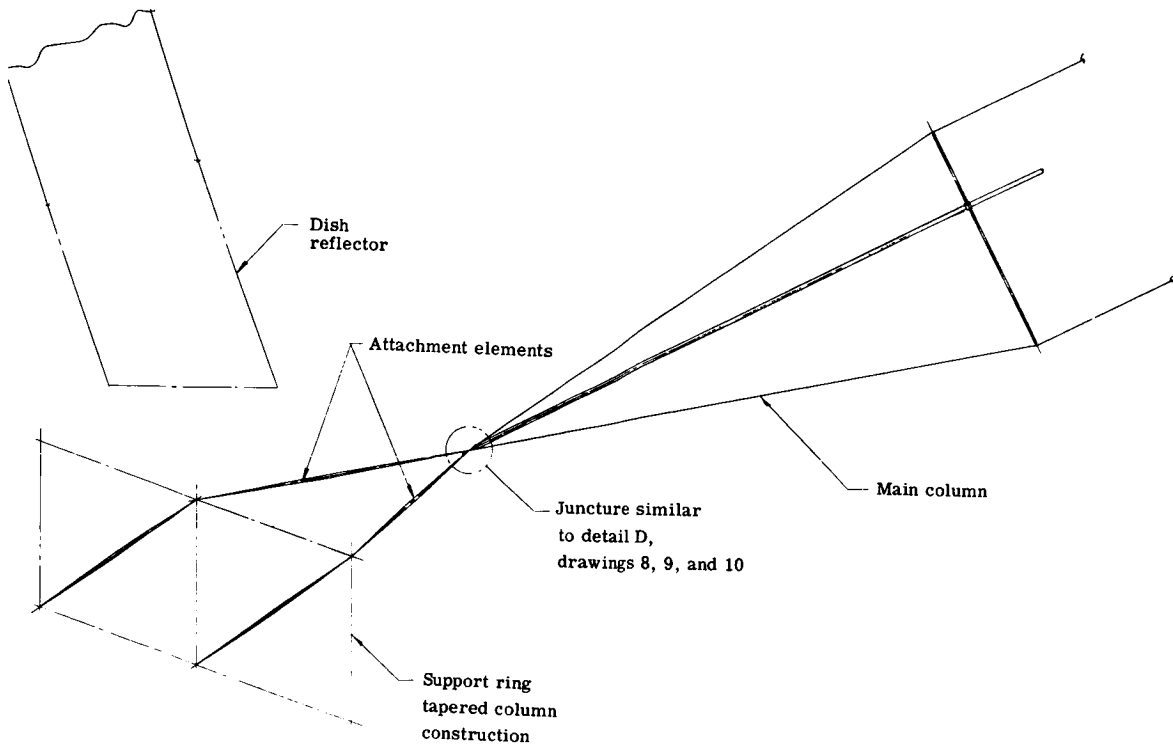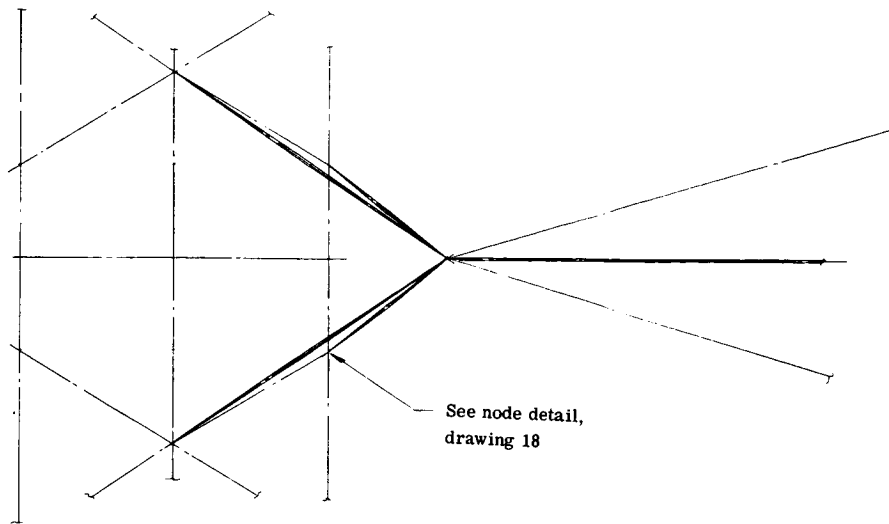
DETAIL C - UPPER COLUMN JUNCTURE

Drawing 7

Side latching end joint

Socket lock in open position

Socket lock

Radiometer structure

Ball and socket joint

Control cable

Tension stabilized columns
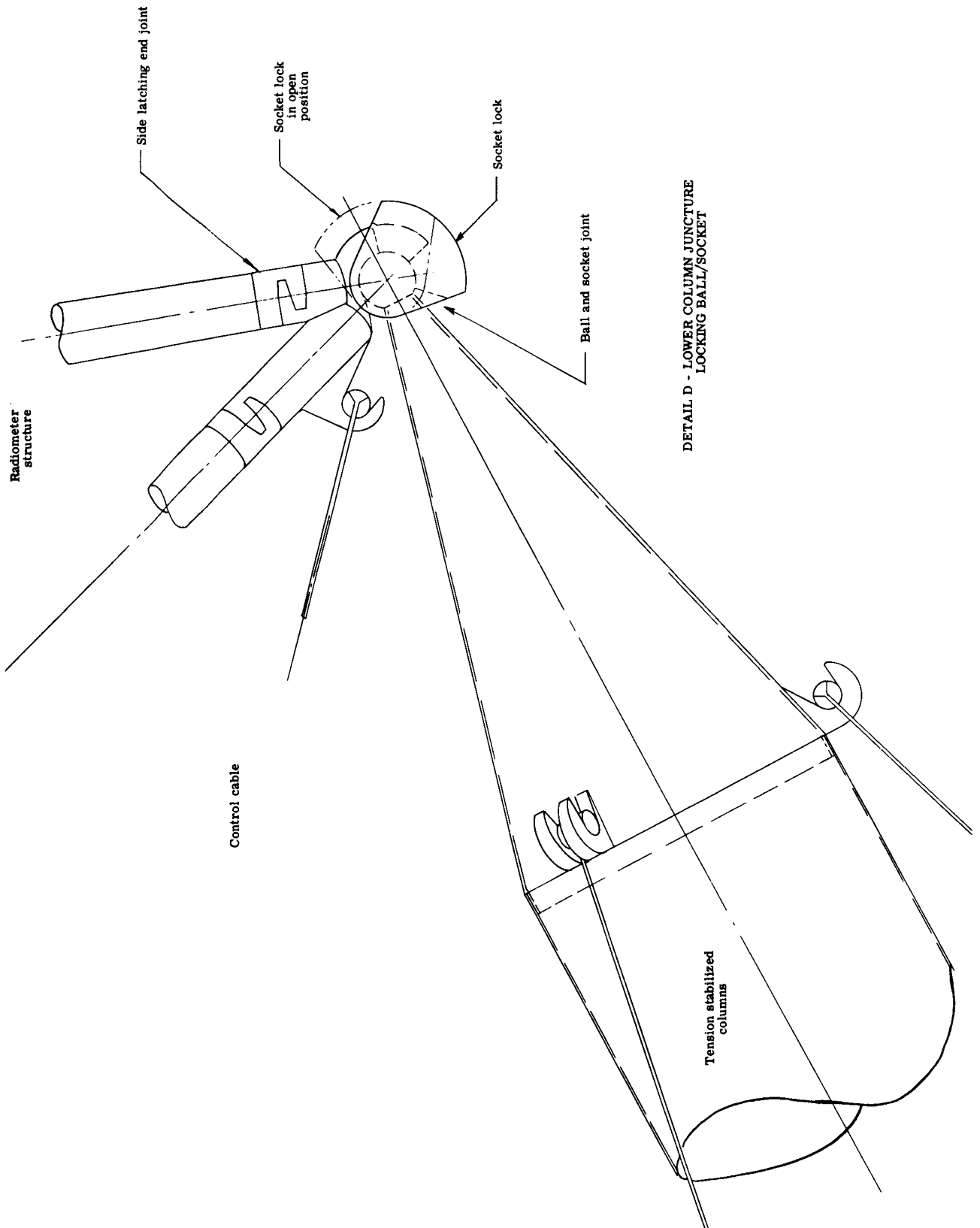
DETAIL D - LOWER COLUMN JUNCTURE LOCKING BALL/SOCKET

Drawing 8

Tapered column

Side latch joint

Prefabricated node

Radiometer structure

Probe and latch joint

Control cable
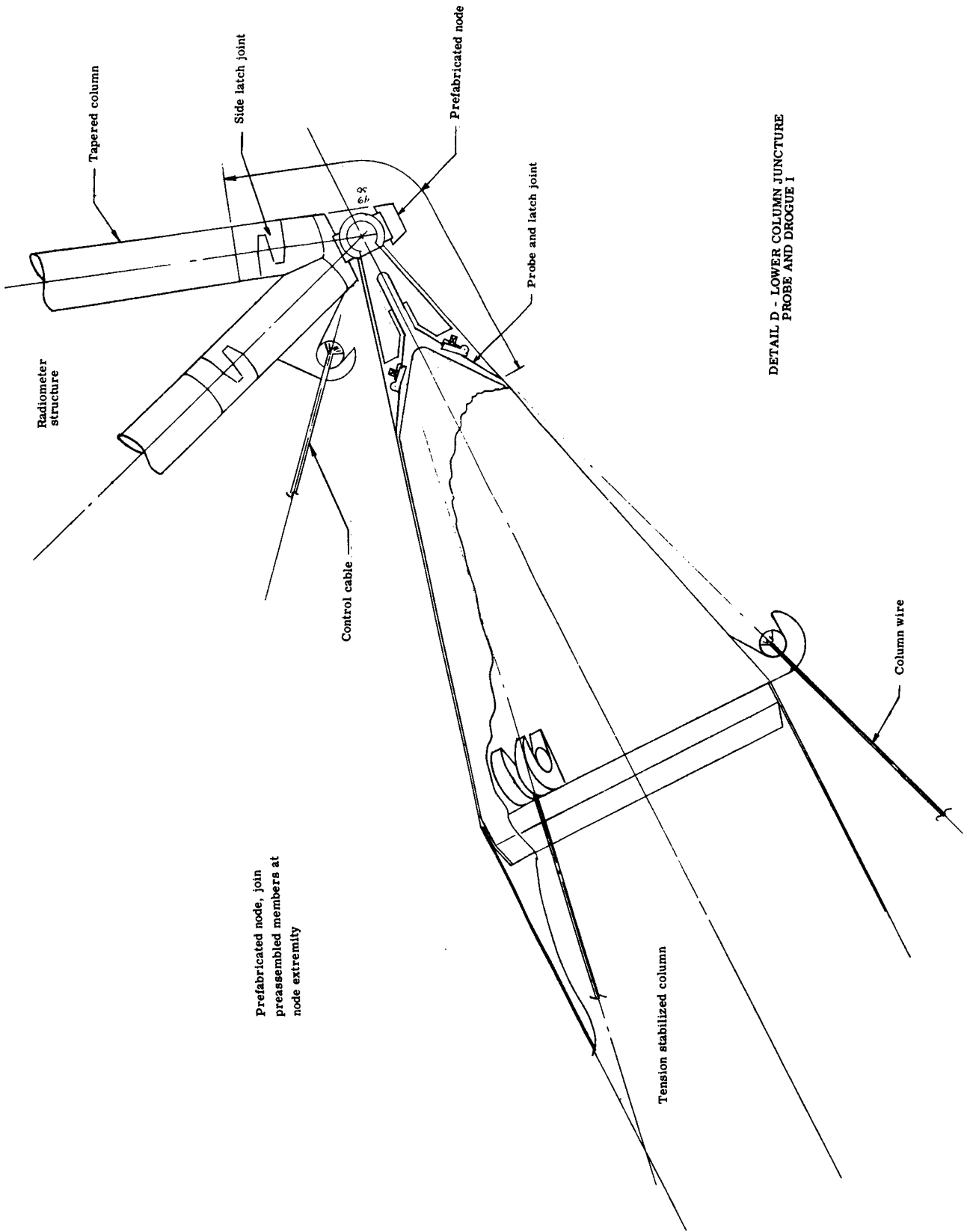
Prefabricated node, join preassembled members at node extremity

Tension stabilized column

Column wire

DETAIL D - LOWER COLUMN JUNCTURE
PROBE AND DROGUE I

Drawing 9

Side latching joint

Radiometer
structure

Control cable

Tension stabilized
columns
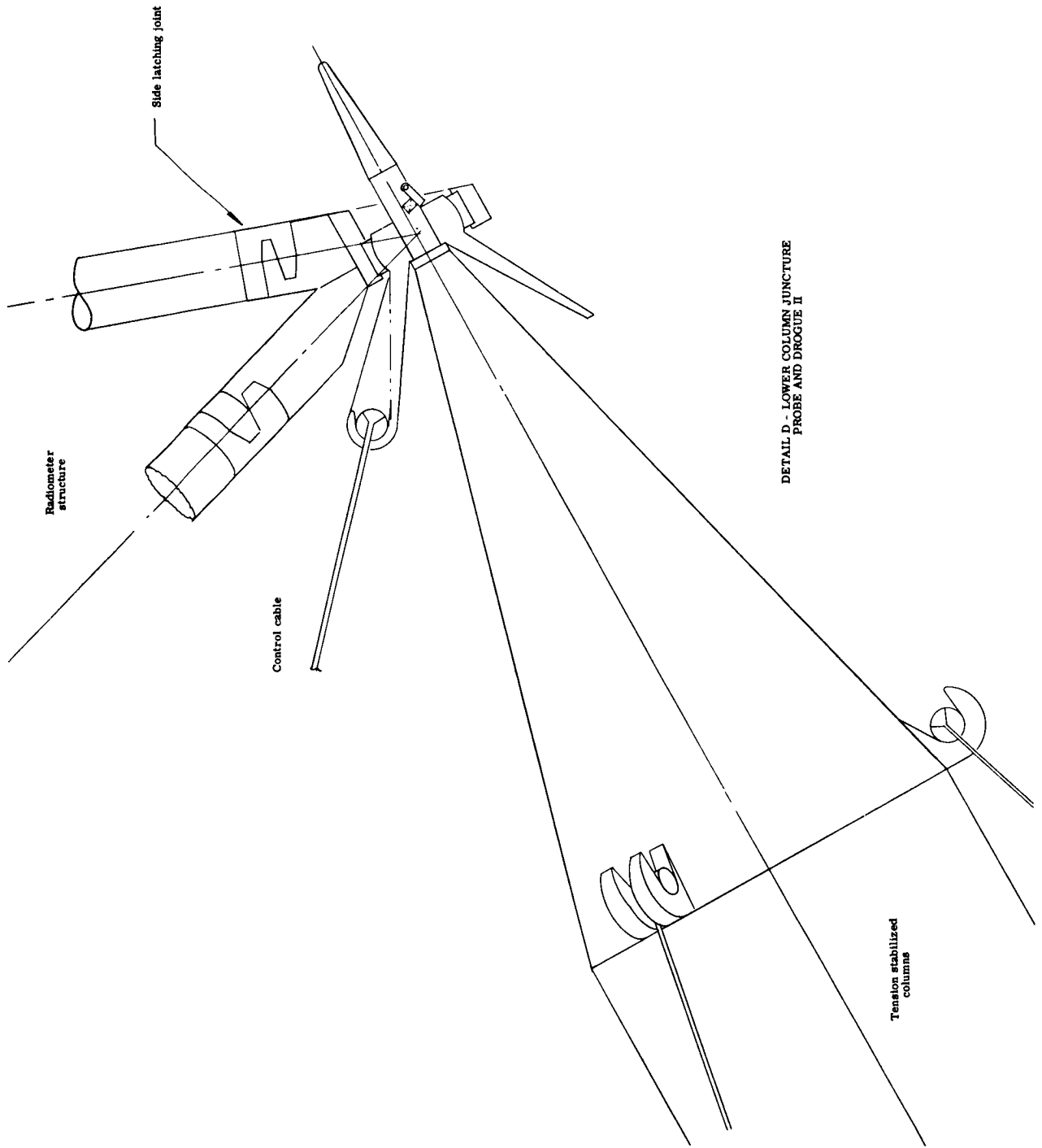
DETAIL D - LOWER COLUMN JUNCTURE
PROBE AND DROGUE II

Drawing 10

232
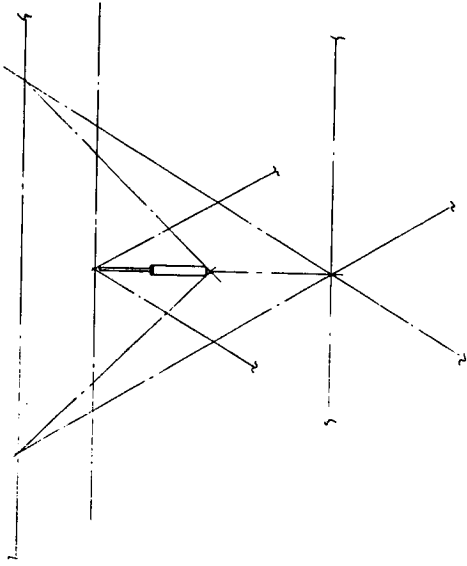
COARSE POINTING ACTUATOR
FIXED MOUNT

Detail E

Dish reflector

See detail F

Support ring

5.0 m total
travel

Linear actuator
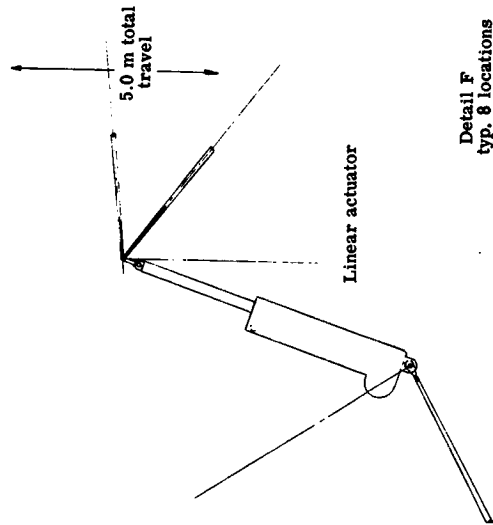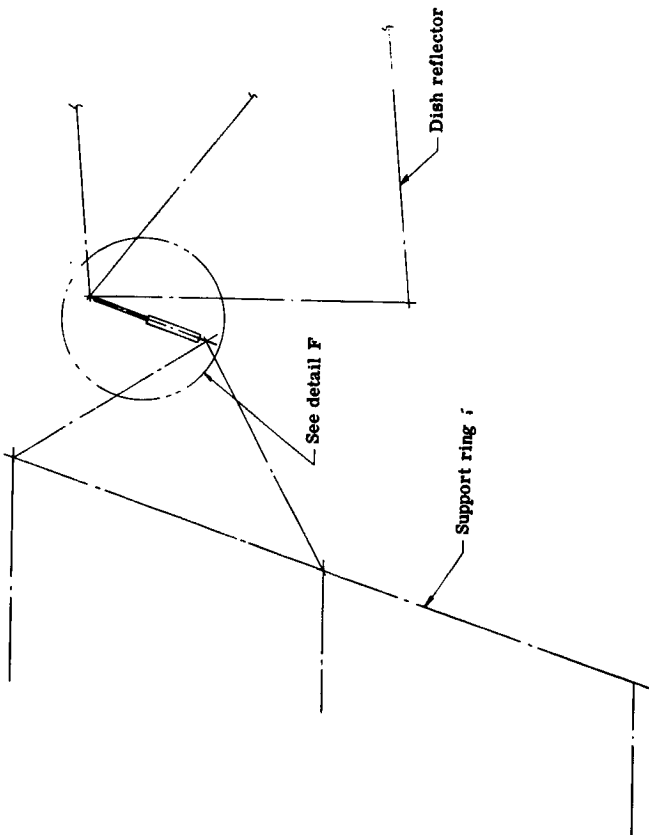
Detail F
typ. 8 locations

Drawing 11

Dish reflector

Detail E

See detail G

Support ring
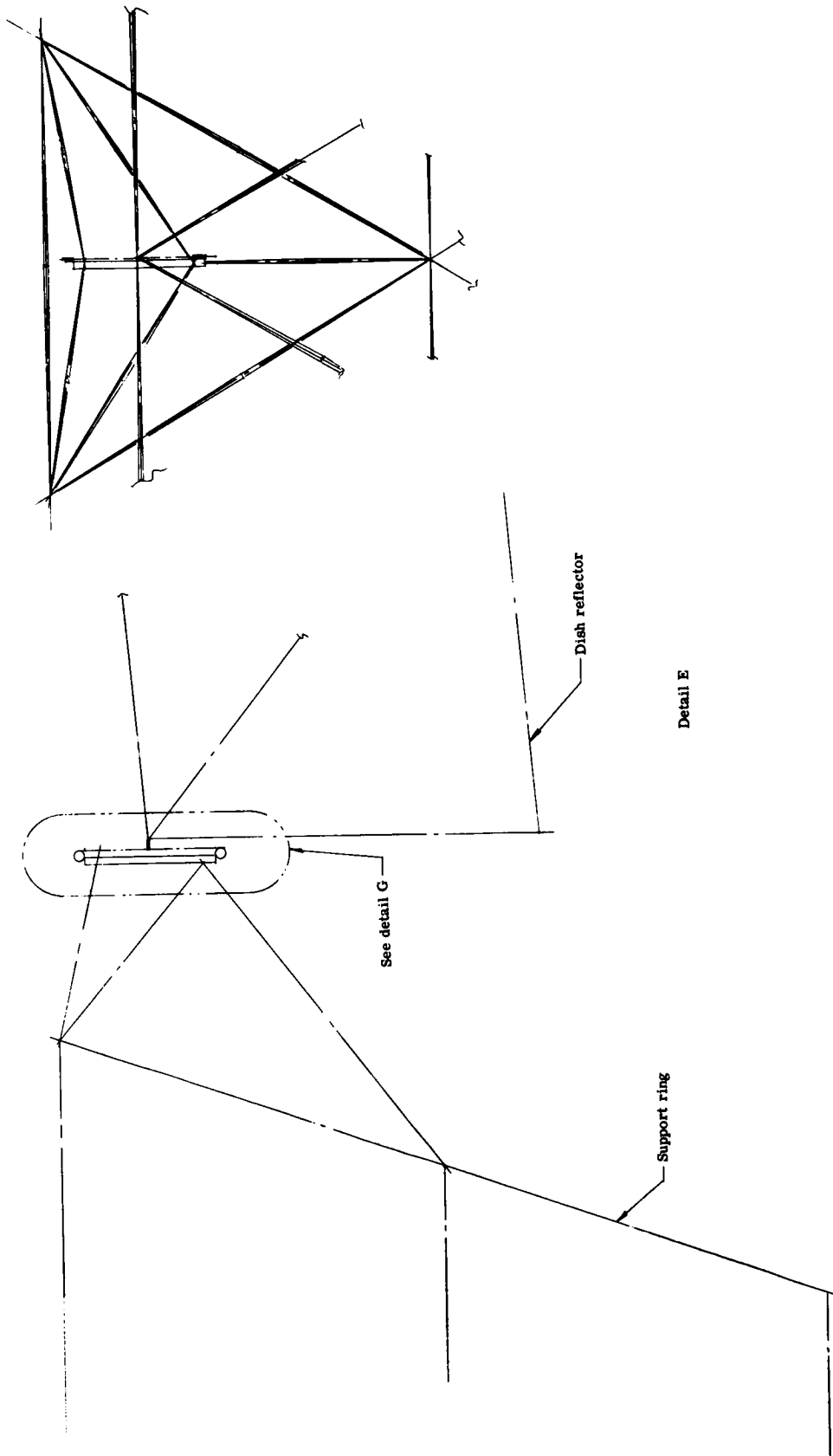
Drawing 12

COARSE POINTING ACTUATOR,
FLEXIBLE MOUNT
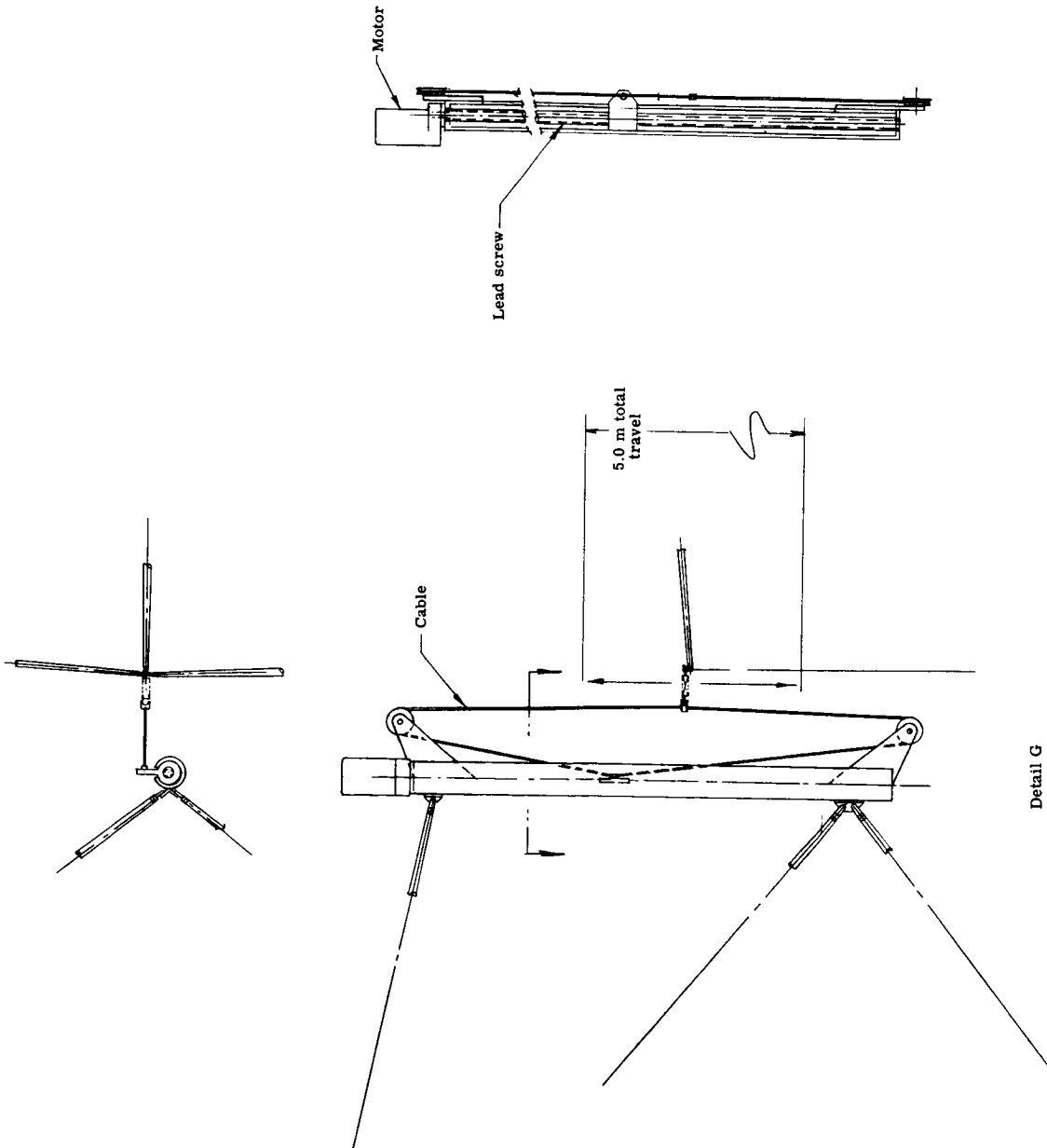
Motor

Lead screw

5.0 m total
travel

Cable

Detail G

Drawing 12

579.53 m

See detail P,
drawing 14

Tension stabilized
740 kg

See detail Q,
drawing 15

Column 4
2758 kg

See detail R,
drawing 16

Column 3
2068 kg

MAIN COLUMNS

Drawing 13

7.50 m diam.

6.50 m. ref.

1.68 m diam.

DETAIL R

Column 3

1.68 m diam.

Tension stabilized

28 m

DETAIL P

Drawing 14

237

View S-S

7.50 m diam.
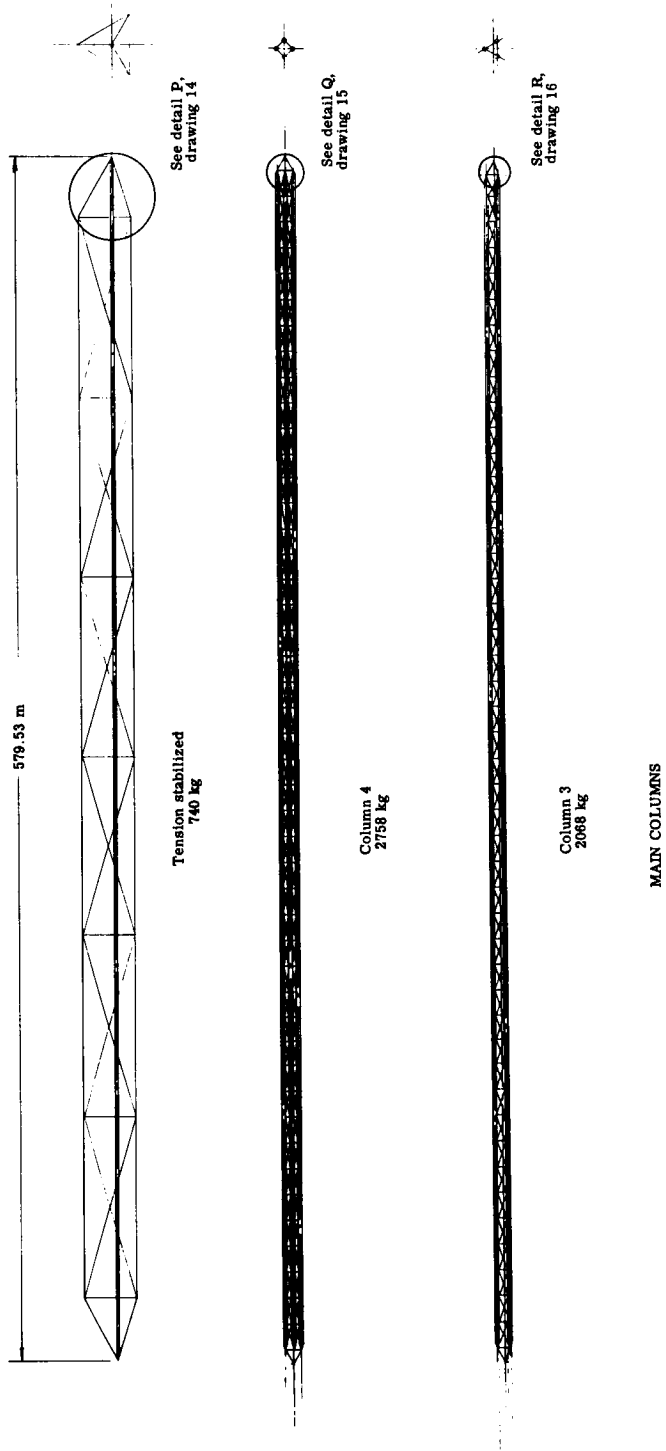
Column 4

1.68 m diam.
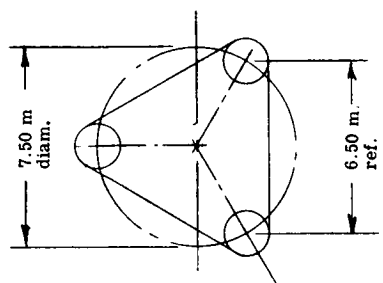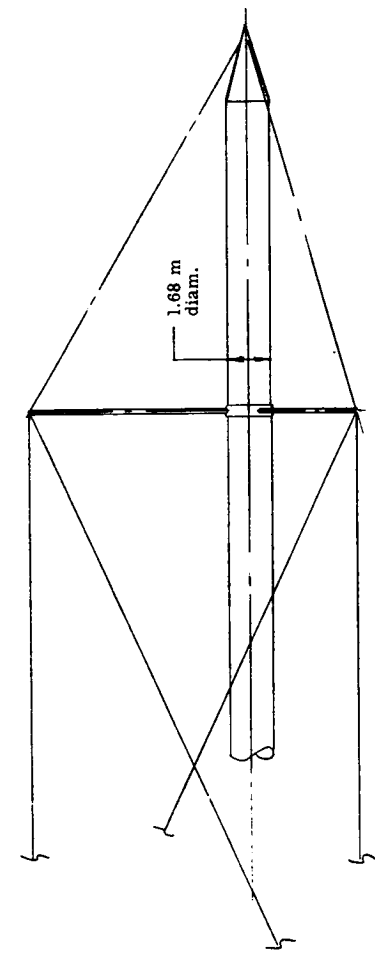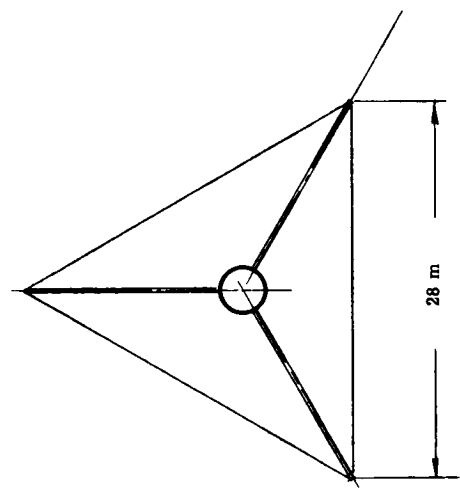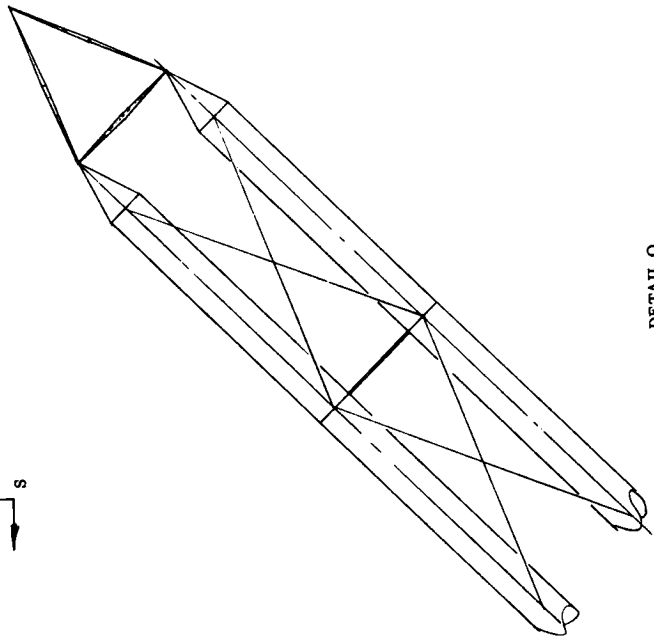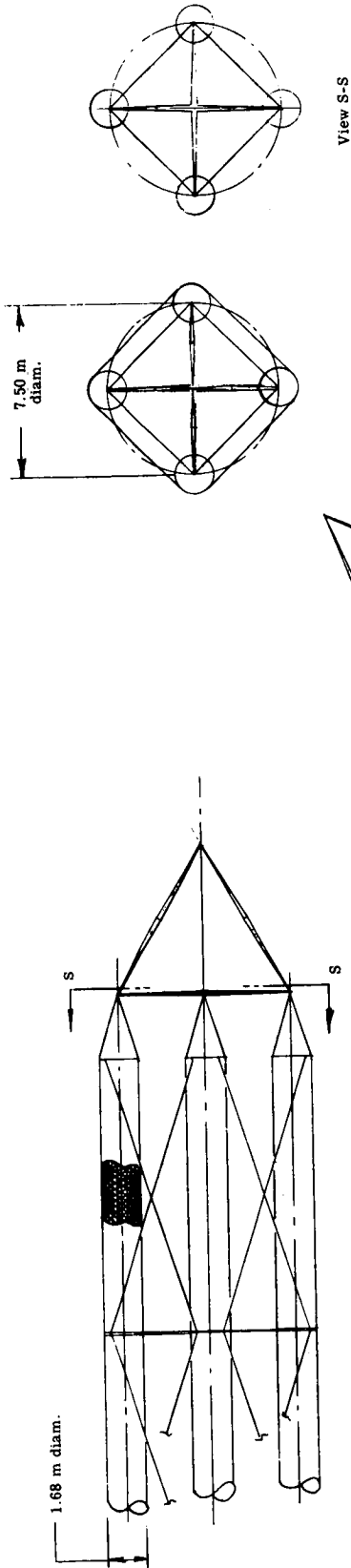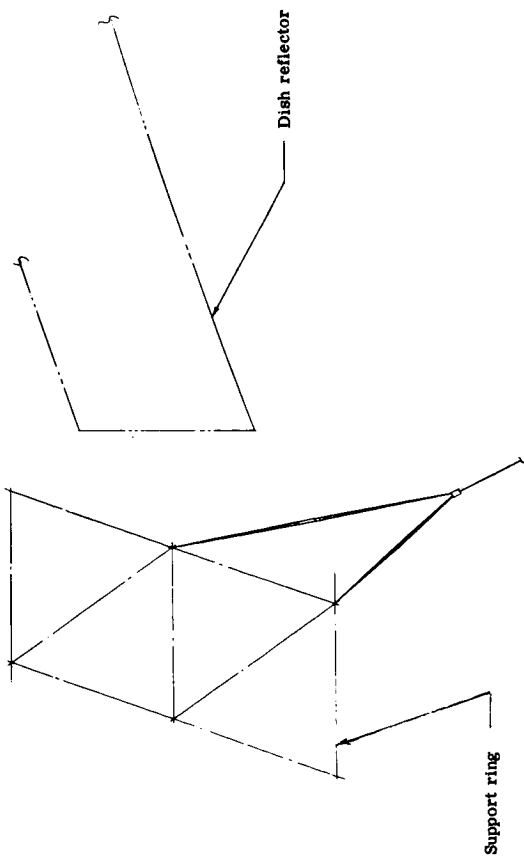
DETAIL Q

Drawing 15

CONTROL CABLE ATTACHMENT

Dish reflector

Support ring

See node detail
drawing 18

See detail B
drawing 17

View A-A
(rotated 180°)

Drawing 16

239

Main tension cables
Kevlar fiber

Feed and control drum

Cable
storage drum

1.02 m

.7 m

Motor

Control unit and
gear box

Honeycomb
platform

CONTROL SYSTEM
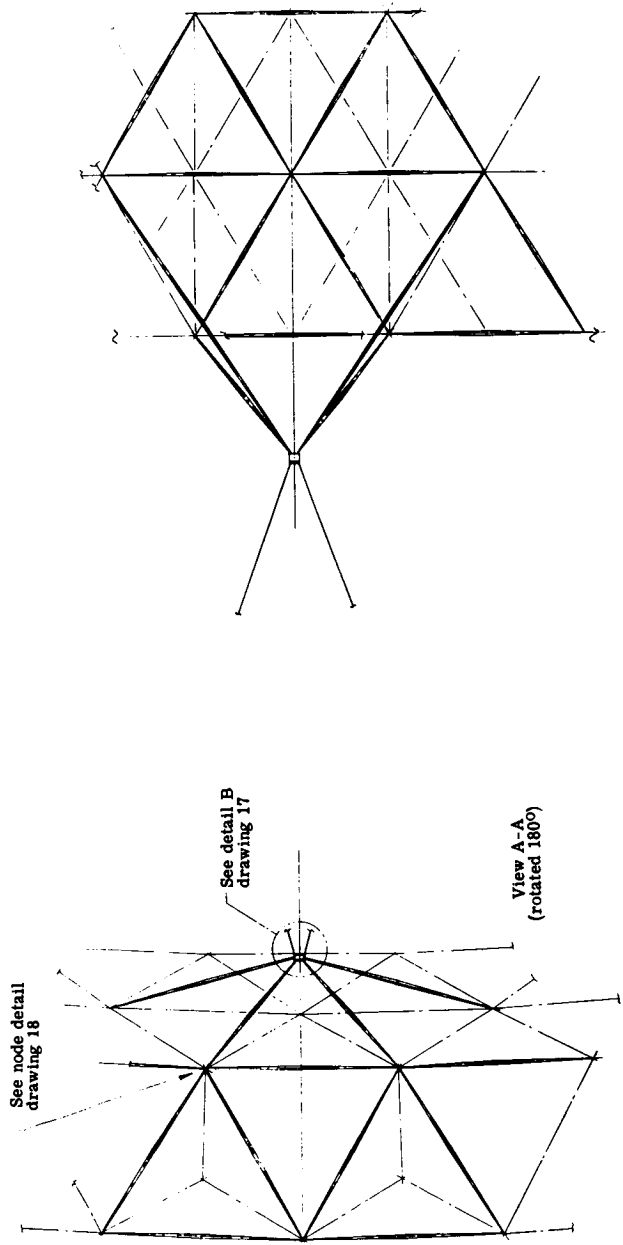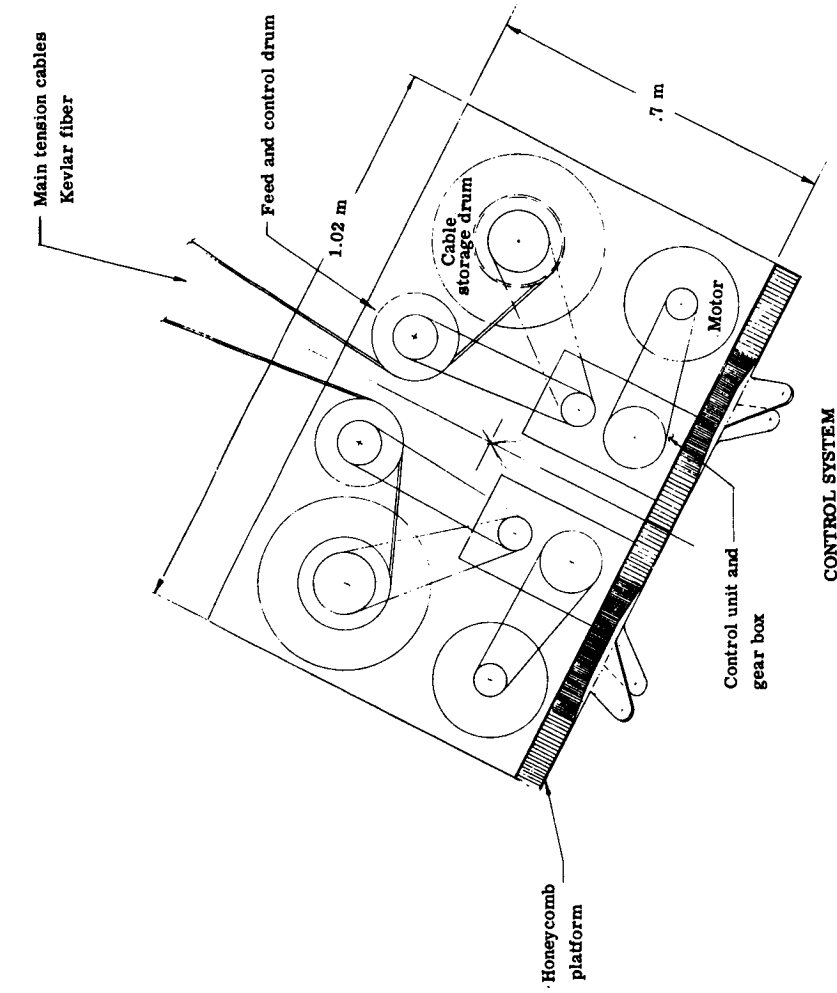
CABLE TENSIONING SYSTEM
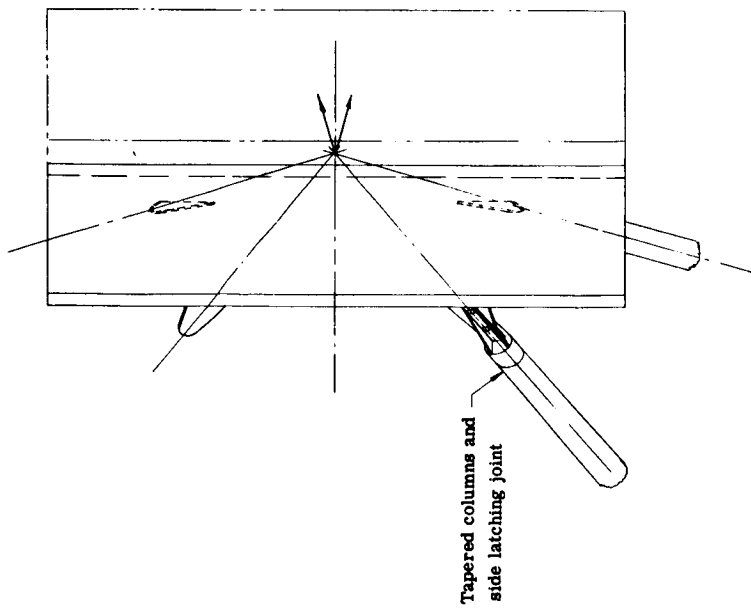
Tapered columns and
side latching joint
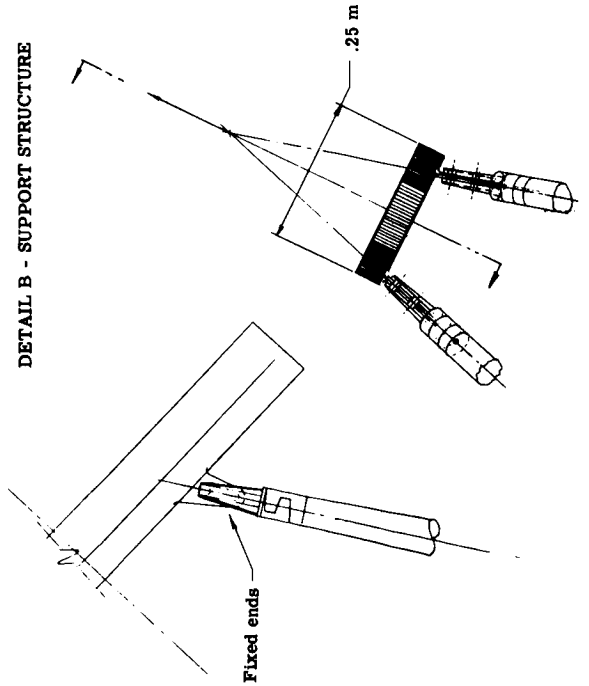
DETAIL B - SUPPORT STRUCTURE

.25 m

Fixed ends

Drawing 17

Side latching joint

Special attachment joint

5.08 cm
diam.

.25 cm wall
thickness

.25 cm
ref.

See detail S

Tapered
column element
ref.

Metal
insert

Detail S
Alternate construction
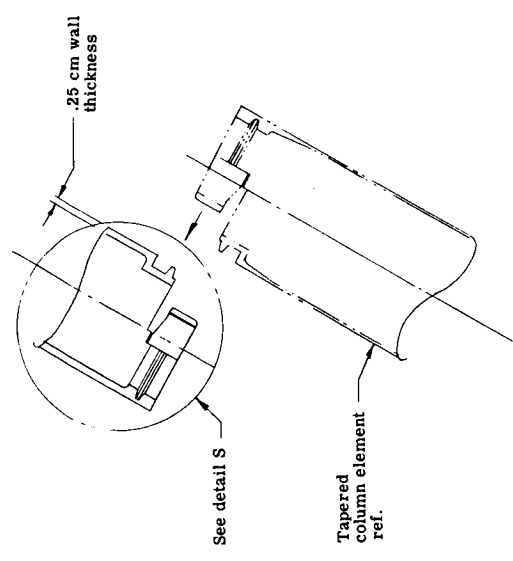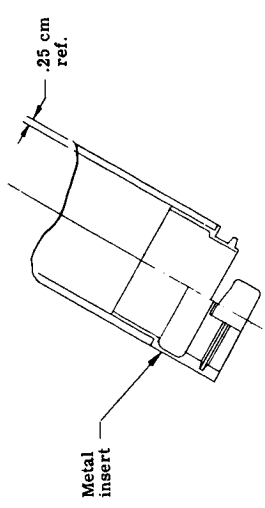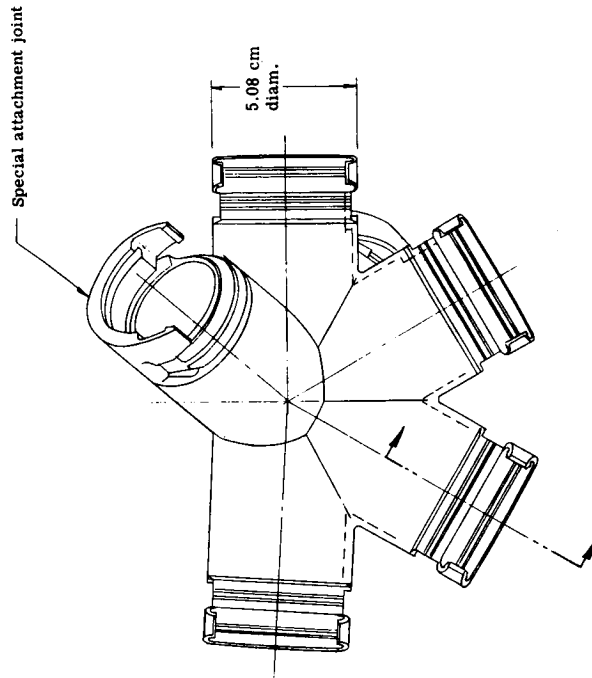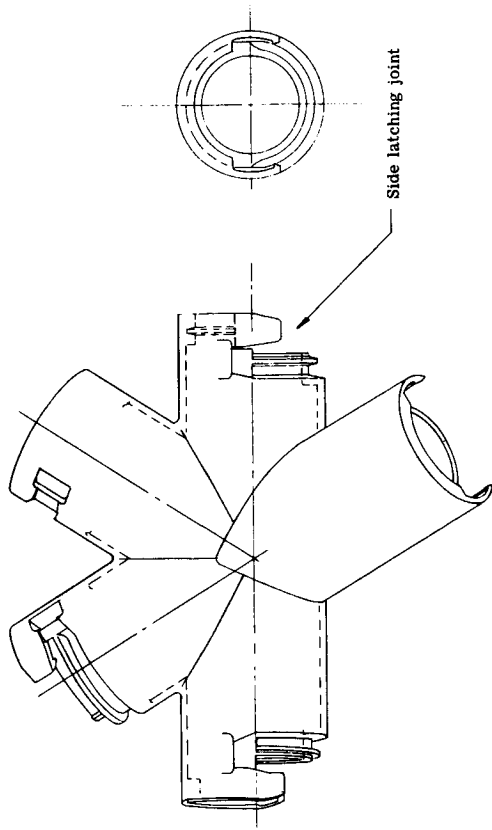
ONE-PIECE NODE
ALL TETRAHEDRAL TRUSS JOINTS

Drawing 18

Epoxy matrix

Frayed filament

Metal terminal

Kevlar cable
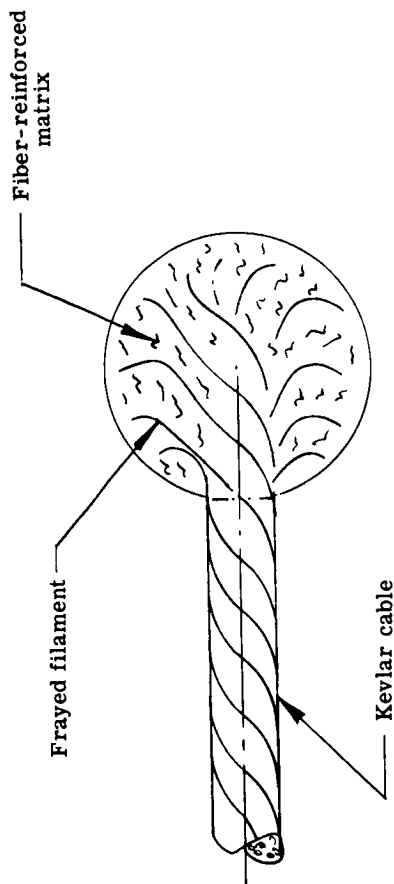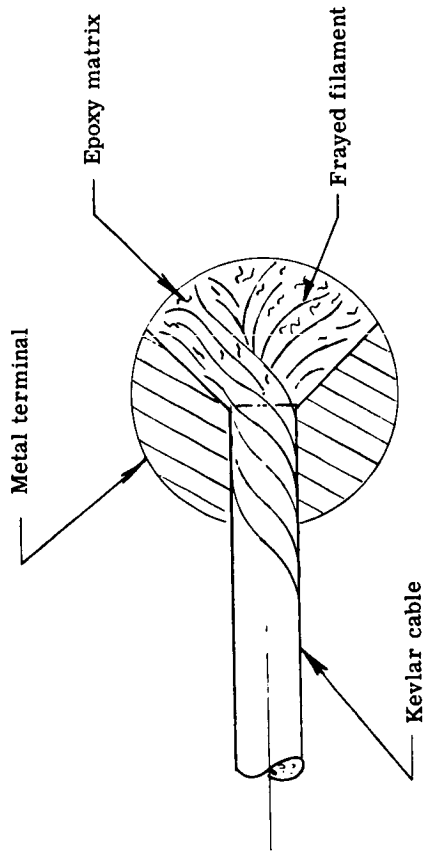
SPHERICAL, METALLIC TERMINAL

Fiber-reinforced matrix

Frayed filament

Kevlar cable

SPHERICAL TERMINAL

Frayed filament

Fiber-reinforced matrix

Limit of matrix

Kevlar cable

LUG OR CLEVIS TERMINAL

Drawing 19

Either a lug or clevis
configuration is possible

Composite
matrix

Bond line

Composite
matrix

Kevlar cable
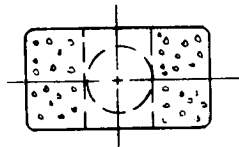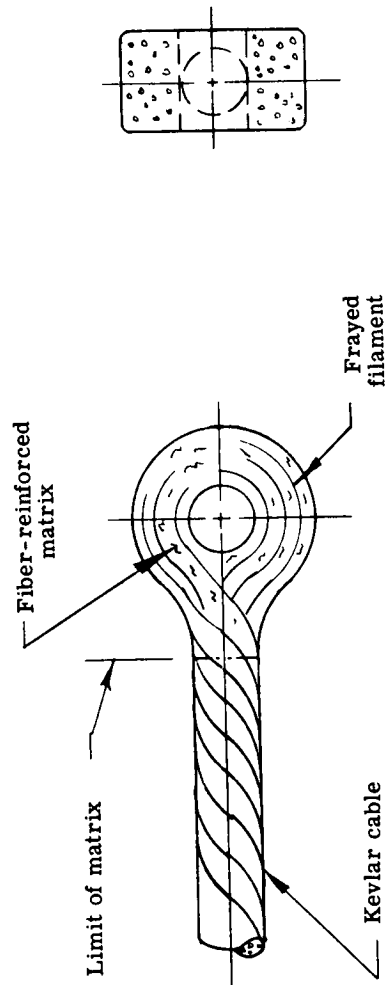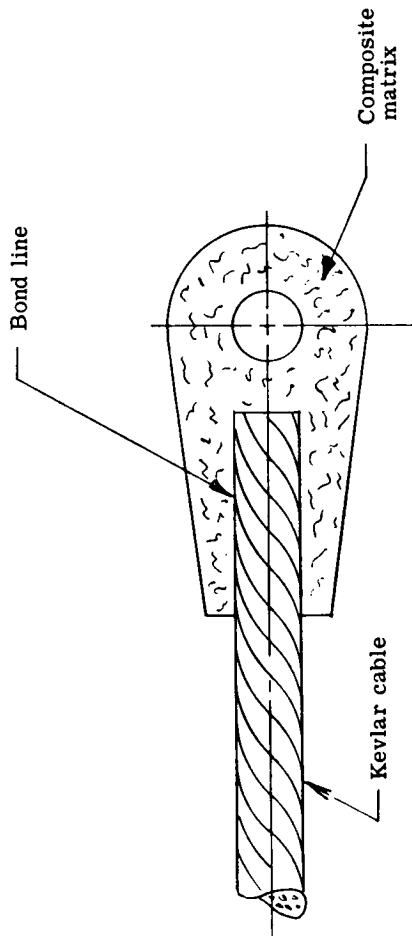
BONDED TERMINAL
(MOULDED SEPARATELY)

Limit of matrix

Kevlar cable
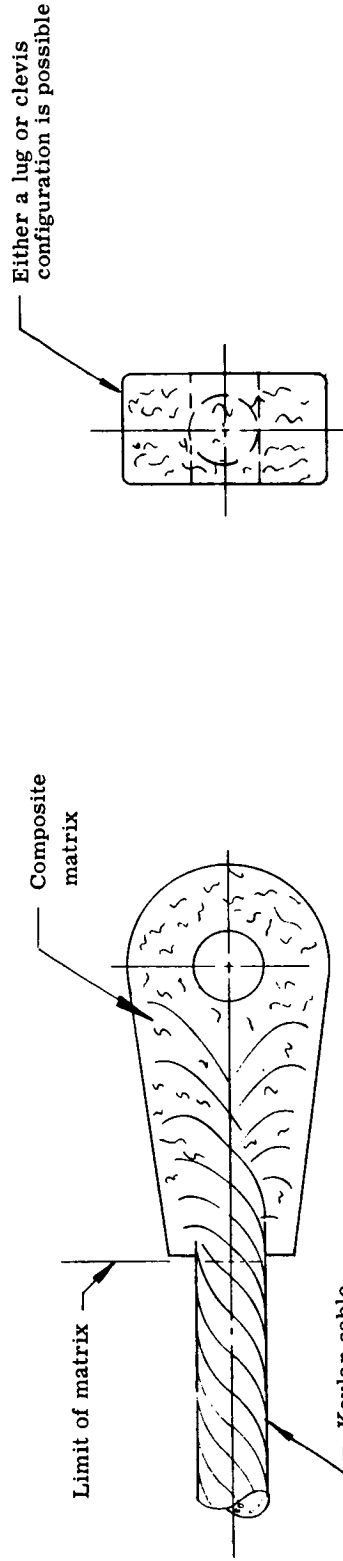
MOULDED-IN-PLACE TERMINAL

Drawing 19

1. Report No. NASA RP-1079	2. Government Accession No.	3. Recipient's Catalog No.
4. Title and Subtitle THE MICROWAVE RADIOMETER SPACECRAFT A Design Study		5. Report Date December 1981
		6. Performing Organization Code 506-62-43-01
7. Author(s) Robert L. Wright, editor		8. Performing Organization Report No. L-14258
		10. Work Unit No.
9. Performing Organization Name and Address NASA Langley Research Center Hampton, VA 23665		11. Contract or Grant No.
		13. Type of Report and Period Covered Reference Publication
12. Sponsoring Agency Name and Address National Aeronautics and Space Administration Washington, DC 20546		
		14. Sponsoring Agency Code

15. Supplementary Notes

16. Abstract

A large passive microwave radiometer spacecraft with near all-weather capability of monitoring soil moisture for global crop forecasting has been designed. The design, emphasizing large space structures technology, characterized the mission hardware at the conceptual level in sufficient detail to identify enabling and pacing technologies. The study concentrated on those research areas requiring the most intense attention: mission and spacecraft requirements, design and structural concepts, electromagnetic concepts, and control concepts. The results of the study in these research areas are presented in 14 papers authored by members of the design study team. Drawings of the baseline spacecraft design are included in an appendix.

17. Key Words (Suggested by Author(s)) Spacecraft design Spacecraft control Large space structures technology Spacecraft antennas Microwave radiometer Mission requirements	18. Distribution Statement Unclassified - Unlimited Subject Category 18

19. Security Classif. (of this report) Unclassified	20. Security Classif. (of this page) Unclassified	21. No. of Pages 250	22. Price All